A STRUCTURAL, ELECTROCHEMICAL AND KINETIC INVESTIGATION OF FLUORINATED AND METALLOCENE-CONTAINING PHOSPHINES AND THEIR RHODIUM COMPLEXES

A thesis submitted in accordance with the requirements for the degree

Philosophiae Doctor

in the

Faculty of Natural and Agricultural Science

Department of Chemistry

at the

University of the Free State

by

Eleanor Fourie

Promoter

Prof. J.C. Swarts

March 2008

Aan my Ouma Lenie

27 September 1916 – 7 November 2007

"U is my toevlug en my veilige vesting, my God op wie ek vertrou."
<div align="right">Psalm 91:2</div>

Dankbetuigings

My opregte dank aan die Here wat my die geleentheid en vermoëns gebied het om sy wonderlike skepping te kan bestudeer, asook vir Sy krag wat my deur elke dag gedra het.

Ek bedank graag Prof. Jannie Swarts vir die uitstekende voorbeeld wat hy stel, asook vir al sy kosbare tyd wat hy afgestaan het en al die kennis wat hy met my gedeel het. Ek bedank ook graag Dr. J. Conradie vir al haar hulp tydens die studie.

My dank gaan ook aan die volgende persone vir hulle insette in die studie:

Prof. D. Lorcy, van die Universiteit van Rennes, Frankryk, wat die tetrathiofulvaleen-bevattende ligande verskaf het.

Prof. C.E.J. Medlen, van die Departement Farmakologie by die Universiteit van Pretoria, vir die uitvoer van sitotoksiese toetse en die opstel van oorlewingsgrafieke. Mnr. J.M. Janse van Rensburg en Dr. A.J. Muller vir die bepaling en oplos van kristalstrukture.

Die NRF vir finansiële steun.

My dank ook aan al die lede van die Fisiese Chemie groep.

Aan my vriende, Lizzie, Frenchie, Nicoline, Nicola, Zeldy, Lizette J en Inus, dankie vir al die ondersteuning en goeie tye.

Aan my ouers, dankie vir julle onvoorwaardelike liefde en ondersteuning.

Eleanor Fourie

Maart 2008

Contents

Chapter 3   Results and Discussion

Abstract

Opsomming

List of Structures

R = CF$_3$ (**1**), CCl$_3$ (**2**),
   CH$_3$ (**3**), (C$_6$F$_5$) (**4**),
   {(C$_5$H$_4$)Fe(C$_5$H$_5$)} (**5**),
   {(C$_5$H$_4$)Ru(C$_5$H$_5$)} (**6**),
   {(C$_5$H$_4$)Os(C$_5$H$_5$)} (**7**)
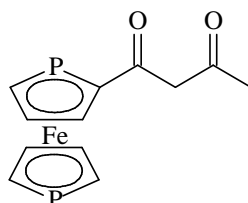
(**8**)
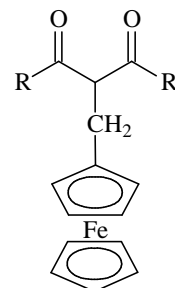
R = R' = CH$_3$ (**9**),
R = R' = Ph (**10**),
R = R' = C(CH$_3$)$_3$ (**11**),
R = Ph, R' = CH$_3$ (**12**)
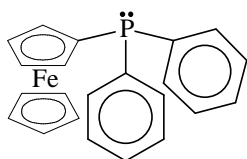
(**13**)
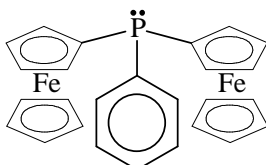
(**14**)
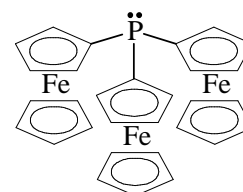
(**15**)
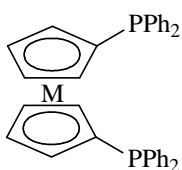
M = Fe (**16**),
   Ru (**17**),
   Os (**18**)

(**19**)
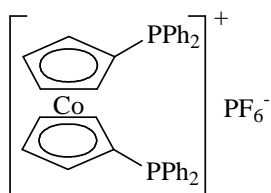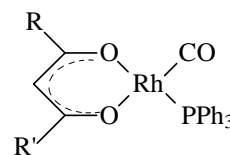
R = CF$_3$, R' = (thiophene) (**20**),
R = CH$_3$, R' = CH$_3$ (**21**),
R = CF$_3$, R' = CH(CH$_3$)$_2$ (**22**),
R = CF$_3$, R' = C(CH$_3$)$_3$ (**23**),
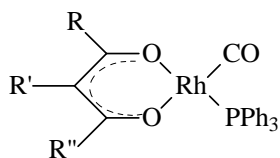
R = CF$_3$, R' = H, R" = CH$_3$ **(24)**,
R = CF$_3$, R' = H, R" = CH$_2$CH$_3$ **(25)**,
R = CH$_3$, R' = CH$_2$(C$_6$H$_5$), R" = CH$_3$ **(24)**,
R = C$_6$H$_5$, R' = H, R" = C$_6$H$_5$ **(27)**
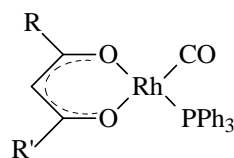
R = Fc, R' = CH$_3$ **(28)**,
R = Fc, R' = CF$_3$ **(29)**,
R = Fc, R' = C$_6$H$_5$ **(30)**,
R = Fc, R' = Fc **(31)**
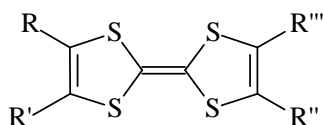
R = R' = PPh$_2$, R" = R''' = Me **(32)**,
R = R" = PPh$_2$, R' = R''' = Me **(33)**,
R = S((CH$_2$)$_3$)PPh$_2$, R' = R" = R''' = Me **(34)**,
R = R" = S((CH$_2$)$_3$)PPh$_2$, R' = R''' = Me **(35)**
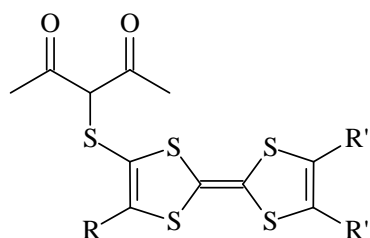
R = R' = R" = Me **(36)**,
R = R" = Me, R' = Sacac **(37)**,
R = R" = Me, R' = SMe **(38)**,
R = R' = R" = SMe **(39)**,
R = H, R' = R" = SMe **(40)**
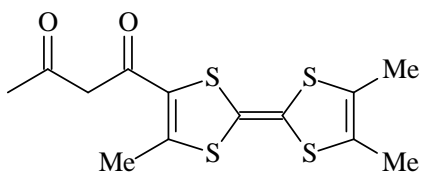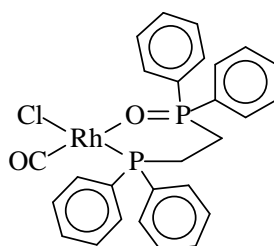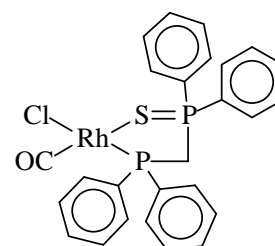
(41)   **(42)**   **(43)**
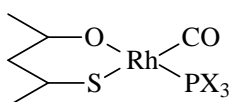
(44)   **(45)**   **(46)**

R = CF$_3$ **(47)**, CCl$_3$ **(48)**,
   CH$_3$ **(49)**, Ph **(50)**, Fc **(51)**
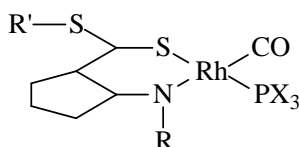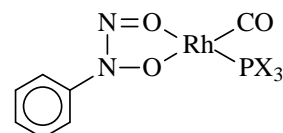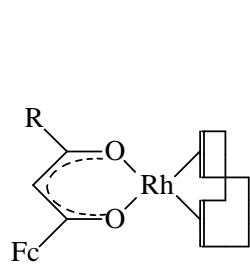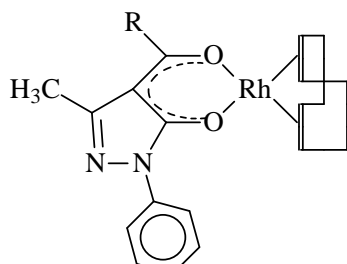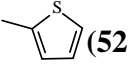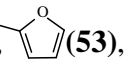
R' = (thienyl) **(52)**, (furyl) **(53)**,
   (neopentyl) **(54)**
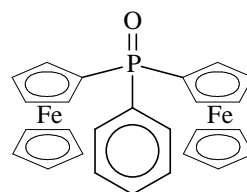
(55)
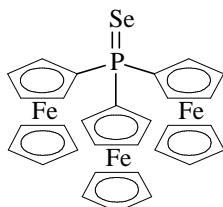
(56)
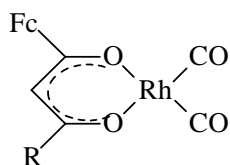
R = CF$_3$ **(57)**, R = CH$_3$ **(58)**,
R = C$_6$H$_5$ **(59)**, R = Fc **(60)**
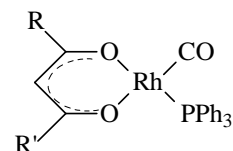
R = C$_6$H$_5$, R' = CH$_3$ **(61)**,
R = C$_6$H$_5$, R' = CF$_3$ **(62)**
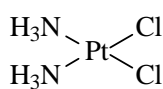
(63)
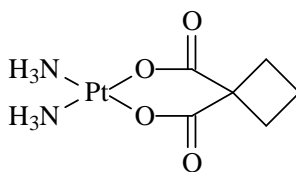
(64)
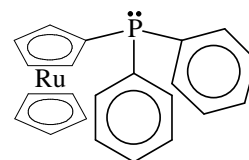
(65)
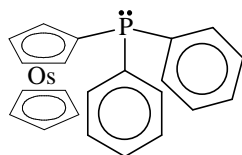
(66)
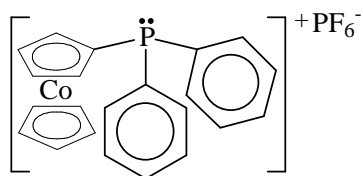
(67)
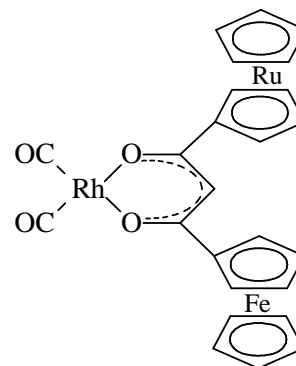
(68)
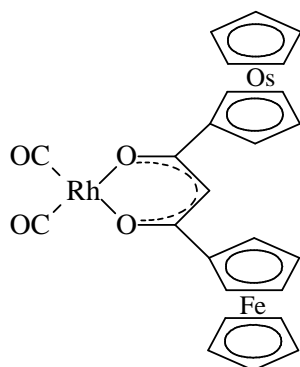
(69)
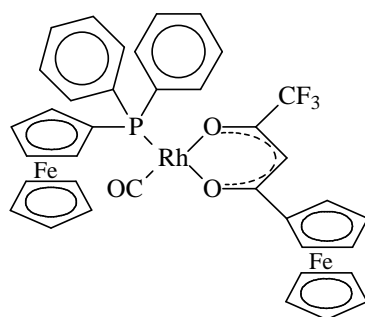
(70)

(71)

(72)

(73)

(74)

(75)

(76)

(77)

(78)   **(79)**   **(80)**

(81)   **(82)**   **(83)**

(84)   **(85)**   **(86)**
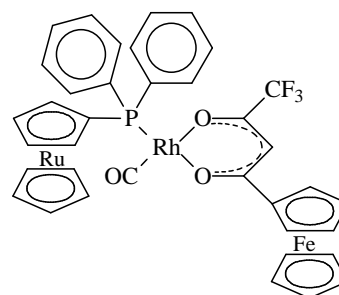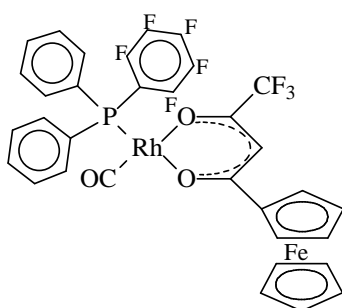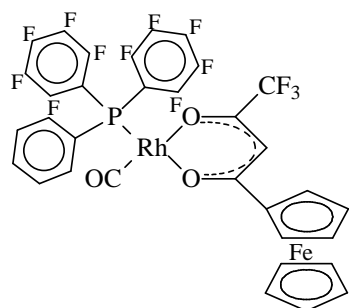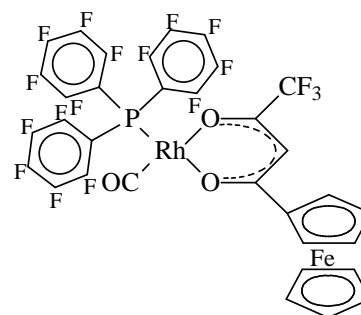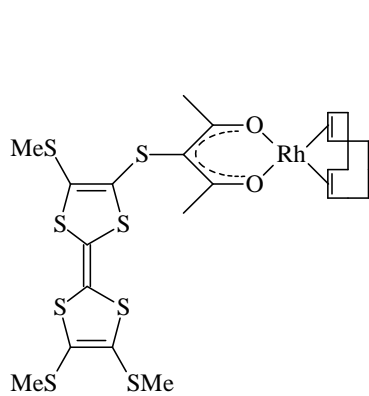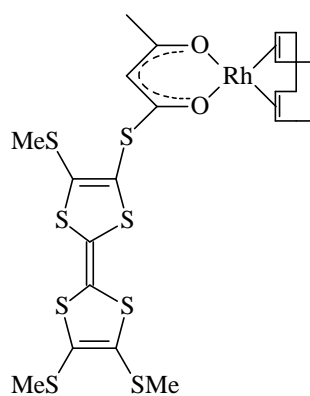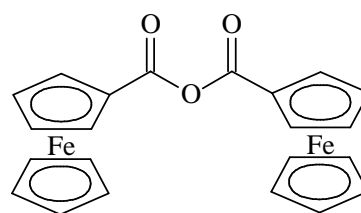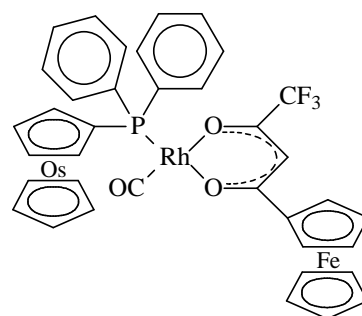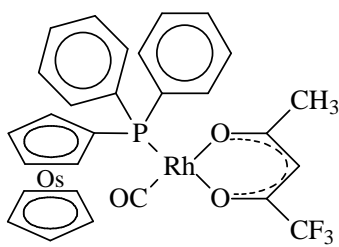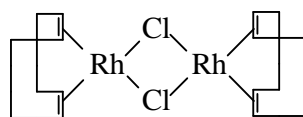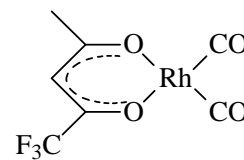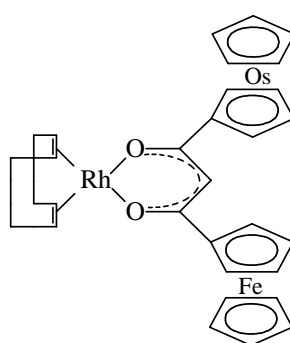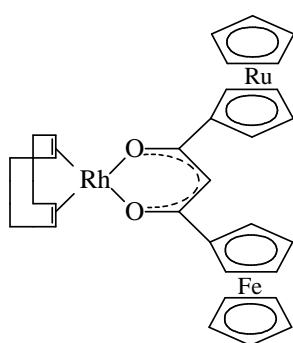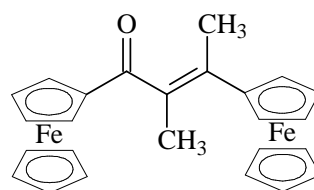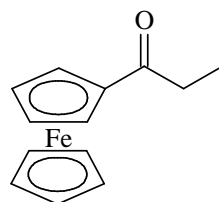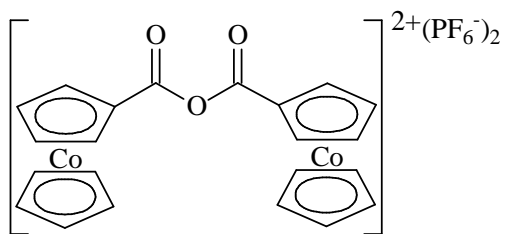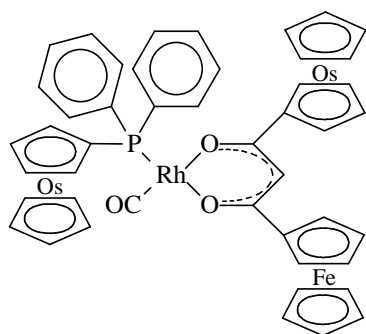
(87)
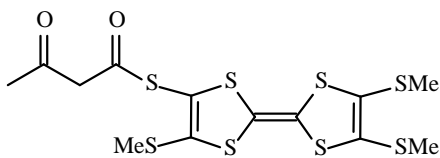
(88)
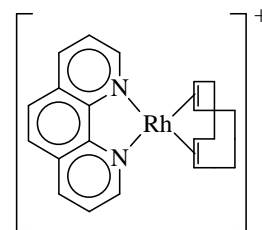
(89)
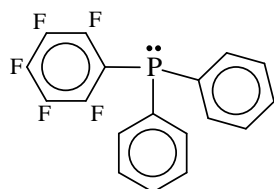
(90)
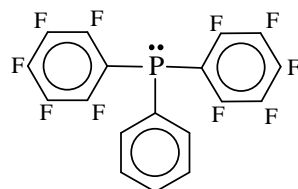
(91)
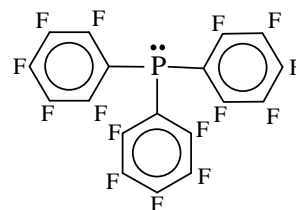
(92)
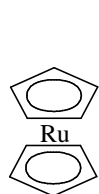
(93)
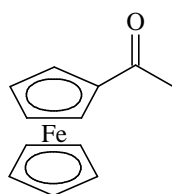
(94)
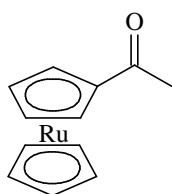
(95)
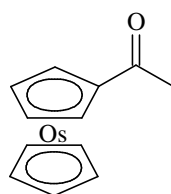
(96)
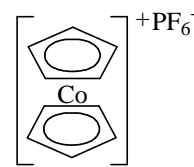
(97)
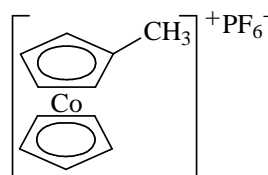
(98)
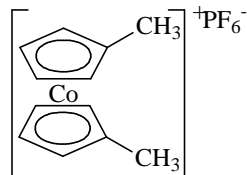
(99)
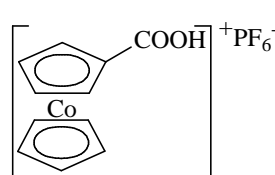
(100)
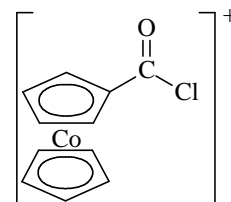
(101)
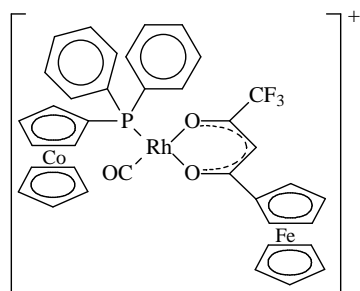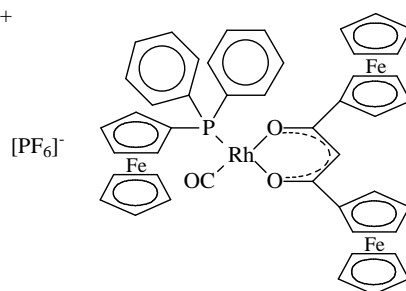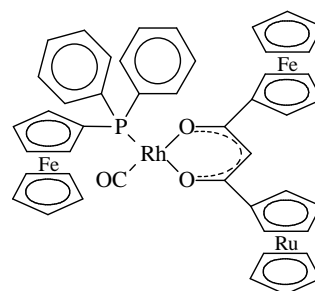
(102)　　　　　　　　**(103)**　　　　　　　　**(104)**
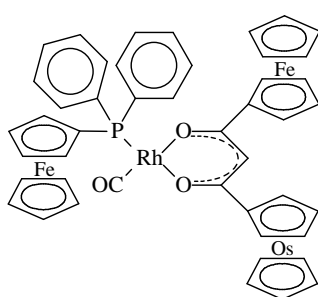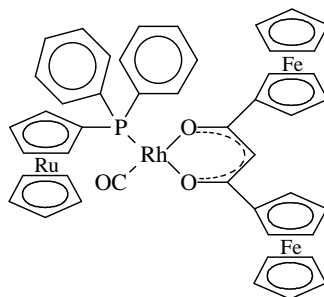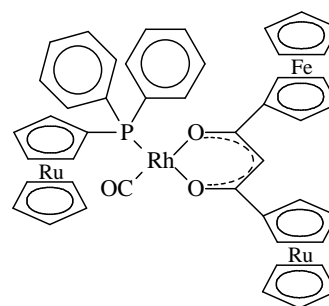
(105)　　　　　　　　**(106)**　　　　　　　　**(107)**
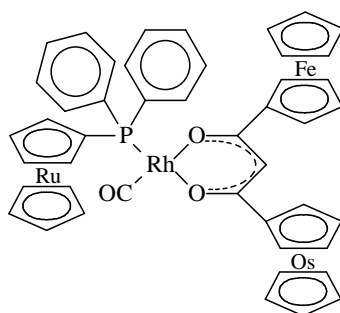
(108)

List of Abbreviations

A	absorbance
Å	angstrom
acac	acetylacetonato
$AlCl_3$	aluminum trichloride
BF_3	boron trifluoride
bipy	2,2'-bipyridyl
BuLi	butyl lithium
Cc^+	cobaltocenium
C_6F_5	pentafluorophenyl
$CHCl_3$	chloroform
CH_2Cl_2	dichloromethane
CH_3CN	acetonitrile
cisplatin	*cis*-diamminedichloroplatinum(II)
CO	carbon monoxide or carbonyl
cod	1,5-cyclooctadiene
CoLo	human colorectal cell line
cp	cyclopentadienyl
CV	cyclic voltammetry
δ	chemical shift
DCM	dichloromethane
DMF	dimethylformamide
DMP	Dess-Martin periodinnane
DMSO	dimethyl sulfoxide
$[(dppc^+)PF6^-]$	1,1'-bis(diphenylphosphino)cobaltocenium hexafluorophosphate
dppe	1.2-bis(diphenylphosphino)ethane
dppf	1,1'-bis(diphenylphosphino)ferrocene
dppo	1,1'-bis(diphenylphosphino)osmocene
dppr	1,1'-bis(diphenylphosphino)ruthenocene
ε	molar extinction coefficient

$E^{o'}$	formal reduction potential
E_a	energy of activation
E_{pa}	anodic peak potential
E_{pc}	cathodic peak potential
ΔE_p	separation of anodic peak and cathodic peak potentials
Et	ethyl
EtOH	ethanol
eq	equivalents
F	Faraday constant
Fc	ferrocene or ferrocenyl
Fc^*	decamethyl ferrocene
FT-IR	Fourier transform infra-red spectroscopy
ΔG^*	Gibbs free energy of activation
h	Planck's constant
ΔH^*	enthalpy of activation
HeLa	human cervix epitheloid cancer cell line
HMPA	hexamethylphosphoric triamide
H_3PO_4	phosphoric acid
IC_{50}	drug dose required to kill 50 % of cancer cells
i_{pa}	anodic peak current
i_{pc}	cathodic peak current
J	coupling constant
k	rate constant
k_b	Boltzmann constant
K_c	equilibrium constant
k_{obs}	observed rate constant
l	path length
LDA	lithium diisopropylamine
LSV	linear sweep voltammetry
M	central metal atom
Mc	metallocene or metallocenyl

Me	methyl
MeOH	methanol
MeI	methyl iodide
N	Avogadro's constant
$[NBu_4][B(C_6F_5)_4]$	tetrabutylammonium tetrakis(pentafluorophenyl)borate
$[NBu_4][PF_6]$	tetrabutylammonium hexafluorophosphate
NMR	nuclear magnetic resonance spectroscopy
Oc	osmocene or osmocenyl
Ph	phenyl
phen	1,10-phenanthroline
pKa	- log K_a, K_a = acid dissociation constant
$PPh_2Cc^+PF_6^-$	diphenylphosphinocobaltocenium hexafluorophosphate
PPh_2Cl	chlorodihenylphosphine
PPh_2Fc	ferrocenyldiphenylphosphine
PPh_2Oc	osmocenyldiphenylphosphine
PPh_2Rc	ruthenocenyldiphenylphosphine
PPh_3	triphenylphosphine
ppm	parts per million
R	gas constant
Rc	ruthenocene or ruthenocenyl
$RhCl_3.3H_2O$	rhodium trichloride
S	solvent
ΔS^*	entropy of activation
SCE	saturated calomel electrode
S_N2	bimolecular nucleophilic substitution
$SOCl_2$	thionyl chloride
SW	square wave voltammetry
t	time
T	temperature
THF	tetrahydrofuran
TTF	tetrathiafulvalene

UV/vis	ultraviolet/visible spectroscopy
υ	infrared stretching frequency
υ	scan rate
ΔV^{*}	volume of activation
X	halogen
χ_R	group electronegativity (Gordy scale) of R group
λ	wavelength

Chapter 1

Introduction and Aim of Study

1.1. Introduction

Platinum group metal complexes are widely used in homogeneous as well as heterogeneous catalysis, in a variety of chemical reactions.[1] Despite problems associated with the purification and separation of products from especially homogeneous catalysts, the high activity and product selectivity that can be achieved by homogeneous catalysis, have allowed platinum group metals to be used extensively in industry. Central to this study are rhodium complexes. Examples of successful rhodium-catalyzed processes are the hydroformylation of alkenes catalyzed by $[RhH(CO)(PPh_3)_3]$, hydrogenation of alkenes in the presence of the well known Wilkinson's catalyst, $[RhCl(PPh_3)_3]$, and the carbonylation of methanol to liberate acetic acid using $[Rh(CO)_2I_2]^-$ in the well known Monsanto process.[2]

The first methanol-to-acetic acid carbonylation process was commercialized by BASF in 1960. It made use of a cobalt catalyst promoted by iodide, and required high temperatures (230°C) and pressures (600 atm). During the 1960's, the Monsanto process was implemented, utilizing the above mentioned rhodium catalyst and operating at much milder conditions (180°C and 40 atm pressure), as well as introducing higher selectivity into the reaction.[3] Despite the improvements, the search for new catalysts operating under milder conditions, has continued. Research has focused on accelerating the rate determining step of the catalytic cycle, which is the oxidative addition of methyl iodide to the rhodium-based catalysts (**Scheme 1.1**). To improve the rhodium-based catalysts, efforts have focused on coordinating more electron-donating ligands to the central rhodium atom, as the increased electron density on the rhodium metal center will increase the rate of the oxidative addition reaction. **Scheme 1.1** shows the catalytic cycle for the conversion of methanol to acetic acid utilizing the rhodium-based catalyst. In contrast,

although electron-withdrawing ligands will slow down the rate of oxidative addition, it will enhance the rate of reductive elimination in the final step of the catalytic cycle. Careful manipulation of the mechanism of oxidative addition will thus have a large influence on the overall efficiency of the catalyst.
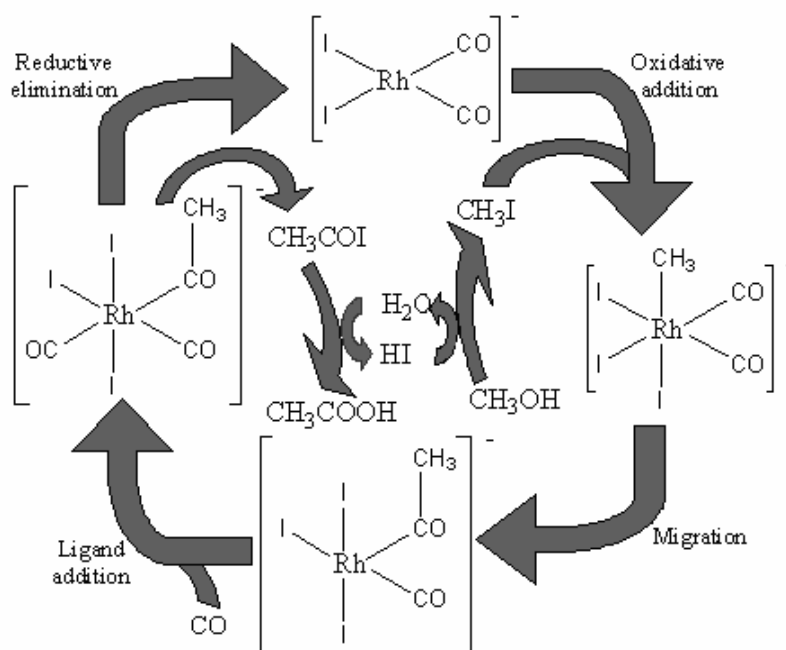
Scheme 1.1. The catalytic cycle of the Monsanto process.

Phosphine ligands generated much interest and a large amount of work has been done on finding new phosphines, with increased electron donor abilities.[4,5] Towards electron-donating ligands, ferrocene-containing phosphine ligands have become very popular in many catalytic processes. The strong electron-donating property of the ferrocenyl group provides the necessary electronic and steric properties to form a highly active and selective catalyst.[6] The question remains unexplained how other metallocene-containing phosphine ligands would influence the rate of oxidative addition during a catalytic cycle.

The platinum group metals are also known for their use in medical applications[1]. Previous work in the UFS research group has described the ferrocenyl- and ruthenocenyl β-diketonato complexes of rhodium as possible anti-cancer drugs.[7] In some cases improved antineoplastic effects over cisplatin [*cis*-diamminedichloroplatinum(II)], the

most widely used metal-containing chemotherapeutic drug, was found.[8] The benefit of these rhodium complexes is lower toxicity, as the use of cisplatin is accompanied with numerous side-effects, and an enhanced activity against platinum resistant cancers. Thus rhodium β-diketonato complexes containing metallocenephosphines could potentially exhibit some anti-cancer properties.

1.2. Aims of study

With the above background, the following goals were set for this study:

1) The synthesis of metallocene-containing β-diketones of the type $FcCOCH_2COR$, where R = CF_3, Fc (ferrocenyl), Rc (ruthenocenyl) and Oc (osmocenyl), *via* known methods, and the synthesis of rhodium complexes, of the type $[Rh(FcCOCHCOR)(CO)_2]$, incorporating these synthesized β-diketones.

2) The synthesis of new and known electron-rich metallocene-containing phosphine ligands of the type $P(Ph)_2R$, where R = Fc (ferrocenyl), Rc (ruthenocenyl), Oc (osmocenyl) and Cc^+ (cobaltocenium), and the synthesis of rhodium phosphine complexes of the type $[Rh(FcCOCHCOCF_3)(CO)(PPh_2R)]$, where R = Fc, Rc and Oc.

3) The synthesis of rhodium phosphine complexes of the type $[Rh(FcCOCHCOR)(CO)\{PPh_n(C_6F_5)_{3-n}\}]$, with $1 \leq n \leq 3$. The electron-withdrawing properties of the pentafluoro phenyl group (C_6F_5) will result in an electron-poor rhodium center.

4) A kinetic study of the oxidative addition reaction between synthesized rhodium phosphine complexes and methyl iodide comparatively studied by FT-IR, UV/vis, ^{1}H NMR, ^{31}P NMR and ^{19}F NMR spectrophotometric techniques.

5) An electrochemical study of all new compounds synthesized.

6) A cytotoxic study of all new ligands and rhodium complexes to determine any antineoplastic activity against cancer cells from human cervix epitheloid (HeLa) and human colorectal (CoLo) cancer cell lines.

[1] J. Conradie, G.J. Lamprecht, S. Otto, J.C. Swarts, *Inorganica Chimica Acta*, 2002, **328**, 191.
[2] M.C. Simpson, D.J. Cole-Hamilton, *Coordination Chemistry Reviews*, 1996, **155**, 163.
[3] C.M. Thomas, G. Süss-Fink, *Coordination Chemistry Reviews*, 2003, **243**, 125.
[4] J. Rankin, A.C. Benyei, A.D. Poole, D.J. Coel-Hamilton, *J. Chem. Soc., Dalton Trans.*, 1999, 3771.

[5] E. Daura-Oller, J.M. Poblet, C. Bo, *J. Chem. Soc., Dalton Trans.*, 2003, 92.

[6] M.D. Sliger, G.A. Broker, S.T. Griffin, R.D. Rogers, K.H. Shaughnessy, *Journal of Organometallic Chemistry*, 2005, **690**, 1478.

[7] W.C. du Plessis, T.G. Vosloo, J.C. Swarts, *J. Chem. Soc., Dalton Trans.*, 1998, 2507.

[8] J.C. Swarts, C.E. Medlen, *European Patent.* EP 1 345 951 B1, bulletin 2004/34, 2004, pp 1-36.

Chapter 2

Literature Survey

2.1. Introduction

This chapter provides a concise literature review on the aims and topics relevant to this study. It covers β-diketone synthesis, phosphine synthesis, rhodium complexation (goals 1-3, Chapter 1), and aspects of rhodium complex kinetics (both substitution and oxidative addition) (goal 4). This is followed by a short appraisal of electrochemical studies (goal 5) and cytotoxic studies (goal 6) of these complexes.

2.2. β - Diketones

The synthesis of β – diketonato complexes has been reported as early as the late 1880's, by Combes[1] as well as Claisen *et al.*[2] β – Diketones can form anions as a result of enolization and ionization, as shown in **Scheme 2.1**, which form very stable chelate complexes with most metals.[3, 4] Thus, the complexes of β – diketones are some of the most widely studied coordination compounds known.[5] It should be pointed out that, although β – diketones are commonly represented in the ketonic form, many of them exist mainly in the enolic form, which is stabilized by a hydrogen bridge.[6]
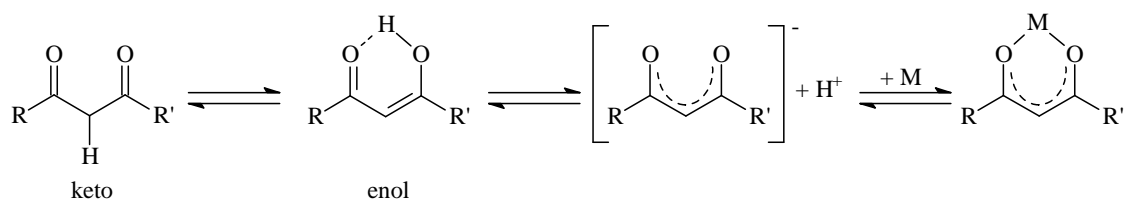
Scheme 2.1. The enolization, ionization and coordination processes of β-diketones.

2.2.1. Synthesis of β – Diketones (basic route)

The most widely used synthetic route for β-diketones is *via* Claisen condensation, which consists of the acylation of a ketone containing an α-hydrogen with either an ester, acid anhydride or acid chloride. This reaction consists of replacing the ketone α-hydrogen

with an acyl group.[7] Generally, the reaction is effected by reacting a ketone and ester in the presence of a strong base, such as sodium, sodium ethoxide, sodium amide or sodium hydride.[6] More recently, lithium diisopropylamide (LDA) has been used as base for the preparation of enolate ions. It is a very strong base, with pKa of approximately 40, very soluble in organic solvents, and it is a hindered base with bulky side chains, preventing it from adding to the carbonyl group in a nucleophillic addition reaction.[8]

The mechanism, as shown in **Scheme 2.2**, proceeds stepwise by firstly deprotonation of the ketone by the base to form an anion, stabilized by the Li$^+$ cation. Secondly, addition of the ester leads to release of an ethoxide ion and formation of a β-diketone. The strongly basic ethoxide anion is then neutralized by proton abstraction from the acidic β-diketone to form a β-diketonato anion that exists in different resonance forms and is stabilized by the Li$^+$ counter ion. Finally, acidification leads to the release of the β-diketone. Theoretically all steps of the mechanism are reversible, but in practice the equilibrium is shifted towards product formation by the precipitation of the β- diketonato anion as its lithium salt.[6]
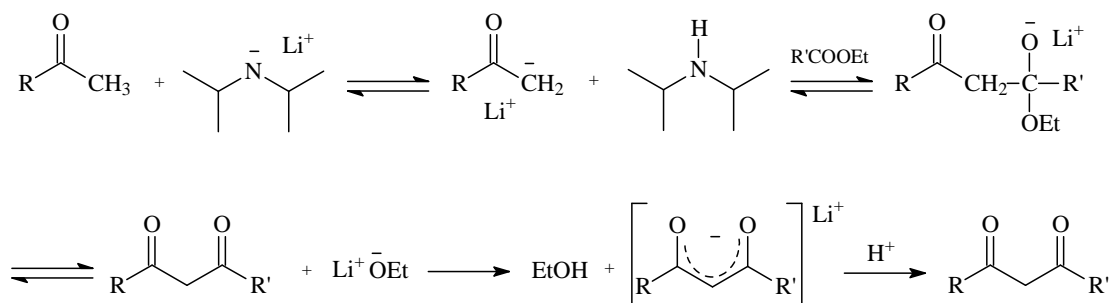
Scheme 2.2. Mechanism of β-diketone formation *via* Claisen condensation.

The success and yield of the reaction depend largely on the reactivity of the ketone and the strength of the base. The more complex the structure of the ketone, the more difficult it is to acylate it. Also, the stronger the base, the more successful is the acylation.[9]

A variety of side reactions is possible. Firstly, self condensation of the ketone is possible *via* aldol condensation, forming a β-hydroxy ketone.[10] This occurs when the ester is

relatively unreactive in comparison to the ketone, especially at elevated temperatures. Secondly, when the ester is more reactive compared to the ketone and possesses an α-hydrogen, self condensation of the ester can take place to form a β-keto ester. Under such circumstances the ester can also undergo aldol condensation forming α-β-unsaturated esters. Thirdly, the base may react directly with the carbonyl group, instead of deprotonation of the α-hydrogen, forming an amide.[11] This, however, can be avoided by using a different, sterically hindered base such as LDA. Most of these side reactions can be limited by adjusting the reaction time, lowering the temperature, or changing the sequence of substrate addition. Slight adjustments of substrate to base stoichiometry can also improve yields.[12]

2.2.2. Synthesis of β-Diketones (acidic route)

An alternative route to the synthesis of β-diketones is possible by an electrophilic substitution reaction of a ketone by an acid anhydride in the presence of boron trifluoride as Lewis acid catalyst.[13] Acylation occurs mainly on the more highly substituted side of the ketone, with the final product actually being a BF_2-containing β-diketone complex. The BF_2-complex can be decomposed by either sodium acetate or aluminium trichloride to give the desired β-diketone product.[14, 15]

Boron trifluoride plays a double role in the mechanism.[16] It assists in the ionization of the anhydride, forming a carbocation, as well as converting the ketone to a boron enolate derivative. Finally condensation of the carbocation and boron enolate takes place to form the BF_2 containing β-diketone complex, as shown in **Scheme 2.3**.

$$(RCO)_2O \ + \ BF_3 \ \rightleftharpoons \ R\overset{+}{C}{=}O \ + \ RCO_2\overset{-}{B}F_3$$

$$R'{-}\underset{\underset{O}{\|}}{C}{-}CH_2{-}R'' \ + \ BF_3 \ \rightleftharpoons \ R'{-}\underset{\underset{O^{-BF_3}}{|}}{C}{=}CH{-}R'' \ + \ H^+$$

$$R'{-}\underset{\underset{O^{-BF_3}}{|}}{C}{=}CH{-}R'' \ + \ R\overset{+}{C}{=}O \ \longrightarrow \ \left[R'{-}\underset{\underset{R''}{\overset{+}{|}}}{\underset{\underset{O^{-BF_3}}{|}}{C}}{-}CH{-}\underset{\underset{O}{\|}}{C}{-}R \right]$$

$$\xrightarrow{\text{-HF}} \ R'{-}\underset{\underset{R''}{|}}{\underset{\underset{O^{\diagdown BF_2 \diagdown O}}{|}}{C}}{=}C{-}\underset{\underset{O}{\|}}{C}{-}R \ \xrightarrow{AlCl_3} \ R'{-}\underset{\underset{O}{\|}}{C}{-}\underset{\underset{R''}{|}}{C}{-}\underset{\underset{O}{\|}}{C}{-}R$$
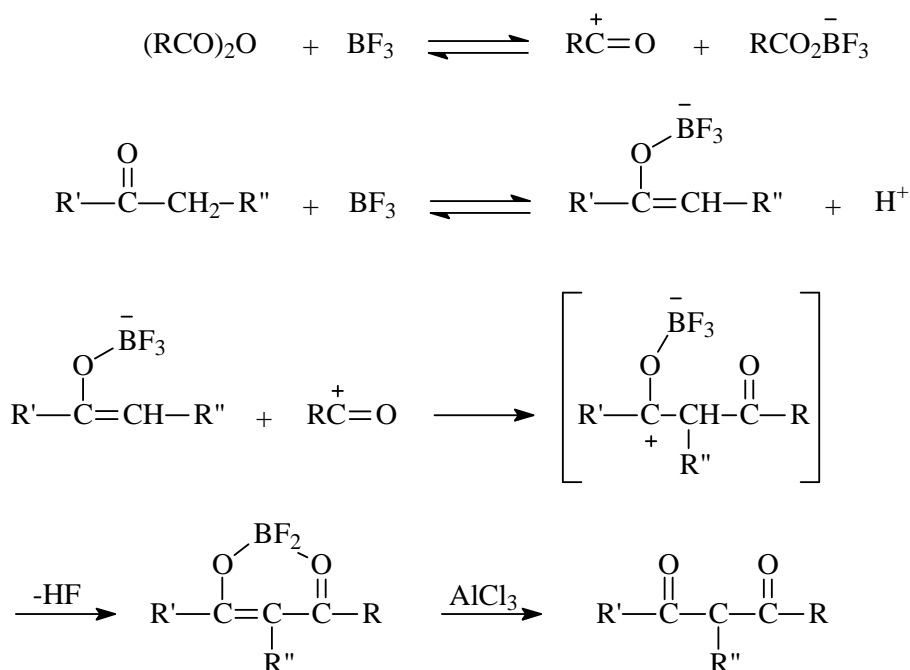
Scheme 2.3. Mechanism of β-diketone formation via BF_3-catalyzed method.

The only side reaction causing occasional difficulties is the self condensation of either the anhydride or the ketone. Since these side reactions can severely lower yields, limitations on the scope of this reaction may exist. In general, the basic route for synthesis of β-diketones (as described in **Section 2.2.1**) seems to have a much wider application than the boron trifluoride method. However, depending on the substrate, the boron trifluoride route may offer better yields and cleaner reactions. The boron trifluoride route is also preferred for synthesizing β-diketones containing side chains on the α-carbon, whereas the basic route mostly yields unsubstituted β-diketones.[17]

2.2.3. Other Methods of Synthesis for β – Diketones

Due to the wide variety of different β-diketones synthesized and wide variety of uses for these β-diketones, new methods of synthesis are constantly being developed to meet specific needs. A solid-phase polymer supported synthesis has been developed by Park and co-workers[18] (reaction **(a)** in **Scheme 2.4**) making use of enamine methodology, with a piperazine linker, yielding a β-diketone with no traces of polymer binding. An alternative three step synthesis from aldehydes has been reported (reaction **(b)** in **Scheme**

2.4), making use of a dianionic β-ketosulphone as a masked equivalent to acetone. Condensation is followed by oxidation and desulfonation to yield the β-diketone.[19] Another method for synthesis of β-diketones is a proline catalyzed aldol-type addition reaction (reaction **(c)** in **Scheme 2.4**), making use of an electron-withdrawing cyano group in an acyl cyanide molecule to enhance reactivity on the carbonyl group and bring about condensation.[20]
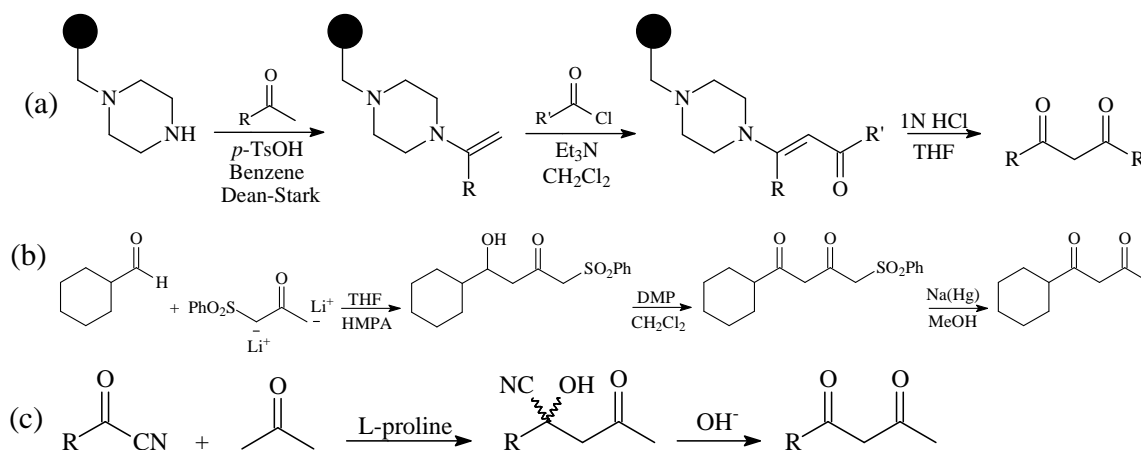
Scheme 2.4. Alternative methods of β-diketone synthesis, where HMPA = hexamethylphosphoric triamide and DMP = Dess-Martin periodinnane.

2.2.4. Keto-enol Tautomerism of β – Diketones

β-Diketones containing an α-hydrogen are capable of converting between the keto and two different enol isomers, thus exhibiting keto-enol tautomerism (**Scheme 2.5**). The α-hydrogen, which is also described as a methine proton, is activated by the adjacent carbonyl groups, thus a conjugate system can arise. An equilibrium exists between the different tautomers, all possessing a *cis* configuration, and under suitable conditions the enolic hydrogen can be replaced by a metal centre, forming a six-membered psuedo-aromatic chelate ring. In the absence of an α-hydrogen, enolization cannot take place and thus no metal coordination occurs.[5]
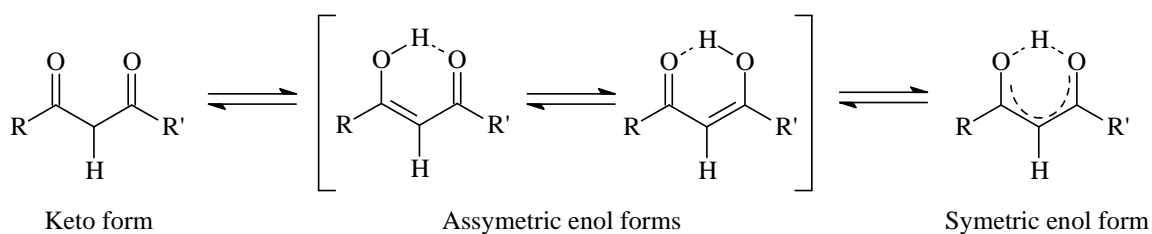
Scheme 2.5. Keto-enol tautomerism in β-diketones.

The position of the equilibrium between the different tautomers is highly variable, and depends on a number of different factors, including electronic properties of substituents, steric effects, aromatic effects, solvent and temperature. In general the equilibrium is shifted more towards the enol with increasing electron withdrawal by the substituents. Pendant aromatic groups often enhance enolization, though steric groups tend to have the opposite effect. The enol form is also generally favoured in non-polar solvents, due to the tendency of enol tautomers to form intramolecular hydrogen bonding. In contrast, the keto form favours hydrogen bonding with polar solvents.

Extensive research has been done to investigate the different factors influencing the position of the equilibrium between the different tautomers. Recent work done by Sloop and co-workers[21] has made use of IR, UV and NMR spectroscopic techniques to determine the equilibrium constants for different β-diketones containing trifluoromethyl R-groups. IR and UV techniques were found more reliable in determining the equilibrium constant between different enol forms. ^{1}H, ^{13}C and ^{19}F NMR studies were also performed, but found not to be useful in this regard, due to the very rapid dynamic equilibrium between the two different enol forms. For their compounds, the dynamic equilibrium is generally too fast to be monitored on the NMR timescale. Small differences in chemical shifts also make it difficult to distinguish between different enol NMR signals.[21] Computational chemistry are becoming more widely used to understand and evaluate the equilibrium between different β-diketone tautomers. It offers a new method for determining equilibrium constants threoretically to complement experimentally obtained results.[22,23]

2.2.5. Ferrocene containing β-Diketones

β-Diketones containing ferrocenyl side chains have long been known.[24] β-Diketones of the type $FcCOCH_2COR$, where R = CH_3, were synthesized *via* Claisen condensation by Cullen and Wickenheiser,[25] as well as Bell and co-workers.[26] Bell also managed to solve the crystal structure of the enol form of 1-ferrocenyl-3-hydroxybut-2-en-1-one.[26] Since then the range of ferrocenyl containing β-diketones has been extended significantly. Du Plessis and co-workers[27] have synthesized a range of such β-diketones, where R = CF_3 **(1)**, CCl_3 **(2)**, CH_3 **(3)**, (C_6H_5) **(4)** and $\{(C_5H_4)Fe(C_5H_5)\}$ **(5)**, as shown in **Figure 2.1**.[28] More recent work in this group has also included the synthesis of β-diketones with other metallocenyl side groups, where R = $\{(C_5H_4)Ru(C_5H_5)\}$ **(6)**,[29] and $\{(C_5H_4)Os(C_5H_5)\}$ **(7)**.[30]

$R = CF_3$ **(1)**, CCl_3 **(2)**,
CH_3 **(3)**, (C_6H_5) **(4)**,
$\{(C_5H_4)Fe(C_5H_5)\}$ **(5)**,
$\{(C_5H_4)Ru(C_5H_5)\}$ **(6)**,
$\{(C_5H_4)Os(C_5H_5)\}$ **(7)**
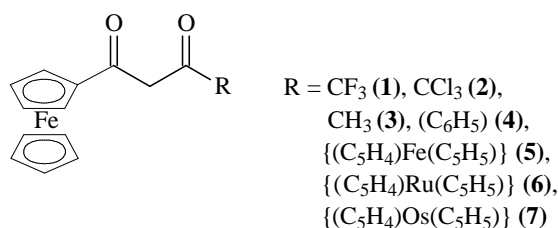
Figure 2.1. Structures of ferrocene containing β-diketones **(1)** - **(7)**.

Structural studies have shown that in the solid state the enol form of **(1)** – **(7)** dominates, due to intramolecular hydrogen bonding. Freshly synthesized **(1)** – **(7)** have large amounts of keto isomers. However, after synthesis it is completely converted to the enol form *via* a slow kinetic process over long periods of time when stored in the solid state. When redissolved, it slowly converts back to the keto form, until equilibrium is reached, offering an explanation to varying reports on the percentage of keto or enol form present.[31] The direction in which enolization takes place was also investigated, and it was found that two main driving forces exist. The first was labelled an electronic driving force, which implies that enolization should take place with the enol on the side of the less electronegative side group. This happens because the carbonyl carbon next to the less electronegative side group will be less positive in character. However, many exceptions to this rule were found. This pointed to a second more important driving force

that governs the direction of enolization. This second driving force was labeled the resonance driving force. In the case of aromatic side groups, the formation of different canonical forms of a specific enol isomer will lower the energy of the isomer enough to allow it to dominate over another enol isomer which might be favoured by the electronic driving force. This leads to enolisation taking place mostly away from the aromatic side group.[28] Physical properties of (1) – (7) have been determined and are summarized in **Table 2.1**. Linear relationships were observed between group electronegativity (χ_R) and formal reduction potentials ($E^{o'}$), as well as pKa' values and group electronegativity.

Table 2.1. Physical properties of β – diketones (1) – (7), $FcCOCH_2COR$

β – Diketone	R =	pKa'	% Enol in solution	χ_R
(1)	CF_3	6.53(3)	97	3.01
(2)	CCl_3	7.15(2)	95	2.76
(3)	CH_3	10.0(2)	78	2.34
(4)	(C_6H_5)	10.41(2)	91	2.21
(5)	$\{(C_5H_4)Fe(C_5H_5)\}$	13.1(1)	67	1.87
(6)	$\{(C_5H_4)Ru(C_5H_5)\}^{28}$	>13	47	1.99
(7)	$\{(C_5H_4)Os(C_5H_5)\}^{29}$	13.04(1)	43	1.90*
-	Fc^+	6.80	-	2.82

*As determined in **Chapter 3**, **Section 3.5.4.1**.

Ferrocene-containing β-diketones have also been synthesized *via* other methods. Compound (3), as well as β-diketones containing phosphaferrocenes, have also been synthesized by BF_3 catalyzed reaction, as shown in **Scheme 2.6**.[15,32]

X = CH (3), P (8)
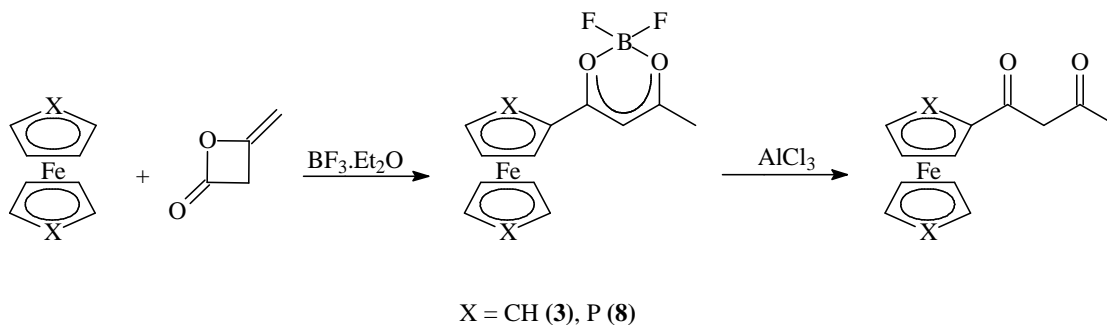
Scheme 2.6. BF_3 catalyzed synthesis of ferrocenyl β-diketones, with X = CH (3) or P (8).

β-Diketones substituted with a ferrocenyl group on the α-position have also been synthesized. Zakaria and co-workers[33] have synthesized a series of 2-(ferrocenylmethyl)-1,3-diketones by reacting (ferrocenylmethyl)trimethylammonium iodide with the mono-sodium salts of a range of β – diketones, as shown in **Scheme 2.7**.

R = R' = CH$_3$ (**9**), or
R = R' = Ph (**10**), or
R = R' = C(CH$_3$)$_3$ (**11**), or
R = Ph, R' = CH$_3$ (**12**)
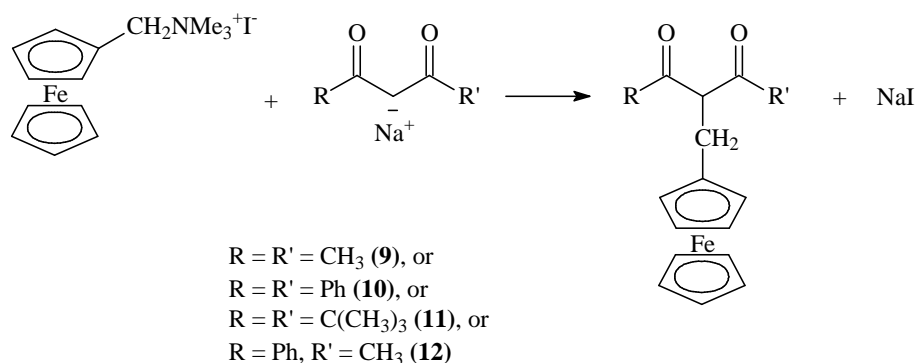
Scheme 2.7. Synthesis of α-substituted β – diketones.

2.3. Metallocene-Containing Phosphine Ligands

Incorporating metallocenes as part of a phosphorus(III) system led to a new class of organophosphines, which are very useful ligands in catalytic processes.[34] Their value as ligand backbone stems from their unique and very specific geometries, as well as their electronic properties.[35] These phosphines can be devided into three major groups, namely monodentate ligands, symmetrical bidentate ligands, and unsymmetrical bidentate ligands.

2.3.1. Monodentate Metallocene Phosphines

Until now, only ferrocene-containing monodentate metallocene phosphines have been known in the literature. Mono- (**13**), di- (**14**) and tri-substituted (**15**) ferrocenyl phosphine compounds (**Figure 2.2**) have been synthesized under Friedel Crafts conditions in the presence of AlCl$_3$, contrary to the general behavior of aromatic compounds. The utility of this method for synthesis of ferrocenylphenylphosphines stems from the fact that it is a simple one pot synthesis with few side-products.[36]

(13)   **(14)**   **(15)**
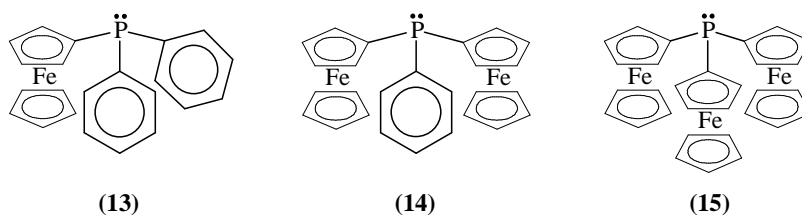
Figure 2.2. Structures of ferrocenyl-containing phosphine compounds **(13)** - **(15)**.

The mechanism proceeds as shown in **Scheme 2.8**. Multiple substitution takes place *via* a stepwise process, meaning that for di- and tri-substituted phosphines the process shown in **Scheme 2.8** will be repeated either 2 or 3 times.

$$Fc \ + \ PPh_nCl_{(3-n)} \ + \ AlCl_3 \longrightarrow Fc \ + \ PPh_nCl_{(2-n)}{}^+ \ + \ AlCl_4{}^- \longrightarrow FcPPh_nCl_{(2-n)} \ + HCl$$
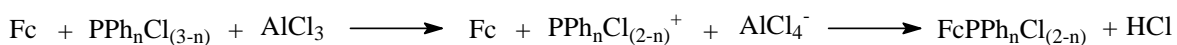
Scheme 2.8. Synthesis of ferrocenylphenylphosphines.

Phosphines **(13)**, **(14)** and **(15)** are all readily air-oxidized in the presence of aluminum trichloride, explaining the observed phosphine oxide formation in early reports, as well as the need for inert reaction conditions during synthesis. However, **(13)** and **(14)** do show stability towards air oxidation similar to that of triphenylphosphine when isolated and stored in the solid state.[37] Triferrocenyl phosphine **(15)** is much less stable towards oxidation, indicating that the presence of at least one phenyl ring largely contributes to the stability of the compound through withdrawal of the lone electron pair on the phosphorous, by the phenyl ring. Once oxidized, various methods have been published recently to reduce the phosphine oxide and regenerate the phosphine, although none has so far been tested on metallocene phosphines.[38, 39, 40]

The σ-donor ability of these ligands was found to increase with the increasing number of ferrocenyl groups. However, the steric size of the ligands also increased, largely influencing the expected chemical behavior of **(15)**.[41]

2.3.2. Symmetrical Bidentate Metallocene Phosphines

A range of symmetrical metallocene-containing phosphines, of the type shown in **Figure 2.3**, is known. The first to be isolated was 1,1'-bis(diphenylphosphino)ferrocene (dppf) **(16),** in 1965. In the past 15 years the series has been extended to include other metal centers, such as ruthenium **(17)** and osmium **(18)**. The side groups on the phosphorous centers have also been varied to include *t*-butyl-, *i*-propyl- and *i*-propylaryl-groups, among others.[42, 43]

M = Fe **(16)**
= Ru **(17)**
= Os **(18)**
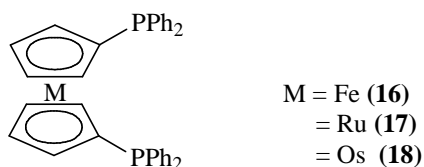
Figure 2.3. Structures of diphosphinometallocene compounds **(16)** - **(18)**.

The general route for synthesis of these phosphines, as shown in **Scheme 2.9**, consists of deprotonation and lithiation on both cyclopentadienyl rings, by addition of two equivalents of an alkyl lithium base, followed by addition of a chlorophospine, to yield the required product.[42, 44] Dppo **(18)** was synthesized by Gusev and co-workers [45] *via* similar methods, but they reported significantly lower yields for **(18)** than for **(16)** and **(17)**, reflecting a lower tendency towards metalation for osmocene compared to ferrocene and ruthenocene.
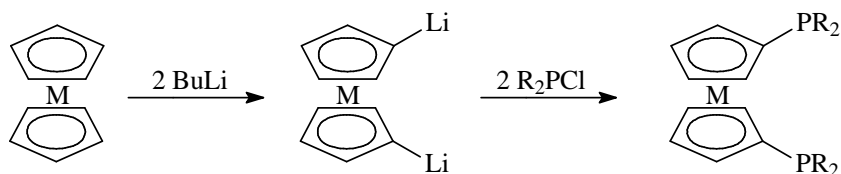
Scheme 2.9. Synthesis of diphosphinometallocene compounds.

These ligands have been complexed to palladium, among other metals, and tested in catalytic processes. It was found that varying the metallocene metal among Fe, Ru and Os, did not significantly change the chemoselectivity or the regioselectivity of the catalyst.[46] It was found however that changing the metal center from Fe to Ru, increases the phosphine bite-angle. This can be attributed to the increased distance between cyclopentadienyl rings for ruthenocene (3.68 Å) compared to ferrocene (3.32 Å).[47] It was

also found that the metal center, as well as type of substituent on the cyclopentadienyl ring, largely influences the chemical stability of the catalyst. It has been shown that metal-to-metal bonding can occur between the metallocene center and the catalytic metal center, which can stabilize catalytic intermediates, and increase the overall success of the catalytic cycle.[46]

Another metallocene-containing phosphine has been synthesized, *viz.* 1,1'-bis(diphenylphosphino)cobaltocenium hexafluorophosphate [(dppc$^+$)PF6$^-$] **(19)**. This phoshine exists as a cationic species due to the cobalt center being in the +3 oxidation state. It therefore requires a different synthetic route as shown in **Scheme 2.10**, where the cyclopentadiene rings are firstly substituted with the phosphine-group, followed by the construction of the metallocene core, and finally precipitation of the product with ammonium hexafluorophosphate. Due to the positively charged nature of **(19)**, its chemical behaviour differs significantly from the above mentioned phosphines, thus requiring fundamental changes in synthetic procedures for complexation.[48]
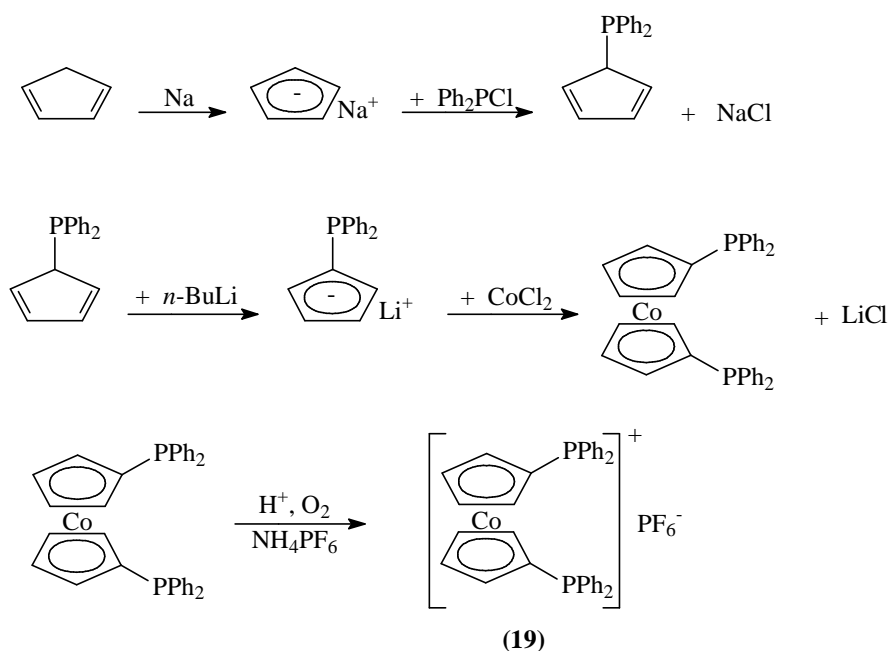
Scheme 2.10. Synthesis of 1,1'-bis(diphenylphosphino)cobaltocenium hexafluorophosphate **(19)**.

2.3.3. Unsymmetrical Bidentate Metallocene Phosphines

A number of different unsymmetrically substituted ferrocenyl phosphine ligands has been synthesized. The pattern of substitution can either be on the same cyclopentadienyl ring (1,2-substitution) or on different cyclopentadienyl rings (1,1'-substitution), as shown in **Figure 2.4**. The number of different applications for these ligands is as diverse as the number of different ligands, and their synthesis and use in catalysis are thoroughly summarized by Atkinson,[35] as well as Colacot.[34]

| 1,2-substitution | 1,1'-subtitution |
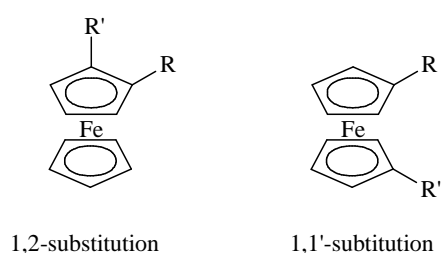
Figure 2.4. The different substitution patterns of unsymmetrical ferrocenyl phosphines.

The two chelating groups can either be two different phosphine groups, or one phosphine group in combination with a different donating group, such as nitrogen, oxygen, or sulphur groups. Utilizing different coordinating groups offers an advantage when one group is more labile towards substitution than the other. The more weakly coordinating group can stabilize coordination sites on the metal center, until displaced by a substrate molecule, but due to the more inert group, the ligand still stays anchored to the metal center. Such ligands are termed "hemi-labile" and are widely used in homogeneous catalysis.[35]

2.4. Rhodium Complexes

A wide range of different rhodium complexes has been synthesized, among other complexes of the type $[RhH(CO)(PPh_3)_3]$, for use as hydroformylation catalyst, $[RhCl(PPh_3)_3]$, a hydrogenation catalyst, and $[Rh(CO)_2I_2]^-$ as carbonylation catalyst. β-Diketones form very stable six-membered cyclic rings when complexed to rhodium, and due to their bidentate nature are less likely to dissociate from the metal center under catalytic conditions than monodentate ligands. The improved stability leads to

widespread application in catalysis. This study, however, has focused on rhodium β-diketonato complexes as substitute for $[RhI_2(CO)_2]$ for the carbonylation of methanol to acetic acid, as stated in goals 3 and 4. Thus rhodium β-diketonato complexes of the type $[Rh(\beta\text{-diketonato})(CO)_2]$ and $[Rh(\beta\text{-diketonato})(CO)(PR_3)]$ will be discussed here.

2.4.1. Rhodium β-Diketonato Complexes

Two general routes are employed for the synthesis of dicarbonyl rhodium β-diketonato complexes, as shown in **Scheme 2.11**.[49, 50] In both routes chloro-bridged dimeric rhodium intermediates are formed from rhodium trichloride, followed by reaction with a β-diketone to form a monomeric rhodium(I) species.
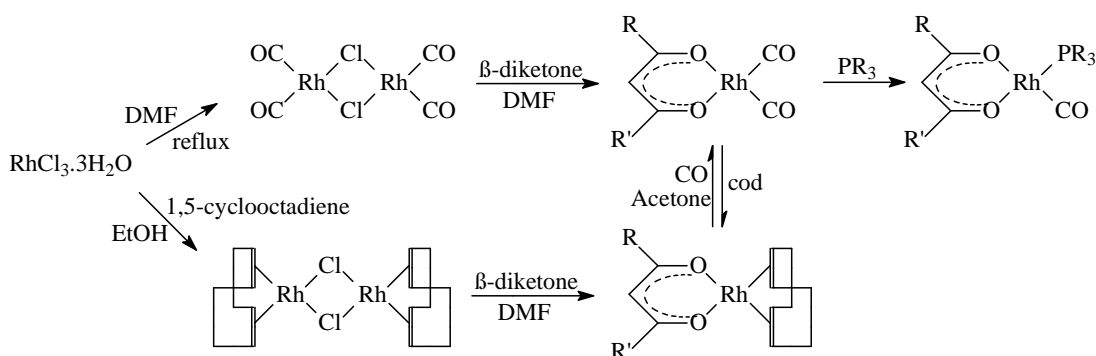
Scheme 2.11. Schematic representation of the two different routes for the synthesis of rhodium β-diketonato complexes.

In the case of the 1,5-cyclooctadiene route (cod), the last step involves bubbling of carbon monoxide gas to substitute the cod-ligand, which is an equilibrium process. The product is isolated in pure form by precipitation from the carbon monoxide saturated acetone solution by addition of water. It was found that the best yields are obtained when the first route (the tetra carbonyl route) is used for β-diketones containing more electron-withdrawing side-groups. The second (cod) route works best for β-diketones containing more electron-donating side-groups.[51]

It has also been found that, in most cases, only mono-substitution of the two carbonyl groups with a phosphine group takes place. In the cases where di-substitution do take place, the reaction is significantly slower and more difficult. Extreme conditions are required, including removal of all free CO by purging with an inert gas and a large excess

of phosphine ligand. A general trend is found where the rate of substitution of the second carbonyl group increases along with an increase in δ-donor abilities and a decrease in π-acceptor properties. Stronger Rh-P bonds are formed with stronger δ-donor properties.[52]

(20) R = CF$_3$, R' = H, R" = (thiophene)   **(24)** R = CF$_3$, R' = H, R" = CH$_3$ **(28)** R = Fc, R' = H, R" = CH$_3$
(21) R = CH$_3$, R' = H, R" = CH$_3$ **(25)** R = CF$_3$, R' = H, R" = CH$_2$CH$_3$ **(29)** R = Fc, R' = H, R" = CF$_3$
(22) R = CF$_3$, R' = H, R" = CH(CH$_3$)$_2$ **(26)** R = CH$_3$, R' = CH$_2$(C$_6$H$_5$), R" = CH$_3$ **(30)** R = Fc, R' = H, R" = C$_6$H$_5$
(23) R = CF$_3$, R' = H, R" = C(CH$_3$)$_3$ **(27)** R = C$_6$H$_5$, R' = H, R" = C$_6$H$_5$ **(31)** R = Fc, R' = H, R" = Fc

Figure 2.5. Rhodium β-diketonato complexes with varied β-diketonato side-groups.

Leipoldt and co-workers synthesized a large number of rhodium complexes **(20)** – **(27)** with varied β-diketonato side-groups (shown in **Figure 2.5**), ranging in size and electron-donating abilities, and investigated the steric and electronic influences of β-diketonato substituents on the crystallized rhodium complexes.[53, 54, 55, 56, 57, 58, 59] Their work focused on determining the influence of the *trans* effect. It was shown that the carbonyl group *trans* to the β-diketone oxygen atom attached to the more electronegative group (e.g. CF$_3$) has the smallest *trans* influence and is least likely to be substituted. However, it was also found that steric hindrance can overrule the electronic effect when bulky side-groups are present on the β-diketone, and causes substitution to take place *trans* to the more electronegative group.[57] More recently rhodium complexes **(28)** – **(31)** with ferrocenyl β-diketonato side-groups have been synthesized. It was observed that two isomers exist in solution, where the ferrocenyl group is either *cis* or *trans* to the phosphine group. The isomer dominating in solution is the more thermodynamically stable solution species, but not necessarily the most stable one to crystallize in the solid state.[51]

Studies have also been carried out to investigate the influence of varied phosphine ligands on the structure and efficiency of rhodium acetylacetonato catalysts.[52, 60] Riihimäki and co-workers[61] have synthesized a series of aryl- and alkyl-containing phosphine ligands ranging in steric size and electronic influence and examined their use

as hydroformylation catalysts. They found the isolation of pure [Rh(acac)(CO)(phosphine)] complexes difficult due to an equilibrium between starting materials and product. It was also observed that steric size can strongly influence and even overrule electronic effects on the activity of the catalyst. One reported case can be found of the synthesis of a ferrocenyl phosphine ligand complexed to rhodium, *viz.* [Rh(acac)(CO)(PPh$_2$Fc)], with a full structural investigation carried out.[62]

2.5. Tetrathiafulvalene-containing Ligands

As an additional part of this study, rhodium complexes with non-metallocene-containing redoxactive β-diketonato ligands have been synthesized. These β-diketonato ligands contain tetrathiafulvalene (TTF) groups, of which a short overview is given here.

Functionalized tetrathiafulvalene (TTF) (shown in **Figure 2.6**) compounds have attracted much interest, due to its unique electronic, magnetic and optical properties and value as organic conductors.[63]

(a)

(b)

(**32**) R = R' = PPh$_2$, R" = R''' = Me
(**33**) R = R" = PPh$_2$, R' = R'''= Me
(**34**) R = S((CH$_2$)$_3$)PPh$_2$, R' = R" = R''' = Me
(**35**) R = R" = S((CH$_2$)$_3$)PPh$_2$, R' = R''' = Me

(c)

(d)

(**36**) R = R' = R" = Me
(**37**) R = R" = Me, R' = Sacac
(**38**) R = R" = Me, R' = SMe
(**39**) R = R' = R" = SMe
(**40**) R' = R" = SMe, R = H

(**41**)
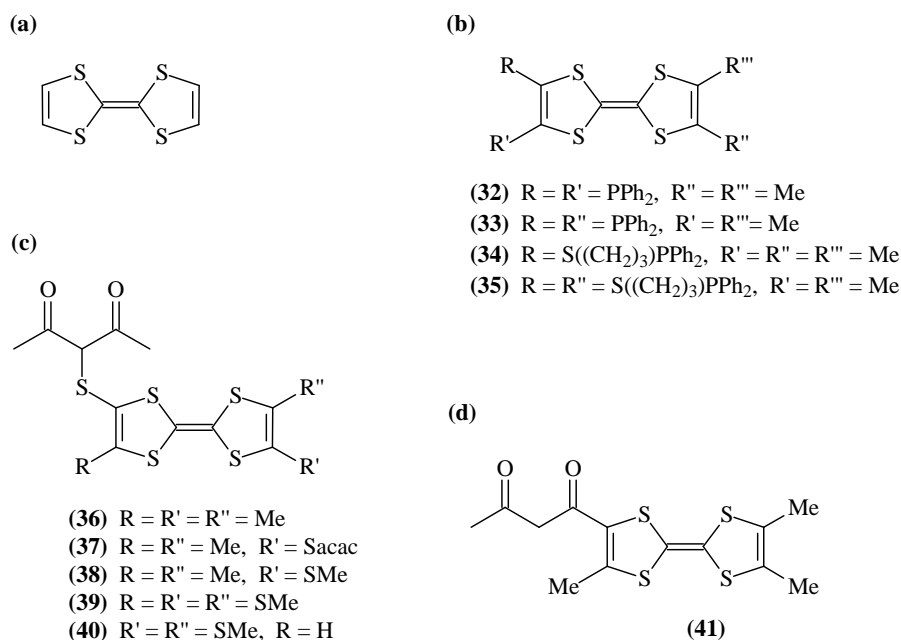
Figure 2.6. Structures of (**a**) the tetrathiafulvalene-backbone, (**b**) TTF-containing phosphine ligands, (**c**) TTF-containing β-diketonato ligands, and (d) TTF-containing β-diketonato ligand with no thio-linker.

Many different compounds have been reported in literature, although only a few examples exist with coordinating groups.[64] TTF-containing compounds, however, show great promise as ligands in coordination chemistry due to their high electron-donating abilities. A range of phosphine ligands containing the TTF-group has been synthesized, varying the position of substitution, as well as the alkyl -chain length between TTF-group and phosphine group, as shown in **Figure 2.6 (b)**. Compounds were fully characterized as well as electrochemical studies carried out.[64] β-Diketonato ligands containing the TTF-group have also been synthesized by Lorcy and Belec ((**36**) - (**39**)),[65,66] as well as Dai and co-workers[67] **(40)**, as shown in **Figure 2.6 (c)**. Crystal structure studies have shown that the acetylacetonato group is positioned nearly perpendicular to the plane of the TTF-core, with rotation possible around the thio-linker unit. The latest report shows a TTF-acac ligand (**41**), with the acetylacetonato group linked directly to the TTF-core with no thio-linker unit, as shown in **Figure 2.6 (d)**. Thus the acetylacetonato group is in the same plane as the TTF-group, with no rotation possible, increasing the possibility of interaction between TTF-units in the crystal form.[68]

To date, very few reports have been made of TTF-containing ligands complexed to metals. The first was made by Lorcy and co-workers,[66] where nickel and zinc have been complexed to TTF-acac ligand (**39**), forming octahedral metal-linked TTF dimers of the type [M(TTFSacac)$_2$(pyridine)$_2$]. Attempts to incorporate other TTF-acac ligands (**36**) - (**38**) resulted in a highly insoluble product, rendering it difficult to work with. Increasing the number of thiamethyl groups increased the solubility of the metal complexes. The co-planar TTF-acac ligand (**41**) has also been complexed with copper, nickel and zinc, forming similar octahedral dimeric species, [M(TTFSacac)$_2$(pyridine)$_2$], with both coordinating groups in the same plane.[68] Other reported metal TTF-complexes containing (**40**) were synthesized by Dai and co-workers,[67] forming square-planar metal-linked TTF dimers with manganese and copper, of the type [M(TTFSacac)$_2$]. In this study, collaboration with the Lorcy group saw the synthesis of the first Rh(I) complexes of (**36**) and (**41**).

2.6. Kinetics

In order for molecules to undergo a chemical reaction, they must pass through some increased energy state that is higher than both the reactants and products. This increased energy state is known as a transition state and the amount of energy needed to reach it is called the activation energy (E_a), as shown in the energy profile given in **Figure 2.7 (a)**. A clear distinction exists between a transition state and an intermediate, which possesses a secondary energy minimum along the reaction coordinate, and needs further activation to reach a transition state to form final products, as shown in **Figure 2.7 (b)**.[69]
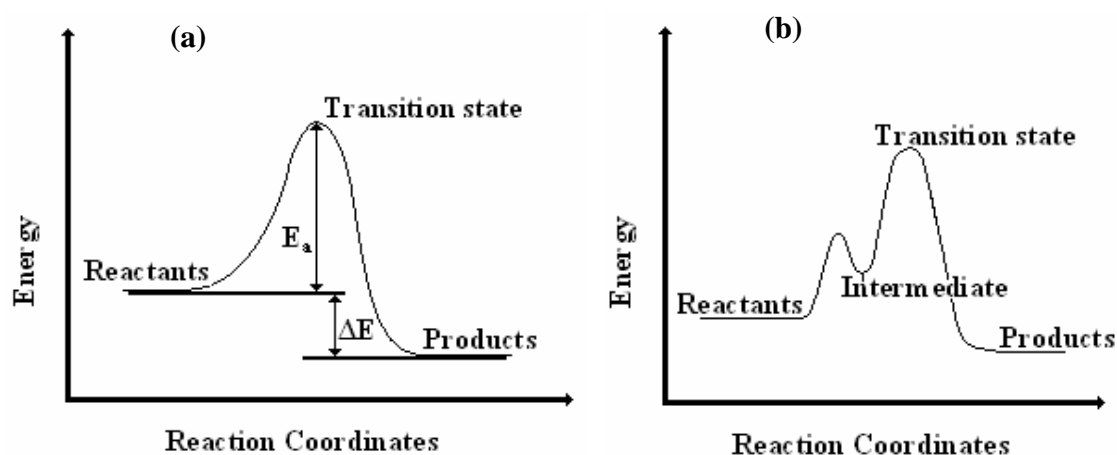
Figure 2.7. Energy profile for a simple chemical reaction (a), and a chemical reaction with an intermediate species forming (b).

The rate of a chemical reaction can be expressed according to one of two ways. The first is according to the familiar Arrhenius equation (**Equation 2.1**).

$$ k = A\,e^{(-Ea/RT)} $$

Equation 2.1

According to the transition state theory, summarized in **Scheme 2.12**, the transition state is in equilibrium with the reagents, before reaction takes place to form the products.

$$ A + B \xrightleftharpoons{K_c^*} [A{\cdot}B]^* \xrightarrow{k} \text{products} $$

Scheme 2.12. Schematic representation of the transition state theory.

The rate of reaction is expressed as the decomposition of the transition state to form products according to the transition state theory, is described by **Equation 2.2**.

$$k \ = \ (RT/Nh) \ K_c^*$$ **Equation 2.2**

In **Equation 2.2**, R = gas constant, T = temperature (in Kelvin), N = Avogadro's constant, h = Planck's constant and K_c^* = equilibrium constant.

The equilibrium constant can also be expressed in terms of the free energy of activation (ΔG^*), as shown in **Equations 2.3** and **2.4**.

$$\Delta G^* \ = \ - \ RT \ln K_c^*$$

or $$K_c^* \ = \ e^{- \ (\Delta G^*)/(RT)}$$ **Equation 2.3**

$$\Delta G^* \ = \ \Delta H^* \ - \ T \, (\Delta S^*)$$ **Equation 2.4**

Combination of **Equations 2.2**, **2.3** and **2.4**, gives **Equation 2.5**.[70]

$$\ln k \ = \ \ln [(RT) \, / \, (Nh)] \ + \ (\Delta S^* \, / \, R) \ - \ (\Delta H^* \, / \, RT)$$ **Equation 2.5**

From these activation parameters, valuable information can be deduced regarding the mechanism of the reaction. The enthalpy of activation (ΔH^*) gives an indication of the bond dissociation enthalpies of the bonds being cleaved during the activation process, but also includes differences in solvation energies, especially for ionic species. The entropy of activation (ΔS^*) gives a direct indication of the mechanism involved. For unimolecular reactions ΔS^* is near zero. Bimolecular reactions having an associative mechanism tend to have large negative ΔS^*-values indicating the loss of entropy from the union of two reacting partners into a single transition state. In the same way, positive ΔS^*-values tend to indicate a dissociative mechanism.[71]

2.6.1. Oxidative Addition

As mentioned in **Chapter 1**, rhodium-based catalysts are utilized for the conversion of methanol to acetic acid (**Scheme 1.1**, **Chapter 1**). This study has focused on investigating the rate-determining first step of this cycle, *viz.* oxidative addition, and will

thus be discussed here. The second step of **Scheme 1.1**, *viz.* carbonyl insertion, frequently cannot be separated from step 1, implying that it is studied jointly. Both will be discussed here.

Oxidative addition can be described as the addition of a neutral molecule (X-Y) to a transition metal, leading to an increase in the metal's oxidation state by two units, as well as the increase of its coordination number by two. This occurs when the transition metal complex can behave as a Lewis acid and a Lewis base, although the actual mechanism may be much more complicated.

2.6.1.1. Mechanisms of Oxidative Addition Reactions

In the oxidative addition of organic halides to metal complexes, either an S_N2 mechanism or a concerted 3-centered mechanism is most common. An S_N2 mechanism, shown in **Scheme 2.13** involves attack of the electron-rich metal center on the more electropositive alkyl-group, forming a linear transition state and leading to *trans*-addition of the alkyl halide.[72]

$$L_n M^n \quad + \quad R-X \quad \longrightarrow \quad \left[L_n M^n \cdots R \cdots X \right]^* \quad \longrightarrow \quad [L_n M^{(n+1)} R] \, X^- \quad \longrightarrow \quad [L_n M^{(n+2)} R \, X]$$
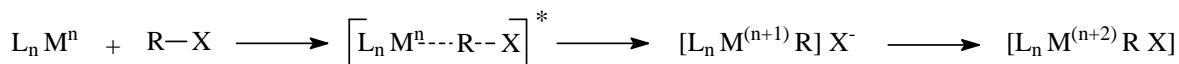
Scheme 2.13. S_N2 mechanism of oxidative addition. R = alkyl group, e.g. CH_3.

The other common mechanism, the concerted 3-centered mechanism, shown in **Scheme 2.14**, involves a three-centered transition state. This leads to *cis*-addition of the alkyl halide and occurs mostly with molecules having little or no polarity.
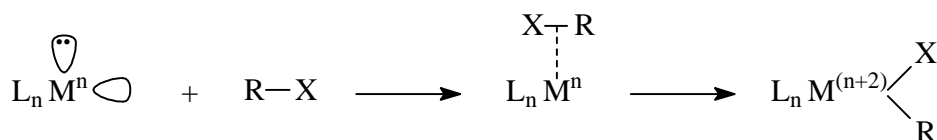
Scheme 2.14. Concerted 3-centered mechanism of oxidative addition. R = alkyl group, e.g. CH_3.

Oxidative addition can also occur *via* a radical mechanism, shown in **Scheme 2.15**, or an ionic mechanism.

$$L_n M^n \quad + \quad R-X \quad \longrightarrow \quad [\, L_n M^n \; X \overset{\frown}{} R \,]^* \quad \longrightarrow \quad [\, R^{\boldsymbol{\cdot}} X M^{\boldsymbol{\cdot}\, n} L_n \,] \quad \longrightarrow \quad [R\, X\, M^{(n+2)} L_n]$$
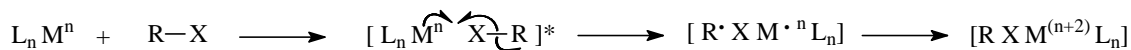
Scheme 2.15. Radical mechanism of oxidative addition.

2.6.1.2. Carbonyl Insertion

The term "insertion" is used in a very wide context and, in general, refers to a reaction where any atom or group is inserted between two atoms initially bonded together, as shown in **Scheme 2.16**. Insertion may be considered 1,1, 1,2, 1,3, etc., depending on the atom to which the migrating group is transferred.

$$\mathbf{L}_n\mathbf{M}\!\!-\!\!\!-\!\!\mathbf{X} \quad + \quad \mathbf{YZ} \quad \longrightarrow \quad \mathbf{L}_n\mathbf{M}\!-\!(\mathbf{YZ})\!-\!\mathbf{X}$$
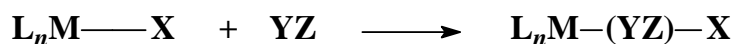
Scheme 2.16. General representation of an insertion reaction.

When insertion of a carbonyl ligand takes place, the CO group is inserted into the metal-alkyl-carbon bond to from a metal acyl complex. In such a case, the CO ligand is derived from one already coordinated to the metal center, and not from an external source. Insertion can be effected by addition of CO, as well as addition of ligands other than CO, or the solvent, and in all cases, the incoming ligand is added *cis* to the acyl group. The migration of an alkyl-group to a *cis*-coordinated CO group is assisted through the polarization of CO. It proceeds through a three-centered transition state, with retention of configuration, as indicated in **Scheme 2.17**.[73]
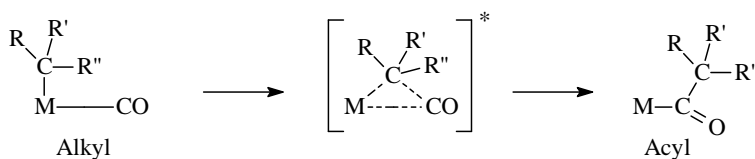
Scheme 2.17. Mechanism of insertion reaction with three-centered transition state.

2.6.1.3. Oxidative Addition in Rhodium Complexes

The oroginal square-planar rhodium catalyst for the carbonylation of methanol is the anionic Monsanto catalyst, $[Rh(CO)_2I_2]^-$. It is known that increasing the electron density on the rhodium center, through electron-donating ligands, increases the rate of oxidative addition.

Rhodium diphosphine catalysts of the type $[Rh(CO)X(PR_3)_2]$, with X a chloro or iodo ligand, have been investigated as possible alternatives. Among these the trialkylphosphine complexes were found to be very active highly selective catalysts.[74] This can be attributed to the very short lifetimes of metal-containing intermediates that are not susceptible to reactions leading to side-products. Kinetic studies showed triethylphosphine complexes to be most effective due to the high electron-density on the metal center, with a decrease in rate with long-chain trialkylphosphines, possibly due to steric interference. It was also observed that, with an increase in rate of oxidative addition, the rate of CO-migration decreased, although the oxidative addition remained the rate-determining step.[75] An S_N2 mechanism was postulated, with *trans*-addition of methyl iodide, and large negative entropy of activation values (ΔS^*) were found. Decomposition of the active catalyst was observed during the reaction to form $[Rh(CO)_2I_2]^-$.[76]

Mixed bidentate ligands, as shown in **Figure 2.8**, have also been shown to be very effective carbonylation catalysts.[77, 78] These hemi-labile ligands were shown to not only increase the rate of oxidative addition, but also increase the rate of CO-insertion. This was an unexpected finding, since careful optimization is usually required to improve parameters in such a way as to afford an effective catalyst. This occurrence was attributed to the steric influence of the bulky phosphine substituents. The high electron-donating abilities increase the rate of oxidative addition, while the large side-groups is responsible for the increase in the rate of insertion. This is due to the six-coordinated rhodium-alkyl species being much less stable under the influence of the bulky side groups than the five-coordinated rhodium-acyl species, promoting CO-insertion.[76] Computational studies were also carried out on these systems, confirming the possible explanation.[79, 80]

(42)   **(43)**
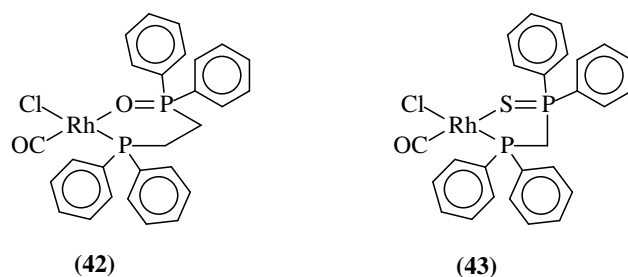
Figure 2.8. Rhodium catalysts with mixed bidentate ligands.

Another method used for increasing the rate of carbonylation is by using additives with the original Monsanto catalyst $[Rh(CO)_2I_2]^-$. It was shown that the addition of transition metal salts notably increased the rate of oxidative addition.[81] The most effective of the transition metals was shown to be nickel. While it is known that nickel compounds can also be used as carbonylation catalysts (industrially used in the BASF process), it is postulated that synergistic effects between the rhodium catalyst and the transition metal are responsible for the rate increase.

The oxidative addition of methyl iodide on rhodium β-diketonato complexes of the type $[Rh(β\text{-}dik)(CO)(PX_3)]$ was studied *via* a combination of spectrophotometric methods by Basson *et al.*[82] Their studies have included variations of substituents with different electronegativity on the β-diketonato group, as well as the phosphine group. Their results favoured an ionic S_N2 mechanism. As shown in **Scheme 2.18**, the reaction proceeds through an equilibrium, leading to a postulated ionic intermediate species with no observable k_2-path, and a final *trans*-addition alkyl complex. As expected, increased rates were observed with an increase in electron-donating abilities of the substituents.

Via IR-studies, they observed the disappearance of the starting Rh(I) complex **(A)** with the simultaneous appearance of an intermediate species **(B)**. The disappearance of the intermediate species **(B)** coincided with the appearance of the Rh(III) acyl species **(C)**. A final, much slower, step was observed with the disappearance of species **(C)** and formation of the final Rh(III) alkyl species **(D)**. Although **(D)** is considered the final reaction product after extended reaction times, mixtures of **(A)**, **(C)** and **(D)** were observed in solution, confirming the overall equilibrium of the process.[83]

27

$$[Rh(\text{ß-dik.})(CO)(PX_3)] \rightleftharpoons [Rh(\text{ß-dik.})(CO)] + PX_3$$

(A)

$$\begin{array}{c} - CH_3I \quad \uparrow\downarrow \quad + CH_3I \\ k_{-1} \quad \quad k_1 \end{array}$$

$$[Rh(\text{ß-dik.})(CO)(CH_3)(PX_3)]^+I^-$$

(B)

$$\begin{array}{c} k_{-3} \quad \uparrow\downarrow \quad k_3 \qquad \qquad k_2 \end{array}$$

$$[Rh(\text{ß-dik.})(COCH_3)(I)(PX_3)] \underset{k_{-4}}{\overset{k_4}{\rightleftharpoons}} [Rh(\text{ß-dik.})(CO)(CH_3)(I)(PX_3)]$$

(C)   **(D)**
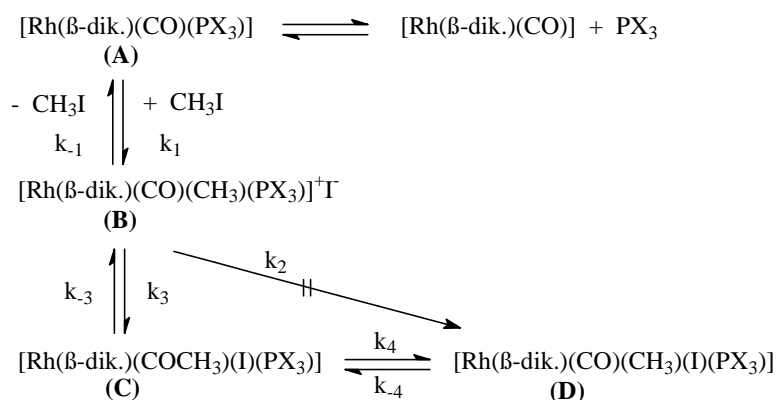
Scheme 2.18. Postulated mechanism for oxidative addition of CH_3I to rhodium β-diketonato complexes.

Further research was done on rhodium complexes containing mixed-donor bidentate ligands, similar to β-diketones, as shown in **Figure 2.9**. In some of these cases, the final product was a Rh(III) acyl species, and not a Rh(III) alkyl species, as in the case of β-diketonato complexes. This is due to the ability of more nucleophilic donor atoms to better stabilize the Rh(III) acyl bond.[84]
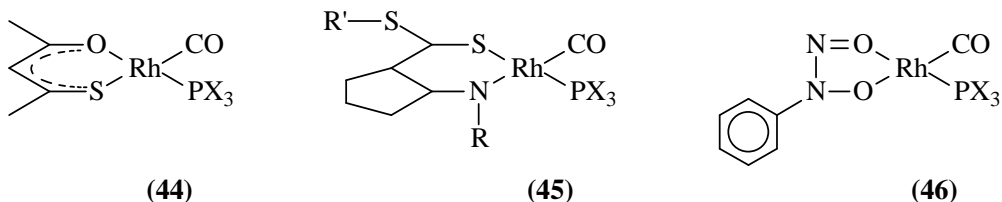
Figure 2.9. Rhodium catalysts with mixed bidentate-ligands.

In the case of the thioacetylacetonato complexes **(44)**, as well as the group of N,S-complexes **(45)**, time dependent overlaid IR spectra showed the Rh(I) starting complex disappears with the simultaneous formation of a low intensity Rh(III) alkyl peak as well as a high intensity peak associated with a Rh(III) acyl species. This indicates that the Rh(III) alkyl species remains at a low concentration in solution and is converted to the Rh(III) acyl species as it forms, pointing to a simple mechanism as illustrated in **Scheme 2.19**.[84] For the N,S-complexes no significant solvent pathway was observed.[85, 86]

$$[Rh(L,L\text{'}bid)(CO)(PX_3)] \quad + \quad CH_3I$$

$$k_{-1} \Big\Uparrow\Big\Downarrow k_1$$

$$[Rh(L,L\text{'}bid)(CO)(CH_3)(I)(PX_3)]$$

$$k_{-2} \Big\Uparrow\Big\Downarrow k_2$$

$$[Rh(L,L\text{'}bid)(COCH_3)(I)(PX_3)]$$
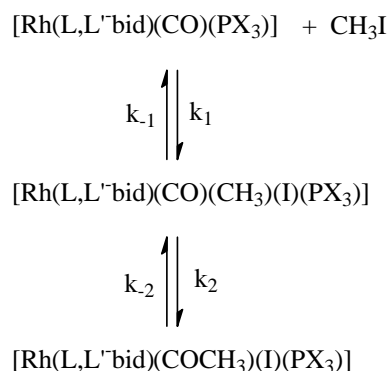
Scheme 2.19. Postulated mechanism for oxidative addition of CH_3I to rhodium thioacetylacetonato complexes **(44)** and N,S-complexes **(45)**.

In the case of the cupferron complexes **(46)**, the reaction proceeds similarly to the β-diketonato complexes, with the Rh(III) alkyl species being the major oxidative addition product. Isolation of the Rh(III) alkyl species indicates *cis*-addition, possibly through a three-centered transition state. Time dependent overlaid IR spectra shows the disappearance of the Rh(I) starting complex, together with the simultaneous appearance of the Rh(III) alkyl species. This is followed by the much slower disappearance of the Rh(III) alkyl species, forming a Rh(III) acyl species. A significant solvent pathway is also observed, as indicated in the mechanism shown in **Scheme 2.20.**[87]

$$[Rh(L,L\text{'}bid)(CO)(PX_3)] \quad + \quad CH_3I$$

$$k_1 \qquad k_2 \qquad + \text{ solvent}$$

$$[Rh(L,L\text{'}bid)(CO)(CH_3)(I)(PX_3)] \xleftarrow{\text{- solvent}} [Rh(L,L\text{'}bid)(CO)(PX_3)(solvent)] \quad + \quad CH_3I$$

$$+ \text{ solvent} \\ \text{slow}$$

$$[Rh(L,L\text{'}bid)(COCH_3)(I)(PX_3)(solvent)]$$
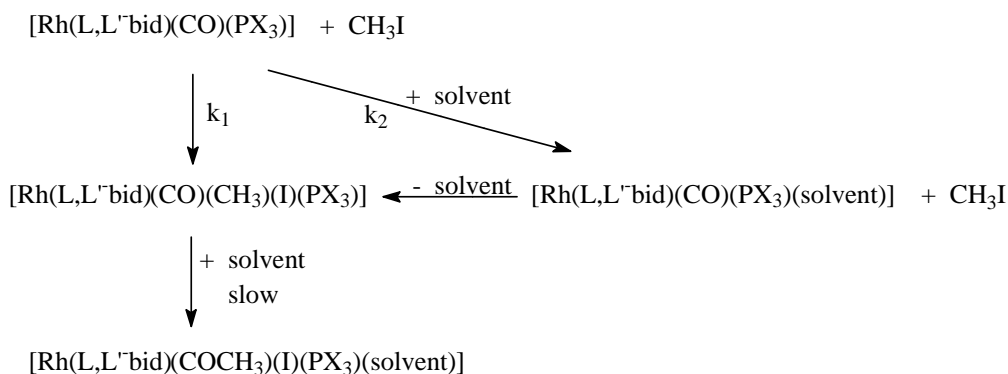
Scheme 2.20. Mechanism of oxidative addition of CH_3I to rhodium cupferron complexes **(46)**.

Activation parameters of the reactions of thioacetylacetonato complexes and cupferron complexes were determined in different solvents. An increase in rate of reaction was also observed in more polar solvents, pointing to the solvent playing an important role in charge separation during the formation of a transition state. The transition state has been

29

reported as either a three-centered intermediate, or a linear S$_N$2-type polar transition state. The three-centered intermediate was shown to be more likely, due to the isolation of the *cis*-addition product for the cupferron complex. In polar solvents though, a linear transition state was shown to be more likely, due to more negative ΔV^*-values.[88]

The oxidative addition of methyl iodide to rhodium complexes with ferrocenyl-containing β-diketonato ligands was studied by Conradie *et al.*[89] A detailed study of [Rh(FcCOCHCOCF$_3$)(CO)(PPh$_3$)] **(29)**, shown in **Figure 2.5** (page 19), was carried out utilizing a variety of spectrophotometric methods, including ^{1}H and ^{31}P NMR. In all cases three general reaction steps were observed. The first step showed a first-order dependence on methyl iodide, with the second and third steps independent thereof. During the first step, the starting Rh(I) species disappears at exactly the same rate as the formation of a Rh(III) alkyl species as well as a Rh(III) acyl species. This indicates the existence of a fast equilibrium between the Rh(III) alkyl species and the Rh(III) acyl species. The second, slower step showed the disappearance of the Rh(III) alkyl and Rh(III) acyl species together with the appearance of a second, geometrically different Rh(III) alkyl species, all at the same rate. The third, much slower step showed the disappearance of the second Rh(III) alkyl species at the same rate as the formation of a second geometrically different Rh(III) acyl species. The same reaction sequence and rates were observed during the NMR studies, but in addition also showed that for each Rh(I) and (Rh(III) complex two isomers A and B exist. These two isomers were showed to be in a fast equilibrium with each other, since the rate of formation and disappearance of each corresponded to its other isomer. Also, the ratio of A to B is independent for each Rh species throughout the reaction sequence. This led to a proposed reaction mechanism as showed in **Scheme 2.21**. This mechanism can be considered a general mechanism, since manipulation of the rate constants will simplify the mechanism to represent all previously proposed mechanisms.

$$\begin{bmatrix} [Rh^{I}(fctfa)(CO)(PPh3)]_A \\ \Updownarrow K_{C1} \\ [Rh^{I}(fctfa)(CO)(PPh3)]_B \end{bmatrix} + CH_3I \underset{k_{-1}}{\overset{k_1}{\rightleftharpoons}} \begin{bmatrix} [Rh^{III}\text{-alkyl1A}] \\ \Updownarrow K_{C2} \\ [Rh^{III}\text{-alkyl1B}] \end{bmatrix} \underset{K_2=k_2/k_{-2}}{\rightleftharpoons} \begin{bmatrix} [Rh^{III}\text{-acyl1A}] \\ \Updownarrow K_{C3} \\ [Rh^{III}\text{-acyl1B}] \end{bmatrix} \underset{k_{-3}}{\overset{k_3}{\rightleftharpoons}} \begin{bmatrix} [Rh^{III}\text{-alkyl2A}] \\ \Updownarrow K_{C4} \\ [Rh^{III}\text{-alkyl2B}] \end{bmatrix} \underset{k_{-4}}{\overset{k_4}{\rightleftharpoons}} \begin{bmatrix} [Rh^{III}\text{-acyl2A}] \\ \Updownarrow K_{C5} \\ [Rh^{III}\text{-acyl2B}] \end{bmatrix}$$

First set of reactions   *Second set of reactions*   *Third set of reactions*
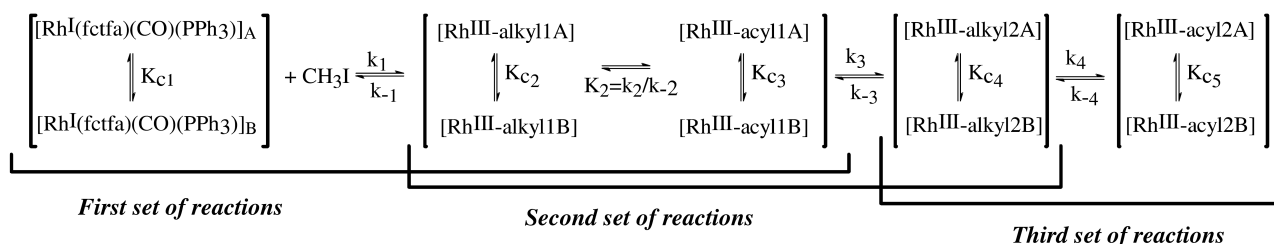
Scheme 2.21. Proposed mechanism for oxidative addition of CH$_3$I to ferrocenyl-containing rhodium β-diketonato complexes.

Activation parameters were determined for all reaction steps, and showed ΔS*-values for the second and third steps of the reaction sequence to be independent of the methyl iodide concentration and approaching zero. ΔS*-values for the first step of the reaction sequence gave large negative values. This is indicative of an associative mechanism for the addition of methyl iodide to the rhodium center, increasing the coordination number from 4 to 6, in agreement with the proposed transition states.

A solvent study was also carried out, showing a rate-dependence on the dielectric constant of the solvent. For the oxidative addition step, a linear increase in rate of reaction was observed with an increase in dielectric constant. The second and third reaction steps showed little solvent effects.

2.6.2. Substitution Reactions

Substitution reactions are one of the most common reaction types in transition metal chemistry. It involves the substitution of one ligand in the coordination sphere of a metal with another, without any change in the final product in the coordination number or the oxidation state of the central metal atom.

2.6.2.1. Mechanisms of Substitution Reactions

Two major reaction pathways exist for substitution reactions, *viz.* the dissociative and the associative mechanism, as shown in **Scheme 2.22**. In the case of a dissociative mechanism, the outgoing ligand (X) leaves the coordinating metal as the first step, forming a three-coordinated intermediate. During the second step, the incoming ligand (Y) binds to the three-coordinated intermediate to form the final substituted product. In

the case of the associative mechanism, the incoming ligand (Y) binds to the metal first to form a five-coordinated intermediate. This intermediate can either be of trigonal bipirimidal or square-pirimidal geometry. The final step consists of dissociation of the leaving ligand (X), to yield the final product.
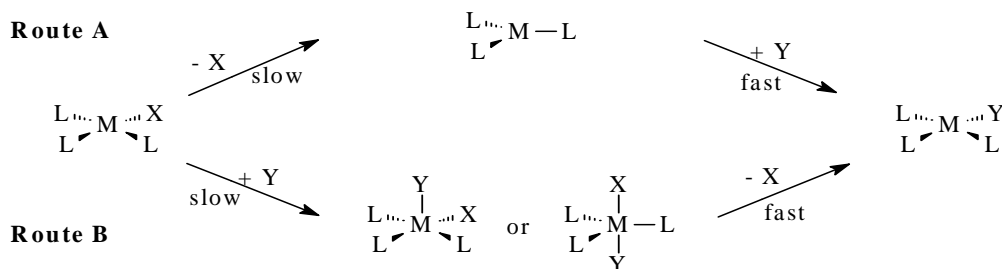
Scheme 2.22. Possible substitution mechanisms for square-planar complexes, *viz.* the dissociative mechanism (**A**) and the associative mechanism (**B**).

In both mechanisms, the first step is the rate-determining step, in the case of an associative mechanism it is bond-formation, and in the case of a dissociative mechanism it is bond-breaking. A dissociative mechanism is thus independent of the concentration of the incoming ligand (Y). Determining the mechanism is, however, not necessarily simple, since the reaction very rarely proceeds *via* such a simplified mechanism. In most cases an interchange mechanism is followed, in which bond-breaking and bond-formation take place simultaneously in a concerted mechanism. This process can frequently be more associative or dissociative in nature.[90]

2.6.2.2. Substitution Reactions in Bidentate Rhodium Complexes

Rhodium β-diketonato cyclooctadiene (cod) complexes can undergo substitution to replace either of the two ligands, as shown in **Scheme 2.23**, depending on the nature of the incoming ligand. In the case of strong σ-donating ligands, such as 1,10-phenanthroline (phen) and 2,2'-bipyridyl (bipy), the σ-donating β-diketonato ligand is replaced. In the case of π-bonding ligands, such as phosphines and phosphates, the π-bonding cod-ligand is replaced. In the case of β-diketonato substitution, the rate of substitution is dependent on the electronegativity of the β-diketonato side groups. An increase in side-group electronegativity is associated with an increase in substitution rate. An increase in pKa of the β-diketone leads to a decrease in rate of substitution.
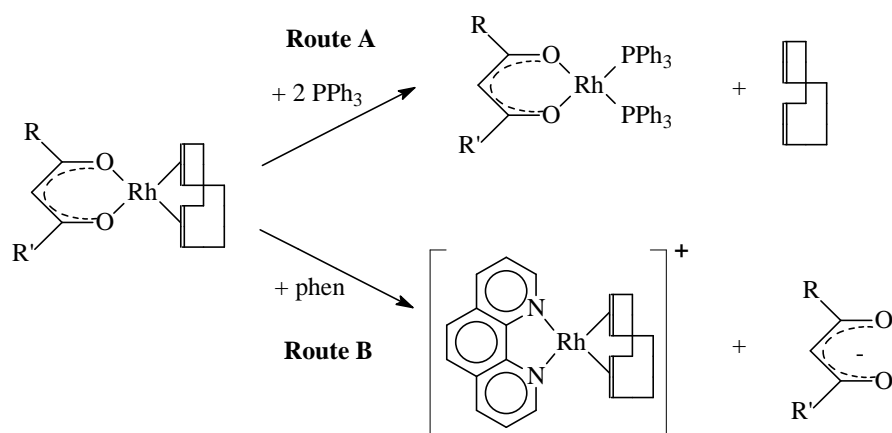
Scheme 2.23. Substitution reactions of rhodium β-diketonato complexes.

The kinetics of substitution for a range of rhodium β-diketonato complexes with phen was investigated by Vosloo *et al.*[91], as shown in route B (**Scheme 2.23**). Complexes studied included ferrocene-containing β-diketonato complexes (**(47) – (51)**), as shown in **Figure 2.10**. Kinetic results showed large negative entropies of activation, indicating that the reaction proceeds *via* an associative mechanism, with breaking of the Rh-O bond being the rate-determining step. Further circumstantial evidence for the associative mechanism can be presented upon considering the possible intermediates. An associative mechanism will proceed *via* an 18-electron five-coordinated intermediate. A dissociative mechanism would require a 12-electron 2-coordinated species, or a 14-electron 3-coordinated species. The last two possibilities are both highly unlikely. This gives further credit to proposing an associative mechanism for the substitution reaction. An exponential relationship was found between the rate of reaction and pK_a of the β-diketone. The rate increased along with a decrease in pK_a. It was also found that for most compounds containing a phenyl β-diketonato side group, a significant solvent pathway existed.

R = CF$_3$ **(47)**, CCl$_3$ **(48)**,
CH$_3$ **(49)**, Ph **(50)**, Fc **(51)**

R' = (52), (53),
(54)
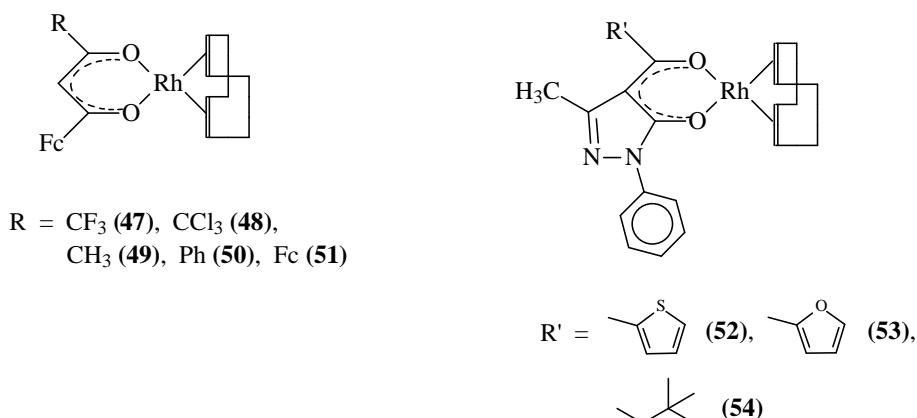
Figure 2.10. Rhodium β-diketonato complexes used to investigate substitution reactions.

The reactivity of acylpyrazolonate rhodium complexes (**Figure 2.10 (52)** – **(54)**) towards substitution was investigated by Pettinari *et al.*[92] The reaction of **(52)** – **(54)** with phen and bipy yielded the [Rh(phen)(cod)]$^+$ and [Rh(bipy)(cod)]$^+$ complexes with the acylpyrazolonate as counterion. The phen-containing complexes was found to be much more stable, and could be isolated in air, while the bipy-containing complexes needed to be isolated under nitrogen and was obtained in lower yields. Compounds **(52)** – **(54)** was also reacted with phosphine ligands, PPh$_3$, dppf and dppe. Substitution of the cod-ligand took place, as shown in route A (**Scheme 2.23**). In the presence of phosphines the rhodium complexes became much more sensitive towards oxidation, yielding Rh(III) oxo species.

2.7. Electrochemistry

This study is concerned with the electrochemistry of a variety of metallocene-containing complexes (goal 5, Chapter 1). A short review of the electrochemical techniques employed, as well as the electrochemistry of relevant metallocene-containing complexes is given here.
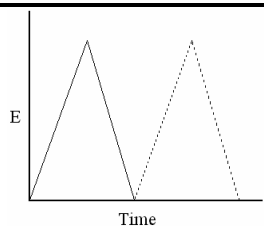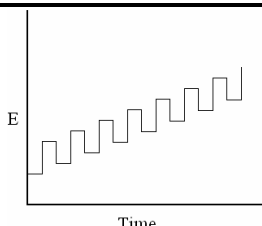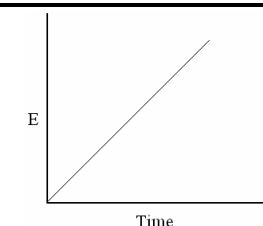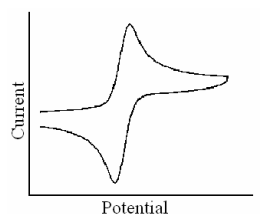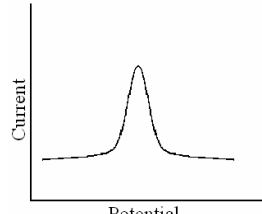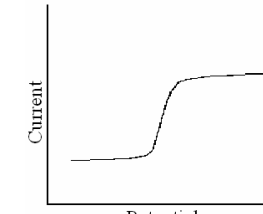
2.7.1. Introduction

Electrochemistry is concerned with the relationship between electrical properties and chemical reactions. This relationship is fundamental and far-reaching, since the structure of matter is basically electrical in nature. Electrochemistry has widespread application in

ionization, electrolysis, metallurgy, battery science, fuel cells, organic chemistry and biochemistry.

Voltammetry consists of changing the potential applied to an electrode, immersed in an unstirred solution containing an electroactive species, and measuring the resulting current that flows between the working and auxiliary electrodes. The potential of this working electrode is controlled *vs*. a reference electrode. The controlling potential can be changed in various ways, depending on the type of voltammetry performed, as summarized in **Table 2.2**.

Table 2.2. Potential excitations used in voltammetry, with the typical voltammograms they produce.

Type Voltammetry	Cyclic Voltammetry (CV)	Square-wave Voltammetry (SW)	Linear-sweep Voltammetry (LSV)
Potential Waveform			
Typical Voltammogram			

In cyclic voltammetry (CV), the potential is cycled in a triangular waveform between two values, increasing linearly to a maximum and then decreasing at the same linear rate to a minimum. This cycle can be repeated numerously, with the current being recorded as a function of time. Square-wave voltammetry (SW) makes use of a square-wave potential excitation signal, with the current measured at various times during the pulse sequence. Better resolution is obtained with SW when CV data does not clearly distinguish between multiple peaks. During linear-sweep voltammetry (LSV) the potential is increased linearly at a very slow rate of no more than 2 mV s^{-1} (compared to a scan rate of at least 50 mV s^{-1} for CV). LSV represents the first wave of the CV at a very slow rate, but can

practically be used to determine the number of electrons transferred during a particular electrochemical process compared to another in the same system. This is the electrochemical equivalent of NMR integration.

2.7.2. Cyclic Voltammetry

Cyclic voltammetry is one of the most versatile and most easily performed electoanalytical techniques in the study of electroactive compounds. It enables the rapid observation of the redox behavior of a given substrate over a wide potential range. CV is capable of rapidly generating a new oxidation state during the forward scan, and then investigating its fate during the reverse scan. There is often very little change in the observed spectrum over multiple scans, but the changes that do occur hold valuable information on electron transfer reaction mechanisms.[93]

An example of a typical CV is given in **Figure 2.11**. The important parameters of a CV are the anodic peak current (i_{pa}), the cathodic peak current (i_{pc}), the anodic peak potential (E_{pa}) and the cathodic peak potential (E_{pc}), as indicated in **Figure 2.11**.
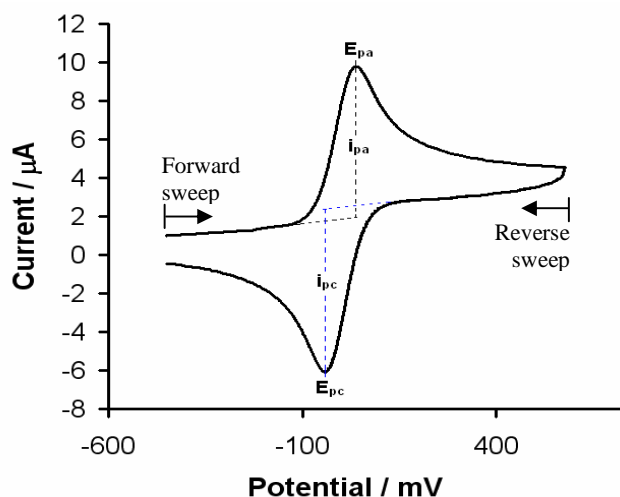
Figure 2.11. A typical cyclic voltammogram.

When measuring the peak current, the correct extrapolation of a baseline is critical, although not always easy, especially with more complicated multiple electron-transfer systems. An electrochemical reversible couple is one in which both oxidized and reduced species rapidly exchange electrons with the working electrode. The formal reduction

36

potential, $E^{o'}$, of an electrochemically reversible redox couple is calculated as the average between the peak potential values $\{E^{o'} = (E_{pa} + E_{pc})/2\}$, and indicates the position of the redox couple. A measured electrochemical reversibility can be obtained by calculating the ΔE_p-value ($E_{pa} - E_{pc}$) for the couple, since a theoretical reversible couple has a ΔE_p-value of 59 mV. In practice, however, a ΔE_p-value of up to 90 mV is still considered to be indicative of a reversible system, while ΔE_p-values of between 90 mV and 150 mV are considered to indicate an electrochemical quasi-reversible process. A ΔE_p-value of more than 150 mV is considered to imply an irreversible process.[94] Electrochemical irreversibility is caused by slow exchange of electrons between the working electrode and substrate. Chemical irreversibility on the other hand is caused when the electrochemically generated oxidized (or reduced) species is labile and prone to further chemical reaction prior to reduction (or oxidation) in a cyclic voltammetry experiment. This is determined by the peak current ratio (i_p (reverse sweep) / i_p (forward sweep)), which approaches 1 for chemically reversible processes. For chemically irreversible systems the oxidized or reduced species undergoes further reaction before it can be reduced or oxidized back to the original species.[95]

2.7.3. Electrochemistry of Metallocene-containing β-diketones

The electrochemistry of a series of ferrocene-containing β-diketones (**1**) – (**5**) have been investigated by Du Plessis *et al.*[31, 27] with CH_3CN and $[NBu_4][PF_6]$ as solvent and electrolyte system. All ferrocenyl peaks showed good electrochemical and chemical reversibility, as summarized in **Figure 2.12** and **Table 2.3**. Peak current ratios were close to unity for all compounds, indicating that no follow-up chemical reactions occurred after the electrochemical oxidation of the iron nucleus.

R	$\upsilon/mV\ s^{-1}$	$\Delta E_p/mV$	$E^{o'}/mV$	i_{pa}/i_{pc}
CF_3 **(1)**	50	74	317	0.96
CCl_3 **(2)**	50	78	293	0.98
CH_3 **(3)**	50	86	236	0.99
C_6F_5 **(4)**	50	73	230	0.97
Fc **(5)**	50	66	187	1.00
Fc **(5)**[*]	50	72	297	1.02

* Second ferrocenyl peak of compound **(5)**
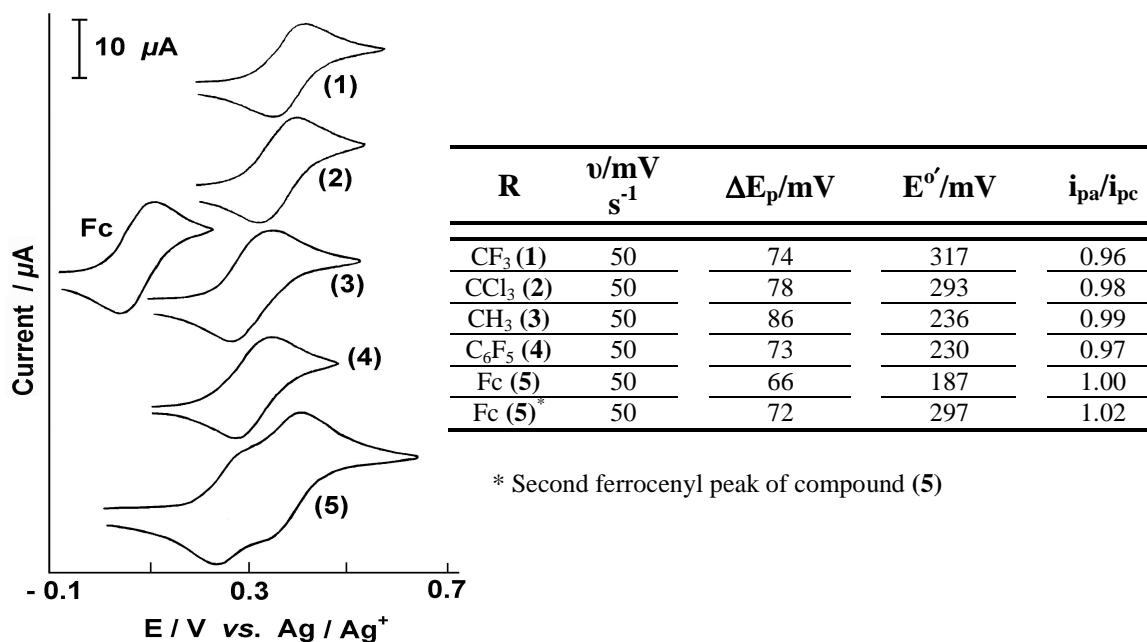
Figure 2.12 & Table 2.3. CV's and electrochemical data of β-diketones **(1)** – **(5)** (FcCOCH$_2$COR).[31, 27]

The electrochemical processes associated with the two ferrocenyl groups of compound **(5)** could be resolved. In contrast, ^{1}H NMR observations could not distinguish between these two ferrocenyl groups. A mixed-valent [FcCOCH$_2$COFc$^+$] species forms when only one ferrocenyl group is oxidized. Good communication between Fc and Fc$^+$, through the β-diketonato backbone, leads to oxidation of the second ferrocenyl group at a different, higher potential than the first under influence of the electron-withdrawing ferrocenium (Fc$^+$) species.

Large variations in $E^{o'}$-values were observed for **(1)** – **(5)** under the influence of side-groups with different group-electronegativities. This also points to good communication between the β-diketonato substituents through the pseudo-aromatic β-diketonato backbone, with oxidation of the ferrocenyl group becoming more difficult with an increase in electronegativity of the other substituent. A linear relationship was established between $E^{o'}$-values of the ferrocenyl-group, and group electronegativities (χ_R) of the other β-diketonato substituent, and could be used to determine selected group electronegativity values.

38

More recent work done in this group has included the electrochemistry of mixed metallocene-containing β-diketones $FcCOCH_2CORc$ **(6)**[29] and $FcCOCH_2COOc$ **(7)**[30]. The electrochemistry of **(6)** and **(7)** showed reversible one-electron oxidations for the ferrocenyl group, and irreversible one-electron oxidations for the ruthenocenyl or osmocenyl groups. It was possible to distinguish electrochemically between keto- and enol-forms of the β-diketones.[96]

2.7.4. Electrochemistry of Metallocene-containing Phosphines

2.7.4.1. Monodentate Ferrocenyl Phosphines

Many reports have been made on the electrochemistry of ferrocenyl phosphine ligands. PPh_2Fc **(13)** have first been studied by Kotz *et al.*[41] in the early 1970's, showing two irreversible oxidation peaks at approximately 0.48 V and 1.5 V (*vs* SCE), as well as a reduction peak at approximately 0.5V, as shown in **Figure 2.13**.
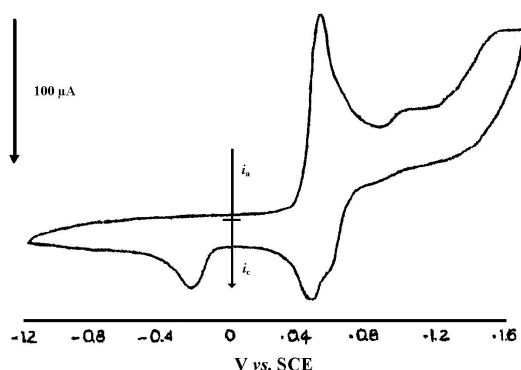
Figure 2.13. CV of PPh_2Fc in CH_3CN with $[NEt_4][ClO_4]$ as supporting electrolyte.[41]

The first oxidation peak becomes practically reversible when the scan is reversed at 0.8 V, before the oxidation process at 1.5 V can take place, with the reduction peak at 0.5 V, also disappearing. These results were later explained by Gref *et al.*[97] as the oxidation of the iron-center of the ferrocenyl group at 0.48 V, followed by a chemical step (C), as summarized in **Scheme 2.24**.

39

$$\text{FcPPh}_2 \quad \xrightleftharpoons{\text{(E)}} \quad [\text{FcPPh}_2]^{\cdot+} \quad + \quad e^- \quad \xrightarrow{\text{(C)}} \quad \text{products}$$
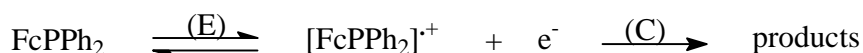
Scheme 2.24. Postulated EC (electrochemical and chemical) mechanism for the redox system of **(13)**.

Coordination of **(13)** to a Lewis acid, or chemical oxidation of the phosphine to FcP(O)Ph$_2$, completely changes the CV. In all such cases only one reversible wave is observed for the Fe-center, which is moved to a slightly higher potential due to the more electron-withdrawing effect of the phosphine-oxide group on the ferrocenyl group. This was also observed for all other ferrocenyl-containing phosphine compounds.[98] This observation, with the phosphorous devoid of a free electron-pair, indicates that the chemical step first postulated by Gref[97] can be linked to the phosphorous atom.

Compounds **(13)** (PPh$_2$Fc), **(14)** (PPhFc$_2$) and **(15)** (PFc$_3$) were also recently investigated by Barrière *et al.*[99], establishing that medium effects play a significant role in the electrochemistry of these compounds, and can go a long way in explaining differences in published results. Their studies made use of CH$_2$Cl$_2$ and [NBu$_4$][B(C$_6$F$_5$)$_4$] as solvent and electrolyte system, which have been shown to be highly non-interacting and limit solvent (CH$_2$Cl$_2$) or electrolyte-analyte association effects to a minimum.

Similar results were obtained to previously reported results, showing irreversible and indistinguishable ferrocenyl redox couples and some follow-up phosphorous activity. The phosphine chalcogenides (Fc$_2$PhP=O) **(55)** and (Fc$_3$P=Se) **(56)**, however, showed CV's with reversible and separated ferrocenyl redox couples, as shown in **Figure 2.14**.
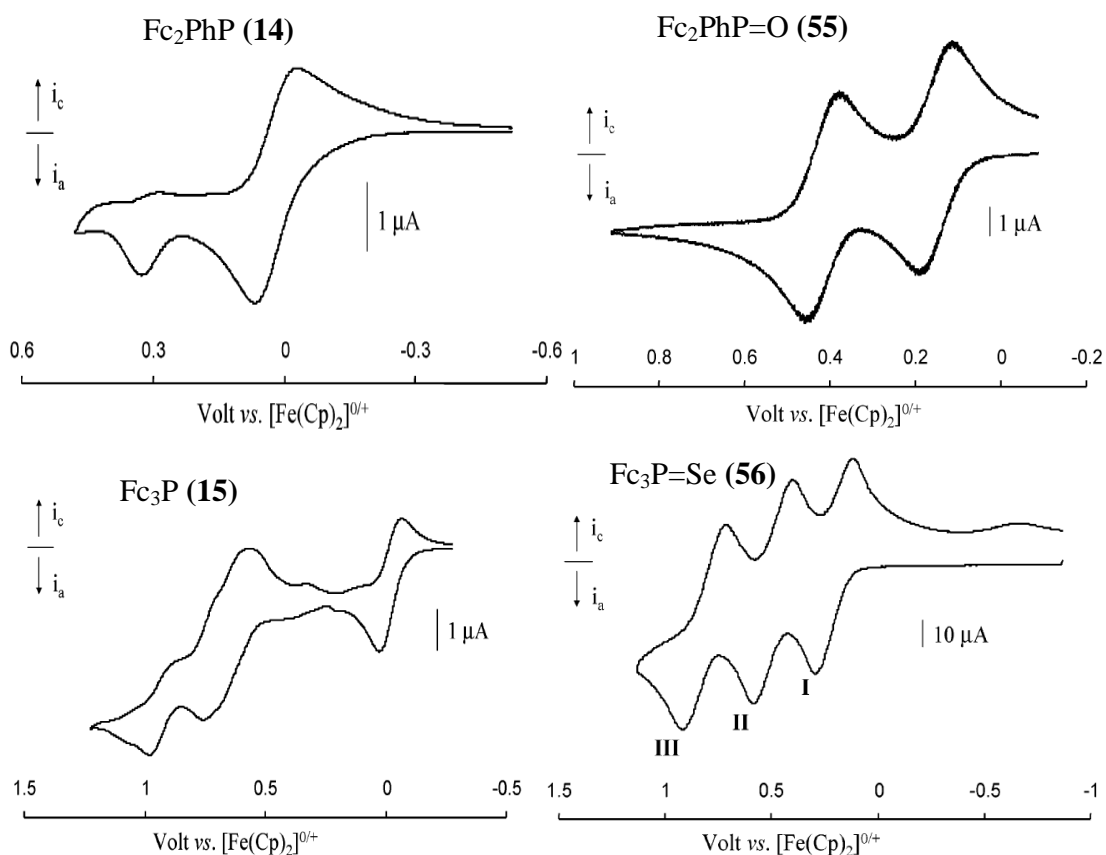
Figure 2.14. CV's of some ferrocenyl phosphine compounds in CH_2Cl_2 with $[NBu_4][B(C_6F_5)_4]$ as supporting electrolyte.[96]

The oxidized species of **(14)** and **(15)** showed significant radical cation character at the phosphorous center, susceptible to attack by nucleophiles such as $[PF_6]^-$, from a supporting electrolyte, other weak nucleophiles, or even the phosphorous group from the neutral starting material. These reactions are considerably slower than ones associated with organic phosphines, such as PPh_3, and are due to the intrinsic charge delocalization of the ferrocenyl groups. When the chalcogenides **(55)** and **(56)** are formed, the free electron-pair of the phosphine is eliminated as a reaction site and the expected ideal ferrocenyl redox couples are observed.

2.7.4.2. Bidentate Metallocenyl Phosphines

The electrochemistry of bidentate metallocene-containing phosphine ligands, dppf **(16)**, dppr **(17)** and dppo **(18)** have been investigated by Nataro *et al.*[100] They have found that, similar to the mono phosphines, oxidation of the metallocene metal center is irreversible

41

and followed by further chemical reaction. It was found to be very dependent on solvent and electrolyte effects as the perchlorate anion, from [NBu$_4$][ClO$_4$], was found to react with the oxidation product of **(16)**, contributing to the irreversibility of the system. The CV's of the ferrocenyl **(16)** and ruthenocenyl compounds **(17)** are given in **Figure 2.15**.
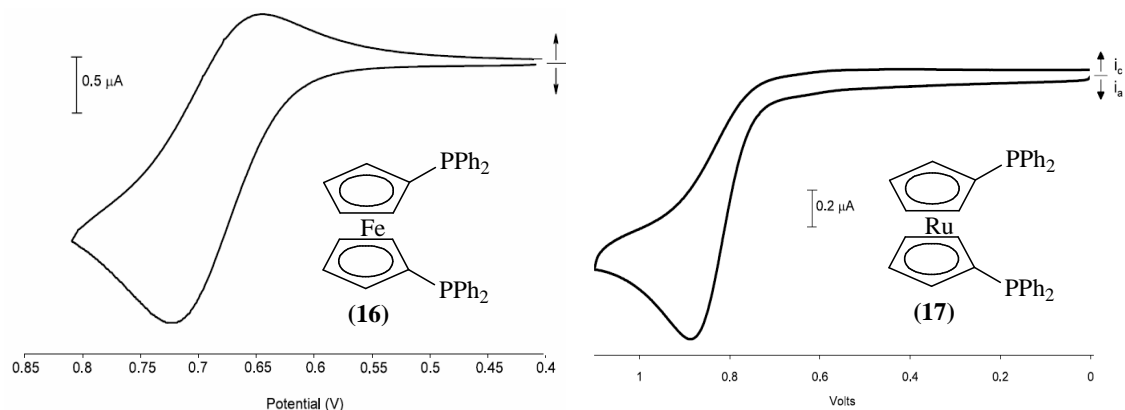
Figure 2.15. CV's of **(16)** and **(17)** in CH$_2$Cl$_2$ with [NBu$_4$][B(C$_6$F$_5$)$_4$] as supporting electrolyte.[100]

Further studies were carried out investigating the electrochemistry of analogue compounds, where no lone electron-pair is available on the phosphorus atom, mostly as the chalcogenide compounds or complexed to metals. In the case of the ferrocene-containing compounds, the electrochemistry showed reversible one-electron systems. This indicates that oxidative instability, in the case of **(16)**, is dependent on the lone electron-pair on the phosphorous atom. After the iron center is oxidized, intramolecular rearrangement with the phosphorous lone pair can take place, forming a phosphorus radical capable of undergoing dimerization, as shown in **Scheme 2.25**. The exact structure of the dimerization product is still under investigation.[101]
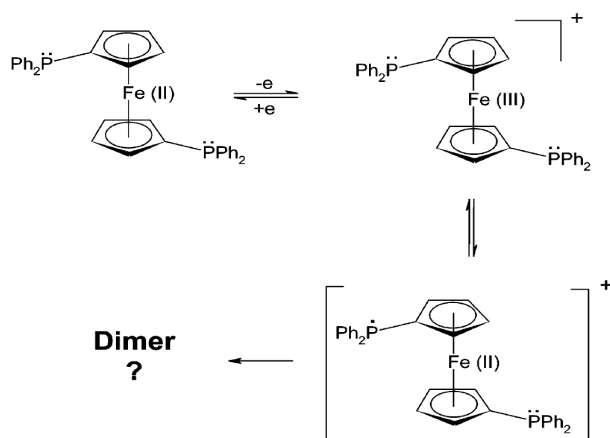
Scheme 2.25. Postulated electrochemical dimerization of (**17**).[101]

In the case of ruthenocene-containing chalcogenide compounds or metal complexes, the CV still showed an irreversible oxidation peak for the metal center, similar to the original compound (**17**). This indicates that dimerization through the phosphorus group is a possible explanation for the irreversible oxidation of (**17**), but probably not the only contributing factor, since complexation with a metal would prevent this type of dimerization. Dimerization through the ruthenium metal centers is also a possibility, as seen in the electrochemistry of pure ruthenocene. But this is thought to be avoided by the use of bulky uncoordinating electrolytes. The increased reactivity of the oxidized ruthenocene species is attributed to the larger distance (approximately 0.3 Å) between the cyclopentadiene rings compared to ferrocenyl compounds. This larger distance makes it sterically more possible for small molecules to react with the metal center. No clear explanation is yet known for the irreversibility of ruthenocene-containing chalcogenide compounds or metal complexes.[100]

The electrochemistry of the osmocenyl bis(diphenylphosphino) compound (**18**) also showed an irreversible one-electron oxidation for the metal center. The oxidation potential was as expected, more positive than the ferrocenyl-compound (**16**), but less positive than the ruthenocenyl compound (**17**), in a similar order to the electrochemistry of the parent metallocenes. The CV of metal-coordinated compounds of (**18**) showed no reversibility, and is thought to behave in the same way as the ruthenocenyl compounds.[102]

43

2.7.5. Electrochemistry of Rhodium(I) compounds

2.7.5.1.   Rhodium(I) Dicarbonyl Compounds

The electrochemistry of ferrocene-containing dicarbonyl rhodium(I) β-diketonato complexes (shown in **Figure 2.16**) was investigated by Conradie *et al.*[103] in CH_3CN as solvent and $[NBu_4][PF_6]$ as supporting electrolyte.

(57) R = CF_3   **(59)** R = C_6H_5
(58) R = CH_3   **(60)** R = Fc
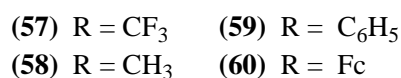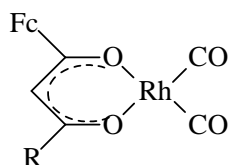
Figure 2.16. Ferrocene-containing dicarbonyl rhodium(I) complexes.

The CV's showed three oxidation waves as shown in **Figure 2.17**. Peaks 1 and 2 are overlapping in most cases, but are best observed for compound **(57)**. Three reduction waves are also observed. The ferrocenyl group showed in all cases a reversible one-electron couple, with $E^{o'}$-values varying between 0.172 V and 0.304 V for compounds **(57)** – **(60)**, depending on the group electronegativities of the β-diketonato side-groups.

It was shown that in CH_3CN as solvent, the CH_3CN coordinates to the rhodium center, forming a five-coordinate trigonal-bipyrimidal complex of the type $[Rh(FcCOCHCOR)(CO)_2(CH_3CN)]$. Rhodium(I) does favour a four-coordinate 16-electron coordination sphere, but 18-electron five-coordinate complexes are known as well. Under the utilized conditions rhodium(I) is oxidized to rhodium(III) and does not exhibit any reversible behavior. Peaks 2 and 3 are both thought to be two-electron Rh(I) to Rh(III) oxidation peaks, one peak 2 belonging to the CH_3CN-adduct, and peak 3 belonging to the unsolvated compound. The intensity of peaks 2 and 3 were found to be dependent on the position of the equilibrium between the CH_3CN-adduct and the unsolvated compound.

(a)

(b)
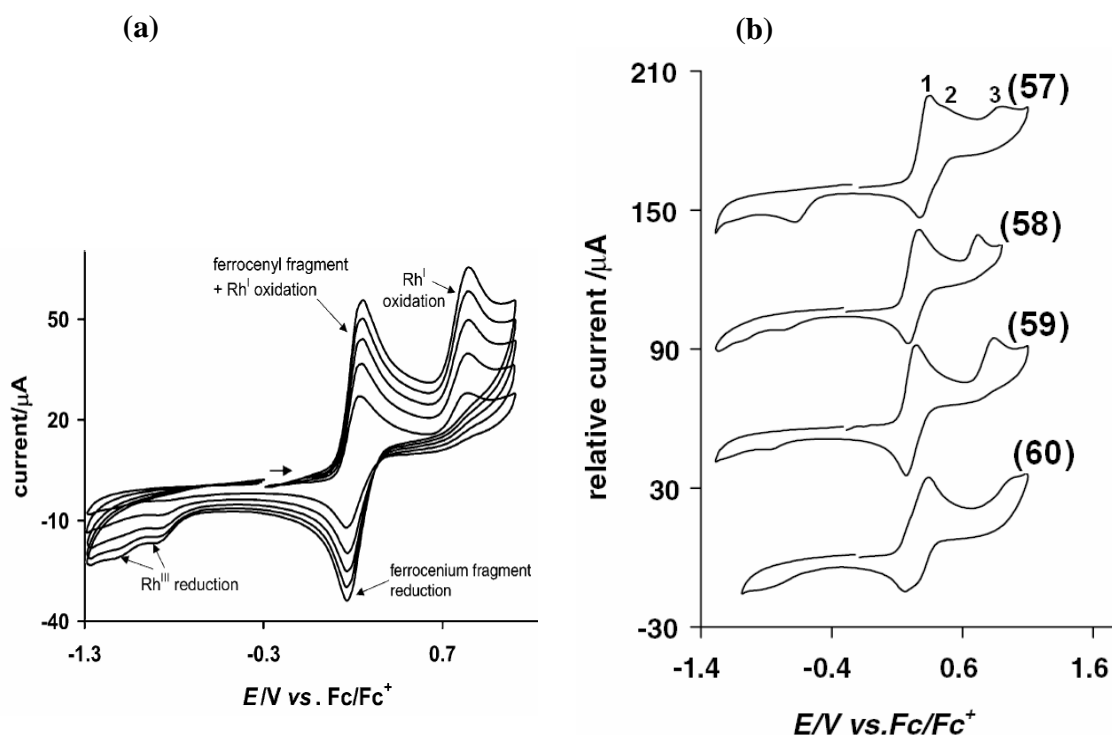
Figure 2.17. CV's of **(a)** compound **(58)** at different scan rates from 50 – 250 mVs[-1], and **(b)** compounds **(57) – (60)**, in CH_3CN with $[NBu_4][PF_6]$ as supporting electrolyte.[103]

Two reduction peaks at much lower potentials are observed for the reduction of Rh(III) to Rh(I), with each of these peaks found to be associated with one of the oxidation peaks. The relatively low intensity of these Rh(III) reduction peaks, compared to the oxidation peaks, can be attributed partially to the high instability of the electrochemically generated Rh(III) species, as no ligands are available to coordinatively saturate the Rh(III) species upon electrochemical formation, as well as the rate of diffusion. By the time that the potential is switched to the cathodic cycle and lowered enough to reduce Rh(III), the majority of the Rh(III) species have either diffused away from the electrode surface, or have decomposed.

2.7.5.2. Rhodium(I) Phosphine Compounds

The electrochemistry of rhodium(I) β-diketonato carbonyl phosphine complexes, shown in **Figure 2.18**, was studied by Lamprecht *et al*.[104] Acetonitrile and $[NBu_4][PF_6]$ were used as solvent and supporting electrolyte respectively.

45
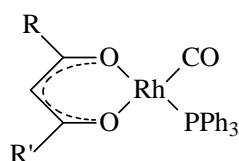
$$(24) \ R = CF_3, \ R' = CH_3 \qquad (61) \ R = C_6H_5, \ R' = CH_3$$
$$(27) \ R = C_6H_5, \ R' = C_6H_5 \qquad (62) \ R = C_6H_5, \ R' = CF_3$$

Figure 2.18. Rhodium(I) β-diketonato phosphine complexes.

The CV's, shown in **Figure 2.19,** illustrated irreversible oxidation peaks for the rhodium center at potentials ranging from 0.308 V to 0.491 V, and correlated to a decrease in pK_a of the free β-diketone. As the pK_a of the free β-diketone ligand increases, the electron density on the rhodium center also increases, making it easier to oxidize, thus reducing the oxidation potential.
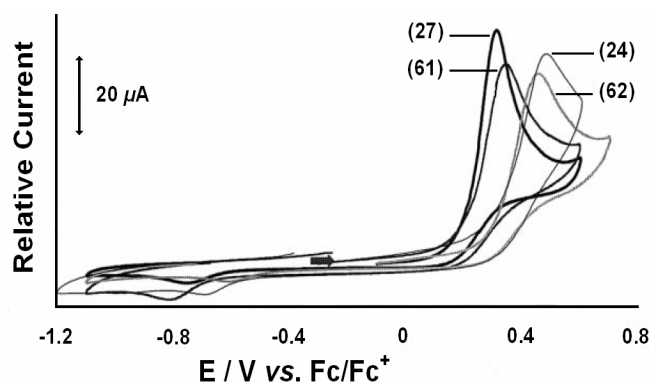
Figure 2.19. CV's of compounds **(24)**, **(27)**, **(61)** and **(62)** in CH$_3$CN with [NBu$_4$][PF$_6$] as supporting electrolyte.[104]

Bulk electrolysis was used to show that it was indeed a two-electron process, oxidizing rhodium(I) to rhodium(III). A reduction peak was shown at a potential more than 1 V more negative than the oxidation peak, indicating the irreversible nature of the rhodium redox processes. The reduction peak of Rh(III) to Rh(I) is of a much lower intensity than the oxidation peak, and can be attributed to the high instability of the electrochemically generated Rh(III) species in the absence of suitable ligands of Rh(III) away from the surface of the electrode, as well as the rate of diffusion being fast.

46

Hill and co-workers[105] have shown that when bulky non-coordinating electrolytic anions, like $[B(C_6F_5)_4]^-$ and $[B(\{(C_6H_3)CF_3\}_2)_4]^-$, are used instead of the normal smaller and more coordinating anions like $[PF_6]^-$ or $[ClO_4]^-$, rhodium is oxidized in a one-electron quasi-reversible process to rhodium(II).

2.8. Anti-Cancer Studies on Metal-Containing Complexes

Metals or metal-containing compounds have been used in cancer and leukemia treatment, as early as the sixteenth century. The discovery of the strong anti-tumor activity of *cis*-diamminedichloroplatinum(II) (cisplatin) **(63)**, shown in **Figure 2.20**, led to increased research on other types of non-organic cytostatic drugs. To date, however, cisplatin and carboplatin **(64)** are still the only widely used metal-containing anti-tumor drugs, despite poor solubility and severe and numerous side-effects suffered from their use. Some of the side-effects experienced include intensive damage to the intestinal linings, leading to loss of appetite (anorexia), as well as nausea and vomiting. Damage to the kidneys and bone marrow may also occur. Cisplatin **(63)** is also a moderate carcinogen, and can lead to lung cancer and other carcinomas. In general, most side-effects of these drugs can be attributed to the lack of differentiating between healthy and cancerous cells.[106]
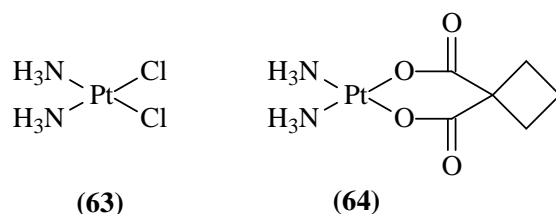
Figure 2.20. Anti-tumor drugs, cisplatin **(63)** and carboplatin **(64)**.

Even if synthetic chemotherapeutic drugs show good in vitro (*i.e.* test tube) anti-cancer properties, it is not necessarily successful in clinical use. Chemotherapeutic drugs are usually poisons to some extent, thus the defense mechanism of the body recognizes them as such and tries to remove them as fast as possible. A quick excretion rate causes large fluctuations in drug concentration in the body, leading to an initial overdose often being responsible for most of the negative side-effects associated with chemotherapeutic drugs. Furthermore, the development of drug resistance by tumour-cells, after prolonged use, is often observed.[106]

Only a small number of non-platinum compounds has made it into clinical trials as potential anti-tumor drugs. Among these are gallium trinitrate, spirogermanium, budotitane (a titanium β-diketonato complex) and titanocene dichloride.[107]

Research has been done on rhodium complexes as possible anti-tumor drugs. A number of Rh(I) complexes has been tested and found to give varying degrees of activity, giving interesting suggestions for the synthesis of further derivatives.[108] Rhodium(I) cyclooctadiene complexes of the type [Rh(cod)(Cl)(L)], as well as the acetylacetonato derivative [Rh(acac)(cod)], have shown promising anti-cancer activity, with only marginal toxicity. Rhodium(I) dicarbonyl complexes with sulfur-containing bidentate ligands have also been found to possess anti-tumor activity, as well as rhodium complexes adsorbed on water-soluble polymers. Despite these positive results, very little is still known about the mechanism of action of these anti-tumor agents.

Ferrocene-containing compounds has also been investigated as possible anti-tumor drugs. Promising results were obtained, especially for complexes posessing the Fe(III) ferrocenium species. These showed significant anti-cancer activity, even at low concentrations.[109]

Previous work in this laboratory have included testing metallocene-containing compounds, as well as their rhodium and titanium derivatives, as possible anti-tumor drugs, with very promising results. As a result, all new compounds synthesized in this study have also been tested for anti-tumor activity, with the hope of finding synergistic effects between more than one active site in the same molecule.

---

[1] A. Combes, *Ann. Chim.*, 1887, **12**, 199; A. Combes, *Compt. Rend.*, 1887, **105**, 869.

[2] L. Claisen, N. Stylos, *Ber.*, 1888, **21**, 1144; L. Claisen, E. F. Erhardt, *Ber.*, 1889, **22**, 1010.

[3] F.A. Cotton, G. Wilkinson, C.A. Murillo, M. Bochmann, *Advanced Inorganic Chemistry*, 6th edition, John Wiley & Sons, Inc, New York, 1999, pp. 479 – 480.

[4] E.C. Constable, *Metals and Ligand Reactivity*, Ellis Horwood Limited, Chichester, West Sussex, 1990, pp. 89 – 90.

[5] R. C. Mehrotra, R. Bohra, D.P. Gaur, *Metal β-Diketonates and Allied Derivatives*, Academic Press, Burlington, USA, 1978, pp. 1-3.

[6] C.R. Hauser, F.W. Swamer, J.T. Adams, *Organic Reactions*, John Wiley & Sons, New York, 1954, vol. 8, pp. 61-64.

[7] C.R. Hauser, R. Levine, R.F. Kibler, *J. Am. Chem. Soc.*, 1946, **68**, 26-29.

[8] J. McMurry, *Organic Chemistry*, Brooks/Cole Publishing Company, Monterey, California, 1984, pp. 825.

[9] J. March, *Advanced Organic Chemistry 4ᵗʰ edition*, John Wiley & Sons Inc., New York, 1992, pp. 491-492.

[10] A.T. Nielson, W.J. Houlihan, *Organic Reactions*, Robert E. Krieger Publishing Company, Huntington, New York, 1975, vol. 16, pp. 19-20.

[11] C.R. Hauser, F.W. Swamer, J.T. Adams, *Organic Reactions*, John Wiley & Sons, New York, 1954, vol. 8, pp. 65-70.

[12] C. Wiles, P. Watts, S.J. Haswell, E. Pombo-Villar, *Tetrahedron Letters*, 2002, **43**, 2945-2948.

[13] J. March, *Advanced Organic Chemistry 3ʳᵈ edition*¸ John Wiley & Sons Inc., New York, 1985, pp. 437.

[14] C. Mao, C.R. Hauser, *Organic Synthesis vol 51*, Editor – R.E. Benson, 1971, John Wiley & Sons Inc, New York, pp. 90-93.

[15] D. Plazuk, A. Klys, J, Zakrzewski, A. Rybarczyk-Pirek, T.A. Olszak, *Organometallics*, 2001, **20**, 4448-4450.

[16] C.R. Hauser, F.W. Swamer, J.T. Adams, *Organic Reactions*, John Wiley & Sons, New York, 1954, vol. 8, pp. 98-100.

[17] C.R. Hauser, F.W. Swamer, J.T. Adams, *Organic Reactions*, John Wiley & Sons, New York, 1954, vol. 8, pp. 101-106.

[18] K. Park, L.J. Cox, *Tetrahedron Letters*, 2003, **44**, 1067-1069.

[19] V. Fargeas, M. Baalouch, E. Metay, J. Baffreau, D. Ménard, P. Gosselin, J. Bergé, C. Barthomeuf, J. Lebreton, *Tetrahedron*, 2004, **60**, 10359-10364.

[20] Z. Shen, B. Lin, L. Wang, Y. Zhang, *Tetrahedron Letters*, 2005, **46**, 8785-8788.

[21] J.C. Sloop, C.L. Bumgardner, G. Washington, W.D. Loehle, S.S. Sankar, A.B. Lewis, *Journal of Fluorine Chemistry*, 2006, **127**, 780-786.

[22] S. Moon, Y. Kwon, *Magnetic Resonance in Chemistry*, 2001, **39**, 89-93.

[23] J.R.B. Gomes, M.A.V. Ribeiro da Silva, *J. Phys. Chem. A*, 2006, **110**, 13948-13955.

[24] C.E. Cain, T.A. Mashburn Jr, C.R. Hauser, *J. Org. Chem.*, 1961, **26**, 1030-1034.

[25] W.R. Cullen, E.B. Wickenheiser, *J. Organomet. Chem.*, 1989, **370**, 141-154.

[26] W. Bell, J.A. Crayston, C. Glidewell, *J. Organomet. Chem.*, 1992, **434**, 115-121.

[27] W.C. du Plessis, J.J.C. Erasmus, G.J. Lamprecht, J. Conradie, T.S. Cameron, A.S. Aquino, J.C. Swarts, *Can. J. Chem.*, 1999, **77**, 378-386.

[28] W.C. du Plessis, T.G. Vosloo, J.C. Swarts, *J. Chem. Soc., Dalton Trans.*, 1998 2507-2514.

[29] K.C. Kemp, M.Sc. Study, *Syntesis, electrochemical, kinetic and thermodynamic studies of new ruthenocene-containing betadiketonato rhodium(I) complexes with biomedical applications*, University of the Free State, R.S.A., 2004.

[30] Z.S. Ambrose, M.Sc. Study, *Synthetic, kinetic and electrochemical studies on new osmocene-containing betadiketonato rhodium(I) complexes with biomedical applications*, University of the Free State, R.S.A., 2006.

[31] W.C. du Plessis, W.L. Davis, S.J. Cronje, J.C. Swarts, *Inorg. Chim. Acta*, 2001, **314**, 97-104.

[32] A.J. Rybarczyk-Pirek, D. Plazuk, J. Zakrzewski, *Acta Cryst.*, 2005, **E61**, m644-m646.

[33] C.M. Zakaria, C.A. Morrison, D. McAndrew, W. Bell, C. Glidewell, *J. Organomet. Chem.*, 1995, **485**, 201-207.

[34] T.J. Colacot, *Chem. Rev.*, 2003, **103**, 3101-3118.

[35] R.C.J. Atkinson, V.C. Gibson, N.J. Long, *Chem. Soc. Rev.*, 2004, **33**, 313-328.

[36] G.P. Sollot, H.E. Mertwoy, S. Portnoy, J.L. Snead, *J. Org. Chem*, 1962, **28**, 1090-1092.

[37] G.P. Sollot, W.R. Peterson Jr., *J. Organomet. Chem.*, 1965, **4**, 491-493.

[38] A. Bootle-Wilbraham, S. Head, J. Longstaff, P. Wyatt, *Tetrahedron Letters*, 1999, **40**, 5267-5270.

[39] C. Baillie, W. Chen, J. Xiao, *Tetrahedron Letters*, 2001, **42**, 9085-9088.

[40] H. Wu, J. Yu, J.B. Spencer, *Org. Lett.*, 2004, **6**, 4675-4678.

[41] J.C. Kotz, C.L. Nivert, *J. Organomet. Chem.*, 1973, **52**, 387-406.

[42] T.J. Colacot, *Platinum Metals Rev.*, 2001, **45**, 22-30.

[43] C. Bianchini, W. Oberhauser, A. Orlandini, C. Giannelli, P. Frediani, *Organometallics*, 2005, **24**, 3692-3702.

[44] S. Li, B. Wei, P.M.N. Low, H.K. Lee, T.S.A. Hor, F.Xue, T.C.W. Mak, *J. Chem. Soc., Dalton Trans.*, 1997, 1289-1293.

[45] O.V. Gusev, A.M. Kalsin, P.V. Petrovskii, K.A. Lyssenko, *Organometallics*, 2003, **22**, 913-915.

[46] C. Bianchini, A. Meli, W. Oberhauser, S. Parisel, O.V. Gusev, A.M. Kal'sin, N.V. Vologdin, F.M. Dolgushin, *J. Molecular Catalysis A: Chemical*, 2004, **224**, 35-49.

[47] T. Hayashi, A. Ohno, S. Lu, Y. Matsumoto, E. Fukuyo, K. Yanagi, *J. Am. Chem. Soc.*, 1994, **116**, 4221-4226.

[48] A.W. Rudie, D. W. Lichtenberg, M.L. Katcher, A. Davison, *Inorganic Chemistry*, 1978, **17**, 2859-2863.

[49] J. Chatt, L.M. Venanzi, *J. Chem. Soc.*, 1957, 4735-4741.

[50] F. Bonati, G. Wilkinson, *J. Chem. Soc.*, 1964, 3156-3160.

[51] J. Conradie, G.J. Lamprecht, S. Otto, J.C. Swarts, *Inorg. Chim. Acta*, 2002, **328**, 191.

[52] W. Simanko, K. Mereiter, R. Schmid, K. Kirchner, A.M. Trzeciak, J.J. Ziolkowski, *J. Organomet. Chem*, 2000, **602**, 59-64.

[53] J.G. Leipoldt, S.S. Basson, L.D.C. Bok, T.I.A. Gerber, *Inorg. Chim. Acta*, 1978, **26**, L35-L37.

[54] J.G. Leipoldt, L.D.C. Bok, J.S. Vollenhoven, A.I. Pieterse, *J. Inorg. and Nuclear Chem.*, 1978, **40**, 61-63.

[55] J.G. Leipoldt, S.S. Basson, J.T. Nel, *Inorg. Chim. Acta.*, 1983, **74**, 85-88.

[56] J.G. Leipoldt, S.S. Basson, *Inorg. Chim. Acta.*, 1986, **117**, L3-L5.

[57] E.C. Steynberg, G.J. Lamprecht, J.G. Leipoldt, *Inorg. Chim. Acta*, 1987, **133**, 33-37.

[58] A. Roodt, J.G. Leipoldt, J.C. Swarts, G.J.J. Steyn, *Acta Cryst.*, 1992, **C48**, 547-549

[59] D. Lamprecht, G.J. Lamprecht, J.M. Botha, K. Umakoshi, Y. Sasaki, *Acta Cryst.*, 1997, **C53**, 1403-1405.

[60] A. Brink, A. Roodt, H.G. Visser, *Acta Cryst.*, 2007, **E63**, m48-m50.

[61] H. Riihimäki, T. Kangas, P. Suomalainen, H.K. Reinius, S. Jääskeläinen, M. Haukka, A.O.I. Krause, T.A. Pakkanen, J.T. Pursiainen, *J. Mol. Cat. A: Chemical*, 2003, **200**, 81-94.

[62] S. Otto, A. Roodt, J.J.C. Erasmus, J.C. Swarts, *Polyhedron*, 1998, **17**, 2447-2453.

[63] N. Bellec, K. Boubekeur, R. Carlier, P. Hapiot, D. Lorcy, A. Tallec, *J. Phys. Chem. A*, 2000, **104**, 9750-9759.

[64] P. Pellon, E. Brulé, N. Bellec, K. Chamontin, D. Lorcy, *J. Chem. Soc., Perkin Trans. I*, 2000, 4409-4412.

[65] N. Bellec, D. Lorcy, *Tetrahedron Letters*, 2001, **42**, 3189-3191.

[66] J. Massue, N. Bellec, S. Chopin, E. Levillain, T. Roisnel, R. Clerac, D. Lorcy, *Inorg. Chem.*, 2005, **44**, 8740-8748.

[67] Q. Zhu, G. Bian, Y. Zhang, J. Dai, D. Zhang, W. Lu, *Inorg. Chim. Acta*, 2006, **359**, 2303-2308.

[68] N. Bellec, J. Massue, T. Roisnel, D. Lorcy, *Inorg. Chem. Comm.*, 2007, **10**, 1172-1176.

[69] J.H. Espenson, *Chemical Kinetics and Reaction Mechanisms*, McGraw-Hill Company, Inc., New York, 1995, pp. 125-127.

[70] G.M. Barrow, *Physical Chemistry*, 6th edition, McGraw-Hill Companies, Inc., New York, 1996, pp. 801-803.

[71] J.H. Espenson, *Chemical Kinetics and Reaction Mechanisms*, McGraw-Hill Company, Inc., New York, 1995, pp. 168-169.

[72] F.A. Cotton, G. Wilkinson, C.A. Murillo, M. Bochmann, *Advanced Inorganic Chemistry*, 6th edition, John Wiley & Sons, Inc, New York, 1999, pp. 1171-1189.

[73] F.A. Cotton, G. Wilkinson, C.A. Murillo, M. Bochmann, *Advanced Inorganic Chemistry*, 6th edition, John Wiley & Sons, Inc, New York, 1999, pp. 1207-1211.

[74] J. Rankin, A.D. Poole, A.C. Benyei, D.J. Cole-Hamilton, *Chem. Commun.*, 1997, 1835.

[75] J. Rankin, A.C. Benyei, A.D. Poole, D.J. Cole-Hamilton, *J. Chem. Soc., Dalton Trans.*, 1999, 3771-3782.

[76] C.M. Thomas, G. Sűss-Fink, *Coordination Chemistry Reviews*, 2003, **243**, 125-142.

[77] R.W. Wegman, A.G. Abatjoglou, A.M. Harrison, *J.Chem. Soc., Chem. Commun.*, 1987, 1891-1892.

[78] M.J. Baker, M.F. Giles, A.G. Orpen, M.J. Taylor, R.J. Watt, *J.Chem. Soc., Chem. Commun.*, 1995, 197-198.

[79] E. Daura-Oller, J.M. Poblet, C. Bo, *Dalton Trans.*, 2003, 92-98.

[80] L. Cavallo, M. Solá, *J. Am. Chem. Soc.*, 2001, **123**, 12294-12302.

[81] S. Zhang, Q. Qian, G. Yuan, *Catalysis Communications*, 2006, **7**, 885-888.

[82] S.S. Basson, J.G. Leipoldt, A. Roodt, J.A. Venter, T.J. van der Walt, *Inorg. Chim. Acta*, 1986, **119**, 35-38.

[83] S.S. Basson, J.G. Leipoldt, A. Roodt, J. A. Venter, *Inorg. Chim. Acta*, 1987, **128**, 31.

[84] J.G. Leipoldt, S.S. Basson, L.J. Botha, *Inorg. Chim. Acta*, 1990, **168**, 215-220.

[85] G.J.J. Steyn, A. Roodt, J.G. Leipoldt, *Inorg. Chem.*, 1992, **31**, 3477-3481.

[86] A. Roodt, G.J.J. Steyn, *Recent Res. Devel. Inorganic Chem.*, 2000, **2**, 1-23.

[87] S.S. Basson, J.G. Leipoldt, J.A. Venter, *Inorg. Chim. Acta*, 1987, **128**, 31-37.

[88] J.A. Venter, J.G. Leipoldt, R. van Eldik, *Inorg. Chem.*, 1991, **30**, 2207-2209.

[89] J. Conradie, G.J. Lamprecht, A. Roodt, J.C. Swarts, *Polyhedron*, 2007, **26**, 5075-5087.

[90] G.E. Rodgers, *Introduction to Coordination, Solid State, and Descriptive Inorganic Chemistry*, McGraw-Hill Inc., New York, 1994, pp. 89-116.

[91] T.G. Vosloo, W.C. du Plessis, J.C. Swarts, *Inorg. Chim. Acta*, 2002, **331**, 188-193.

[92] C. Pettinari, F. Marchetti, A. Cingolani, G. Bianchini, A. Drozdov, V. Vertlib, S. Troyanov, *J. Organomet. Chem*, 2002, **651**, 5-14.

[93] G.A. Mabbott, *J. Chem. Ed.*, 1983, **60**, 697-701.

[94] A. Auger, J.C. Swarts, *Organometallics*, 2007, **26**, 102-109.

[95] P.T. Kissinger, W.R. Heinemam, *J. Chem. Ed.*, 1983, **60**, 702-706.

[96] K.C. Kemp, E. Fourie, J. Conradie, J.C. Swarts, *Organometallics*, 2008, *in press.*

[97] A. Gref, P. Diter, D. Guillaneux, H.B. Kagan, *New J. Chem.*, 1997, **21**, 1353-1358.

[98] J.C. Kotz, C.L. Nivert, J.M. Lieber, *J. Organomet. Chem.*, 1975, **91**, 87-95.

[99] F. Barrière, R.U. Kirss, W.E. Geiger, *Organometallics*, 2005, **24**, 48-52.

[100] C. Nataro, A.N. Campbell, M.A. Ferguson, C.D. Incarvito, A.L. Rheingold, *J. Organomet. Chem.*, 2003, **673**, 47-55.

[101] B.D. Swartz, C. Nataro, *Organometallics*, 2005, **24**, 2447-2451.

[102] S.L. Martinak, L.A. Sites, S.J. Kolb, K.M. Bocage, W.R. McNamara, A.L. Rheingold, J.A. Golen, C. Nataro, *J. Organomet. Chem.*, 2006, **691**, 3627-3632.

[103] J. Conradie, T.S. Cameron, M.A.S. Aquino, G.J. Lamprecht, J.C. Swarts, *Inorg. Chim. Acta*, 2005, **358**, 2530-2542.

[104] D. Lampbrecht, G.J. Lamprecht, *Inorg. Chim Acta*, 2000, **309**, 72-76.

[105] M.G. Hill, W.M. Lamanna, K.R. Mann, *Inorg. Chem.*, 1991, **30**, 4687-4690.

[106] M. David Maree, Eberhard W. Neuse, Elizabeth Erasmus and Jannie C. Swarts, Metal-Based Drugs, 2008, In Press.

[107] N. Katsaros, A. Anagnostopoulou, *Critical Reviews in Oncology / Hematology*, 2002, **42**, 297-308.

[108] G. Sava, S. Zorzet, L. Perissin, G. Mestroni, G. Zassinovich, A. Bontempi, *Inorg. Chim. Acta*, 1987, **137**, 69-71.

[109] E.W. Neuse, F. Kanzawa, *Applied Organomet. Chem.*, 1990, **4**, 19-26.

Chapter 3

Results and Discussion

3.1. Introduction

In this chapter, the synthesis and characterization of a series of mostly new metallocene-containing ligands and their rhodium(I) complexes are described. These include the ferrocene-containing β-diketone ligands, $FcCOCH_2COR$ with R = CF_3 **(1)**, Fc **(5)**, Rc **(6)**, Oc **(7)**, shown in **Figure 3.1**, which were synthesized by Claisen condensation. The new phosphine ligands were synthesized by various different methods, and include ferrocenyl-diphenylphosphine (PPh_2Fc) **(13)**, ruthenocenyldiphenylphosphine (PPh_2Rc) **(65)**, osmocenyldiphenylphosphine (PPh_2Oc) **(66)** and diphenylphosphinocobaltocenium hexafluorophosphate ($PPh_2Cc^+PF_6^-$) **(67)**.

By complexing the above-mentioned electron-rich ligands with suitable rhodium(I) centers, the rhodium(I) β-diketonato complexes [Rh(FcCOCHCOR)(CO)$_2$] and [Rh(FcCOCHCOCF$_3$)(CO)(PPh$_2$Mc)], with R = Fc, Rc, Oc and CF$_3$, and Mc = Fc or Rc, were obtained. Electron-poor rhodium(I) complexes of the fluorinated phosphines $P(Ph)_n(C_6F_5)_{3-n}$, n = 0, 1 or 2, are also described, as well as two rhodium(I) cyclooctadiene tetrathiafulvalene-containing complexes, as shown in **Figure 3.1**.

Characterization studies of the above new complexes included proton nuclear magnetic resonance (^{1}H NMR), Fourier transform infrared (FT-IR) and ultraviolet (UV) spectroscopy, as well as fluorine (^{19}F) and phosphorus (^{31}P) NMR, where appropriate. Single-crystal crystallography was also performed on 1-ferrocenyl-3-osmocenylpropan-1,3-dione **(7)**, ruthenocenyldiphenylphosphine **(65)** and 1-ferrocenyl-4,4,4-trifluorobutane-1,3-dionato carbonyl diphenylferrocenyl phosphino rhodium(I) **(70)**.
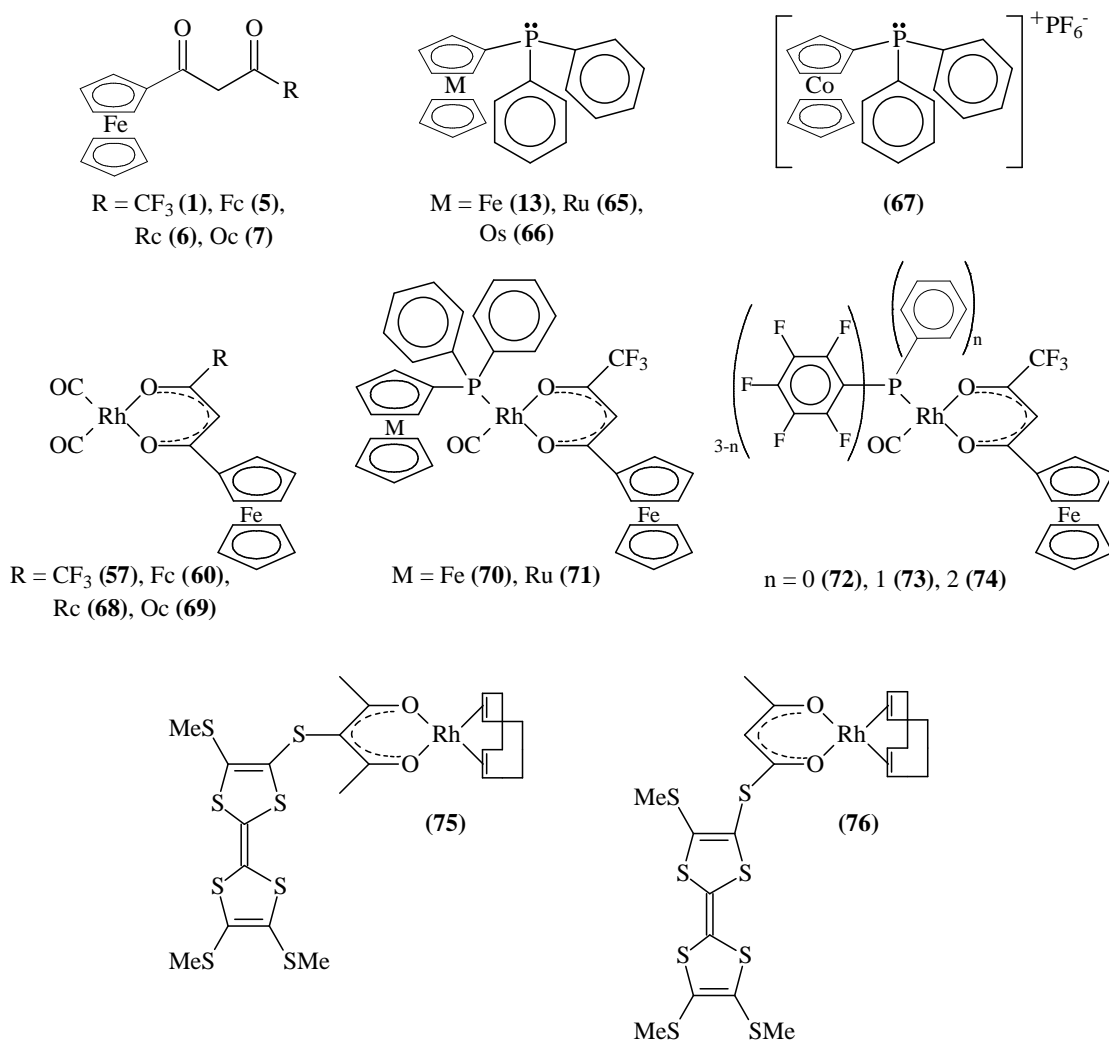
Figure 3.1. Structures of metallocene-containing compounds synthesized during this study.

Reactivity studies of the new compounds included electron-transfer studies utilizing electrochemical techniques, oxidative addition kinetic studies utilizing UV/vis, FT-IR, ^{1}H NMR, ^{19}F NMR and ^{31}P NMR techniques, as well as fast substitution kinetic studies utilizing stopped-flow techniques. Where appropriate, spectro-electrochemical studies were also used to highlight mechanistic factors. This study is also the first ever to demonstrate the use of cyclic voltammetry to successfully probe the kinetics of enolisation of a keto-enriched β-diketone.

The cytotoxic properties of selected synthesized compounds on cancer cells were also determined and are presented here.

3.2. Synthesis

3.2.1. Ferrocenyl β-Diketones

The ferrocene-containing β-diketones FcCOCHCOR [where R = CF$_3$ **(1)** (59 % yield), Fc **(5)** (62 %), Rc **(6)** (29 %) and Oc **(7)** (31 %)] were synthesized by Claisen condensation, with complex **(7)** new. In the case of **(1)** and **(5)**, acetyl ferrocene was deprotonated by LDA and reacted with the appropriate ester, while in the case of **(6)** and **(7)**, acetyl ruthenocene and acetyl osmocene were used as the initial ketone to react with methyl ferrocenoate. Ferrocene complexes were reddish, ruthenocene complexes have a dark yellow colour, while osmocene derivatives are off-white in colour.

Acetyl ruthenocene was prepared by a Friedel-Crafts acetylation of ruthenocene by acetic anhydride in the presence of aluminum trichloride (AlCl$_3$) in 55 % yield. In contrast, acetylation of ferrocene (60 %) and osmocene (55 %) were carried out in the presence of phosphoric acid (H$_3$PO$_4$), which is a much milder Lewis acid catalyst. In the case of osmocene, much longer reaction times of at least 4 hours were required to obtain good yields, in contrast to reaction times of 10 minutes for ferrocene.
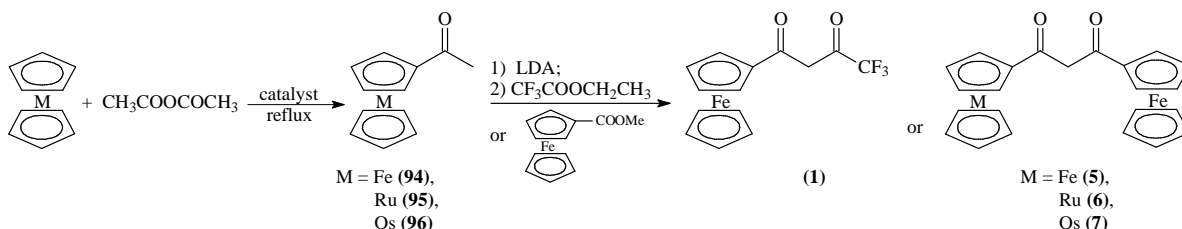
Scheme 3.1. Synthetic route for acetylation of metallocenes and the synthesis of ferrocenyl β-diketones. When M = Fe and Os, catalyst = H$_3$PO$_4$, and when M = Ru, catalyst = AlCl$_3$.

Deprotonation of the acetyl metallocene with LDA (lithium diisopropylamide) yields an *in situ* generated nucleophile McCOCH$_2^-$ (Mc = Fc, Rc or Oc), which can attack unreacted acetyl metallocene and lead to self-condensation, forming an aldol side-product. To avoid this, the added base was marginally in excess, not to be the limiting reagent. Careful optimization of the reaction time before addition of the ester is also needed to avoid self-condensation. In our hands, best results were obtained by allowing

LDA to react with the ketone to generate the nucleophilic species (MeCOCH$_2^-$), for no more than 30 minutes, before addition of the appropriate ester.

3.2.2. Attempted β-Diketone Synthesis *via* BF$_3$ Catalyst

As part of this study attempts were made to extend the known series of β-diketones to include cobaltocenium-containing β-diketones. The known instability of cobaltocenium derivatives to strong basic compounds (cyclopentadienyl cleavage takes place) necessitated an alternative synthetic approach. The Lewis acid approach using boron trifluoride as catalyst (as described in **Chapter 2**, section **2.2.2**) offers an alternative to the basic LDA route. Reactants are a ketone and an anhydride. Ferrocenoic anhydride **(77)** and cobaltocenoic anhydride hexafluorophosphate **(78)**, **Scheme 3.2**, were synthesized from the appropriate metallocenoic acid and acid chloride, in the presence of pyridine, by adaptation of known general procedures.[1]
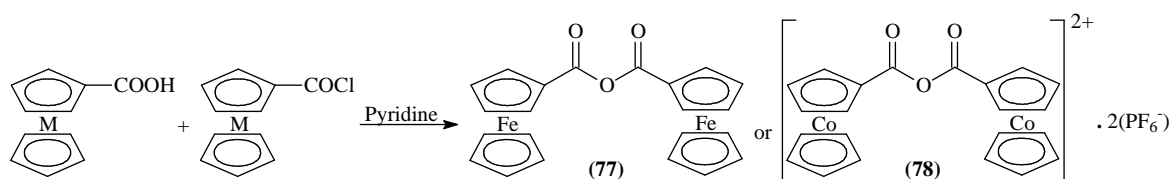
Scheme 3.2. Synthesis of ferrocenoic anhydride **(77)** (M = Fe) and cobaltocenoic anhydride hexafluorophosphate **(78)**, (M = Co . PF$_6^-$).

First attempts focused on the reaction between acetyl ferrocene and either acetic anhydride or trifluoro acetic anhydride as a test reaction. However, all attempts failed as only starting materials were recovered. This result was considered to imply that the strong electron-donating properties of the ferrocenyl group forces the equilibrium shown in **Scheme 3.3** so far to the left that the reactive intermediate necessary for β-diketone synthesis does not form in synthetically useful quantities.
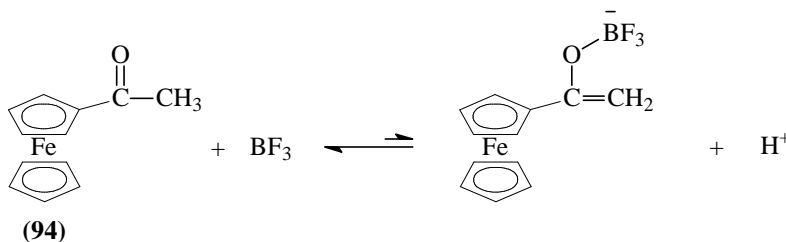
Scheme 3.3. Electron-donating properties of the ferrocenyl group disfavours formation of the BF$_3$ anionic complexes.

56

To overcome this problem, propanoylferrocene **(79)** was synthesized by Friedel Crafts-acylation. It was thought that the larger ketone side-chain would stabilize the anionic BF_3 complexes. Despite this modification, the desired β-diketone was never obtained. Reacting **(79)** with a range of anhydrides, including **(77)** and **(78)**, as well as acetic anhydride and trifluoro acetic anhydride, all led to the self aldol condensation product **(80)**, shown in **Scheme 3.4**. The Aldol reaction is a competing side-reaction with BF_3-catalysed β-diketone formation reactions and hence this synthetic route was not further pursued.

$$R = CH_3, CF_3, Fc, Cc^+PF_6^-$$
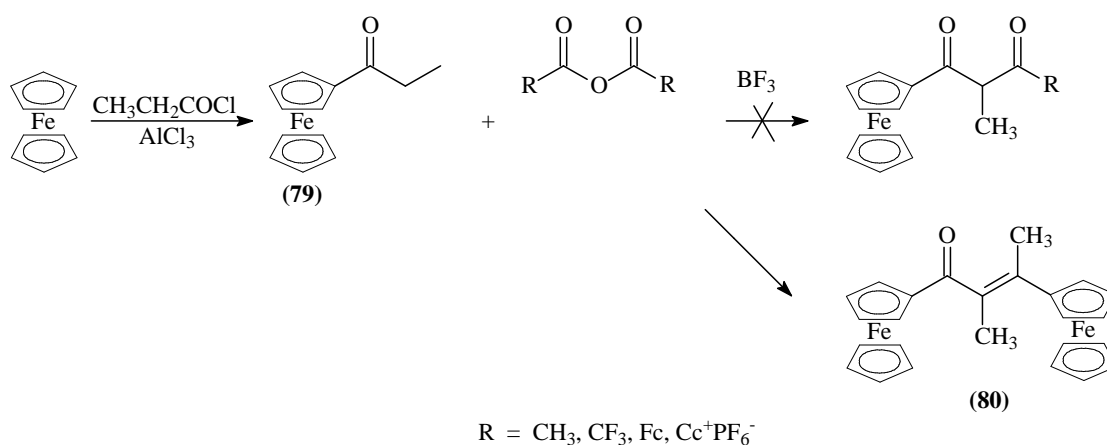
Scheme 3.4. Aldol formation during attempted β-diketone synthesis with BF_3 as catalyst.

3.2.3. Metallocene-containing Phosphine Ligands

The metallocene-containing diphenylphosphine ligands ferrocenyldiphenylphosphine (PPh$_2$Fc) **(13)**, ruthenocenyldiphenylphosphine (PPh$_2$Rc) **(65)**, osmocenyldiphenyl-phosphine (PPh$_2$Oc) **(66)** and the positively-charged compound diphenyl-phosphinocobaltocenium hexafluorophosphate (PPh$_2$Cc$^+$PF$_6^-$) **(67)**, where the cobalt-center is in a +3 oxidation state, have been synthesized.

A different synthetic route was required for each of the different metallocene phosphines, due to the different reactivity of each parent metallocene, as summarized in **Scheme 3.5**. PPh$_2$Fc **(13)** was synthesized by Friedel Crafts reaction of ferrocene and chloro-diphenylphosphine, in the presence of AlCl$_3$, according to known methods, as shown in reaction **(a)**.[2] In our hands slightly better yields, at shorter reaction times were obtained

in n-heptane (36 %) due to its higher boiling point (98 °C) compared to n-hexane (69 °C, with 31 % yield). For phosphines **(65)**, reaction **(b)**, and **(66)**, reaction **(c)**, the metallocene was firstly deprotonated with a strong base, followed by reaction with chloro diphenylphosphine. Yields were low (19 % and 13 % respectively), but acceptable, considering unreacted metallocene was recovered. Compound **(67)** required a different approach, since it exists as a cationic species, due to the cobalt center being in the +3 oxidation state. For **(13)**, **(65)** and **(66)**, the Fe, Ru and Os metal centers are all in the +2 oxidation state. Similarly to the synthesis of the bidentate cobaltocenium phosphine **(19)**, cyclopentadiene is firstly derivatised to cyclopentadienyldiphenylphosphine. After addition of an equal amount of unsubstituted cyclopentadiene, complexation with CoBr$_2$ led to a statistical mixture of cobaltocenium, diphenylphosphinocobaltocenium hexafluorophosphate **(67)** and 1,1'-bis(diphenylphosphino)cobaltocenium hexafluoro-phosphate.[3] These three products could be separated from each other by recrystallization.
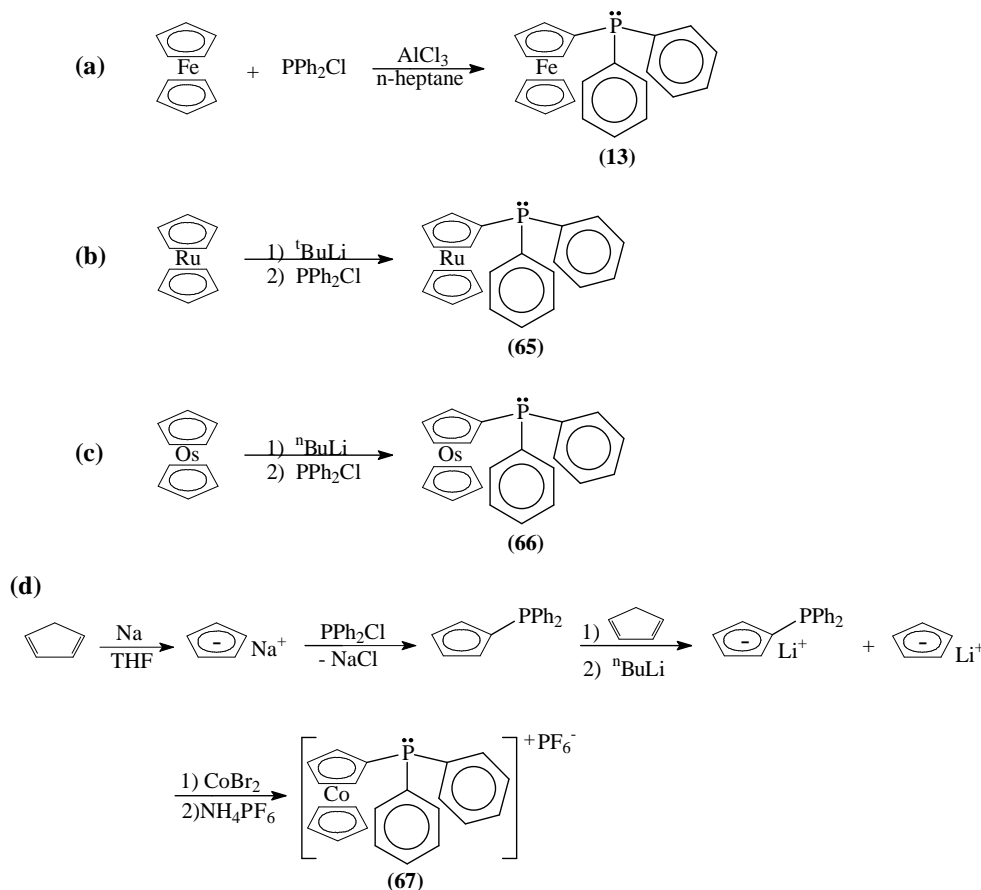
Scheme 3.5. Synthesis of metallocene-containing phosphines PPh$_2$Fc **(a)**, PPh$_2$Rc **(b)**, PPh$_2$Oc **(c)** and PPh$_2$Cc$^+$PF$_6^-$ **(d)**.

Purification of phosphines **(13)**, **(65)** and **(66)** proved difficult as the phosphine and the parent metallocene was not easily separated. Compound **(67)** was easily purified by recrystallization and contained little impurities, while compound **(13)** required repeated recrystallization. Compounds **(65)** and **(66)** were purified by repeated column chromatography of dilute solutions as described in the experimental section.

3.2.4. Rhodium Dicarbonyl Complexes

The known dicarbonyl complex **(83)**, bearing no ferrocenyl substituent on the β-diketone, was synthesized *via* route **A** (**Scheme 3.6**), according to published methods.[4] The synthesis proceeds in a one-pot process, with the *in situ* formation of the chloro-bridged tetra-carbonyl rhodium dimer [Rh$_2$Cl$_2$(CO)$_4$] being reacted, without isolation, with trifluoro acetylacetone, to yield complex **(83)**. This route, however, gave poor yields for the metallocene-containing complexes **(57)**, **(60)**, **(68)** and **(69)**. Hence, to obtain these complexes, route **B** (**Scheme 3.6**) was followed.
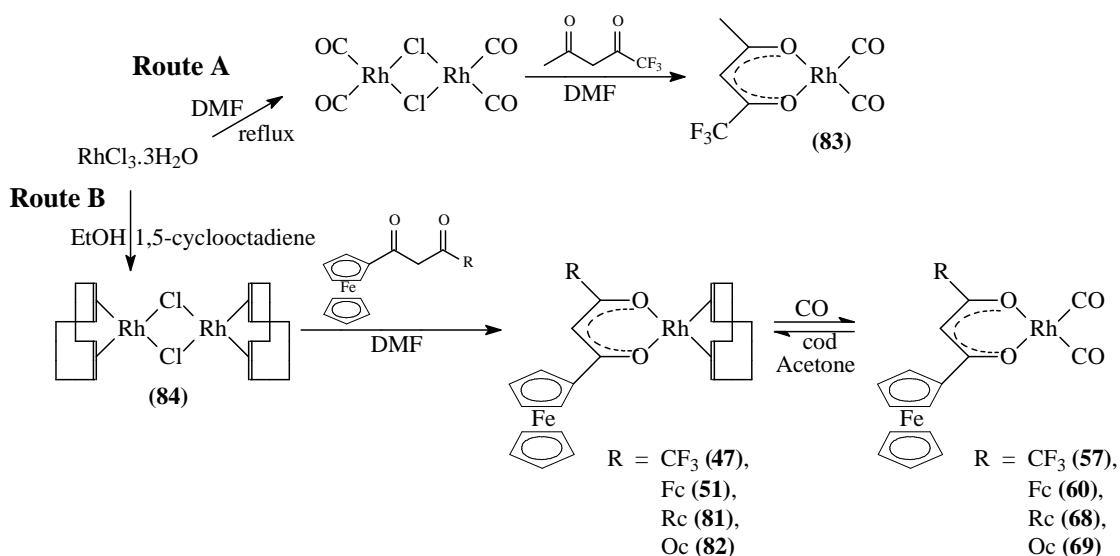
Scheme 3.6. Synthetic routes used for the synthesis of rhodium(I) β-diketonato dicarbonyl complexes.

The synthetic approach, demonstrated by route **B,** involves first the synthesis and isolation of a rhodium-chloro-cod dimer **(84)** followed by the isolation of the rhodium(I) β-diketonato cod complexes **(47)**, **(51)**, **(81)** and **(82)**. Only then was substitution of the cod ligand achieved by bubbling of CO gas, at a pressure of approximately 10 mm Hg

above atmospheric pressure, through an acetone solution of the rhodium(I) cod complexes, yielding the desired complexes. All rhodium(I) cod complexes were synthesized at room temperature and isolated in excellent yields (77 - 91 %). The displacement of cod by CO is an equilibrium process. The products **(57)**, **(60)**, **(68)** and **(69)** were precipitated from solution and care was taken to separate the precipitate from the liberated cod that float on top of the aqueous phase, to prevent the backward reaction. Yields varied between 74 and 97 %.

3.2.5. Rhodium(I) Phosphine Complexes

3.2.5.1. Rhodium(I) Complexes with Metallocene Phosphines

The new rhodium(I) complexes containing metallocene phosphine ligands, shown in **Scheme 3.7**, have been synthesized by addition of an equivalent amount of phosphine to a solution of [Rh(FcCOCHCOCF$_3$)(CO)$_2$] in the minimum amount of either n-hexane or benzene as solvent. In some cases bubbling was observed due to the rapid release of the substituted CO ligand. Phosphine substitution to obtain **(29)**[5] and the new complexes **(70)** and **(71)** were long; generally reactants were stirred 16 hours to ensure high yields. All complexes were isolated by slow evaporation of the solvent, forming crystalline solids in good yield (> 75 %). It was observed that benzene as solvent yielded cleaner reactions with fewer impurities in the final product.
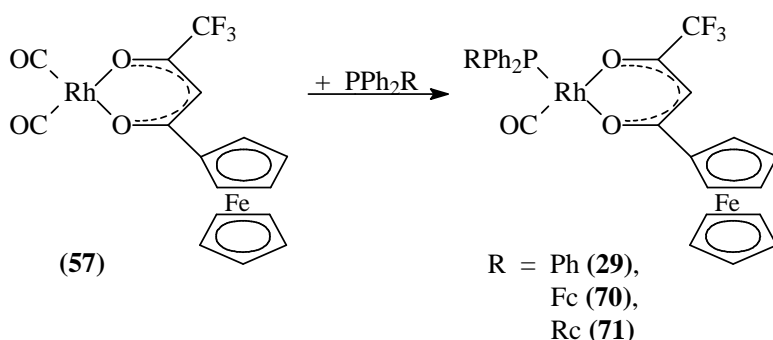
Scheme 3.7. Synthesis of rhodium(I) β-diketonato phosphine complexes.

^{1}H-NMR spectra (**Figure 3.2**) of compounds **(29)**, **(70)** and **(71)** all showed the existence of two isomers in solution. The two observed isomers, shown in **Scheme 3.8**, is

considered either a *cis*-isomer (isomer 1), where the phosphine ligand is *cis* to the β-diketonato oxygen closest to the ferrocenyl-group, or a *trans*-isomer (isomer 2), where the phosphine ligand is *trans* to the β-diketonato oxygen closest to the ferrocenyl group. These isomers are in equilibrium in solution, but are expected to crystallize in only one structural orientation. In this study, the crystal structure of the *cis*-isomer of **(70)** was solved, see **Section 3.4**.

R = Ph **(29)**, Fc **(70)** or Rc **(71)**
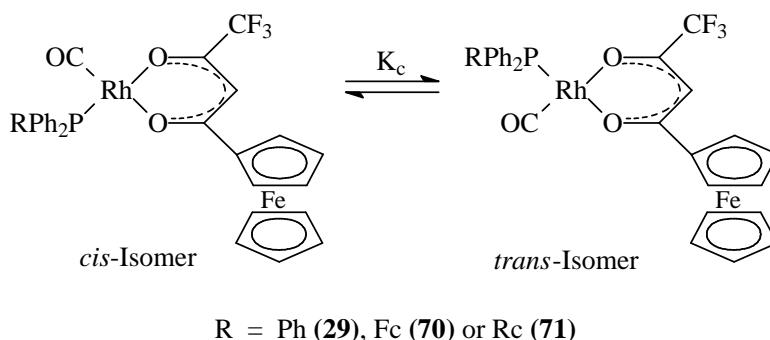
Scheme 3.8. *Cis* and *trans* isomers of rhodium(I) β-diketonato phosphine complexes, **(29)**, **(70)** and **(71)**.

Large δ_H shifts were observed for the different isomers, especially with regard to the metallocenyl peaks of the β-diketonato and phosphine ligands. This made it possible to distinguish between different isomers. It is known that electron-withdrawing substituents move the proton peaks downfield. For example, the acetyl group in acetyl ferrocene moves cyclopentadienyl peaks to lower peak positions.[6] In contrast, electron-donating substituents move the proton peaks upfield, as was described for ethyl ferrocene.[7] By recognizing that *trans* influences in square-planar complexes are stronger effects than cis influences, it is possible to assign ^{1}H NMR peaks to the *cis*- and *trans*-isomers. For the *trans*-isomer (isomer 2 in **Figure 3.2**), the phosphine ligand donates electron density *via* the σ-bond, across the rhodium center, to the *trans* located β-diketonato oxygen. This increases the electrondensity on the β-diketonato ferrocenyl group, thus moving the ferrocenyl peaks of this isomer upfield. The ^{1}H-NMR spectrum of **(71)** is shown in **Figure 3.2**, indicating the location of *cis*- and *trans*-isomer peaks. The equilibrium constant (K_c = [*trans*-isomer]/[*cis*-isomer]) can be determined from the NMR-data as {(Integral of *trans*-peak)/(Integral of *cis*-peak)}. This can be determined for each peak in the spectrum, e.g. {(0.556)/(0.432)} for the methine-peak of compound **(70)**, giving a K_c-

value of 1.287. The average K_c-value for compounds (70) and (71) was determined and is listed in **Table 3.1**.

Isomer 1 (*cis*)   Isomer 2 (*trans*)
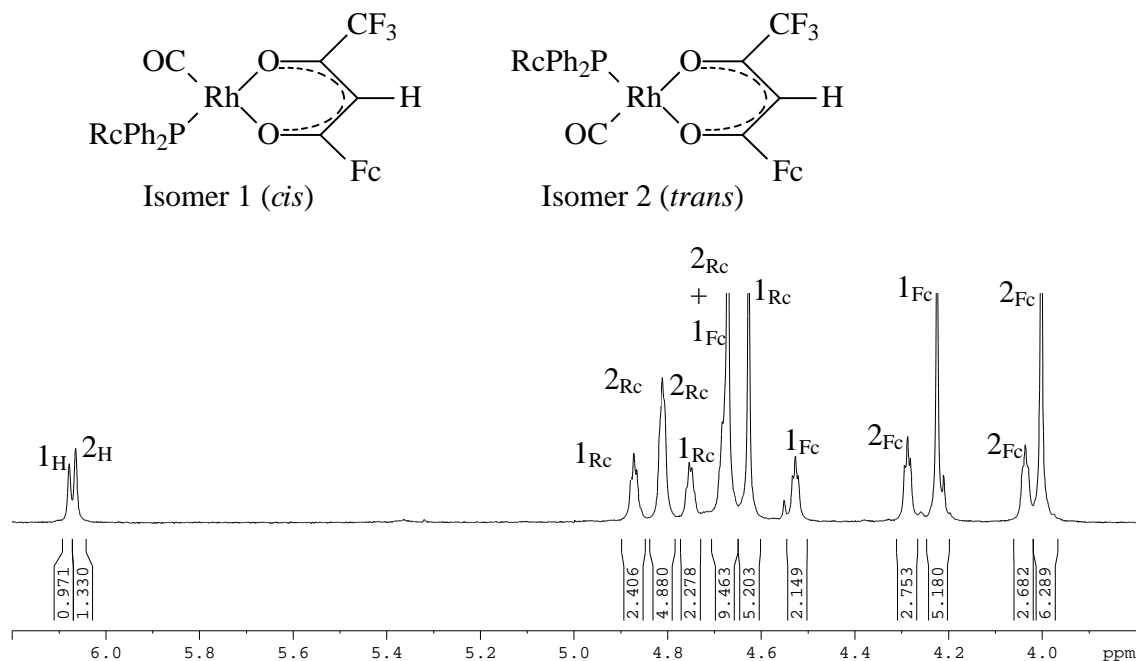
Figure 3.2. ^{1}H NMR spectrum of rhodium(I) β-diketonato phosphine complex (71). The footnotes (Fc) indicates signals from the β-diketonato ferrocenyl group, (Rc) indicates signals from the phosphine ruthenocenyl group and (H) indicates the signals associated with the β-diketonato methine protons.

^{31}P NMR spectra of complexes (29), as well as (70) and (71), shown in **Figure 3.3**, also showed two isomers in solution. A doublet is observed for each isomer, due to coupling with the Rh center. No signal overlapping was observed. Physical data for compounds (29), (70) and (71) are summarized in **Table 3.1.**
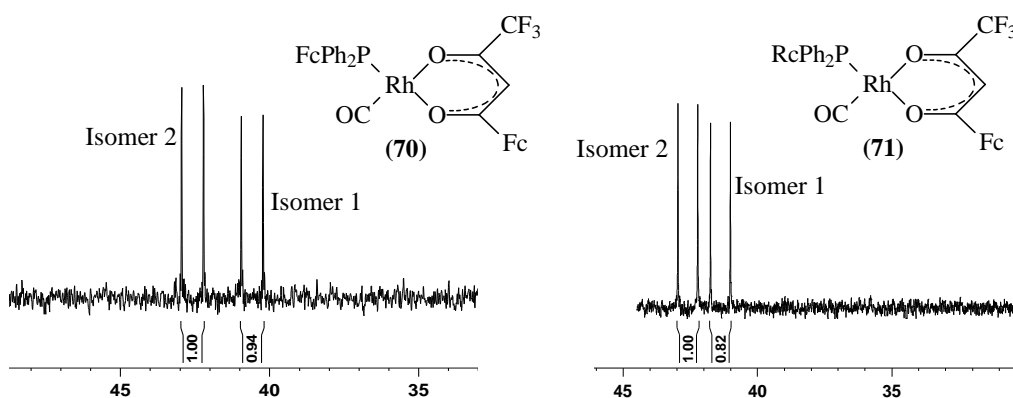
Figure 3.3. ^{31}P NMR spectra of rhodium(I) β-diketonato phosphine complexes (70) and (71).

62

Table 3.1. Physical parameters of [Rh(FcCOCHCOCF$_3$)(CO)(PPh$_2$R)] complexes **(29)**, **(70)** and **(71)**.

Compound	Isomer	δ^{31}P / ppm	$^1J(^{31}$P-^{103}Rh) / Hz	δ^1H / ppm (methine peak)	Isomer Ratio	Average K_c	υ(CO) / cm^{-1}
(29)[8],	*cis* -1	48.04	176.4	6.05	40 %	1.47	1987
R = Ph	*trans* -2	48.04	176.4	6.05	60 %		
(70),	*cis* -1	40.59	171.3	6.12	44 %	1.23	1975
R = Fc	*trans* -2	42.59	171.3	6.10	56 %		
(71),	*cis* -1	41.39	170.5	6.08	43 %	1.29	1978
R = Rc	*trans* -2	42.59	170.5	6.06	57 %		

Attempts were made to synthesize rhodium(I) complexes containing the osmocenyl phosphine ligand, as shown in **Scheme 3.9**. PPh$_2$Oc **(66)** was firstly reacted with [Rh(FcCOCHCOOc)(CO)$_2$] **(69)**. A ^{1}H NMR of the crude mixture showed the presence of the desired product **(87)**, mixed with large portions of reactants. Attempts to purify the compound by column chromatography led to decomposition and fixation of the product on the origin. The mixture could, however, be enriched in the product **(87)** by fractional precipitation from CH$_2$Cl$_2$ by the slow addition of n-hexane. The product could never be obtained in a pure state due to an apparent equilibrium between reactants and product.

(83) R = CH$_3$, R' = CF$_3$
(57) R = Fc, R' = CF$_3$
(69) R = Fc, R' = Oc

(85) R = CH$_3$, R' = CF$_3$
(86) R = Fc, R' = CF$_3$
(87) R = Fc, R' = Oc
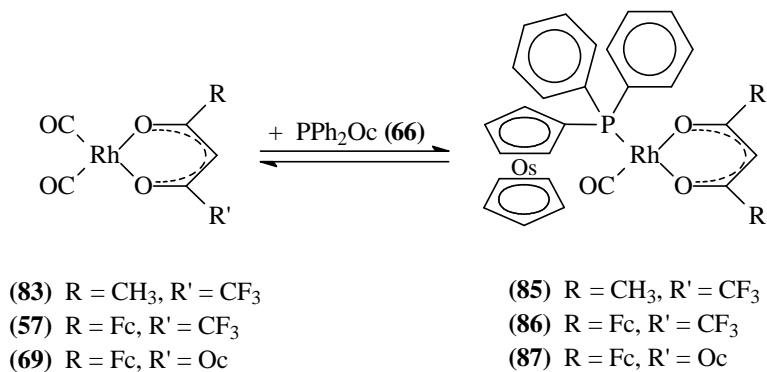
Scheme 3.9. Synthesis of rhodium(I) osmocenyl phosphine complexes.

A similar equilibrium that prevented product isolation was observed when the phosphine **(66)** was reacted with [Rh(FcCOCHCOCF$_3$)(CO)$_2$] **(57)** and [Rh(CH$_3$COCHCOCF$_3$)(CO)$_2$] **(83)**, as shown in **Scheme 3.9**. A mixture of reactants in equilibrium with the desired product was obtained.
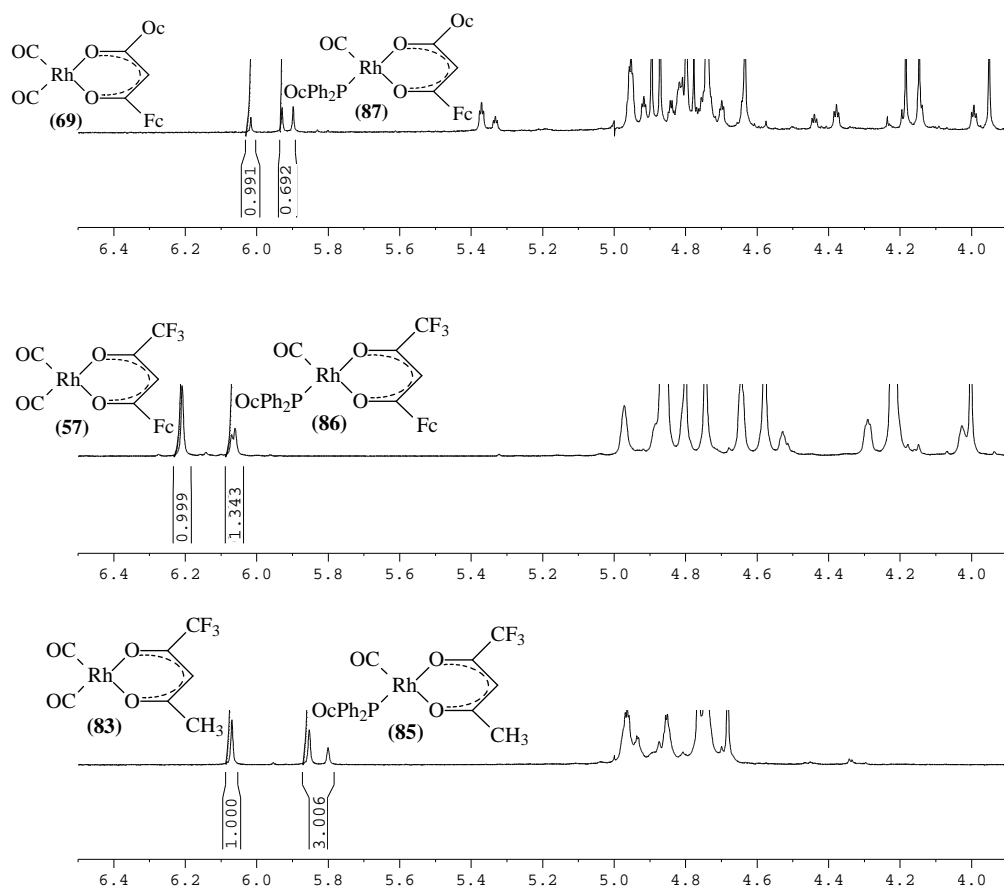
Figure 3.4. ^{1}H NMR spectra of the best purified reaction mixtures of **(85)** - **(87)**, showing reactants still present in the solution.

When focusing on the methine protons of the ^{1}H NMR of the best purified mixtures of products, shown in **Figure 3.4**, two peaks are observed for the two isomers of the product as well as the methine peak of the starting material. This was used to determine the ratio of product to reactant. A general trend is observed that with an increase in group electronegativity (χ_R) of the β-diketonato side-groups, the equilibrium moves more in the direction of the products, *i.e.* complex with mono CO substitution. Thus, the more electron-poor the rhodium center, the more successful substitution of one of the carbonyl ligands in [Rh(β-diketonato)(CO)$_2$], with a highly electron-donating phosphine ligand takes place. This trend is summarized in **Figure 3.5** and **Table 3.2**.

64
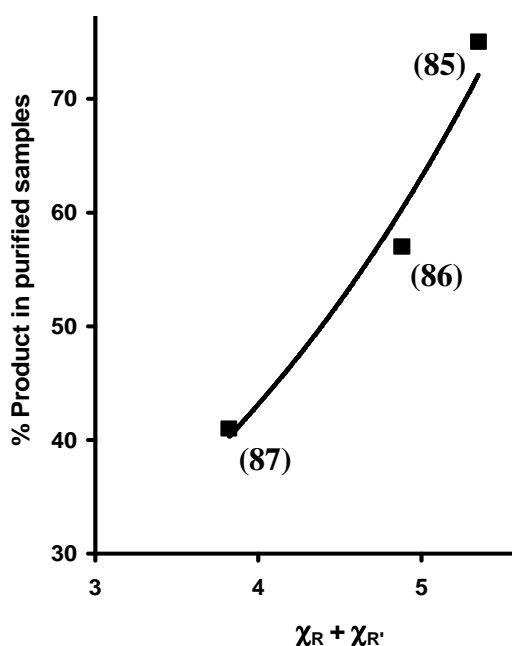
Product	$\chi_R + \chi_{R'}$	% Product
[Rh(CF$_3$COCHCOCH$_3$)(CO)(PPh$_2$Oc)] **(85)**	5.35	75
[Rh(FcCOCHCO CF$_3$)(CO)(PPh$_2$Oc)] **(86)**	4.88	57
[Rh(FcCOCHCOOc)(CO)(PPh$_2$Oc)] **(87)**	3.77	41

Figure 3.5 & Table 3.2. Relationship between substituent group electronegativity ($\chi_R + \chi_{R'}$) of β-diketonato side-groups on product formation of [Rh(β-diketonato)(CO)(PPh$_2$Oc)], with R = CF$_3$, R' = CH$_3$ **(84)**, or R = CF$_3$, R' = Fc **(85)**, or R = Fc, R' = Oc **(86)**.

Reactions were also carried out between metallocene phosphine ligands PPh$_2$Fc **(13)** or PPh$_2$Rc **(65)** and rhodium(I) complexes [Rh(FcCOCHCOFc)(CO)$_2$] **(60)**, [Rh(FcCOCHCORc)(CO)$_2$] **(68)** and [Rh(FcCOCHCOOc)(CO)$_2$] **(69)**. In all cases an equilibrium was observed and the desired product could not be isolated as single species.

3.2.5.2. Rhodium(I) Complexes with Fluorinated Phosphines

Rhodium(I) complexes of the type [Rh(FcCOCHCOCF$_3$)(CO)(PPh$_n$(C$_6$F$_5$)$_{3-n}$)], with n = 0, 1, 2 and C$_6$F$_5$ = pentafluorophenyl, have also been synthesized, as shown in **Scheme 3.10**.
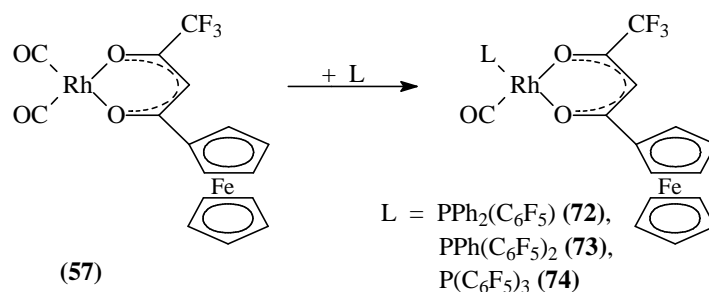
Scheme 3.10. Synthesis of rhodium(I) β-diketonato phosphine complexes.

^{1}H-NMR spectra of complexes **(72)** - **(74)** showed the existence of two isomers in solution, either a *cis*-isomer (isomer 1), where the phosphine ligand is *cis* to the β-diketonato oxygen closest to the ferrocenyl group, or a *trans*-isomer (isomer 2), where the phosphine ligand is *trans* to the β-diketonato oxygen closest to the ferrocenyl group. The β-diketonato portion of the ^{1}H-NMR spectrum of **(72)** is shown in **Figure 3.6**. The position of *cis*- and *trans*-isomer peaks, identified by using the same principles as described in **Section 3.2.5.1**, is highlighted. K_c-values were also determined and are listed in **Table 3.3**.
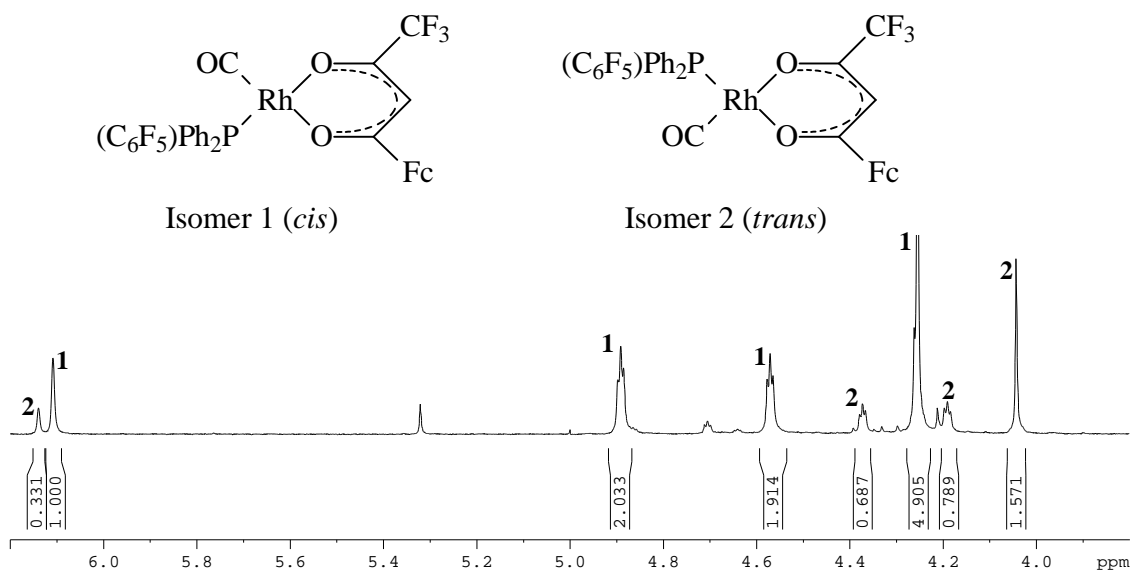
Figure 3.6. The β-diketonato portion of the ^{1}H NMR spectrum of complex **(72)**.

The ^{19}F NMR spectra of compounds **(72)**, **(73)** and **(74)**, shown in **Figure 3.7**, also showed two isomers in solution. In all cases a singlet peak is observed for the β-diketonato CF$_3$-group for each of the two isomers, between -73.5 and -75.5 ppm. Three sets of peaks are observed, to higher field, for F's in either the orto-, meta- and para-position of the phenyl rings. Of these, the more electron-poor meta-position is to highest field, and has been shown in literature to occur at around -160 ppm for pentafluorophenyl rings.[9] Similarly, fluorine substituents in the para-position have been shown to occur between -145 to -155 ppm and fluorine substituents in the ortho-position between -125 and -145 ppm.[10, 11] The fluorine peaks can thus be assigned as shown in **Figure 3.7**. Two isomers can also be observed in these peaks, for **(72)**. In the case of **(73)** and **(74)**,

rotation around the Rh-P bond is limited and not all phenyl rings equivalent, due to the bulkiness of the phosphine ligand, leading to the peaks of isomer 2 being split. Physical data for compounds **(72)**, **(73)** and **(74)** are summarized in **Table 3.3**. δ-Values are reported relative to $CFCl_3$ at 0 ppm, using C_6H_5F as standard at -113.15 ppm.
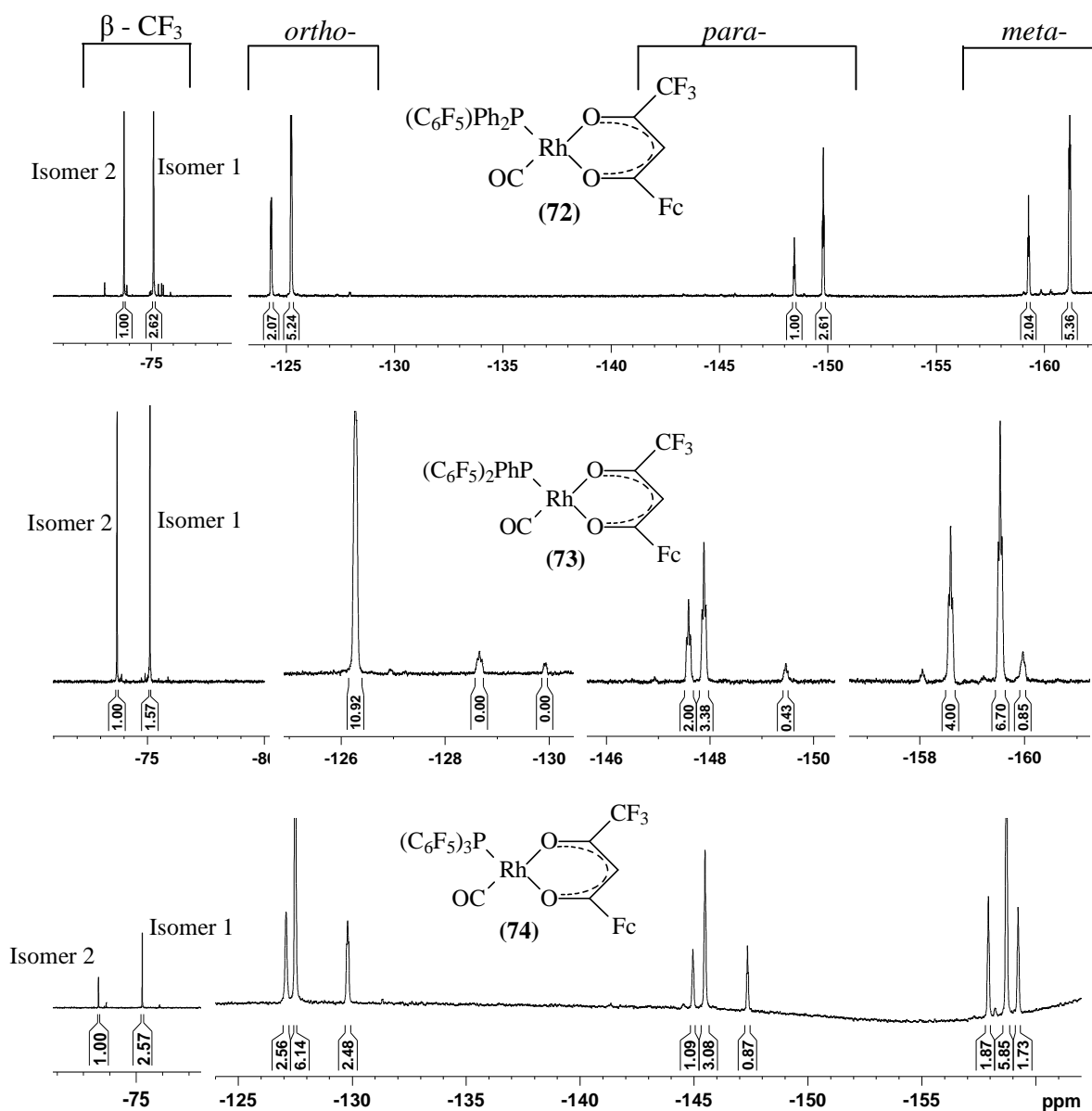
Figure 3.7. ^{19}F NMR spectra of rhodium(I) β-diketonato phosphine complexes **(72)**, **(73)** and **(74)** in deuterated chloroform as solvent.

Table 3.3. Selected spectral data of [Rh(FcCOCHCOCF$_3$)(CO)(PPh$_n$(C$_6$F$_5$)$_{3-n}$)].

Compound	Isomer	δ^{19}F / ppm (CF$_3$)-group	δ^1H / ppm (methine peak)	Isomer Ratio	Average K$_c$	υ(CO) / cm^{-1}
(72)	*cis* -1	-73.7	6.14	73 %	0.36	1986
n = 2	*trans* -2	-75.1	6.11	27 %		
(73)	*cis* -1	-73.8	6.14	61 %	0.66	1991
n = 1	*trans* -2	-75.1	6.11	39 %		
(74)	*cis* -1	-73.6	6.13	72 %	0.41	1998
n = 0	*trans* -2	-75.2	6.09	28 %		

3.2.6. Tetrathiafulvalene-containing Rhodium(I) Complexes

The Lorcy group[12] provided us with β-diketones **(39)** and **(88)**. These were reacted with [Rh$_2$Cl$_2$(cod)$_2$] **(84)** to give [Rh(α-TTF-Sacac)(cod)] **(75)** and [Rh(β-TTF-Sacac)(cod)] **(76)** containing tetrathiafulvalene groups substituted on β-diketones in either the α- or the β-position of the acetylacetonato group, as shown in **Scheme 3.11**.
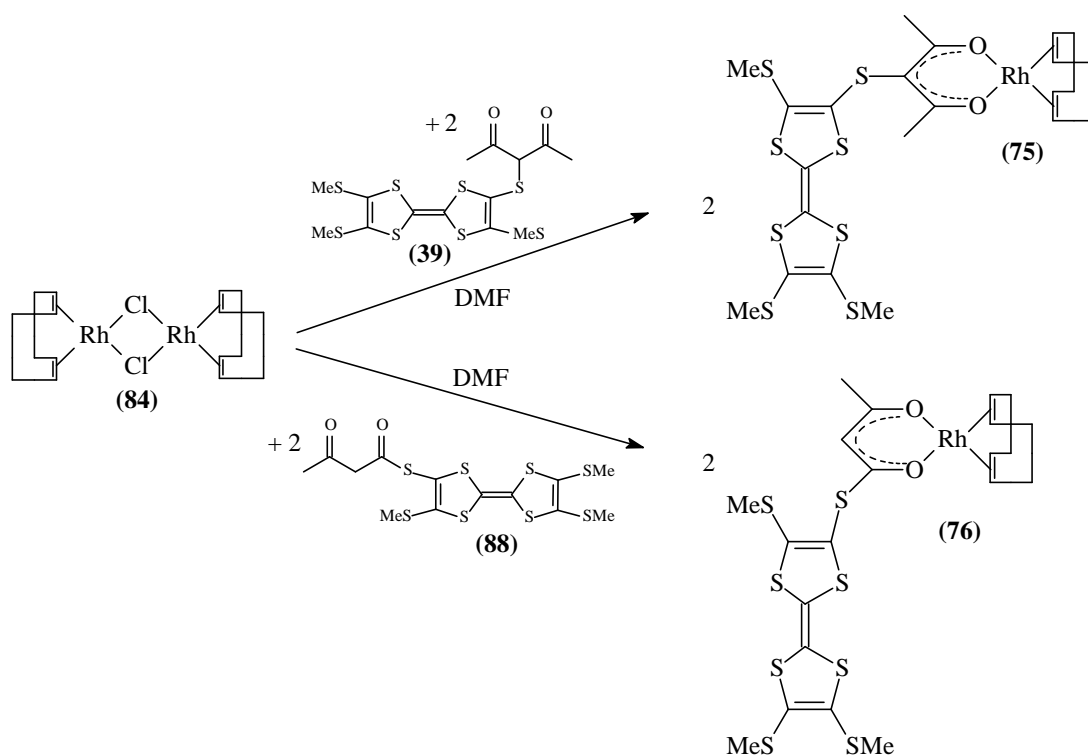
Scheme 3.11. Synthesis of rhodium(I) complexes with TTF-containing β-diketonato ligands.

Compounds **(75)** and **(76)** were synthesized (shown in **Scheme 3.11**) by the addition of 2 equivalents of the appropriate β-diketone to a stirred solution of the rhodium(I) cod-dimer [Rh$_2$Cl$_2$(cod)$_2$)] in DMF. The product could be purified by flash column

68

chromatography, and was obtained in very good yield (> 70 %). Unreacted β-diketone was recovered. ^{1}H NMR data, summarized in **Table 3.4**, showed little difference between compounds **(75)** and **(76)**, due to their similar electronic properties. Compound **(76)** showed the presence of a methane proton (5.46 ppm). Compound **(75)** showed the presence of 5 methyl groups, and compound **(76)** 4 methyl groups, with some overlapping observable.

Table 3.4. ^{1}H NMR data for of rhodium(I) complexes **(75)** and **(76)** with tetrathiafulvalene-containing β-diketonato ligands.

Compound	δ^1H / ppm (methine peak)	δ^1H / ppm (cod)	δ^1H / ppm (methyl-groups)
(75)	-	4.13, 2.52, 1.86	2.54, 2.48, 2.44, 2 x 2.39
(76)	5.46	4.12, 2.49, 1.85	2.19, 2.02, 2 x 1.95

3.3. Kinetics

3.3.1. Oxidative Addition

In this study the oxidative addition reaction of methyl iodide with rhodium(I) phosphine complexes [Rh(FcCOCHCOCF$_3$)(CO)(PPh$_2$Fc)] **(70)**, [Rh(FcCOCHCOCF$_3$)(CO)(PPh$_2$Rc)] **(71)**, [Rh(FcCOCHCOCF$_3$)(CO)(PPh$_2$(C$_6$F$_5$))] **(72)**, [Rh(FcCOCHCOCF$_3$)(CO)(PPh(C$_6$F$_5$)$_2$)] **(73)** and [Rh(FcCOCHCOCF$_3$)(CO)(P(C$_6$F$_5$)$_3$)] **(74)** was investigated, with chloroform as solvent throughout. Complexes **(70)** and **(71)** have electron-rich PPh$_2$Fc and PPh$_2$Rc ligands due to the electron-donating effect of the Fc and Rc groups on the phosphine ligands. Complexes **(72)**, **(73)** and **(74)** become more electron-poor as the phosphine ligand has progressively more C$_6$F$_5$ groups on them. Kinetic rate constants for metallocene-containing compounds **(70)** and **(71)** were determined by IR, UV, ^{1}H NMR and ^{31}P NMR spectroscopy, and IR, UV, ^{1}H NMR and ^{19}F NMR spectroscopy were used for fluorinated compounds **(72)** – **(74)**.

Previous studies of oxidative addition reactions of rhodium(I) complexes with methyl iodide proposed a variety of mechanisms, as discussed in **Chapter 2** (**Section 2.6.1.3**). The most recent of these, proposed by Conradie *et al.*,[13] and shown in **Scheme 3.12**, can

be considered a general mechanism, with previously proposed mechanisms being special cases of this more general mechanism.
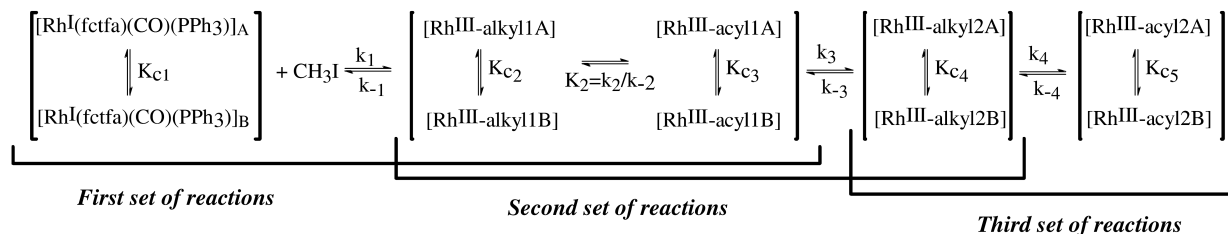
Scheme 3.12. Proposed general mechanism for the oxidative addition of CH_3I to rhodium(I) complexes.

In this study we investigated the oxidative addition reactions of compounds **(70)** – **(74)** which showed that these compounds also follow the above-mentioned general mechanism. The following discussion will show that the fluorinated compounds **(72)** – **(74)** and the metallocene-containing compounds **(70)** and **(71)**, have differently emphasized equilibrium positions in the overall general **Scheme 3.12**.

3.3.1.1. Extinction Coefficient Determinations

To study the kinetics of the above-mentioned oxidative addition reactions by UV/vis spectroscopy, it is important to show that the Beer Lambert law is valid over the concentration ranges used. The UV/vis spectra of compounds **(70)** – **(74)** are shown in **Figure 3.8**.
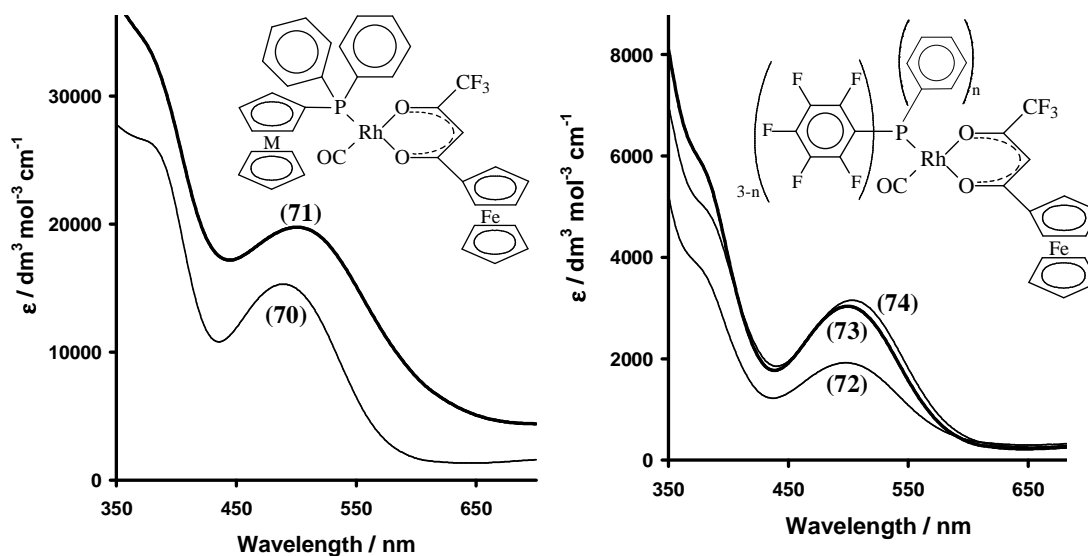
Figure 3.8. UV/vis spectra of rhodium(I) complexes containing metallocene phosphines (M = Fe **(70)**, or Ru **(71)** (bold line)) (left), and fluorinated phosphines (n = 2 **(72)**, 1 **(73)** (bold line), or 0 **(74)** (right).

The validity of the Beer Lambert law was confirmed by determining the linear relationship between the UV absorbance (A) and concentration (c) for compounds **(70)** – **(74)**, as shown in **Figure 3.9**. According to the Beer Lambert relationship (A = ε c l) the extinction coefficient (ε) can be determined from the gradient of the linear relationship between absorbance and concentration. The path length l = 1 cm. A linear relationship was found, and extinction coefficients for compounds **(70)** - **(74)** are summarized in **Table 3.5**, at the indicated wavelength maxima (λ_{max}). The error of all data is presented according to crystallographic conventions. For example ε = 1730(30) dm^{3}mol^{-1}cm^{-1} implies ε = (1730 ± 30) dm^{3}mol^{-1}cm^{-1}.
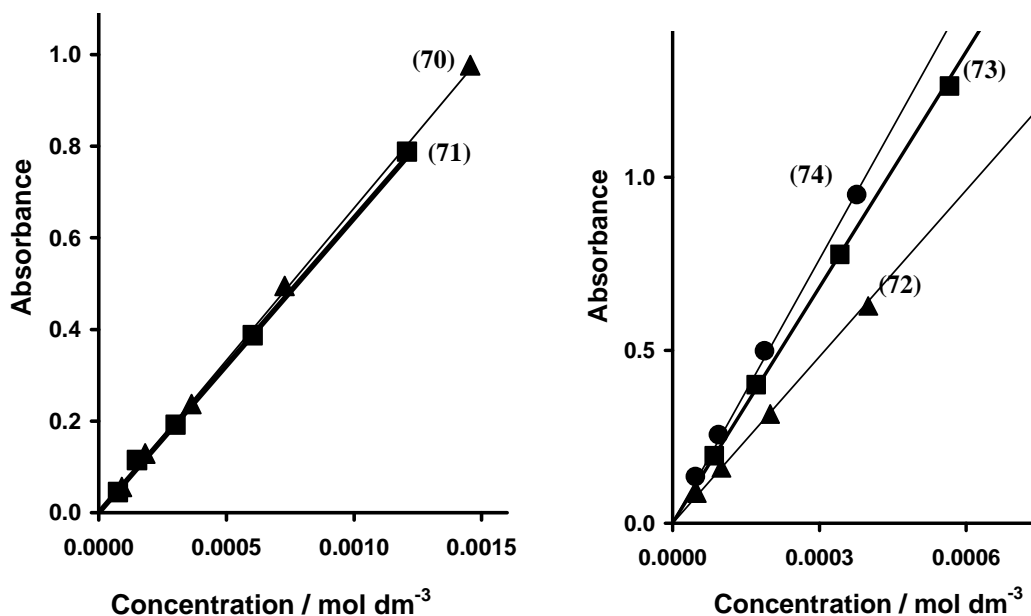
Figure 3.9. Absorbance *vs.* concentration graphs used to determine validity of the Beer Lambert relationship for rhodium(I) complexes containing metallocene phosphines (M = Fe **(70)** (▲), and Ru **(71)** (■, bold line)) (left), and fluorinated phosphines {n = 2 **(72)** (▲), 1 **(73)** (■, bold line), or 0 **(74)** (●) (right)}.

Table 3.5. Molar extinction coefficients for rhodium(I) phosphine complexes in chloroform as solvent at the indicated wavelenghts.

Compound	Wavelength (λ_{max}) / nm	Wavelength (λ_{exp}) / nm	ε / dm^3 mol^{-1} cm^{-1}
[Rh(FcCOCHCOCF$_3$)(CO)(PPh$_2$Fc)] **(70)**	501	490	1730(30)
[Rh(FcCOCHCOCF$_3$)(CO)(PPh$_2$Rc)] **(71)**	489	490	2000(20)
[Rh(FcCOCHCOCF$_3$)(CO)(PPh$_2$(C$_6$F$_5$))] **(72)**	498	500	1600(20)
[Rh(FcCOCHCOCF$_3$)(CO)(PPh(C$_6$F$_5$)$_2$)] **(73)**	500	500	2000(20)
[Rh(FcCOCHCOCF$_3$)(CO)(P(C$_6$F$_5$)$_3$)] **(74)**	503	500	2540(30)

3.3.1.2. Rhodium(I) Complexes with Metallocene Phosphines

A (a)   The reaction between [Rh(FcCOCHCOCF₃)(CO)(PPh₂Fc)] (70) and CH₃I monitored by IR.

The reaction trace of the carbonyl peaks of the reaction between **(70)** and CH_3I at 25 °C, shown in **Figure 3.10**, as monitored by infrared spectroscopy, shows 3 consecutive reaction steps. The first step consists of the disappearance of the Rh(I) starting compound (at 1987 cm^{-1}), together with the simultaneous formation of a Rh(III) alkyl species labeled "Alkyl 1" (at 2072 cm^{-1}), as well as a Rh(III) acyl species labeled "Acyl 1" (at 1724 cm^{-1}), all at the same rate. This indicates a fast equilibrium between the two formed Rh(III) alkyl 1 and Rh(III) acyl 1 species with an equilibrium constant $K_2 = k_2 / k_{-2}$, where k_2 = the rate of the forward reaction and k_{-2} = the rate of the reverse reaction. The first step, with a half-life of 104 s at a methyl iodide concentration of 1 M, can thus be summarized in **Scheme 3.13**.

$$\text{Rh(I) phosphine} \; + \; CH_3I \; \underset{k_{-1}}{\overset{k_1}{\rightleftharpoons}} \; \left[\text{Rh(III) alkyl 1} \; \underset{k_{-2}}{\overset{k_2}{\rightleftharpoons}} \; \text{Rh(III) acyl 1} \right]$$
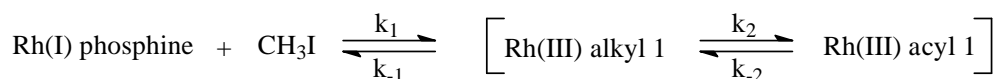
Scheme 3.13. The first reaction step for the oxidative addition of CH_3I to **(70)**.

The observed rate constant, for the first reaction step, k_{obs}, was found to be dependent on the CH_3I concentration. With $[CH_3I] \gg [$Rh(I) phosphine$]$, the pseudo first-order rate law, shown in **Equation 3.1**, was used to calculate the reaction parameters k_1 and k_{-1} graphically, with k_1 = slope = rate constant of the forward oxidative addition reaction, and k_{-1} = y-intercept = rate constant of the reverse reductive elimination reaction.

$$k_{obs} \; = \; k_1 \, [CH_3I] \; + \; k_{-1} \qquad\qquad \textbf{Equation 3.1}$$
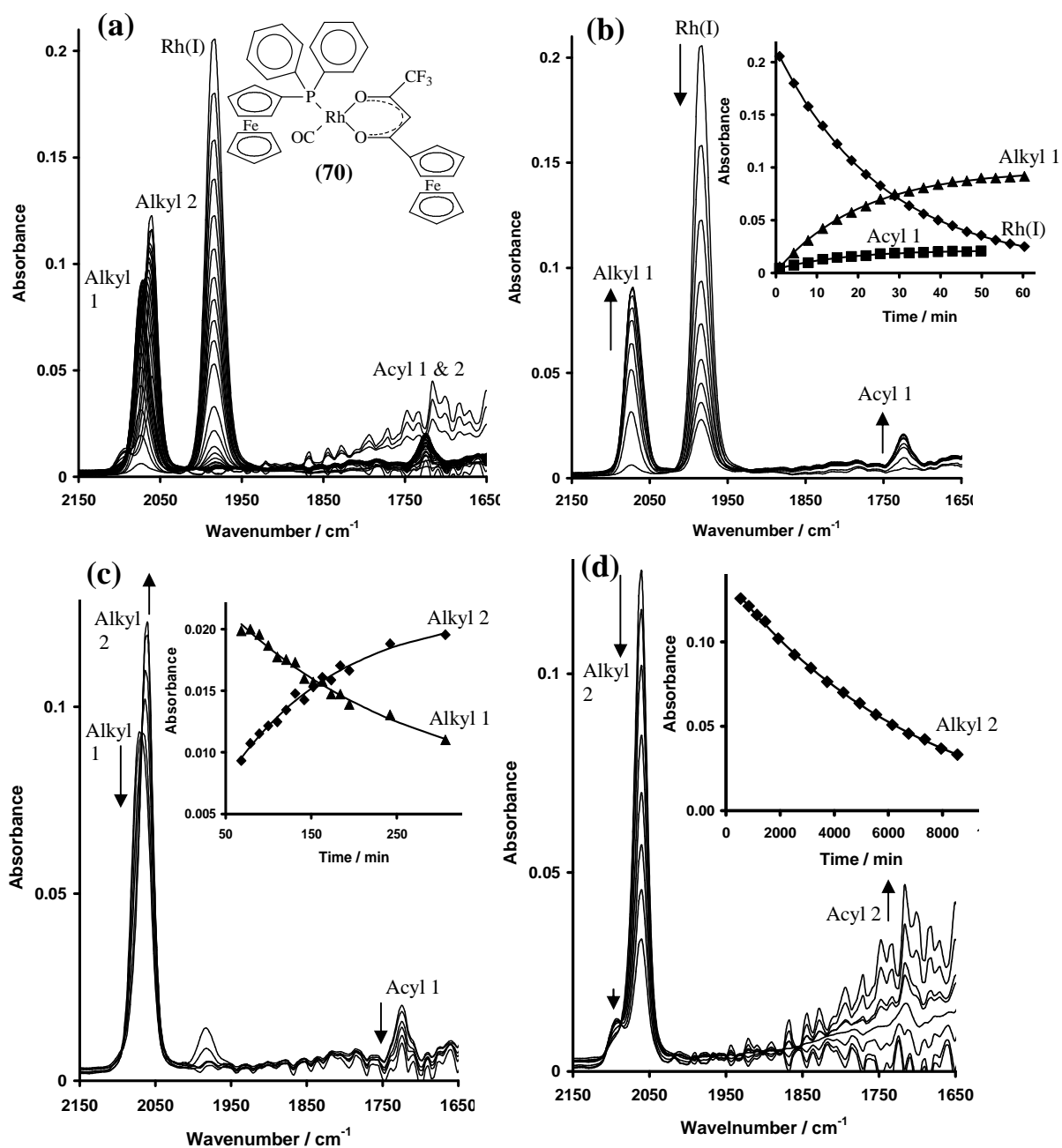
Figure 3.10. **(a)** IR-spectra at different times of the oxidative addition reaction between CH₃I and **(70)** for the complete reaction, between 0.8 and 8500 mins. Peaks labelled as per the proposed mechanism. **(b)** IR-spectra of the first reaction step recorded between 0.8 and 60 mins. The insert shows an absorbance *vs*. time graph following the formation and disappearance of all three peaks. **(c)** IR-spectra of the second reaction step recorded between 60 and 340 mins. The insert shows an absorbance *vs*. time graph following the formation and disappearance of the Alkyl 2- and Alkyl 1-species. **(d)** IR-spectra of the third reaction step recorded between 500 and 8500 mins. The insert shows an absorbance *vs*. time graph following the disappearance of the Alkyl 2-peak.

73

The second step, according to the IR-data, showed the simultaneous disappearance of the Rh(III) alkyl 1 and Rh(III) acyl 1 species, formed during the first step, together with the formation of a second Rh(III) alkyl species at 2060 cm^{-1} (Rh(III) alkyl 2). This step was found to be independent of the CH$_3$I concentration. The disappearance of the Rh(III) alkyl 1 and Rh(III) acyl 1 species taking place at the same rate, gives further evidence for the existence of a rapid equilibrium between the two species. This is a much slower step, with a half-life of 115 minutes, and can be summarized according to **Scheme 3.14**.

$$\left[\text{Rh(III) alkyl 1} \quad \underset{k_{-2}}{\overset{k_2}{\rightleftharpoons}} \quad \text{Rh(III) acyl 1} \right] \quad \xrightarrow{k_3} \quad \text{Rh(III) alkyl 2}$$
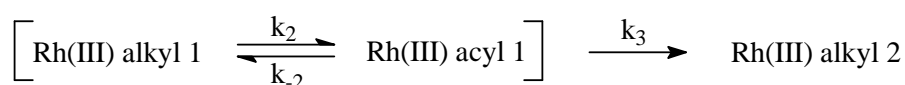
Scheme 3.14. The second reaction step for the oxidative addition of CH$_3$I to **(70)**.

The third and final observable reaction step (shown in **Scheme 3.15**) consists of the disappearance of the second Rh(III) alkyl species, and the formation of a second Rh(III) acyl species, also independent of the CH$_3$I concentration. This is a much slower step, with a half-life of approximately 75 hours. Measuring the rate of formation for the Rh(III) acyl 2 peak proved difficult due to the long reaction time and the relative low peak intensity, leading to baseline interference. The rate of reaction for the third reaction step was thus only determined from the rate of disappearance of the Rh(III) alkyl 2 species.

$$\text{Rh(III) alkyl 2} \quad \xrightarrow{k_4} \quad \text{Rh(III) acyl 2}$$
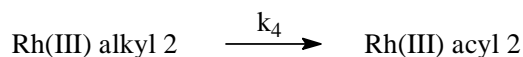
Scheme 3.15. The third reaction step for the oxidative addition of CH$_3$I to **(70)**.

The overall reaction sequence for the oxidative addition reaction of CH$_3$I to [Rh(FcCOCHCOCF$_3$)(CO)(PPh$_2$Fc)] **(70)**, as measured by IR, can be summarized as shown in **Scheme 3.16**.

$$[Rh^{I}(FcCOCHCOCF_3)(CO)(PPh_2Fc)] \quad + \quad CH_3I$$

$$k_{-1} \Big\updownarrow k_1$$

$$\left[[Rh^{III}(FcCOCHCOCF_3)(CO)(PPh_2Fc)(CH_3)(I)]_{alkyl1} \underset{k_{-2}}{\overset{k_2}{\rightleftharpoons}} \quad [Rh^{III}(FcCOCHCOCF_3)(PPh_2Fc)(COCH_3)(I)]_{acyl1} \right]$$

$$\Big\downarrow k_3$$

$$[Rh^{III}(FcCOCHCOCF_3)(CO)(PPh_2Fc)(CH_3)(I)]_{alkyl2}$$

$$\Big\downarrow k_4$$

$$[Rh^{III}(FcCOCHCOCF_3)(PPh_2Fc)(COCH_3)(I)]_{acyl2}$$
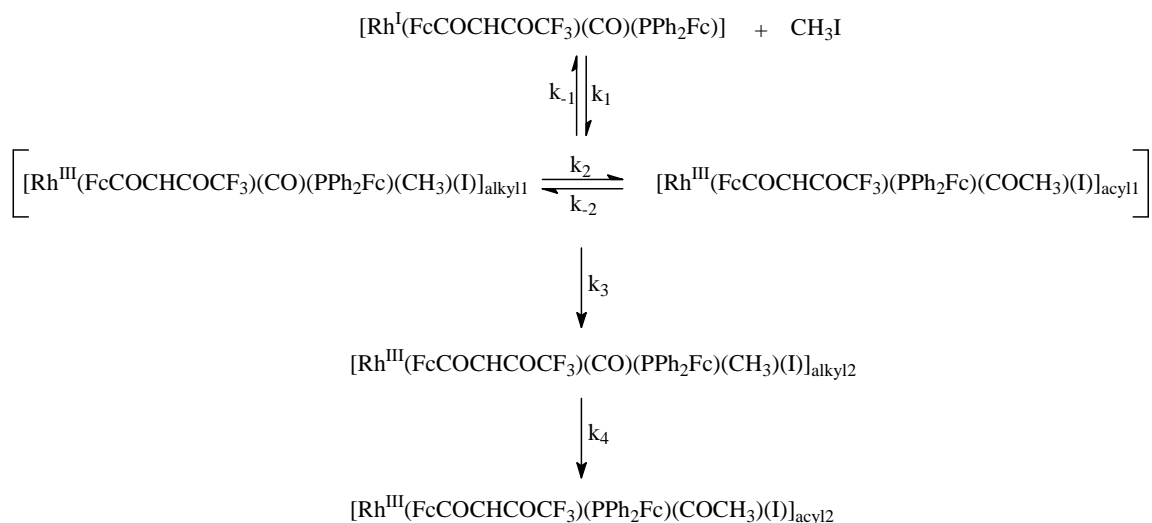
Scheme 3.16. The overall reaction scheme for the oxidative addition of CH$_3$I to **(70)**.

The rate constants for the reaction at 25 °C, obtained by varying CH$_3$I concentrations between 0.02 and 0.25 M, are summarized in **Table 3.6**. Rate constants obtained for the reverse reaction, k_{-1}, are dramatically smaller than k_1-values. This indicates that the reverse reaction has no significant influence on the overall reaction, and can be considered omissible. The relationship between the observed rate constant (k_{obs}) and methyl iodide concentration, for all reaction steps, are shown in **Figure 3.11**.
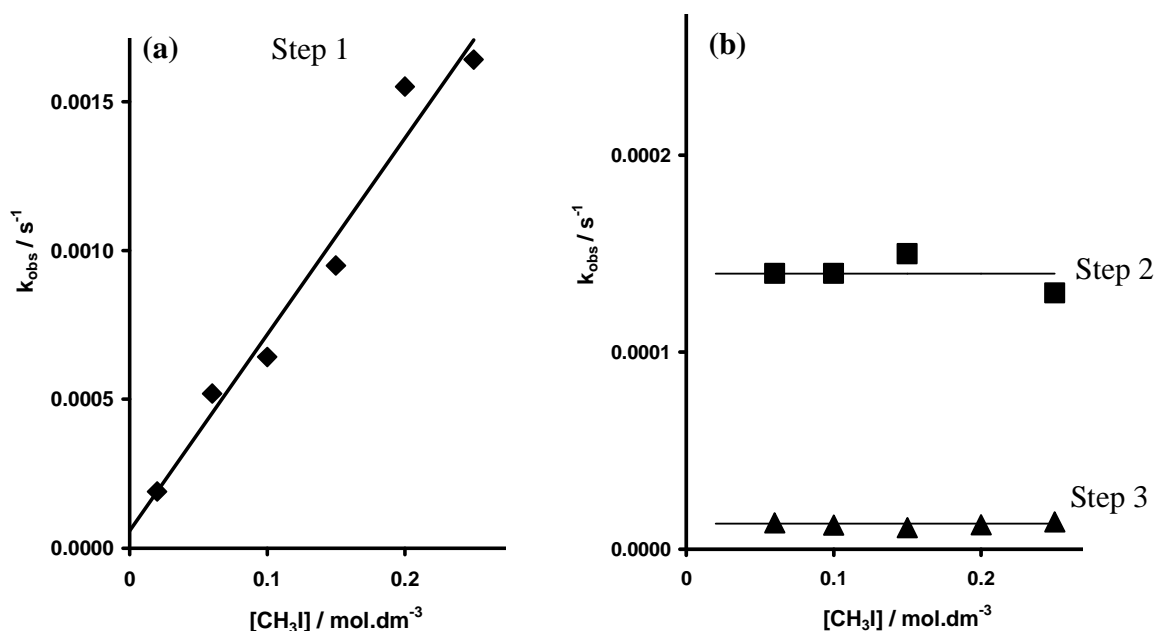
Figure 3.11. (a) Graph of k$_{obs}$ *vs.* methyl iodide concentration for the first reaction step, and (b) the second and third reaction steps, as measured by IR.

75

Table 3.6. Kinetic rate constants for the IR-monitored reaction between **(70)** and CH_3I at 25 °C.

First reaction step	k_1 / $dm^3mol^{-1}s^{-1}$	k_{-1} / s^{-1}
Rh(I) disappearance	0.0066(6)	0.00005(9)
Rh(III)-alkyl 1 formation	0.0071(7)	0.00002(1)
Rh(III)-acyl 1 formation	0.0081(6)	0.000021(2)
Second reaction step	k_3 / s^{-1}	
Rh(III)-acyl 1 disappearance	0.000096(5)	
Rh(III)-alkyl 2 formation	0.00013(1)	
Third reaction step	k_4 / s^{-1}	
Rh(III)-alkyl 2 disappearance	0.0000026(5)	

A (b)   The reaction between [Rh(FcCOCHCOCF₃)(CO)(PPh₂Fc)] (70) and CH₃I monitored by UV.

The reaction between [Rh(FcCOCHCOCF$_3$)(CO)(PPh$_2$Fc)] **(70)** and CH_3I also showed three consecutive reaction steps when monitored by UV, as shown in **Figure 3.13**. The rate constants obtained for the three reaction steps corresponded with the rate constants obtained for the three reaction steps identified by IR.

The first reaction step showed significant increases at 490, 435 and 370 nm, but was only followed at 490 nm to avoid interference with reaction steps 2 and 3, still to follow. Step 1 corresponded to the disappearance of the Rh(I) starting compound together with the simultaneous formation of the Rh(III) alkyl 1 and Rh(II) acyl 1 species in equilibrium. Mutually consistent rate constants obtained from increases at 435 and 370 nm corresponded to the simultaneous disappearance of the Rh(III) alkyl 1 and Rh(II) acyl 1 species together with the formation of the Rh(III) alkyl 2 species. The final step, showing a decrease at 435 and 370 nm, corresponded to the final step observed by IR as the disappearance of the Rh(III) alkyl 2 species together with the formation of the Rh(III) acyl 2 species. Rate constants obtained by UV at 25 °C is summarized in **Table 3.7**. It is important to note that, although UV/vis spectrometry could detect three consecutive reaction steps, it would not be possible to assign what each reaction step actually represents, without the information obtained by IR spectrometry described in the previous section. Rate constants obtained for the reverse reaction, k_{-1}, are dramatically smaller

than k_1-values (*ca.* 400 times), and approaching zero, as shown in **Figure 3.12**. This indicates that the reverse reaction has no significant influence on the overall reaction, and can be considered omissible.

Table 3.7. Kinetic rate constants for the UV-monitored reaction between (**70**) and CH_3I at 25 °C.

First reaction step	k_1 / $dm^3mol^{-1}s^{-1}$	k_{-1} / s^{-1}
490 nm	0.0081(4)	0.00002(3)
Second reaction step	k_3 / s^{-1}	
435 nm	0.00013(4)	
370 nm	0.00013(1)	
Third reaction step	k_4 / s^{-1}	
435 nm	0.0000034(6)	
370 nm	0.0000026(4)	
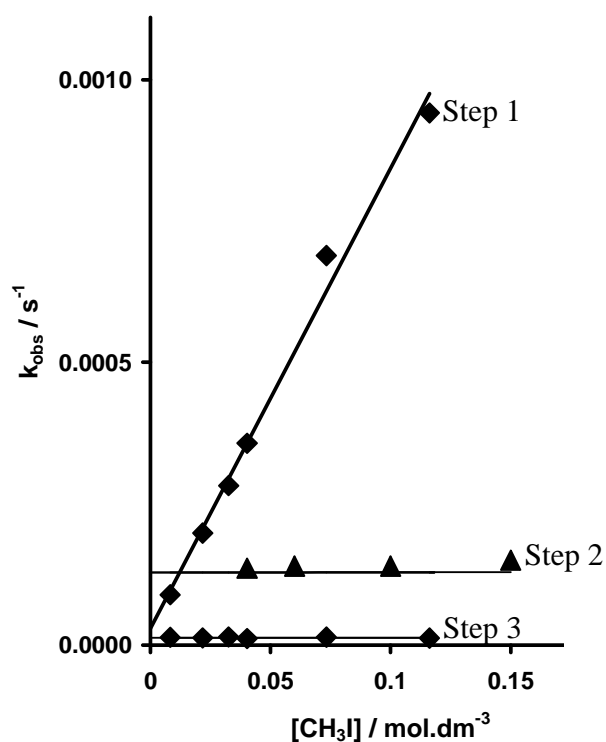
Figure 3.12. Graph of k_{obs} *vs.* methyl iodide concentration for reaction steps 1, 2 and 3, as measured by UV/vis.
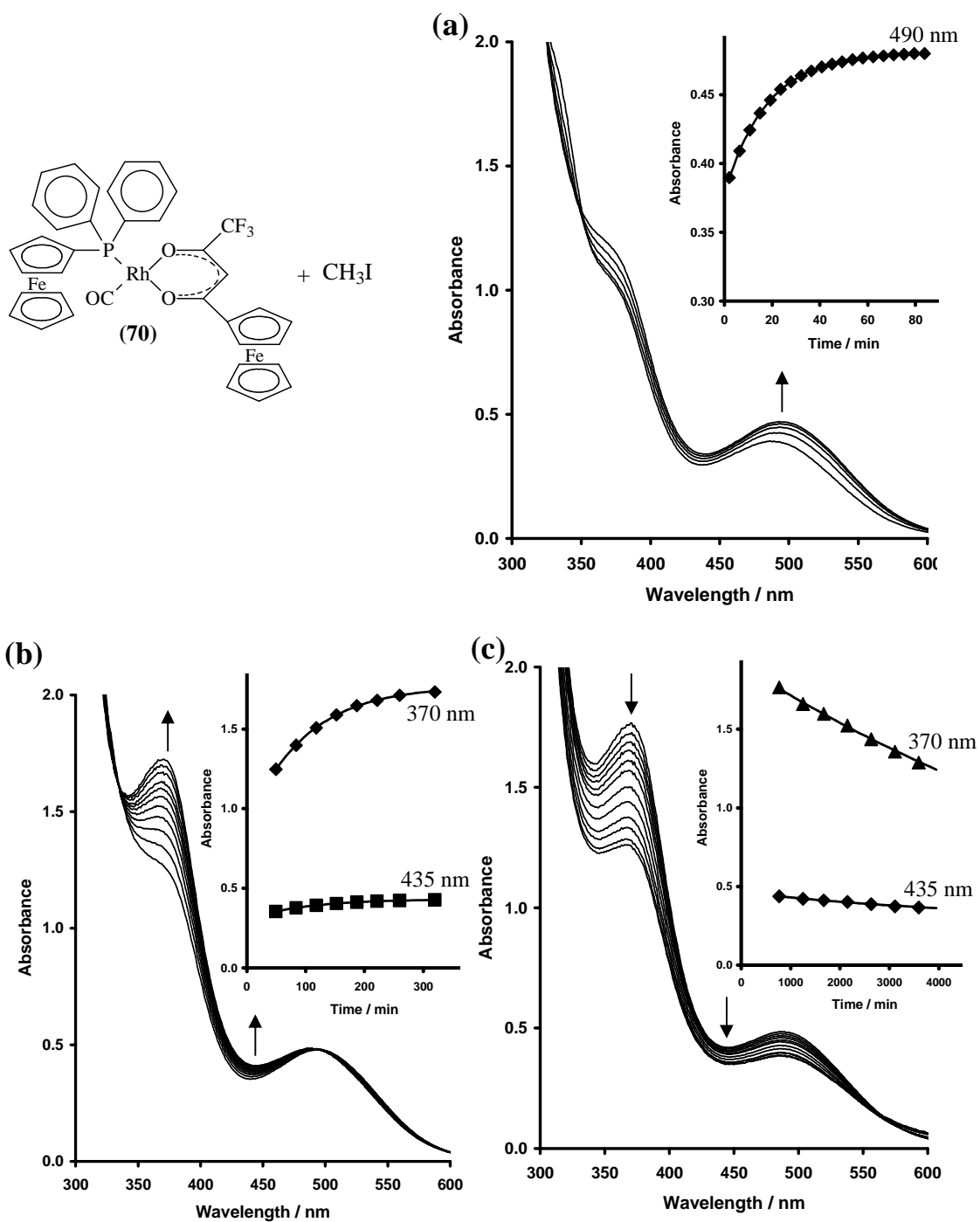
Figure 3.13. **(a)** Time-based UV/vis-spectra for the oxidative addition reaction between CH_3I and **(70)** showing the first reaction step recorded between 0.8 and 60 mins. **(b)** UV-spectra of the second reaction step recorded between 60 and 340 mins. **(c)** UV-spectra of the third reaction step recorded between 500 and 6000 mins.

The temperature dependence of the oxidative addition reaction was monitored by UV at 490 nm. This was used to determine activation parameters, ΔH^* and ΔS^*, according to the Eyring relationship, given in **Equation 3.2**.[14]

$$\ln k \ = \ \ln[(RT)/(Nh)] \ + \ (\Delta S^*/R) \ - \ (\Delta H^*/RT) \qquad \textbf{Equation 3.2}$$

A linear plot of $(\ln k / T)$ *vs* $(1 / T)$ gives a slope of $(-\Delta H^* / R)$ and a y-intercept of $\{\ln(R / Nh) + (\Delta S^* / R)\} = \{23.760 + (\Delta S^* / R)\}$, where R is the gas constant, N is Avogadro's constant and h is Planck's constant. This linear relationship for the oxidative addition reaction of CH_3I to **(70)** is shown in **Figure 3.14**. Rate constants and activation parameters are summarized in **Table 3.8**.

T / K	k_1 / $dm^3mol^{-1}s^{-1}$	ΔH^* / $kJ\,mol^{-1}$	ΔS^* / $J\,mol^{-1}K^{-1}$
278.15	0.00017(1)	**Step 1**	
288.15	0.00034(1)	19.1(2)	-197(1)
298.15	0.00093(1)		
308.15	0.00098(4)	**Step 2**	
314.15	0.00150(6)	-9.2(3)	19.5(2)
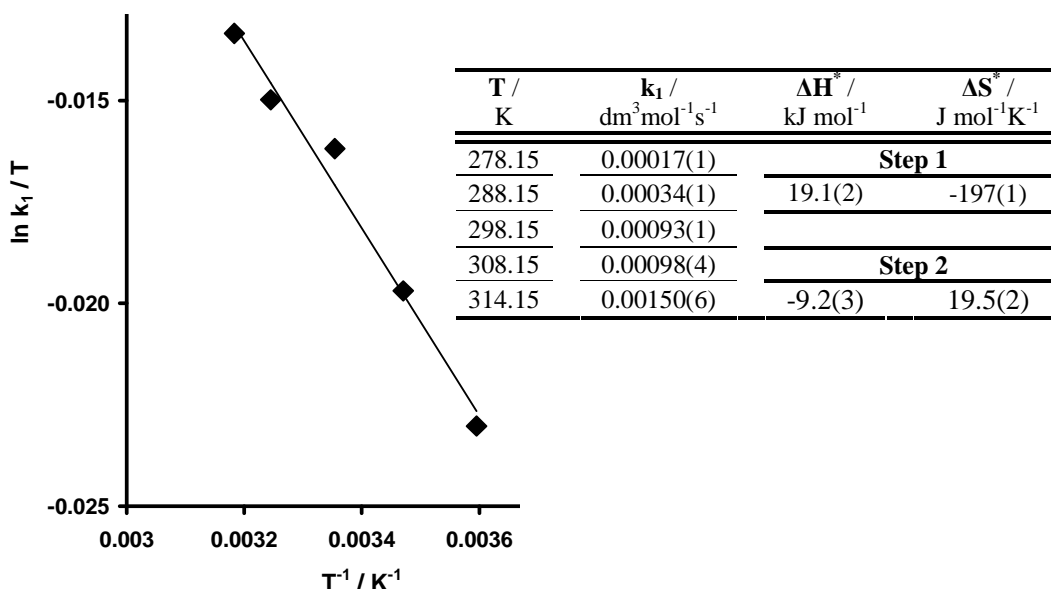
Figure 3.14 & Table 3.8. Eyring plot and activation parameters for the first step of the oxidative addition of CH_3I to **(70)**.

A (c)   The reaction between [Rh(FcCOCHCOCF₃)(CO)(PPh₂Fc)] (70) and CH₃I monitored by ¹H and ³¹P NMR.

^1H and ^{31}P NMR was also used to study the oxidative addition reaction between **(70)** and CH_3I. During ^1H NMR, the methine (CH from β-diketone) and methyl (CH_3 from CH_3I added) signals were used to follow the kinetics of the reaction. Extensive signal overlapping in the ferrocenyl region was observed, making it too difficult to interpret them.

The ^{1}H NMR spectra, shown in **Figure 3.15**, followed the same reaction steps observed during IR-studies, showing three reaction steps. Furthermore, each species was observed to have two isomers, indicated as A and B. In the first step the two isomers of the rhodium(I) starting complex {Rh(I) A and Rh(I) B} react with CH_3I to form two observable isomers of the Rh(III) alkyl 1 species (A and B) in equilibrium with the two isomers observed for the Rh(III) acyl 1 species (A and B). The two isomers of the Rh(III)-alkyl 1 and Rh(III) acyl 1 species disappear at the same rate as the formation of two isomers of the Rh(III) alkyl 2 species, during the second step. In the final step the two isomers of the Rh(III) alkyl 2 species disappears, but the formation of the Rh(III) acyl 2 species is not observed due to interference from background noise. ^{1}H NMR-data was used to determine the equilibrium constant (K_c), as indicated in **Scheme 3.17** (page 81), for the equilibrium between two isomers of the same species, and is listed in **Table 3.9**.
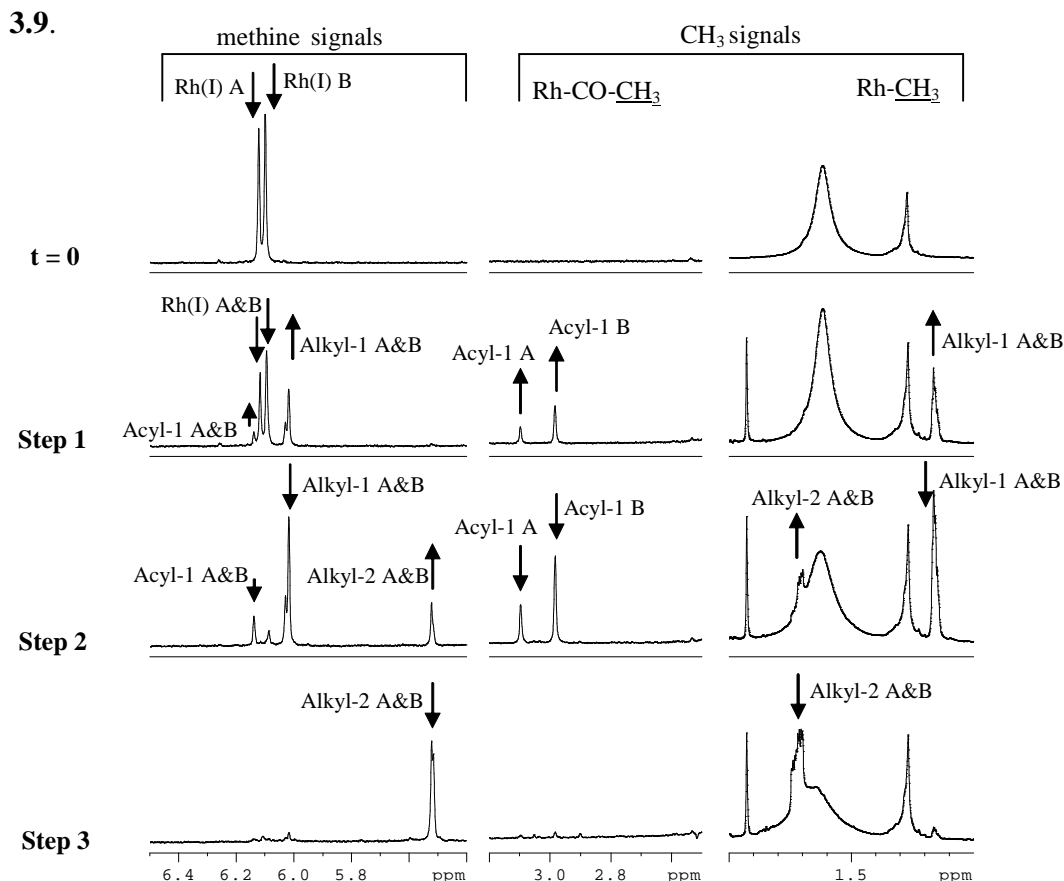
Figure 3.15. ^{1}H NMR-spectra of the reaction between **(70)** and CH_3I at times 0 (top), 4.5, 51.5, 860 (bottom) minutes.

The ^{31}P NMR spectra, shown in **Figure 3.16**, followed the same reaction steps as described above. During ^{31}P NMR, only the phosphorus atom on the phosphine group is observable, giving doublets through coupling with the rhodium center. Two isomers were also observed throughout for all species. However, the intensity of the Rh(III) acyl peaks, as well as the Rh(III) alkyl 1B peaks, proved too low to be used accurately for following the reaction kinetics. Due to the long times required to produce a ^{31}P NMR spectrum (approximately 15 minutes) only four data-points were obtained for the first reaction step, making accurate determinations of rate constants difficult.
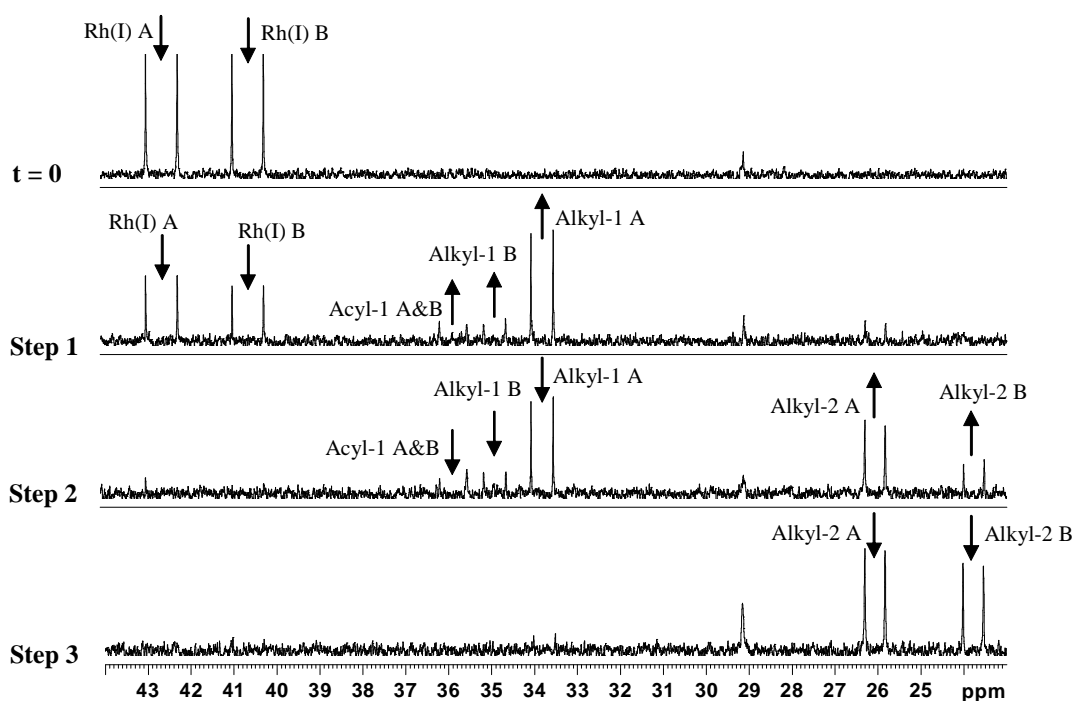
Figure 3.16. ^{31}P NMR spectra of the reaction between (**70**) and CH_3I at times 0 (top), 23.6, 75.4, 2 013 (bottom) minutes.

The observed rate constants for the formation and disappearance of A and B isomers of any species were, within experimental error, found to be the same. Furthermore, the ratios of A and B isomers were not the same for different species, implying that A isomers did not exist separately from the B isomers. This means that a fast equilibrium exists between the A and B isomers of each species and that the equilibrium position is different for each set of products. The overall mechanism can thus be summarized as in **Scheme 3.17**, with rate constants summarized in **Table 3.10**.

Table 3.9. K_c-values determined from non-overlapping peaks for Rh(III)-intermediate species.

Rh(III)-species	Equilibrium constant	Average K_c
Alkyl 1	K_{c1}	0.41
Acyl 1	K_{c2}	0.49
Alkyl 2	K_{c3}	0.69
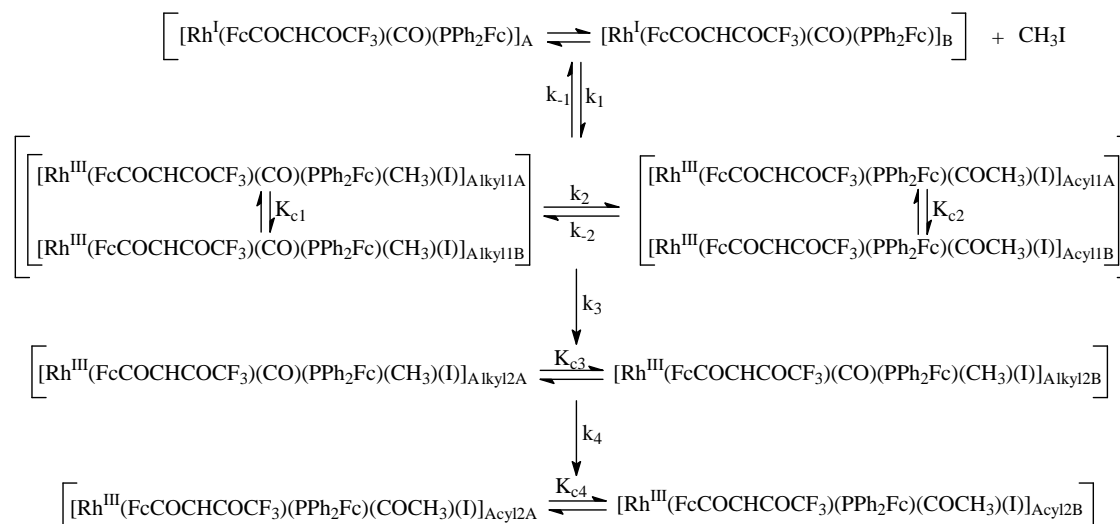
Scheme 3.17. Complete reaction mechanism for the oxidative addition of CH_3I to **(70)**.

Table 3.10. Kinetic rate constants for the NMR-monitored reaction between **(70)** and CH_3I at 25 °C.

Isomer	^{31}P NMR		^{1}H NMR			
	δ ^{31}P / ppm	k_1 / $dm^3mol^{-1}s^{-1}$	δ ^{1}H CH / ppm	k_1 / $dm^3mol^{-1}s^{-1}$	δ^1H CH_3 / ppm	k_1 / $dm^3mol^{-1}s^{-1}$
Step 1						
Rh(I) A	42.6	0.001(2)	6.12	0.006(1)	-	-
Rh(I) B	40.6	0.002(2)	6.10		-	-
Alkyl 1 A	34.9	-	6.02	0.006(1)	1.20	0.006(1)
Alkyl 1 B	33.7	0.0002(1)	6.00		1.20	0.006(1)
Acyl 1 A	35.8	-	6.15	0.007(1)	3.10	0.009(1)
Acyl 1 B			6.13		3.00	0.008(1)
Step 2						
	δ ^{31}P / ppm	k_3 / s^{-1}	δ ^{1}H CH / ppm	k_3 / s^{-1}	δ^1H CH_3 / ppm	k_3 / s^{-1}
Alkyl 1 A	34.9	-	6.02	0.00013(1)	1.20	0.00012(1)
Alkyl 1 B	33.7	0.0002(4)	6.00		1.20	
Acyl 1 A	35.8	-	6.15	0.00013(3)	3.10	0.00015(2)
Acyl 1 B			6.13		3.00	0.00014(2)
Alkyl 2 A	26.0	0.0002(3)	5.50	0.00012(1)	-	-
Alkyl 2 B	23.8	0.0001(3)	5.49		-	-
Step 3						
	δ ^{31}P / ppm	k_4 / s^{-1}	δ ^{1}H CH / ppm	k_4 / s^{-1}	δ^1H CH_3 / ppm	k_4 / s^{-1}
Alkyl 2 A	26.0	-	5.50	0.000005(1)	-	-
Alkyl 2 B	23.8	-	5.49		-	-

B (a) ***The reaction between [Rh(FcCOCHCOCF₃)(CO)(PPh₂Rc)] (71) and CH₃I***
monitored by IR.

In contrast to the [Rh(FcCOCHCOCF$_3$)(CO)(PPh$_2$Fc)] **(70)** reaction, the reaction between **(71)** and CH$_3$I at 25 °C, as monitored by infrared spectroscopy, shown in **Figure 3.17**, shows only two reaction steps. The first step consists of the disappearance of the Rh(I) starting compound (at 1987 cm^{-1}), together with the simultaneous formation of the first Rh(III) alkyl species (Alkyl 1, at 2075 cm^{-1}), and Rh(III) acyl species (Acyl 1, at 1720 cm^{-1}), all taking place at the same rate, indicating a fast equilibrium with each other. The first step, as summarized in **Scheme 3.18**, possesses a half-life of 39 s at a methyl iodide concentration of 1 M. The rate of reaction was found to be dependent on the methyl iodide concentration.

$$\text{Rh(I)-phosphine} \;+\; \text{CH}_3\text{I} \;\underset{k_{-1}}{\overset{k_1}{\rightleftharpoons}}\; \left[\text{Rh(III)-alkyl 1} \;\underset{k_{-2}}{\overset{k_2}{\rightleftharpoons}}\; \text{Rh(III)-acyl 1} \right]$$
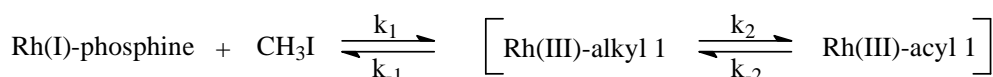
Scheme 3.18. The first reaction step for the oxidative addition of CH$_3$I to **(71)**.
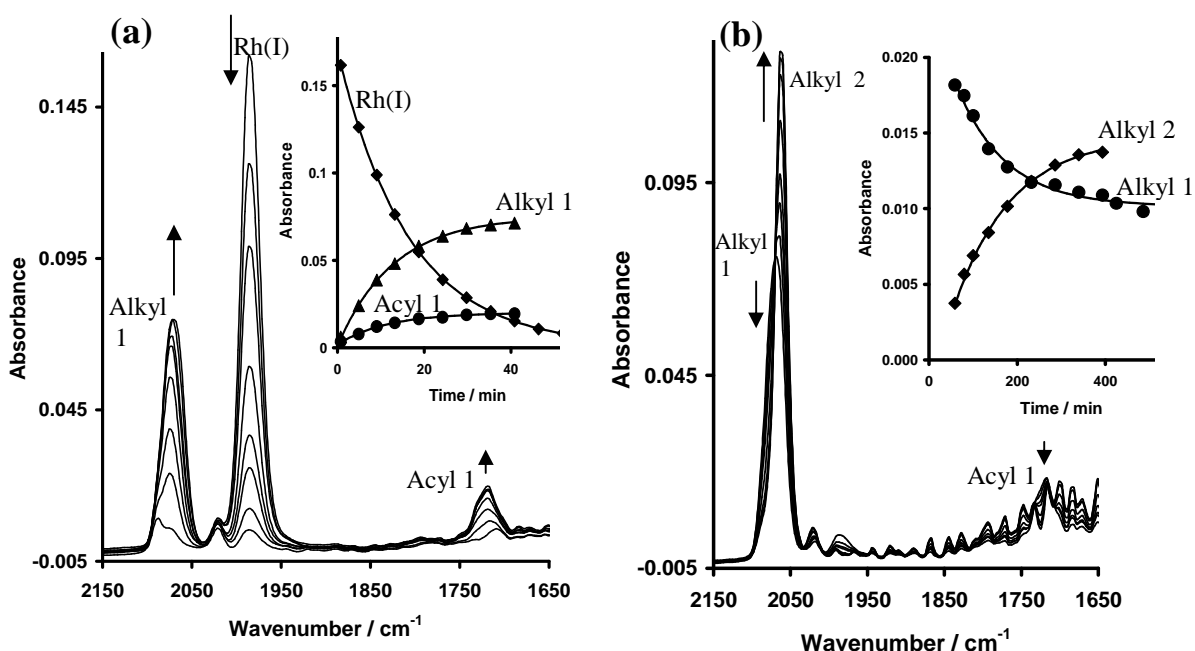
Figure 3.17. **(a)** IR-spectra at different times of the oxidative addition reaction between CH$_3$I and **(71)** for first reaction step, recorded between 0.6 and 50 mins. **(b)** Time-based IR-spectra of the second reaction step recorded between 60 and 450 mins.

According to the IR-data, the second step showed the simultaneous disappearance of the Rh(III) alkyl 1 and Rh(III) acyl 1 species, together with the formation of the second Rh(III) alkyl species at 2063 cm^{-1} (Rh(III) alkyl 2), independently of the CH$_3$I concentration. This step took place at a much slower rate, with a half-life of 80 minutes, and is represented by **Scheme 3.19**. No third step was observed and the Rh(III) alkyl 2 species appeared stable in solution for up to 7 days, with no second Rh(III) acyl species forming. In terms of the complete general mechanism shown in **Scheme 3.12** (page 69) this means k$_4$ = 0.

$$\left[\text{Rh(III)-alkyl 1} \underset{k_{-2}}{\overset{k_2}{\rightleftharpoons}} \text{Rh(III)-acyl 1} \right] \xrightarrow{k_3} \text{Rh(III)-alkyl 2}$$
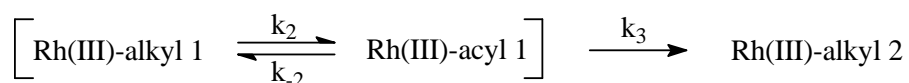
Scheme 3.19. The second reaction step for the oxidative addition of CH$_3$I to **(71)**.

The overall reaction sequence for the oxidative addition reaction of CH$_3$I to [Rh(FcCOCHCOCF$_3$)(CO)(PPh$_2$Rc)] **(71),** from the IR-data only, can be summarized according to **Scheme 3.20**. The rate constants for the reaction monitored by IR spectroscopy, at 25 °C, are summarized in **Table 3.11**.

[Rh^I(FcCOCHCOCF$_3$)(CO)(PPh$_2$Rc)]   +   CH$_3$I

k$_{-1}$ $\Updownarrow$ k$_1$

$$\left[\text{[Rh}^{III}\text{(FcCOCHCOCF}_3\text{)(CO)(PPh}_2\text{Rc)(CH}_3\text{)(I)]}_{\text{Alkyl1}} \underset{k_{-2}}{\overset{k_2}{\rightleftharpoons}} \text{[Rh}^{III}\text{(FcCOCHCOCF}_3\text{)(PPh}_2\text{Rc)(COCH}_3\text{)(I)]}_{\text{Acyl1}} \right]$$

k$_3$ $\downarrow$

[Rh^{III}(FcCOCHCOCF$_3$)(CO)(PPh$_2$Rc)(CH$_3$)(I)]$_{\text{Alkyl2}}$
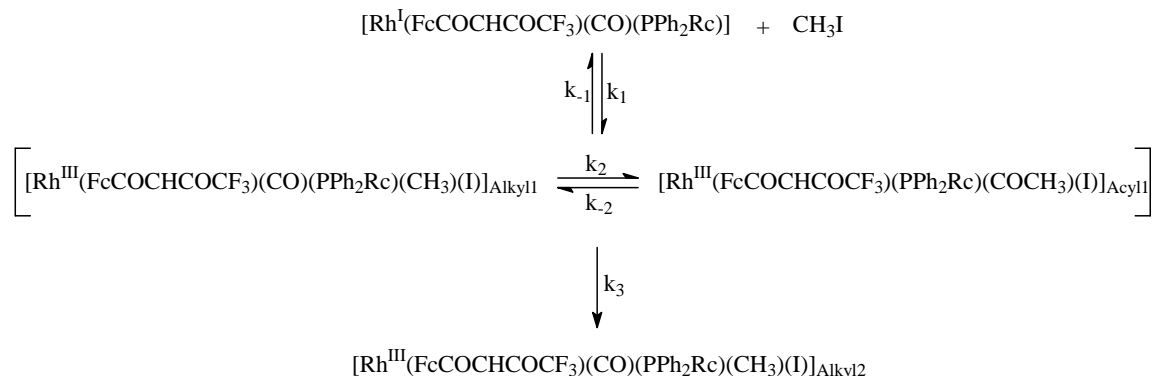
Scheme 3.20. The overall reaction scheme for the oxidative addition of CH$_3$I to **(71)**.

Table 3.11. Kinetic rate constants for the IR-monitored reaction between **(71)** and CH$_3$I at 25 °C.

First reaction step	k$_1$ / dm^{3}mol^{-1}s^{-1}
Rh(I) disappearance	0.0098(1)
Rh(III)-alkyl 1 formation	0.0129(1)
Rh(III)-acyl 1 formation	0.0140(5)
Second reaction step	**k$_3$ / s^{-1}**
Rh(III)-acyl 1 disappearance	0.00013(6)
Rh(III)-alkyl 2 formation	0.00015(1)

B (b) ***The reaction between [Rh(FcCOCHCOCF₃)(CO)(PPh₂Rc)] (71) and CH₃I***
monitored by UV.

Two reaction steps could also be observed when following the reaction between [Rh(FcCOCHCOCF₃)(CO)(PPh₂Rc)] **(71)** and CH₃I by UV, as shown in **Figure 3.18**. Rate constants obtained for these steps corresponded well with the rate constants obtained for the reaction steps identified by IR.
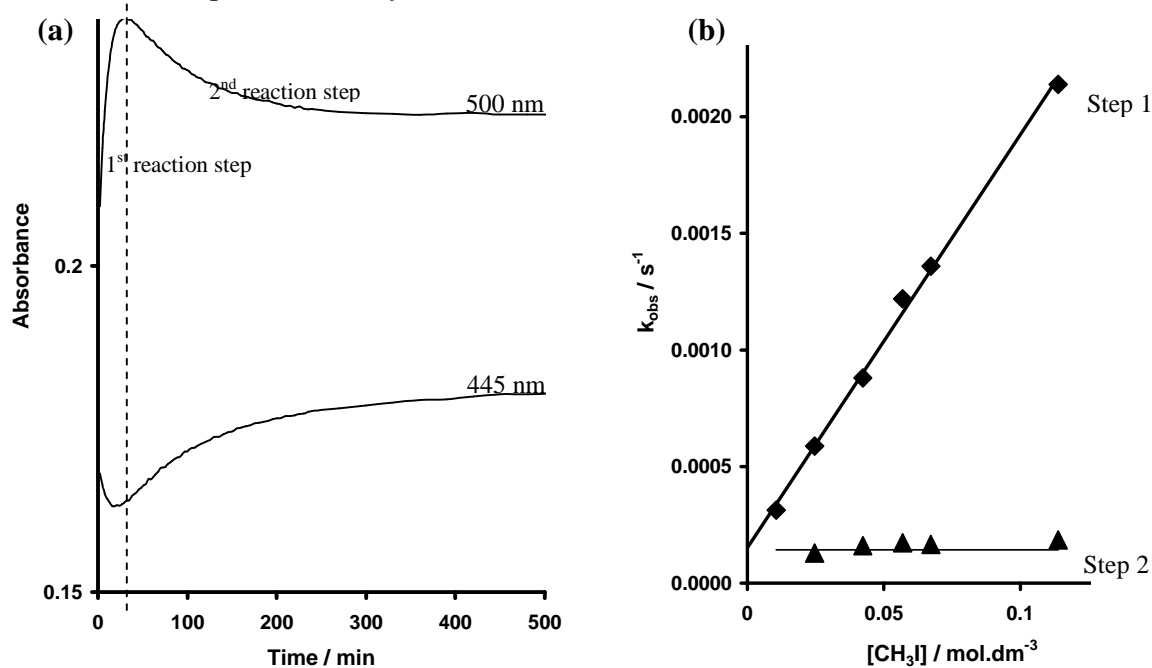
Figure 3.18. **(a)** UV time trace of the oxidative addition reaction between CH₃I and **(71)** showing the first (0.8 - 50 mins) and second (60 – 500 mins) reaction steps at 445 and 500 nm. **(b)** Graph of k_{obs} *vs.* methyl iodide concentration for the first and second reaction steps.

The first reaction step was followed at 490 nm to avoid interference with the second reaction step. This step corresponded to the disappearance of the Rh(I) starting compound together with the formation of the simultaneous formation of the Rh(III) alkyl 1 and Rh(III) acyl 1 species in equilibrium. Similarly, rate constants obtained from increases at 445 and 370 nm corresponded to the simultaneous disappearance of the Rh(III) alkyl 1 and Rh(III) acyl 1 species together with the formation of the Rh(III) alkyl 2 species. The rate of reaction for the first reaction step was found to be dependent on the methyl iodide concentration, while the second step was independent thereof, as illustrated in **Figure 3.18**. Rate constants obtained by UV are summarized in **Table 3.12**.

A temperature study was carried out at 490 nm in order to determine the activation parameters, ΔH^* and ΔS^*, according to the Eyring relationship. This linear relationship for the oxidative addition reaction of CH₃I to **(71)** is shown in **Figure 3.19**. Temperature dependent rate constants as well as activation parameters are summarized in **Table 3.12**.

Table 3.12. Kinetic rate constants and activation parameters for the UV-monitored reaction between **(71)** and CH₃I.

First reaction step	k_1 / dm³mol⁻¹s⁻¹	k_{-1} / s⁻¹
490 nm	0.0177(5)	0.00015(3)

Second reaction step	k_3 / s⁻¹
445 nm	0.000124(4)
370 nm	0.000162(2)

Step 1			
T / K	k_1 / dm³mol⁻¹s⁻¹	ΔH^* / kJ mol⁻¹	ΔS^* / J mol⁻¹K⁻¹
278.15	0.00113(2)	31.5(9)	-196(5)
288.15	0.0064(3)	**Step 2**	
298.15	0.0188(1)	ΔH^* / kJ mol⁻¹	ΔS^* / J mol⁻¹K⁻¹
308.15	0.0313(4)		
314.15	0.1008(7)	-7.1(4)	19.8(6)
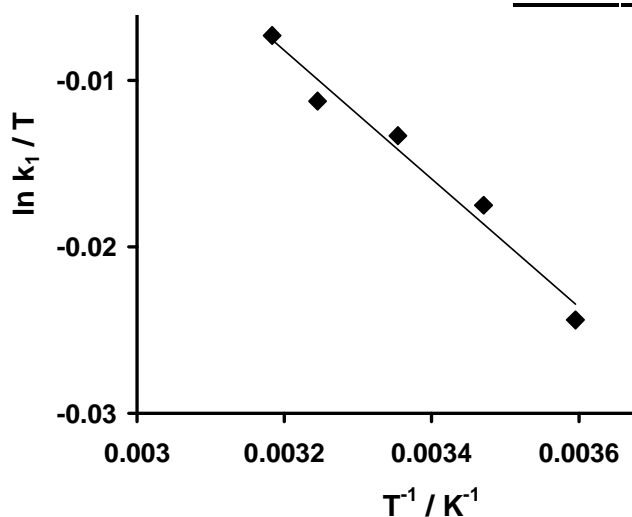
Figure 3.19. Eyring plot for the oxidative addition of CH₃I to **(71)**.

B (c) The reaction between [Rh(FcCOCHCOCF₃)(CO)(PPh₂Rc)] (71) and CH₃I monitored by ¹H and ³¹P NMR.

¹H and ³¹P NMR were also used to follow the oxidative addition reaction between **(71)** and CH₃I. During ¹H NMR, the methine (CH from β-diketone) and methyl (CH₃ from CH₃I added) signals were used to follow the kinetics of the reaction. No ferrocenyl peaks were used to follow the reaction, due to extensive peak overlapping.

The ^{1}H NMR, as well as ^{31}P NMR spectra, allowed detection of the same two reaction steps that were observed during IR and UV studies. During ^{31}P NMR, only the phosphorus atom on the phosphine group is observable, giving doublets through coupling with the rhodium center. As with compound (**70**), the PPh$_2$Fc-complex, each PPh$_2$Rc species was observed to have two isomers, indicated as A and B. In the first reaction step the two isomers of the rhodium(I) starting complex {Rh(I) A and Rh(I) B} react with CH$_3$I to form two observable isomers of the Rh(III) alkyl 1 species (A and B) in equilibrium with the two isomers observed for the Rh(III) acyl 1 species (A and B). The two isomers of the Rh(III) alkyl 1 and Rh(III) acyl 1 species disappear at the same rate as the formation of two isomers of the Rh(III) alkyl 2 species during the second step. Once again, the Rh(III) alkyl 2 species was shown to be stable in solution for up to a week. ^{1}H NMR-data was used to determine the equilibrium constant (K$_c$), as indicated in **Scheme 3.21**, for the equilibrium between two isomers of the same species, and is listed in **Table 3.13**. The equilibrium amended reaction mechanism is summarized in **Scheme 3.21**.
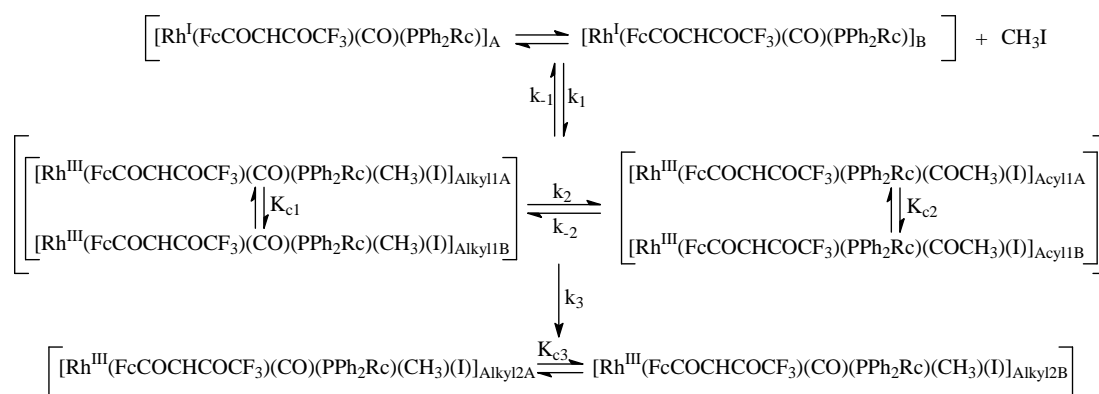
Scheme 3.21. Reaction mechanism for the oxidative addition of CH$_3$I to (**71**).

Table 3.13. K$_c$-values determined from non-overlapping peaks for Rh(III)-intermediate species.

Rh(III)-species	Equilibrium constant	Average K$_c$
Alkyl 1	K$_{c1}$	0.37
Acyl 1	K$_{c2}$	0.47
Alkyl 2	K$_{c3}$	0.85

The observed rate constants for the formation and disappearance of A and B isomers of any species were, within experimental error, again found to be the same, again indicating a fast equilibrium between the A and B isomers of each species. Observed rate data is

summarized in **Table 3.14**. During ^{31}P NMR studies, the Rh(III) acyl peaks, as well as one of the Rh(III) alkyl 1 peaks, proved too small to be used accurately for following the reaction kinetics. Once again, only four data points were obtained for the first reaction step, due to long acquisition times required to obtain a usable ^{31}P NMR spectrum. This made accurate determinations of rate constants difficult.

Table 3.14. Kinetic rate constants for the NMR-monitored reaction between **(71)** and CH_3I at 25 °C.

Isomer	^{31}P NMR		^{1}H NMR			
	δ [31]P / ppm	k_1 / dm^{3}mol^{-1}s^{-1}	δ[1]H CH / ppm	k_1 / dm^{3}mol^{-1}s^{-1}	δ[1]H CH$_3$ / ppm	k_1 / dm^{3}mol^{-1}s^{-1}
Step 1						
Rh(I) A	42.60	0.007(5)	6.08	0.011(1)	-	-
Rh(I) B	41.39	0.008(6)	6.06	0.010(1)	-	-
Alkyl 1 A	31.00	0.014(5)	6.04	0.026(2)	1.35	0.018(2)
Alkyl 1 B	30.60	-	6.02	0.016(2)		
Acyl 1 A	35.58	-	6.12	0.015(2)	3.10	0.011(3)
Acyl 1 B	33.81	-	6.10	0.015(1)	3.00	0.013(2)
Step 2						
	δ [31]P / ppm	k_3 / s^{-1}	δ[1]H CH / ppm	k_3 / s^{-1}	δ[1]H CH$_3$ / ppm	k_3 / s^{-1}
Alkyl 1 A	31.00	0.0003(1)	6.04	0.00032(3)	1.35	0.00038(4)
Alkyl 1 B	30.60	-	6.02	0.00031(1)		
Acyl 1 A	35.58	-	6.12	0.00029(4)	3.10	0.00034(3)
Acyl 1 B	33.81	-	6.10	0.00070(1)	3.00	0.00034(2)
Alkyl 2 A	24.47	0.0004(1)	5.52	0.00025(1)	-	-
Alkyl 2 B	22.08	0.0002(1)	5.50	0.00032(1)	-	-

C Summary of kinetic data obtained by various spectroscopic techniques.

Kinetic data, obtained from various spectroscopic techniques for the oxidative addition reactions of rhodium complexes containing metallocene-phosphines, [Rh(FcCOCHCOCF$_3$)(CO)(PPh$_2$Fc)] **(70)** and [Rh(FcCOCHCOCF$_3$)(CO)(PPh$_2$Rc)] **(71)**, are summarized in **Table 3.15**, as well as literature values[13] for the similar non-metallocene phosphine complex [Rh(FcCOCHCOCF$_3$)(CO)(PPh$_3$)] **(29)**. Very good agreement was found between results obtained by different spectroscopic techniques. Only ^{31}P NMR data for the first reaction step (k_1) showed a small deviation from k_1-values determined by other techniques. This is due to too few data points obtained, as discussed earlier. Despite this, the kinetic data obtained by ^{31}P NMR are still considered

mutually consistent with those obtained by other techniques. A deviation of less than one order of magnitude was observed.

Table 3.15. Average kinetic rate constants, obtained by various spectroscopic techniques, for compounds **(29)**, **(70)** and **(71)**.

Compound	$[Rh(FcCOCHCOCF_3)(CO)(PPh_3)]$ **(29)** [13]			
	k_1 / $dm^3 mol^{-1} s^{-1}$	k_{-1} / s^{-1}	k_3 / s^{-1}	k_4 / s^{-1}
UV	0.0060(1)	0.0005(1)	0.00017(2)	0.000004(1)
ΔH^* / $kJ\ mol^{-1}$			29(3)	
ΔS^* / $J\ mol^{-1} K^{-1}$			-188(9)	
Compound	$[Rh(FcCOCHCOCF_3)(CO)(PPh_2Fc)]$ **(70)**			
Method	k_1 / $dm^3 mol^{-1} s^{-1}$	k_{-1} / s^{-1}	k_3 / s^{-1}	k_4 / s^{-1}
IR	0.0073(6)	0.00003(2)	0.00011(4)	0.000002(1)
UV	0.0081(4)	0.00002(3)	0.00013(3)	0.000003(1)
^{1}H NMR	0.0070(4)	-	0.00013(2)	0.000005(1)
^{31}P NMR	0.0020(6)	-	0.00018(5)	-
ΔH^* / $kJ\ mol^{-1}$		19.1(2)		
ΔS^* / $J\ mol^{-1} K^{-1}$		-197(1)		
Compound	$[Rh(FcCOCHCOCF_3)(CO)(PPh_2Rc)]$ **(71)**			
Method	k_1 / $dm^3 mol^{-1} s^{-1}$	k_{-1} / s^{-1}	k_3 / s^{-1}	k_4 / s^{-1}
IR	0.012(3)	-	0.00014(4)	-
UV	0.018(1)	0.00015(3)	0.00014(1)	-
^{1}H NMR	0.015(2)	-	0.00036(2)	-
^{31}P NMR	0.008(6)	-	0.00029(3)	-
ΔH^* / $kJ\ mol^{-1}$		31.5 (9)		
ΔS^* / $J\ mol^{-1} K^{-1}$		-196(5)		

The rate constants for reductive elimination (reverse reaction, k_{-1}) could be measured for compounds **(70)** and **(71)**, although it was found to be very small. In the case of compound **(29)** the rate of the reverse reaction was approximately 8 % of the forward reaction. In contrast, the rate of the reverse reaction was found to be 0.4 % and 1.1 % of the forward reaction respectively for **(70)** and **(71)**. This approaches zero, and can be considered to have no significant influence on the overall reaction.

In general an increase in electron density on the metal center leads to an increase in the rate of oxidative addition (see **Chapter 2**, **Section 2.6.1**). Considering the group

electronegativities of the different phosphine substituents, it was expected that both compounds **(70)** {χ_R(Fc) =1.87} and **(71)** {χ_R(Rc) =1.99} would show larger k_1-values than compound **(29)** {χ_R(Ph) =2.21}. The k_1 rate constant for **(70)** was 1.2 times larger than that of **(29)**, and 2 times larger for **(71)**. However, there is no simple linear relationship between k_1 and χ_R.

Large negative ΔS^*-values for the k_1-step were obtained for both **(70)** and **(71)**, indicating an associative mechanism for both, with a possible three-centered transition state. The Rh(III) alkyl 1 and Rh(III) acyl 1 species were found to exist in a fast equilibrium, which is only possible when the CH$_3$ and CO groups are in a *cis* configuration to each other. This configuration is most probable from the collapse of a three-centered transition state. Due to the fast equilibrium observed we do not favour the argument that the Rh(III) alkyl 1 species could have undergone isomerization to produce the suitable *cis* configuration for CO migration, but with the present evidence we cannot exclude this possibility.

It is clear from the NMR results that at least two isomers of each species exist in equilibrium with each other, and react at the same rate. All the different spectroscopic techniques also show that a fast equilibrium exists between the Rh(III) alkyl 1 and Rh(III) acyl 1 species. All evidence thus indicates that the reaction between CH$_3$I and [Rh(FcCOCHCOCF$_3$)(CO)(PPh$_2$Fc)] **(70)** follow the same reaction mechanism as that proposed by Conradie *et al.* for the similar [Rh(FcCOCHCOCF$_3$)(CO)(PPh$_3$)] **(29)**, see **Scheme 3.22**.[13] For [Rh(FcCOCHCOCF$_3$)(CO)(PPh$_2$Rc)] **(71)** the main difference to this mechanism is the absence of a third reaction step, with the reaction ending at the Rh(III) alkyl 2 species, *i.e.* $k_4 = 0$.

$$\left[\text{[Rh}^{\text{I}}(\text{FcCOCHCOCF}_3)(\text{CO})(\text{PPh}_2\text{R})]_A \underset{}{\overset{K_c}{\rightleftharpoons}} \text{[Rh}^{\text{I}}(\text{FcCOCHCOCF}_3)(\text{CO})(\text{PPh}_2\text{R})]_B \right] + \text{CH}_3\text{I}$$

$$k_{-1} \Updownarrow k_1$$

$$\left[\begin{array}{c} \text{[Rh}^{\text{III}}(\text{FcCOCHCOCF}_3)(\text{CO})(\text{PPh}_2\text{R})(\text{CH}_3)(\text{I})]_{\text{Alkyl1A}} \\ K_{c1} \Updownarrow \\ \text{[Rh}^{\text{III}}(\text{FcCOCHCOCF}_3)(\text{CO})(\text{PPh}_2\text{R})(\text{CH}_3)(\text{I})]_{\text{Alkyl1B}} \end{array} \right] \underset{k_{-2}}{\overset{k_2}{\rightleftharpoons}} \left[\begin{array}{c} \text{[Rh}^{\text{III}}(\text{FcCOCHCOCF}_3)(\text{PPh}_2\text{R})(\text{COCH}_3)(\text{I})]_{\text{Acyl1A}} \\ K_{c2} \Updownarrow \\ \text{[Rh}^{\text{III}}(\text{FcCOCHCOCF}_3)(\text{PPh}_2\text{R})(\text{COCH}_3)(\text{I})]_{\text{Acyl1B}} \end{array} \right]$$

$$k_{-3} = 0 \Updownarrow k_3$$

$$\left[\text{[Rh}^{\text{III}}(\text{FcCOCHCOCF}_3)(\text{CO})(\text{PPh}_2\text{R})(\text{CH}_3)(\text{I})]_{\text{Alkyl2A}} \overset{K_{c3}}{\rightleftharpoons} \text{[Rh}^{\text{III}}(\text{FcCOCHCOCF}_3)(\text{CO})(\text{PPh}_2\text{R})(\text{CH}_3)(\text{I})]_{\text{Alkyl2B}} \right]$$

$$k_{-4} = 0 \Updownarrow k_4$$

$$\left[\text{[Rh}^{\text{III}}(\text{FcCOCHCOCF}_3)(\text{PPh}_2\text{R})(\text{COCH}_3)(\text{I})]_{\text{Acyl2A}} \overset{K_{c4}}{\rightleftharpoons} \text{[Rh}^{\text{III}}(\text{FcCOCHCOCF}_3)(\text{PPh}_2\text{R})(\text{COCH}_3)(\text{I})]_{\text{Acyl2B}} \right]$$

R = Fc, Rc (For Rc, $k_4 = 0$)

Scheme 3.22. Overall reaction mechanism for the oxidative addition of CH$_3$I to rhodium complexes **(70)** (R = Fc), and **(71)** (R = Rc).

3.3.1.3. Rhodium(I) Complexes with Fluorinated Phosphines

A (a) The reaction between [Rh(FcCOCHCOCF$_3$)(CO){PPh$_2$(C$_6$F$_5$)}]] (72) and CH$_3$I monitored by IR.

In contrast to the metallocene phosphine complexes **(70)** and **(71)**, which were very electron-rich, the rhodium(I) complexes of the fluorinated phosphines discussed in this section were chosen to be all electron-poor. This was done to highlight any mechanistic differences that may be obtained as a function of phosphine-rhodium electron density. The IR spectra for the reaction between **(72)** and CH$_3$I at 25 °C shows only one reaction step, as illustrated in **Figure 3.20**. The reaction takes place at a much slower rate than that observed with above mentioned metallocene-containing compounds, and has a half-life of approximately 30 minutes at a methyl iodide concentration of 1 M (the $t_{1/2}$ for **(71)** was 39 seconds at the same methyl iodide concentration). The IR data shows the disappearance of the Rh(I) starting compound (1994 cm^{-1}), together with the simultaneous formation of a Rh(III) acyl species (1728 cm^{-1}). A very small amount of a Rh(III) alkyl species is observed at 2071 cm^{-1}, but too little to be quantified. For both Rh(III) alkyl and Rh(III) acyl species two peaks were observed by IR, indicated as A and B. This was the first instance where it was possible to identify the two isomers by any

other spectroscopic technique than ^{1}H NMR. Since an alkyl species is necessary in order to undergo carbonyl insertion to form an acyl species, it is clear that as soon as the alkyl species forms, it immediately transforms fast to the acyl species. This observation is consistent with a fast equilibrium between the Rh(I) starting compound and the Rh(III) alkyl species, with the formation of the Rh(III) acyl species being the rate determining step. This is summarized in **Scheme 3.23**. The equilibrium for k_1/k_{-1} is proposed because even after 20 hours, a significant amount of Rh(I) species is still visible in solution, with no further concentration change being observed. In addition, the k_2/k_{-2} equilibrium lies very far to the right because the Rh(III) alkyl species is only detected in very low concentrations, and the Rh(III) acyl species dominates.
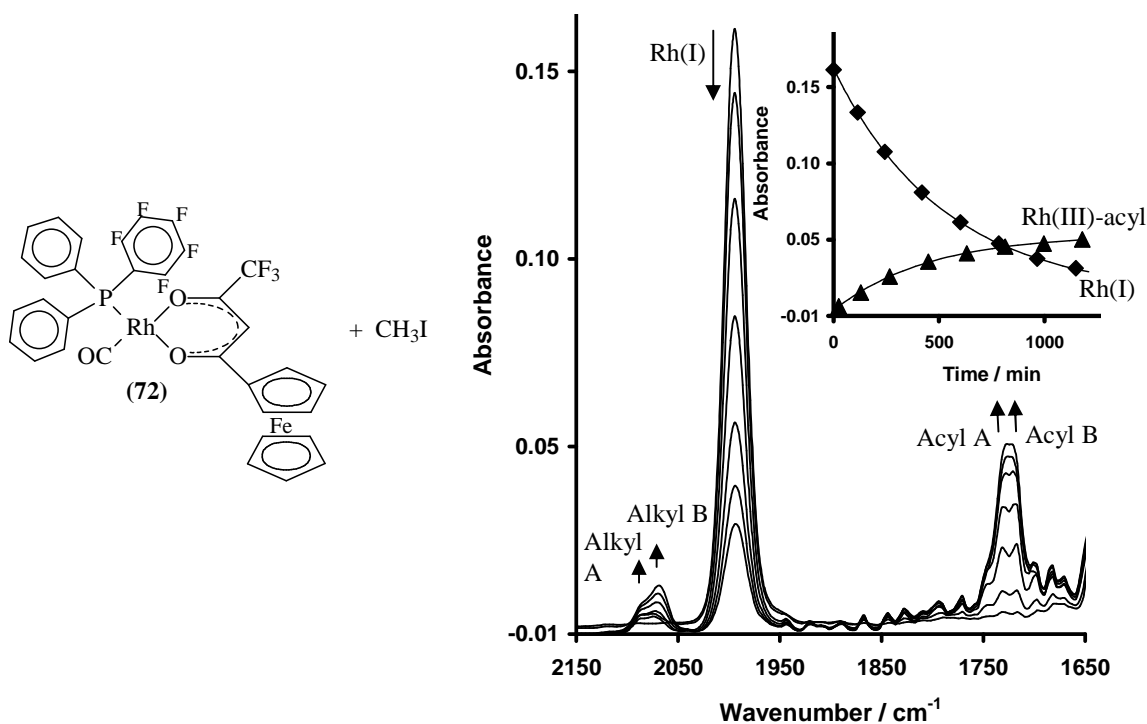
Figure 3.20. IR-specta of the oxidative addition reaction between CH$_3$I and **(72)**, recorded between 1 and 1200 mins.
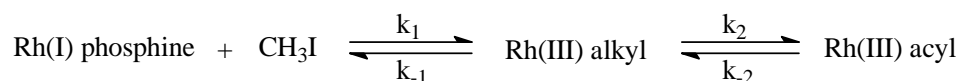
Scheme 3.23. The oxidative addition reaction between CH$_3$I and **(72)**.

The observed rate of reaction was found to show a first-order dependency on the CH$_3$I concentration. Thus, pseudo first-order conditions {[CH$_3$I] >> [Rh(I) phosphine]} were

92

utilized to calculate the reaction parameters k_2 and k_{-2}. The rate constants for the reaction monitored by IR spectroscopy at 25 °C are summarized in **Table 3.16**.

Table 3.16. Rate constants for the IR-monitored reaction between **(72)** and CH$_3$I at 25 °C.

	k_2
Rh(I) disappearance	0.00032(1)
Rh(III)-acyl formation	0.00037(1)

A (b) The reaction between [Rh(FcCOCHCOCF₃)(CO)(PPh₂(C₆F₅))] (72) and CH₃I monitored by UV.

The reaction between [Rh(FcCOCHCOCF$_3$)(CO)(PPh$_2$(C$_6$F$_5$))] **(72)** and CH$_3$I, when followed by UV, showed also just one reaction step. Rate constants obtained for this reaction corresponded well with the rate constants obtained by IR. The reaction showed an increase in UV absorbance at 530 nm, as shown in **Figure 3.21**. Rate constants were obtained under pseudo first-order conditions with methyl iodide concentrations between 0.01 and 0.15 M, and are summarized in **Table 3.17**.
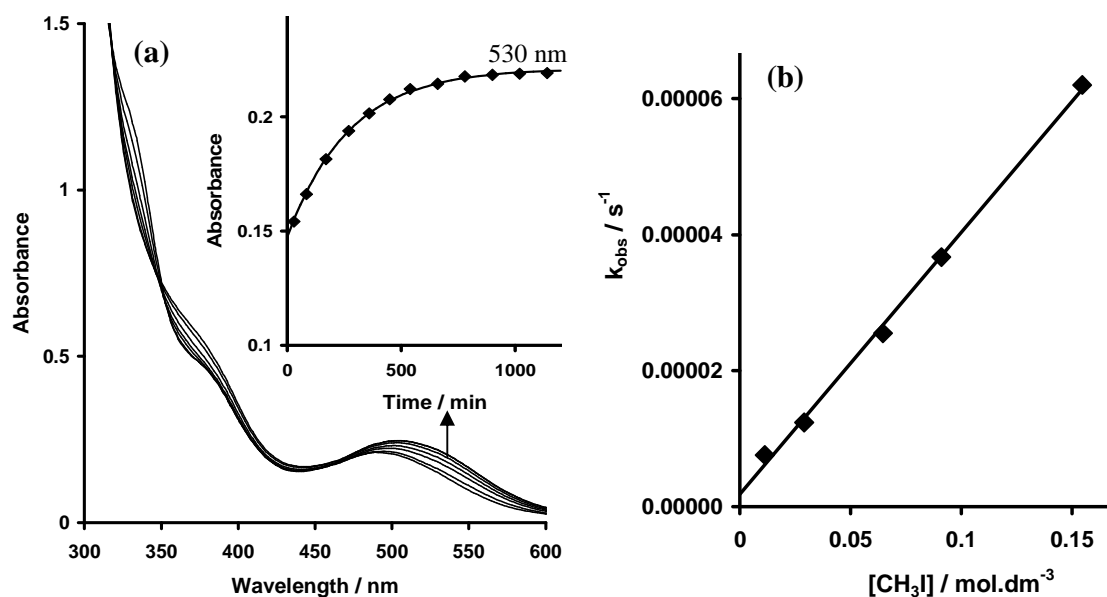
Figure 3.21. (a) UV time trace of the oxidative addition reaction between CH$_3$I and **(72)**. (b) Graph of k_{obs} *vs.* methyl iodide concentration for the reaction between CH$_3$I and **(72)**.

A temperature study was also carried out at 530 nm in order to determine the activation parameters, ΔH^* and ΔS^*, according to the Eyring relationship. The temperature was

varied between 15 and 41 °C. Due to the long reaction times, difficulty was experienced in controlling the temperature at 5 °C, and could thus not be used in the temperature study. The linear relationship for the oxidative addition reaction of CH₃I to (72) is shown in **Figure 3.22**, and activation parameters are summarized in **Table 3.17**.
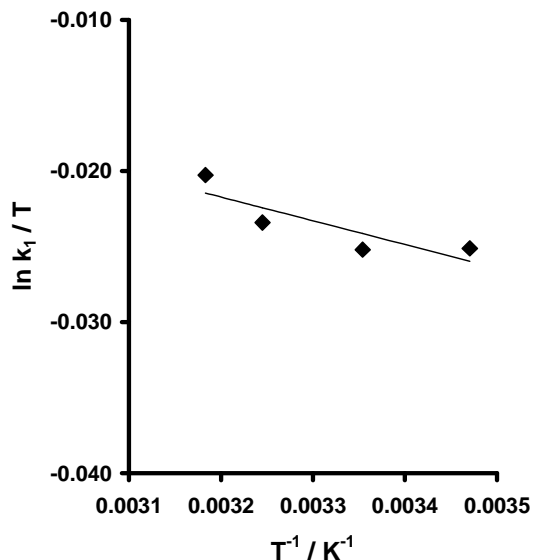
Figure 3.22. Eyring plot for the reaction between **(72)** and CH₃I.

Table 3.17. Kinetic rate constants and activation parameters for the UV-monitored reaction between **(72)** and CH₃I.

Wavelenght	k_1 / $dm^3mol^{-1}s^{-1}$	k_{-1} / s^{-1}	T / K	k_1 / $dm^3mol^{-1}s^{-1}$	ΔH^* / $kJ\ mol^{-1}$
530 nm	0.00038(1)	0.0000019(9)	288.15	0.000717(3)	13.3(2)
			298.15	0.000544(2)	ΔS^* /
			308.15	0.000736(3)	$J\ mol^{-1}K^{-1}$
			314.15	0.001714(4)	-197(5)

A (c)   The reaction between [Rh(FcCOCHCOCF₃)(CO)(PPh₂(C₆F₅))] (72) and CH₃I monitored by ¹H and ¹⁹F NMR.

¹H and ¹⁹F NMR were used to follow the oxidative addition reaction between **(72)** and CH₃I. For ¹H NMR measurements, the methine (CH from β-diketone) and methyl (CH₃ from CH₃I added) signals were monitored to follow the kinetics of the reaction. No ferrocenyl peaks were used to follow the reaction, due to extensive peak overlapping in the ferrocenyl region. For the ¹⁹F NMR study, peaks from the CF₃-group were used, as well as lone standing peaks from the (C₆F₅)-region (*i.e.* peaks that did not overlap). The

94

¹H NMR, as well as ¹⁹F NMR spectra (showed in **Figures 3.23** and **3.24**), followed the same reaction path observed during IR and UV studies. Additionally, each species also showed two isomers, indicated as A and B.

Figure 3.23. ^{1}H NMR spectra for the reaction between CH$_3$I and **(72)**, at times 0 (top), 210 and 840 (bottom) minutes.
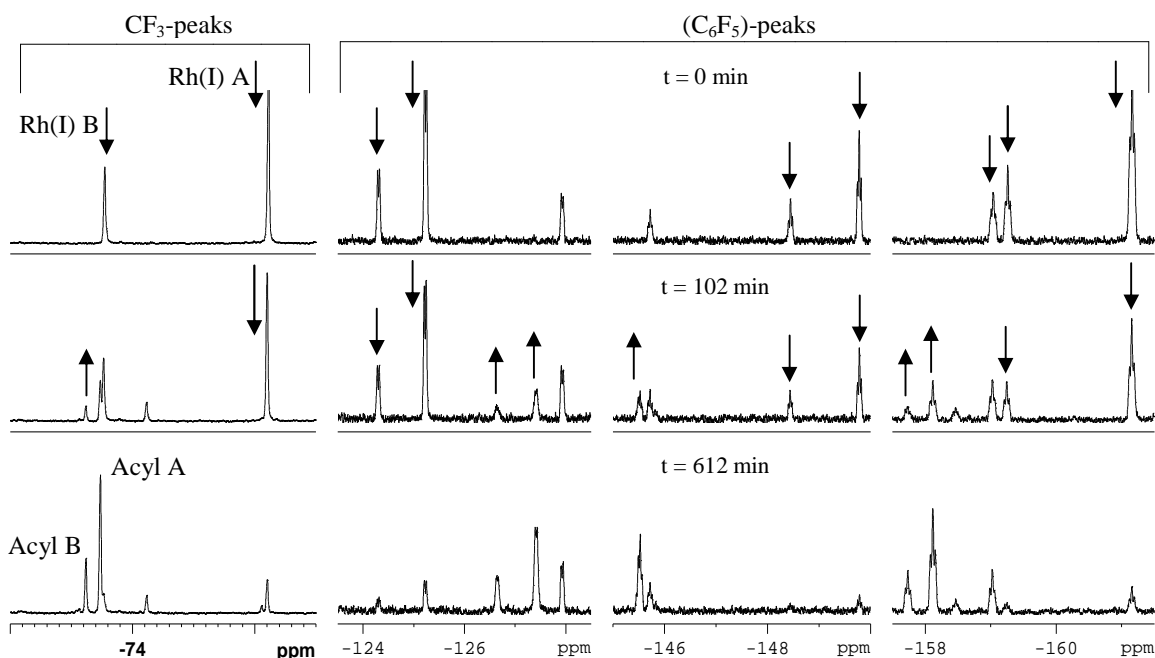
Figure 3.24. ^{19}F NMR spectra for the reaction between CH$_3$I and **(72)**, at times 0 (top), 102 and 612 (bottom) minutes.

The spectra show the disappearance of the two rhodium(I) isomers {Rh(I) A and Rh(I) B}, together with the formation of two observable isomers of the Rh(III) acyl species (A and B). The observed rate constants for the formation and disappearance of A and B isomers of any species were again found to be the same, within experimental error, again indicating a fast equilibrium between the A and B isomers of each species. The equilibrium constant (K_{c2}) between the two acyl isomers was also determined, and is listed in **Table 3.18**. The reaction mechanism can be summarized as indicated in **Scheme 3.24**. Observed rate data are summarized in **Table 3.18**.

$$\left[[Rh^{I}(FcCOCHCOCF_3)(CO)(PPh_2(C_6F_5))]_A \rightleftharpoons [Rh^{I}(FcCOCHCOCF_3)(CO)(PPh_2(C_6F_5))]_B \right] + CH_3I$$

$$k_{-1} \Updownarrow k_1$$

$$\left[[Rh^{III}(FcCOCHCOCF_3)(CO)(PPh_2(C_6F_5))(CH_3)(I)]_{Alkyl\ A} \xrightleftharpoons{K_{c1}} [Rh^{III}(FcCOCHCOCF_3)(CO)(PPh_2(C_6F_5))(CH_3)(I)]_{Alkyl\ B} \right]$$

$$k_{-2} \Updownarrow k_2$$

$$\left[[Rh^{III}(FcCOCHCOCF_3)(PPh_2(C_6F_5))(COCH_3)(I)]_{Acyl\ A} \xrightleftharpoons{K_{c2}} [Rh^{III}(FcCOCHCOCF_3)(PPh_2(C_6F_5))(COCH_3)(I)]_{Acyl\ B} \right]$$
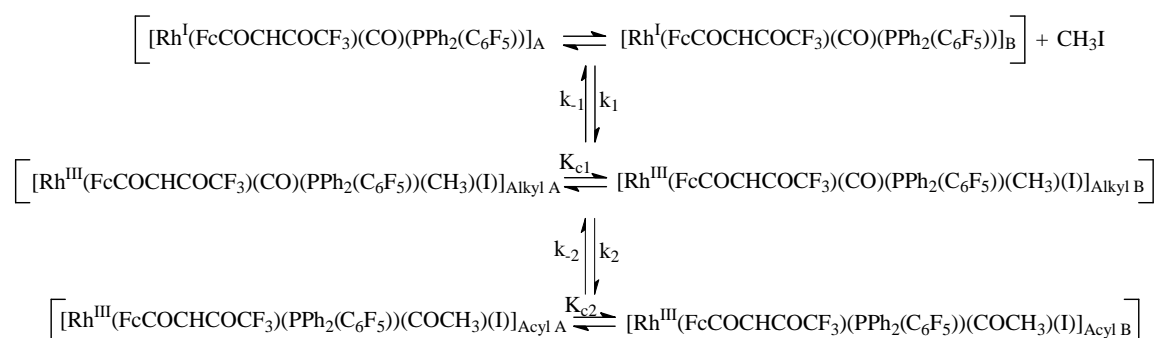
Scheme 3.24. Reaction mechanism for the oxidative addition of CH_3I to **(72)**.

Table 3.18. Kinetic rate constants for the NMR-monitored reaction between **(72)** and CH_3I at 25 °C.

Isomer	^{1}H NMR				Average K_{c2}
	$\delta\ ^1$H CH / ppm	k_1 / dm^{3}mol^{-1}s^{-1}	$\delta\ ^1$H CH$_3$ / ppm	k_1 / dm^{3}mol^{-1}s^{-1}	
Rh(I) A	6.15	0.00030(1)	-	-	0.36
Rh(I) B	6.13		-	-	
Acyl A	6.10	0.00026(1)	3.05	0.00025(2)	0.39
Acyl B	6.09		2.09	0.00025(2)	

	^{19}F NMR							
	δ CF$_3$ / ppm	k_1 / dm^{3}mol^{-1}s^{-1}	δ(C$_6$F$_5$) / ppm	k_1 / dm^{3}mol^{-1}s^{-1}	δ(C$_6$F$_5$) / ppm	k_1 / dm^{3}mol^{-1}s^{-1}	δ(C$_6$F$_5$) / ppm	k_1 / dm^{3}mol^{-1}s^{-1}
Rh(I) A	-73.8	0.00024(1)	-124.3	0.00026(1)	-149.8	0.00028(1)	-161.1	0.00030(1)
Rh(I) B	-75.1	0.00031(1)	-125.5	0.00028(1)	-	-	-	-
Acyl A	-73.6	0.00030(1)	-126.6	0.00028(1)	-145.5	0.00028(1)	-158.1	0.00030(1)
Acyl B	-73.7	0.00030(1)	-127.4	0.00028(1)	-	-	-157.7	0.00030(1)

B (a) The reaction between [Rh(FcCOCHCOCF₃)(CO)(PPh(C₆F₅)₂)] (73) and CH₃I monitored by IR.

The IR spectra of the reaction between **(73)** and CH_3I at 25 °C (shown in **Figure 3.25**), shows only one reaction step, similarly to the oxidative addition reaction of **(72)**, as discussed above. The reaction takes place at an even slower rate, with a half-life of more than 18 hours at a methyl iodide concentration of 1 M. The IR data shows the disappearance of the Rh(I) starting compound (2006 cm^{-1}), together with the simultaneous formation of a Rh(III) acyl species (1747 cm^{-1}). A small amount of a Rh(III) alkyl species is observed at 2077 cm^{-1}, but very little. The reaction mechanism must consist of a fast equilibrium between the Rh(I) starting compound and the Rh(III) alkyl species, since an alkyl species is necessary in order to undergo carbonyl insertion to form an acyl species. This is followed by the formation of the Rh(III) acyl species as the rate-determining step.
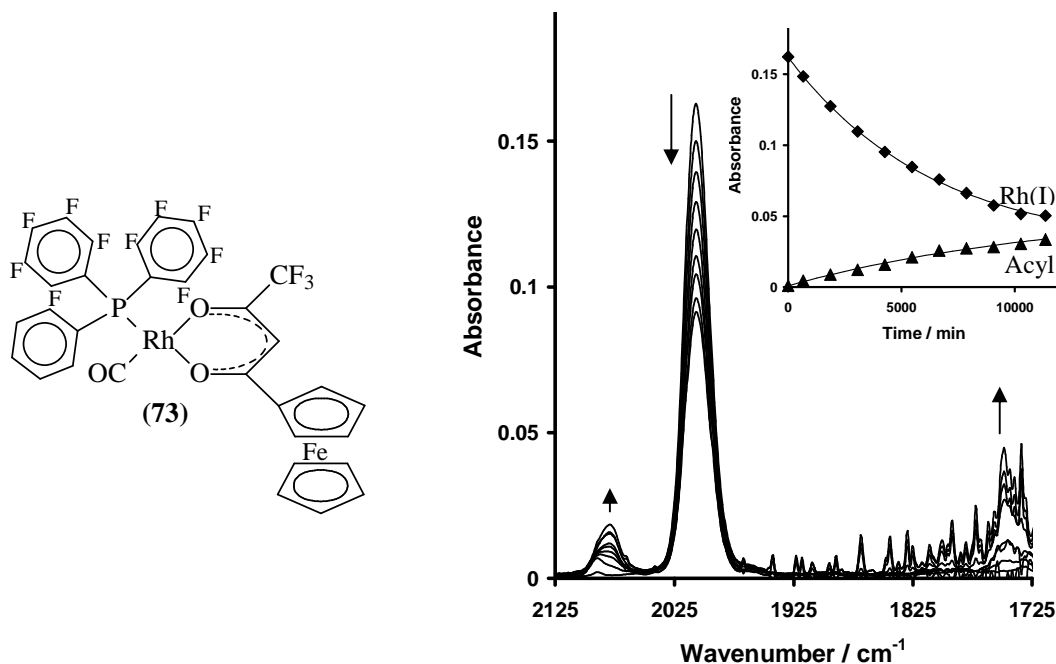
Figure 3.25. IR-spectra of the oxidative addition reaction between CH_3I and **(73)**, recorded between 1 and 12 000 mins.

The observed rate of reaction was determined under pseudo first-order conditions {[CH₃I] ≫ [Rh(I) phosphine]}, at 25 °C, and the rate constants are summarized in **Table 3.19**.

97

Table 3.19. Kinetic rate constants for the IR-monitored reaction between (**73**) and CH$_3$I at 25 °C.

	$\mathbf{k_1}$
Rh(I) disappearance	0.000015(1)
Rh(III)-acyl formation	0.000009(2)

B (b) The reaction between [Rh(FcCOCHCOCF$_3$)(CO)(PPh(C$_6$F$_5$)$_2$)] (73) and CH$_3$I monitored by UV.

The reaction between [Rh(FcCOCHCOCF$_3$)(CO)(PPh(C$_6$F$_5$)$_2$)] (**73**) and CH$_3$I showed only one reaction when followed by UV, as shown in **Figure 3.26**. Rate constants were obtained under pseudo first-order conditions with methyl iodide concentrations between 0.017 and 0.18 M, and are summarized in **Table 3.20**. An increase in absorbance, measured at 500 nm, was used to interpret the results. Rate constants obtained for this reaction corresponded well with the rate constants obtained by IR for the disappearance of the Rh(I) starting compound and formation of a Rh(III) acyl species.
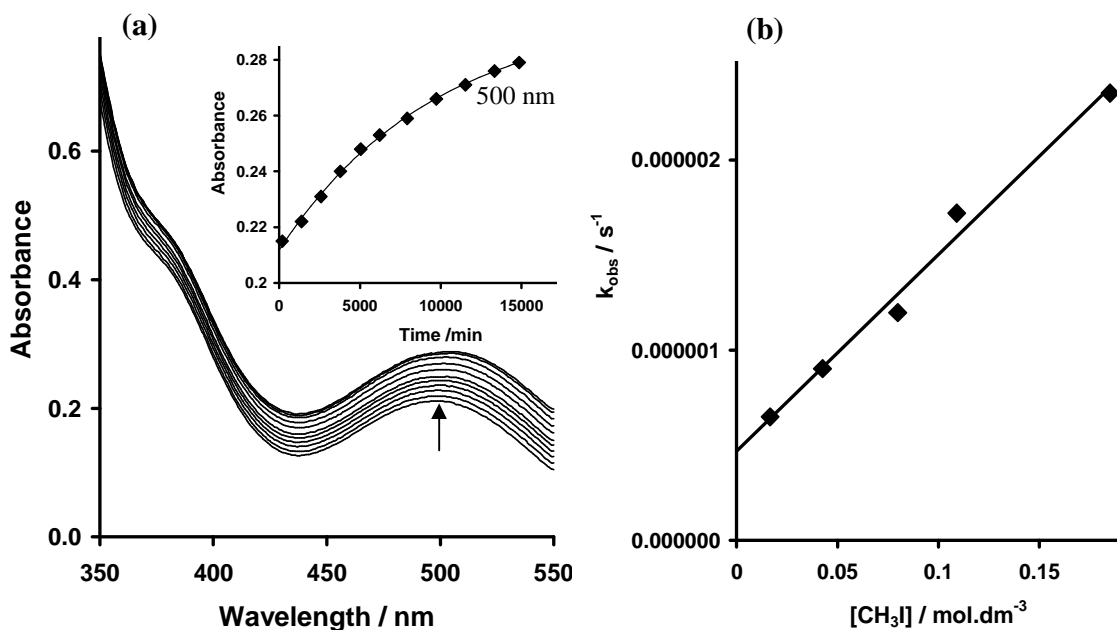
Figure 3.26. (a) Time-based UV/vis spectra for the oxidative addition reaction between CH$_3$I and (**73**). (b) Graph of k$_{obs}$ *vs.* methyl iodide concentration for for the reaction between CH$_3$I and (**73**).

A temperature study, carried out at 500 nm, was used to determine the activation parameters, ΔH^* and ΔS^*, according to the Eyring relationship. The temperature was

varied between 15 and 41 °C. Due to the long reaction times, difficulty was experienced in controlling the temperature at 5 °C, and could thus not be used in the temperature study. The linear relationship for the oxidative addition reaction of CH₃I to **(73)** is shown in **Figure 3.27**, and activation parameters are summarized in **Table 3.20**.

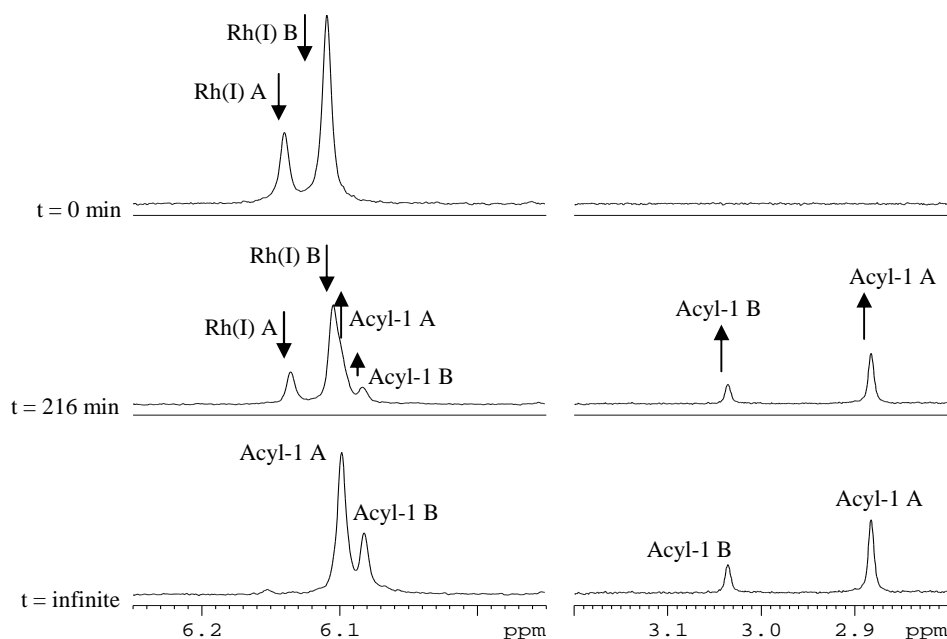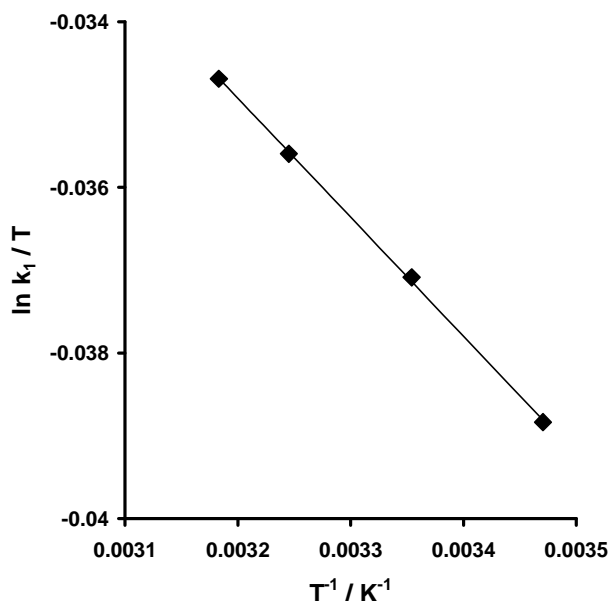**Figure 3.27.** Eyring plot for the reaction between **(73)** and CH₃I.

Table 3.20. Kinetic rate constants and activation parameters for the UV-monitored reaction between **(73)** and CH₃I.

Wavelenght	k_1 / $dm^3mol^{-1}s^{-1}$	k_{-1} / s^{-1}	T / K	k_1 / $dm^3mol^{-1}s^{-1}$	ΔH^* / $kJ\ mol^{-1}$
500 nm	0.0000103(7)	0.00000047(7)	288.15	0.000014(1)	11.9(7)
			298.15	0.000016(1)	ΔS^* /
			308.15	0.000017(2)	$J\ mol^{-1}K^{-1}$
			314.15	0.000019(1)	-197(4)

B (c) The reaction between [Rh(FcCOCHCOCF₃)(CO)(PPh(C₆F₅)₂)] (73) and CH₃I monitored by ¹H and ¹⁹F NMR.

¹H and ¹⁹F NMR was used to follow the oxidative addition reaction between **(73)** and CH₃I (**Figures 3.28** and **3.29**). The methine (CH from β-diketone) and methyl (CH₃ from CH₃I added) signals were used during ¹H NMR to follow the reaction. Peaks from the CF₃ group were used during ¹⁹F NMR, as well as selected peaks from the C₆F₅ region

that could uniquely be identified and were free from overlapping by neighbouring peaks. The ^{1}H NMR, as well as ^{19}F NMR spectra followed the same reaction path observed during IR and UV studies, similarly to the reaction mechanism observed for compound **(72)**. Each species also showed two isomers, A and B.
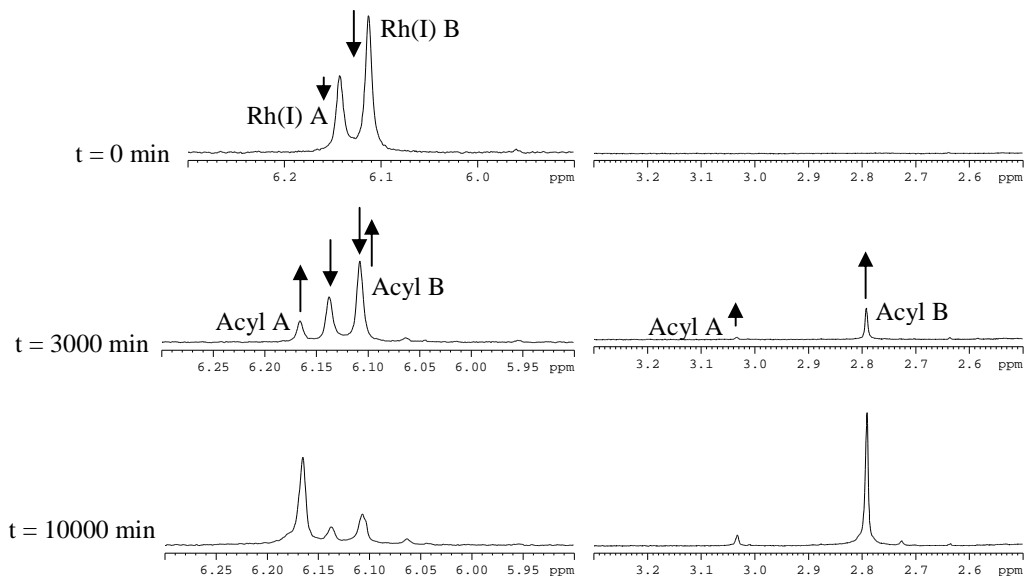
Figure 3.28. ^{1}H NMR spectra for the reaction between CH_3I and **(73)**, at times 0 (top), 3000 and 10000 (bottom) minutes.
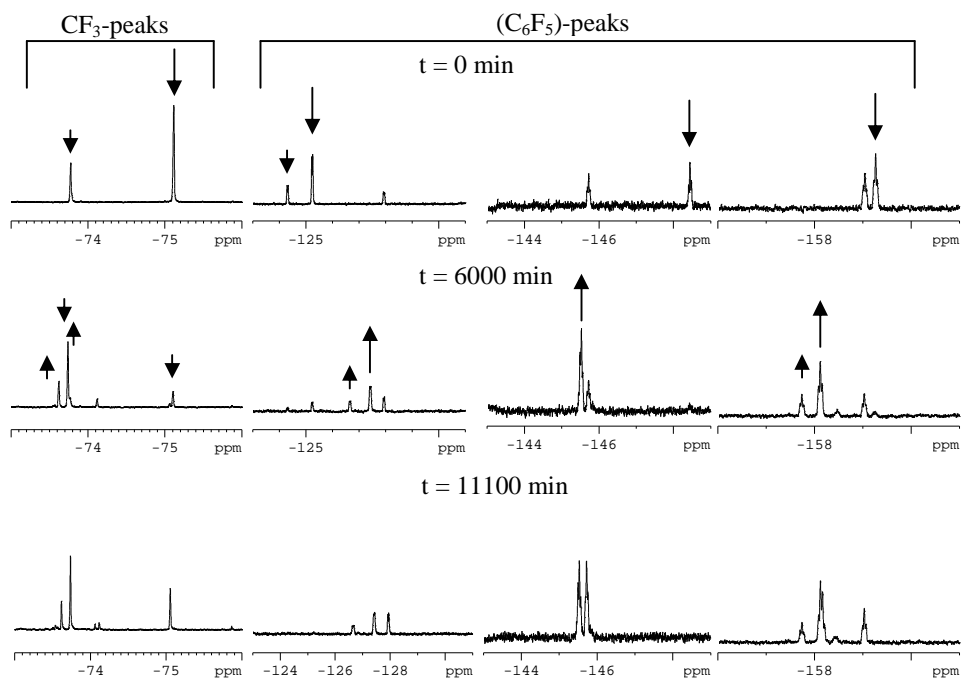
Figure 3.29. ^{19}F NMR spectra for the reaction between CH_3I and **(73)**, at times 0 (top), 6000 and 11100 (bottom) minutes.

100

The reaction showed the disappearance of the two rhodium(I) isomers {Rh(I) A and Rh(I) B}, together with the formation of two observable isomers of the Rh(III) acyl species (A and B). The observed rate constants for the formation and disappearance of A and B isomers of any species were again found to be the same, within experimental error, indicating a fast equilibrium between the A and B isomers of each species. The reaction mechanism can be summarized as indicated in **Scheme 3.25**. Observed rate data are summarized in **Table 3.21**.

$$\left[[Rh^I(FcCOCHCOCF_3)(CO)(PPh(C_6F_5)_2)]_A \overset{K_c}{\rightleftharpoons} [Rh^I(FcCOCHCOCF_3)(CO)(PPh(C_6F_5)_2)]_B \right] + CH_3I$$

$$k_{-1} \updownarrow k_1$$

$$\left[[Rh^{III}(FcCOCHCOCF_3)(CO)(PPh(C_6F_5)_2)(CH_3)(I)]_{AlkylA} \overset{K_{c1}}{\rightleftharpoons} [Rh^{III}(FcCOCHCOCF_3)(CO)(PPh(C_6F_5)_2)(CH_3)(I)]_{AlkylB} \right]$$

$$k_{-2} \updownarrow k_2$$

$$\left[[Rh^{III}(FcCOCHCOCF_3)(PPh(C_6F_5)_2)(COCH_3)(I)]_{AcylA} \overset{K_{c2}}{\rightleftharpoons} [Rh^{III}(FcCOCHCOCF_3)(PPh(C_6F_5)_2)(COCH_3)(I)]_{AcylB} \right]$$
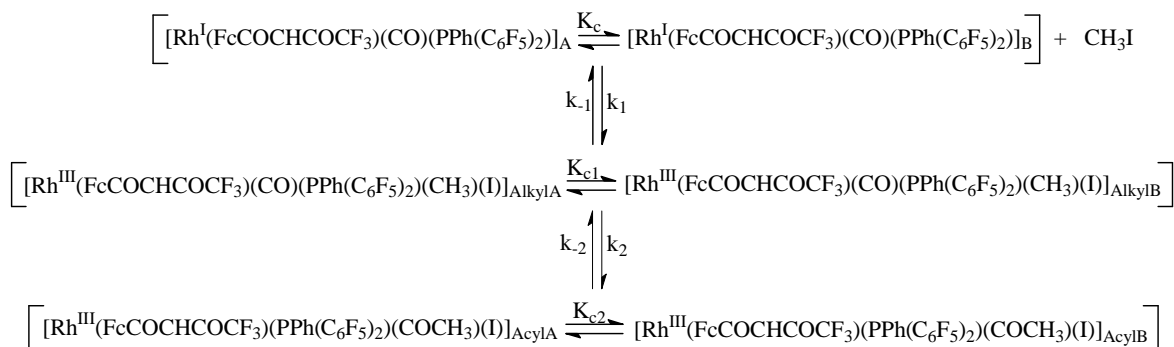
Scheme 3.25. Reaction mechanism for the oxidative addition of CH_3I to **(73)**.

Table 3.21. Kinetic rate constants for the NMR-monitored reaction between **(73)** and CH_3I at 25 °C.

Isomer	^1H NMR				Average K_c
	$\delta\ ^1H\ CH$ / ppm	k_1 / $dm^3mol^{-1}s^{-1}$	$\delta^1H\ CH_3$ / ppm	k_1 / $dm^3mol^{-1}s^{-1}$	
Rh(I) A	6.14	0.000010(4)	-	-	0.66
Rh(I) B	6.11	0.000008(3)	-	-	
Acyl A	6.17	0.000016(3)	3.00	0.000017(7)	0.09
Acyl B	6.15	-	2.80	0.000016(2)	

	^{19}F NMR							
	$\delta\ CF_3$ / ppm	k_1 / $dm^3mol^{-1}s^{-1}$	$\delta(C_6F_5)$ / ppm	k_1 / $dm^3mol^{-1}s^{-1}$	$\delta(C_6F_5)$ / ppm	k_1 / $dm^3mol^{-1}s^{-1}$	$\delta(C_6F_5)$ / ppm	k_1 / $dm^3mol^{-1}s^{-1}$
Rh(I) A	-73.7	0.00001(1)	-126.3	0.00001(1)	-147.6	0.00001(1)	-159.5	0.00001(1)
Rh(I) B	-75.1	0.00001(1)	-	-	-147.8	0.00001(1)	-158.6	0.00001(1)
Acyl A	-74.2	0.00001(1)	-129.9	0.00001(1)	-144.9	0.00001(1)	-158.3	0.00001(1)
Acyl B	-73.9	-	-127.7	0.00001(1)	-45.2	0.00001(1)	-158.9	0.00001(1)

C The reaction between [Rh(FcCOCHCOCF₃)(CO)(P(C₆F₅)₃)] (74) and CH₃I.

A possible reaction between $[Rh(FcCOCHCOCF_3)(CO)(P(C_6F_5)_3)]$ **(74)** and CH_3I was searched for by IR and ^1H NMR techniques. Both experiments showed conclusively that

no reaction takes place over 7 days at 25°C and a methyl iodide concentration of 0.1 M. **Figure 3.30** shows the ^{1}H NMR spectra of **(74)** and 0.27 M CH$_3$I in a chloroform solution immediately after CH$_3$I addition (top), and after 4 days (bottom).
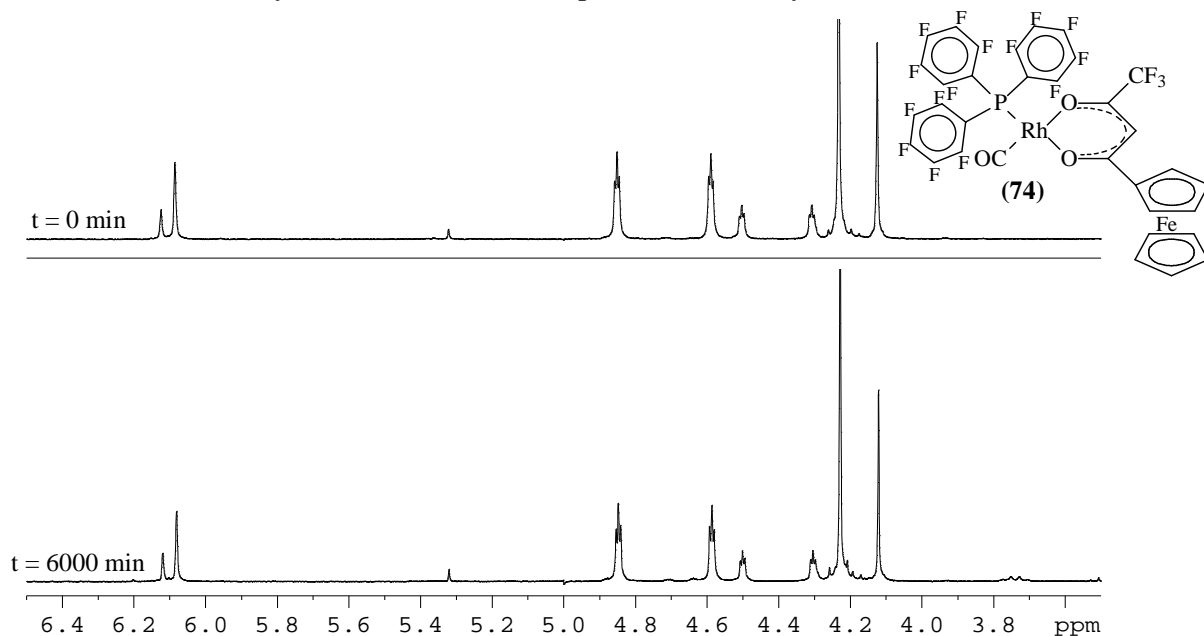
Figure 3.30. ^{1}H NMR spectra of **(74)** and CH$_3$I immediately after mixing (top), and after 4 days in solution (bottom).

D Summary of kinetic data obtained by various spectroscopic techniques.

Kinetic data obtained from various spectroscopic techniques for the oxidative addition reactions of rhodium complexes containing fluorinated phosphine ligands, [Rh (FcCOCHCOCF$_3$)(CO)(PPh$_2$(C$_6$F$_5$))] **(72)** and [Rh(FcCOCHCOCF$_3$)(CO)(PPh(C$_6$F$_5$)$_2$)] **(73)**, are summarized in **Table 3.22**. Rate constants obtained by different spectroscopic techniques were mutually consistent. It is known that a decrease in electron density on the metal center leads to a decrease in the rate of oxidative addition (as discussed in **Chapter 2**, **Section 2.6.1**). Considering the increase in group electronegativities of the phosphine ligand as additional C$_6$F$_5$ groups are added, it was expected that the rate of oxidative addition would decrease in going from **(72)** to **(73)** and **(74)**. This was indeed the case. Complex **(73)** reacted almost 40x slower than **(72)**, and **(74)** were found not to undergo oxidative addition at all.

The rate of reductive elimination (reverse reaction, k_{-1}) for compounds **(72)** and **(73)**, was found to be 0.6 % and 4.4 % of the forward reaction respectively. For compound **(72)**, this can be considered insignificant, but for **(73)**, the rate of the forward reaction becomes so slow that the small rate of the reverse reaction can have a significant influence. For **(74)**, the reductive elimination reaction must completely dominate.

Table 3.22. Average kinetic rate constants obtained by various spectroscopic techniques for compounds **(72)** and **(73)**.

Compound	[Rh(FcCOCHCOCF$_3$)(CO)(PPh$_2$(C$_6$F$_5$))] (72)	
Method	k_1 / dm^{3}mol^{-1}s^{-1}	k_{-1} / s^{-1}
IR	0.00031(4)	-
UV	0.00038(1)	0.0000019(9)
^{1}H NMR	0.00027(3)	-
^{19}F NMR	0.00029(7)	-
ΔH^* / kJ mol^{-1}		13.3(2)
ΔS^* / J mol^{-1}K^{-1}		-197(5)
Compound	[Rh(FcCOCHCOCF$_3$)(CO)(PPh(C$_6$F$_5$)$_2$)] (73)	
Method	k_1 / dm^{3}mol^{-1}s^{-1}	k_{-1} / s^{-1}
IR	0.000011(2)	-
UV	0.000010(1)	0.0000005(1)
^{1}H NMR	0.000014(2)	-
^{19}F NMR	0.000010(1)	-
ΔH^* / kJ mol^{-1}		11.9(7)
ΔS^* / J mol^{-1}K^{-1}		-197(4)
Compound	[Rh(FcCOCHCOCF$_3$)(CO)(P(C$_6$F$_5$)$_3$)] (74)	
Method	k_1 / dm^{3}mol^{-1}s^{-1}	k_{-1} / s^{-1}
IR	0	0
^{1}H NMR	0	0

Large negative ΔS^*-values were obtained for both **(72)** and **(73)**, indicating an associative mechanism for both. It is clear from the NMR results that at least two isomers of each species exist in equilibrium with each other, and react at the same rate. All the different spectroscopic techniques also showed a fast equilibrium between the Rh(I) starting compound and the Rh(III) alkyl species, followed by the rate-determining carbonyl insertion step to form the Rh(III) acyl species. This indicates that the reaction between CH$_3$I and **(72)** or **(73)** is a special case of the reaction mechanism proposed by Conradie

et al.,[13] for [Rh(FcCOCHCOCF$_3$)(CO)(PPh$_3$)] **(29)**, with the exception that no Alkyl-2 or Acyl-2 species is observed. This means that the rate constants that generate them are zero. The modified reaction mechanism is summarized in **Scheme 3.26**.

$$\left[[Rh^I(FcCOCHCOCF_3)(CO)(PPh_n(C_6F_5)_{3-n})]_A \rightleftharpoons [Rh^I(FcCOCHCOCF_3)(CO)(PPh_n(C_6F_5)_{3-n})]_B \right] + CH_3I$$

$$k_{-1} \Big\Updownarrow k_1$$

$$\left[[Rh^{III}(FcCOCHCOCF_3)(CO)(PPh_n(C_6F_5)_{3-n})(CH_3)(I)]_{AlkylA} \xrightleftharpoons{K_{c1}} [Rh^{III}(FcCOCHCOCF_3)(CO)(PPh_n(C_6F_5)_{3-n})(CH_3)(I)]_{AlkylB} \right]$$

$$k_{-2} \Big\Updownarrow k_2$$

$$\left[[Rh^{III}(FcCOCHCOCF_3)(PPh_n(C_6F_5)_{3-n})(COCH_3)(I)]_{AcylA} \xrightleftharpoons{K_{c2}} [Rh^{III}(FcCOCHCOCF_3)(PPh_n(C_6F_5)_{3-n})(COCH_3)(I)]_{AcylB} \right]$$
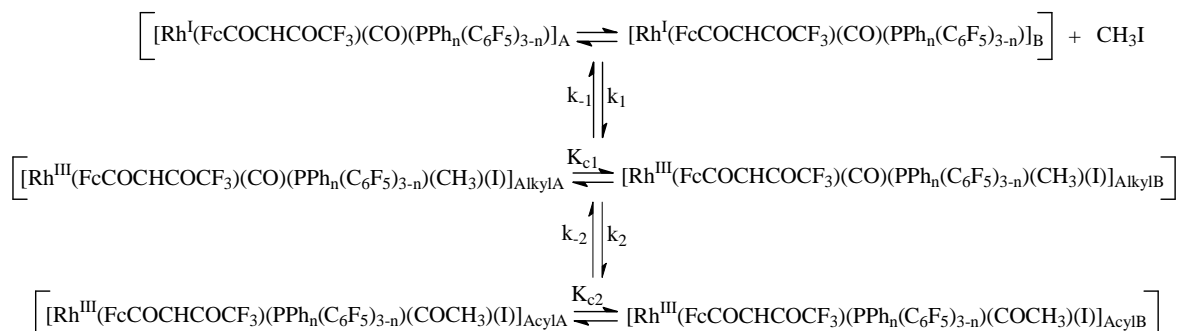
Scheme 3.26. Overall reaction mechanism for the oxidative addition of CH$_3$I to rhodium complexes **(72)** , with n = 2, and **(73)**, with n = 1, containing fluorinated phosphines.

3.3.1.4. Conclusion

All complexes investigated as possible oxidative addition catalysts possess very similar chemical structure, [Rh(FcCOCHCOCF$_3$)(CO)(*phosphine*)], with large electronic differences present in the phosphine ligands. It is thus possible to compare the complexes containing metallocene phosphines {[Rh(FcCOCHCOCF$_3$)(CO)(PPh$_2$Mc)] with Mc = Fc **(70)** (χ_R = 1.87) or Rc **(71)** (χ_R = 1.99)}[15] and fluorinated phosphines {[Rh (FcCOCHCOCF$_3$)(CO)(PPh$_n$(C$_6$F$_5$)$_{3-n}$)] with n = 2 **(72)** , 1 **(73)** or 0 **(74)**, (χ_{Ph} = 2.21, $\chi_{(C6F5)}$ = 2.46)}[16] on the basis of group electronegativity. A graph of the rate of reaction *vs*. the sum of group electronegativity for the phosphine substituents is shown in **Figure 3.31**. An approximately linear relationship seems to exist between rate of reaction and total group electronegativity for the phosphine ligand, with a maximum χ_R of 7.1 before the rate of oxidative addition becomes insignificant. The rate of reaction for **(70)** does not conform to the linear relationship shown in **Figure 3.31**, and can be considered an anomaly.
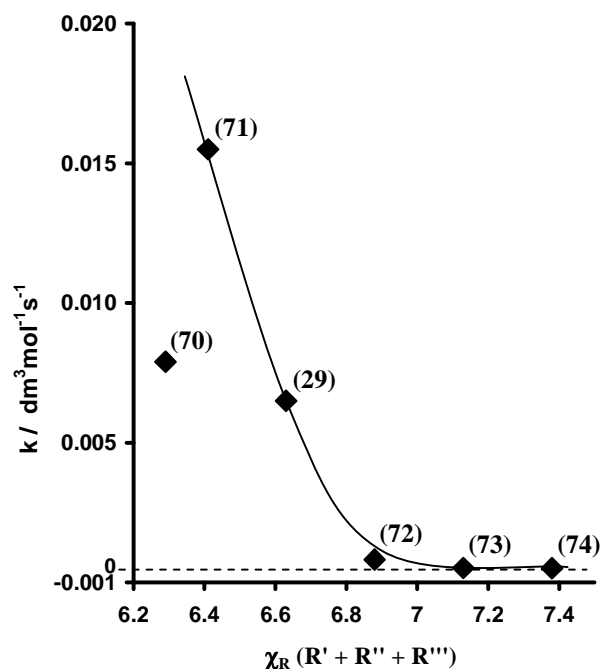
Figure 3.31. Graph showing the relationship between group electronegativity (χ_R) and rate of reaction. (With R', R", R''' = phosphine side groups.)

3.3.2. Substitution Reactions

Having studied some of the factors that control oxidative addition to rhodium(I) complexes, it was decided to investigate an aspect of substitution reactions involving the rhodium(I) center. Oxidative addition is of importance to catalysis, while substitution reactions plays a key role in the anti-cancer properties of rhodium(I) complexes.

The substitution reaction of the rhodium complexes [Rh(α-TTF-Sacac)(cod)] **(75)** and [Rh(β-TTF-Sacac)(cod)] **(76)** with 1,10-phenanthroline in methanol as solvent, was studied by stopped-flow techniques. The reaction with 1,10-phenanthroline proceeds, as shown in **Scheme 3.27**, with the replacement of the β-diketone to form [Rh(cod)(phen)]$^+$ **(89)**. Results will highlight the influence of the position of β-diketonato substituents on rates of β-diketonato substitution.
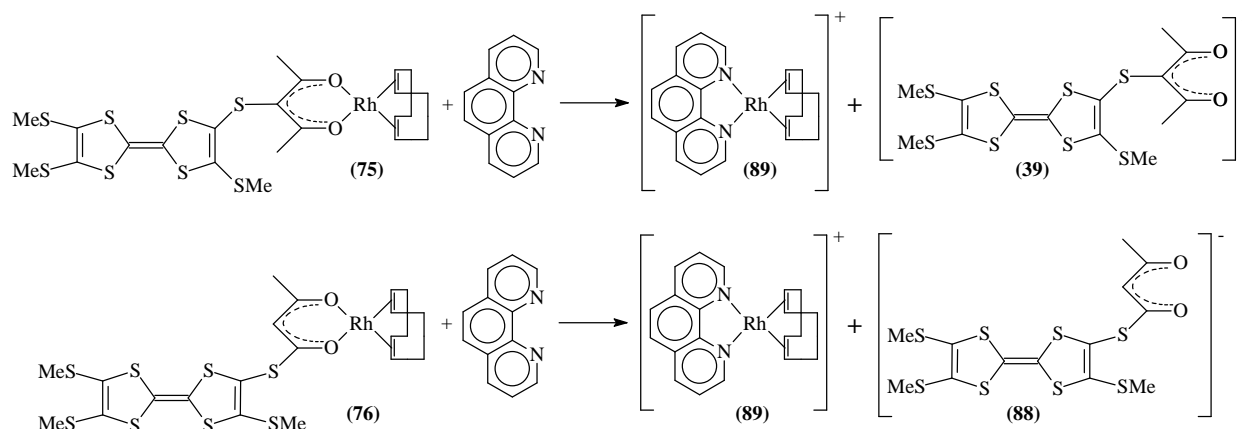
Scheme 3.27. The substitution reaction of **(75)** and **(76)** with 1,10-phenanthroline, to give [Rh(cod)(phen)]$^+$ **(89)**.

The UV spectra of **(75)** and **(76)**, as well as their substitution reaction product, [Rh(phen)(cod)]$^+$, are shown in **Figure 3.32** (**a** and **c**). The linear relationship between the absorbance and concentration for both **(75)** and **(76)**, also shown in **Figure 3.32** (**b** and **d**), confirms the validity of the Beer Lambert law for both these complexes. Molar extinction coefficients were determined at experimental wavelengths where substitution was monitored, and these are summarized in **Table 3.23**.

Table 3.23. Molar extinction coefficients (ε) for Rh(TTF-Sacac)(cod)] complexes at indicated experimental wavelengths.

Complex	λ_{exp} / nm	ε / dm^3 mol^{-1} cm^{-1}
(75)	240	2024(12)
(76)	490	1865(13)

106
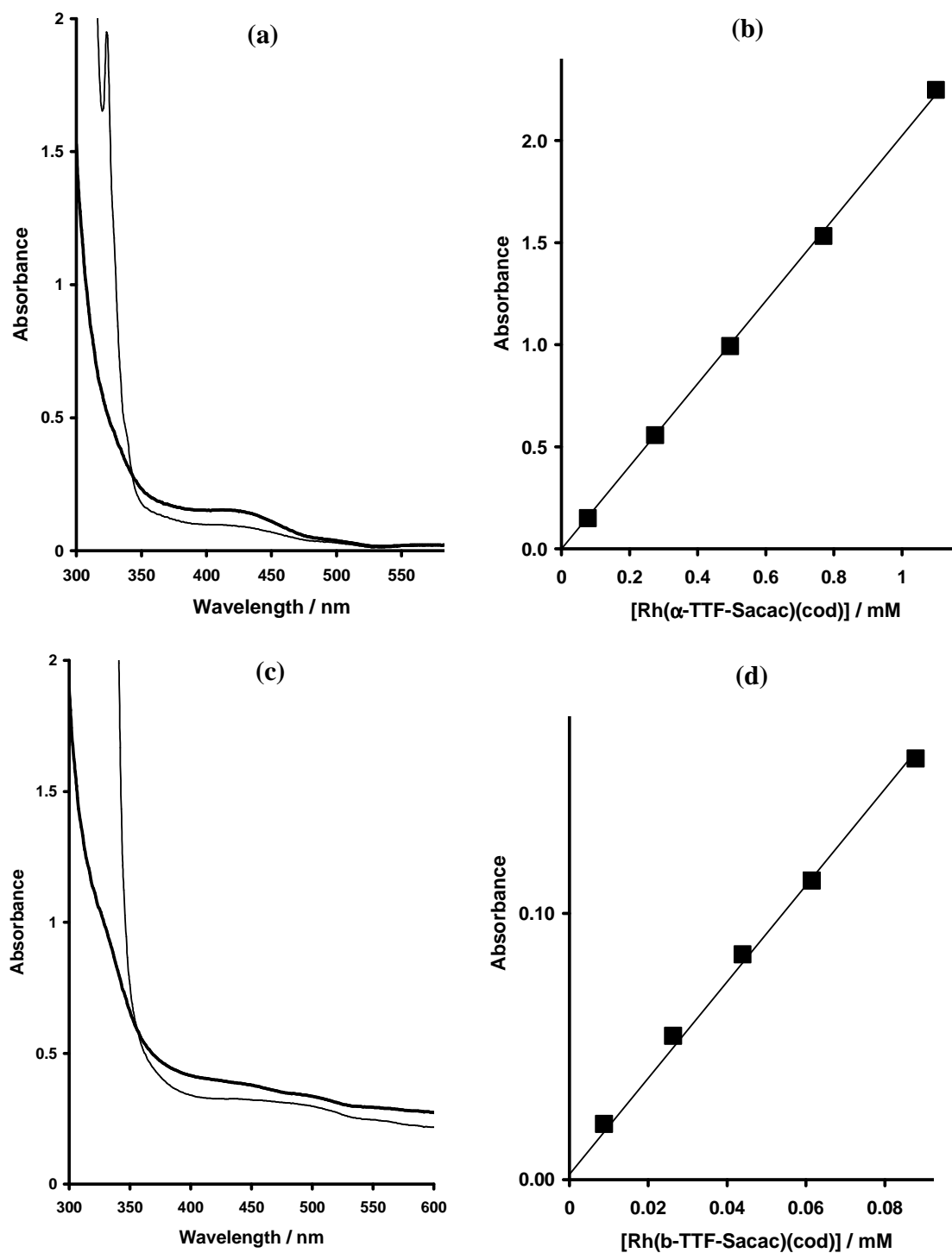
Figure 3.32. **(a)** UV spectra of **(75)** and [Rh(phen)(cod)]⁺ **(89)** (bold line) in methanol at 25°C. **(b)** Linear graph of absorbance *vs* concentration of **(75)** at 240 nm. **(c)** UV spectra of **(76)** and [Rh(phen)(cod)]⁺ **(89)** (bold line), under similar conditions. **(d)** Linear graph of absorbance *vs* concentration of **(76)** at 490 nm.

The rate constants were obtained by following the formation of [Rh(cod)(phen)]$^+$ at 240 nm for compound (75), and 490 nm for compound (76). Pseudo-first-order rate constants were obtained by utilizing a 5 to 500 fold excess of 1,10-phenanthroline over Rh(I) reactants (75) and (76). 1,10-Phenanthroline pseudo first-order linear plots are shown in **Figure 3.33** (**a** and **c**). Second-order rate constants (k_2) were obtained according to **Equation 3.3** by measuring observed rate constants (k_{obs}) at varied 1,10-phenanthroline concentrations and at different reaction temperatures (5 - 41°C). Values obtained from the temperature variation were used to determine the activation parameters graphically according to the Eyring equation, as shown in **Figure 3.33** (**b** and **d**). Results are summarized in **Table 3.24**.

$$\text{Rate} = (k_s + k_2 \text{ [phen]}) \text{ [Rh(TTF-Sacac)(cod)]}$$
$$= k_{obs} \text{ [Rh(TTF-Sacac)(cod)]} \quad \text{with} \quad k_{obs} = k_2 \text{ [phen]} + k_s \qquad \textbf{Equation 3.3}$$

Very large second-order rate constants were obtained for both compounds, with (76) having a second-order rate constant approximately double to that of (75). Although this is not a very large difference, it is significant and indicates that the position of bulky side-groups can influence the rate of substitution reactions. In the case of (76), the very bulky TTF-side group is positioned on the terminal carbon of the β-diketone, and less likely to interfere with attacking nucleophiles on the rhodium(I) center. In the case of (75), the bulky group is positioned much closer to the rhodium center, and more likely to protrude above the square-planar plane of the rhodium center. This can offer steric interference with attacking incoming nucleophilic groups, and offers a possible explanation for the slower reaction rate.

Another notable observation is a k_s value of 42 s^{-1} for the substitution reaction of (76) with 1,10-phenanthroline. This indicates a solvent pathway as alternative route towards the reaction product. This rare observation has been observed in only a few other cases, and usually is associated with β-diketonato ligands having phenyl substituents. The likelihood of a bidentate ligand like β-diketones being replaced by a monodentate solvent molecule, here methanol, is low; hence k_s values, if observed, are usually very small

compared to the k_2 value. For the present study involving **(76)**, k_s is very large. It means even at 1,10-phenanthroline concentrations as high as 0.024 mol dm^{-3} (a 300-fold excess over **(76)**), still more than half of the substituted product **(89)** is generated by the solvent pathway.
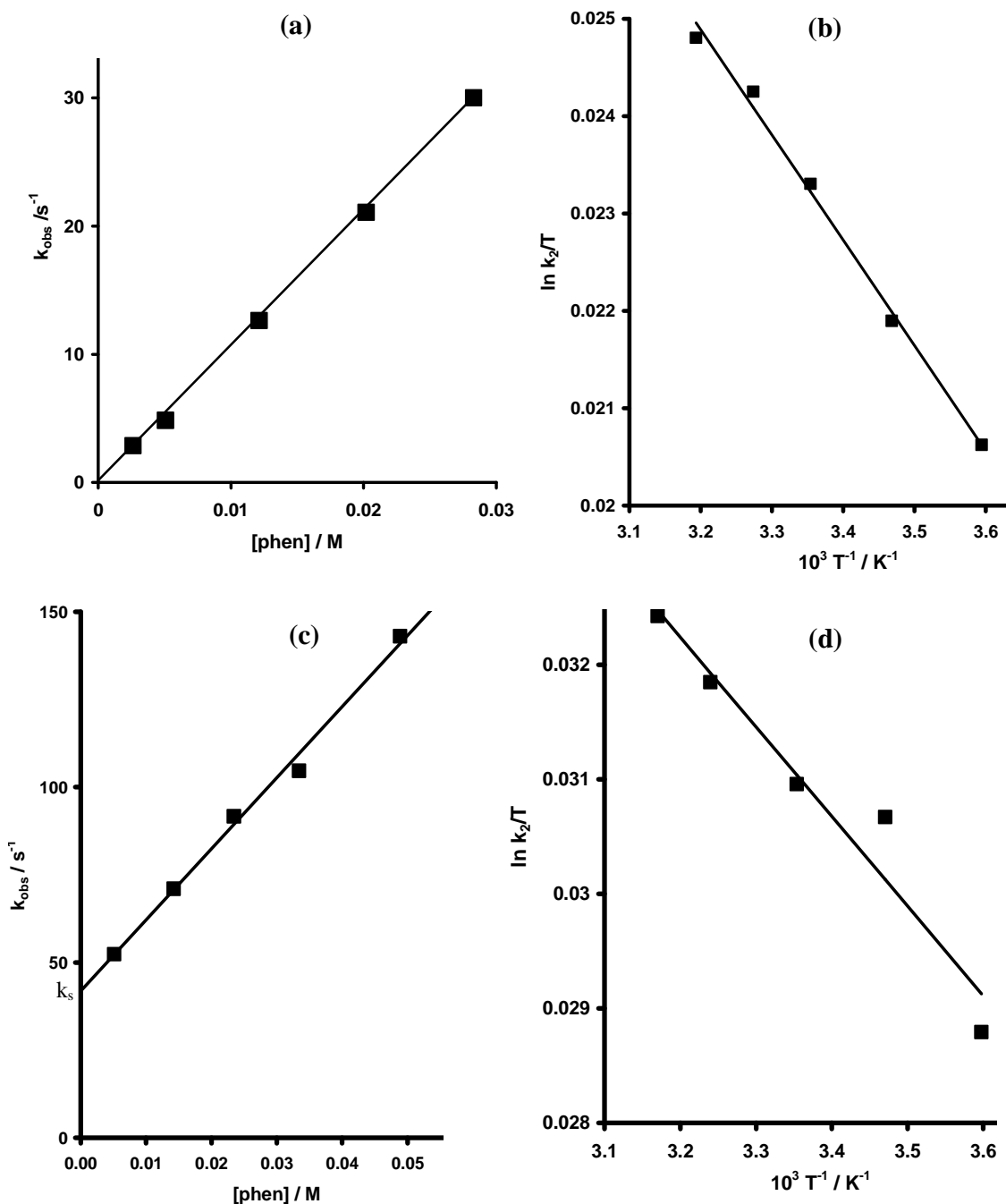
Figure 3.33. {**(a)** and **(c)**} Graphs of pseudo first-order rate constants (k_{obs}) *vs* concentration 1,10-phenanthroline for **(75)** (graph **(a)**) and **(76)** (graph **(c)**), at 25°C. {**(b)** and **(d)**} Eyring plots of ln (k_2/T) *vs* T^{-1} for **(75)** (graph **(b)**) and **(76)** (graph **(d)**), measured at temperatures ranging from 5 - 41°C.

Table 3.24. Second-order rate constants (k_2), as well as activation parameters for substitution reactions measured at given wavelengths.

Complex	λ_{exp} / nm	k_2 / dm^3 mol^{-1} s^{-1}	k_S / s^{-1}	ΔH^* / J mol^{-1}	ΔS^* / J K^{-1} mol^{-1}
(75)	240	1051(8)	0	90(5)	-197(1)
(76)	490	2028(90)	42(3)	65(7)	-197(1)

From the slope and intercept of the Eyring plots ΔS^* and ΔH^* were determined (**Chapter 2**, **Section 2.6**). A large negative ΔS^* value for both **(75)** and **(76)** indicates that substitution proceeds *via* an associative mechanism, as shown in **Scheme 3.28**. The first rate-determining step consists of association of the 1,10-phenanthroline *via* one of its nitrogen atoms, forming a five-coordinate transition state species. Secondly, breakage of one of the β-diketonato rhodium-oxygen bonds occurs, together with bond formation towards the uncoordinated nitrogen atom of 1,10-phenanthroline, forming another five-coordinated transition species. This quickly dissociates to form [Rh(cod)(phen)]$^+$ as product and liberates the β-diketonato anion. It has been shown before that, in the first step, bond-breakage occurs at the oxygen atom attached to the more electron-withdrawing side-group (as discussed in **Chapter 2**). Thus it can be assumed that oxygen bond-breakage occurs at the O atom closest to the CH$_3$ group in **(76)**. For **(75)**, oxygen bond-breakage can occur at either of the two equivalent O atoms due to its symmetric substitution pattern.
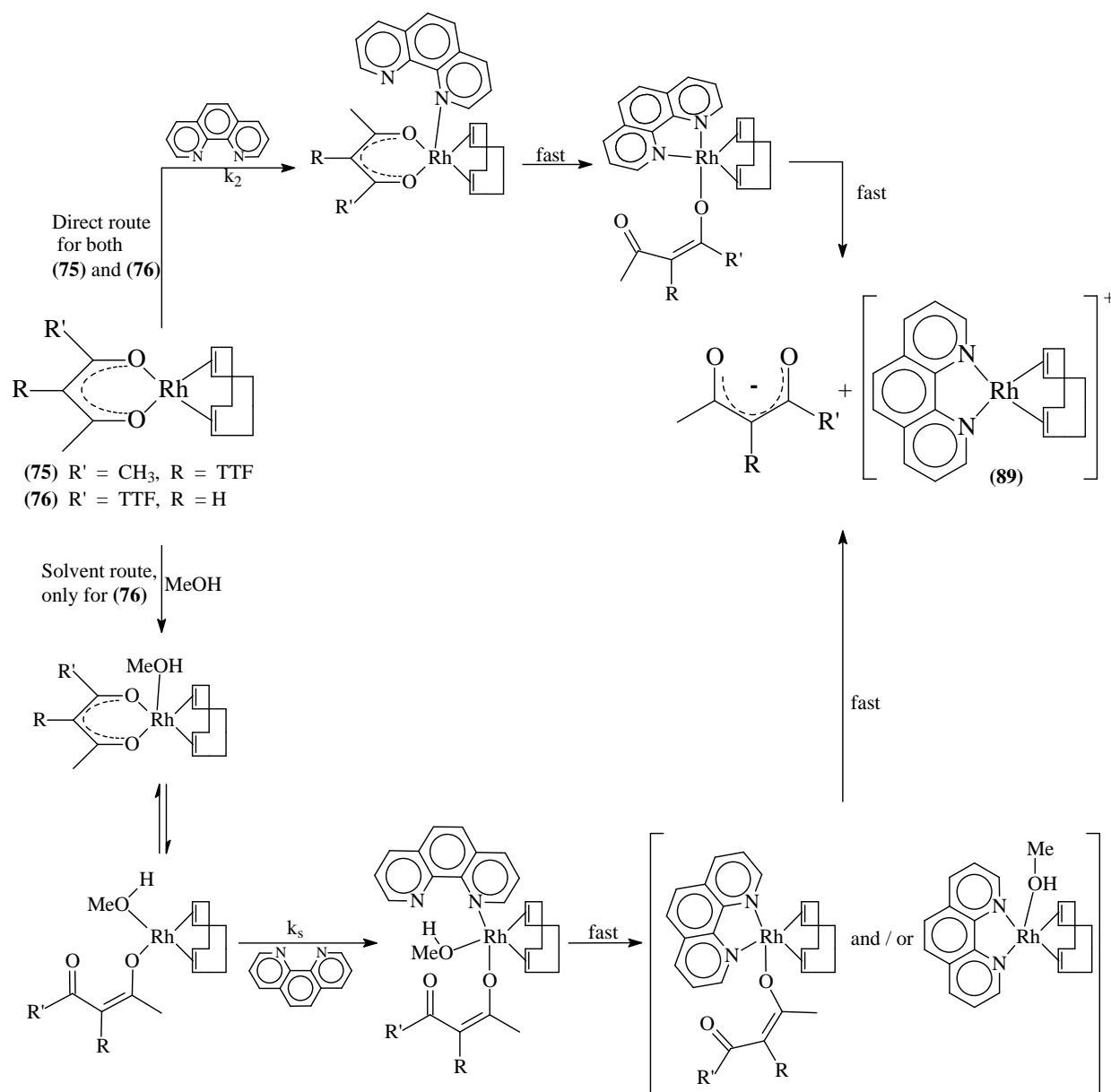
Scheme 3.28. Schematic representation of the associative mechanism of substitution of [Rh(TTF-Sacac)(cod)] complexes with 1,10-phenanthroline. The direct route (top) is valid for both **(75)** and **(76)**, while the solvent route (bottom) is only applicable to **(76)**. TTF = tetrathiafulvalene.

3.4.   Crystal Structure Determinations

3.4.1. 1-Ferrocenyl-3-osmocenylpropan-1,3-dione (7)

Mr. M.J. Janse van Rensburg, from the Department of Chemistry at the University of the Free State, is acknowledged for determining the single crystal structure of

FcCOCH$_2$COOc (**7**). Refinement of the crystal structure proved unsuccessful to date, and requires the crystal data to be recollected. A perspective view of the unrefined structure of (**7**) is shown in **Figure 3.34**
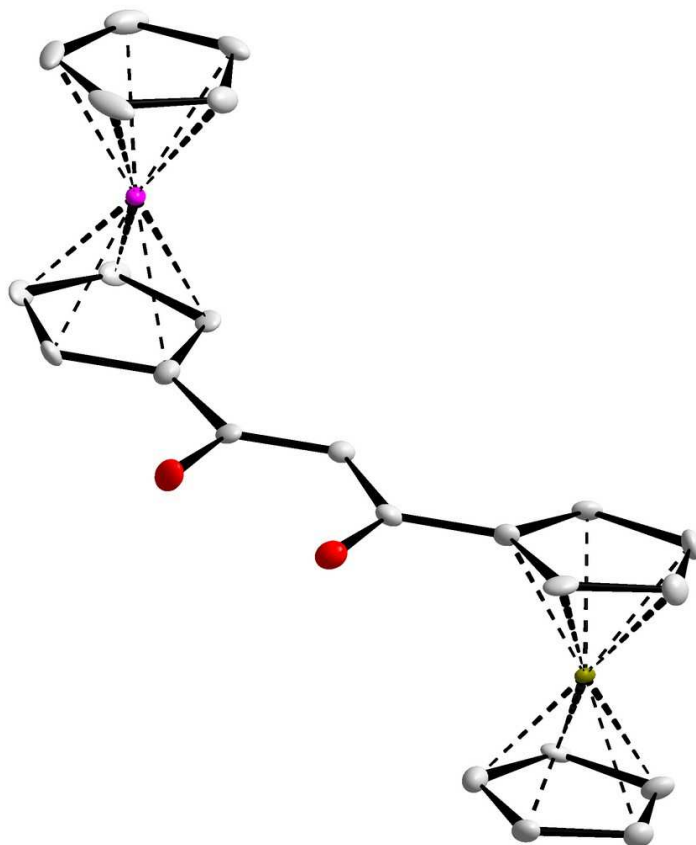
Figure 3.34. A perspective view of FcCOCH$_2$COOc (**7**). Hydrogen atoms are omitted for clarity.

3.4.2. Ruthenocenyldiphenylphosphine (65)

Mr. M.J. Janse van Rensburg, from the Department of Chemistry at the University of the Free State, is acknowledged for determining and solving the single crystal structure of PPh$_2$Rc (**65**).

A perspective view of (**65**) is shown in **Figure 3.35**, showing the numbering system for atoms in the molecule. Crystal data is summarized in **Table 3.25**, and bond lengths and angles are given in **Table 3.26**.
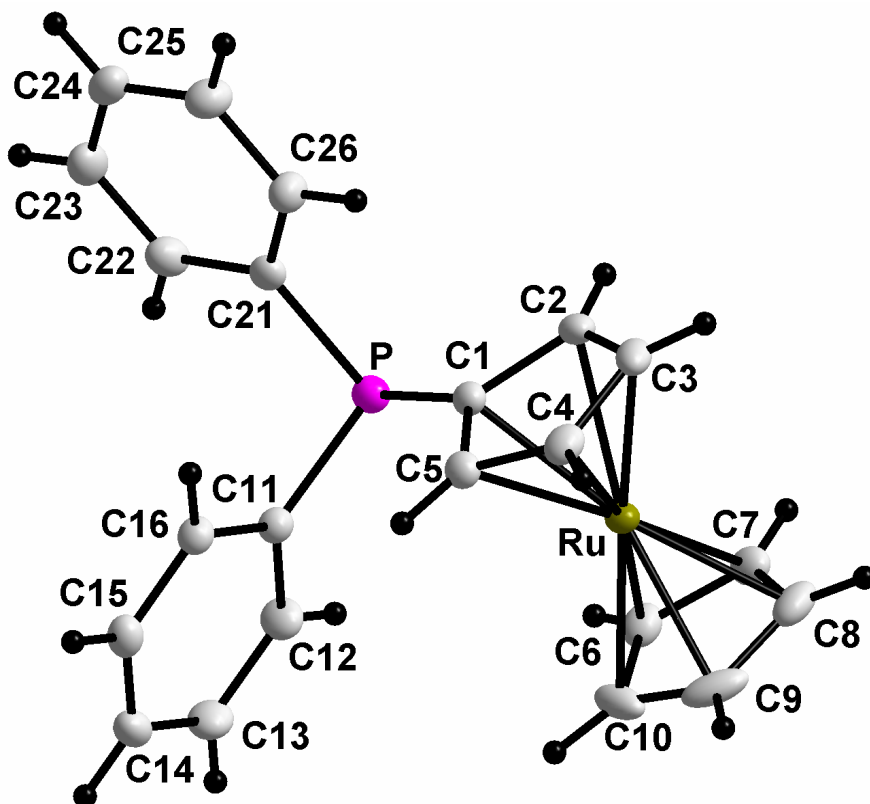
Figure 3.35. A perspective view of PPh₂Rc **(65)**, showing atom labeling.

The crystal structure of PPh$_2$Rc **(65)** shows that the P-atom has distorted tetrahedral geometry. C-P bond angles deviates with up to 12° from the expected 109°28' angle for a standard tetrahedron, with C(1)-P-C(11) 102.35°, C(1)-P-C(21) 102.46° and C(11)-P-C(21) 100.70°. The average bond distance of the two phenyl ring C atoms attached to the P atom is 1.834 Å, while the C(1)-P bond to the ruthenocene group is 1.812 Å. This indicates a stronger bond between the ruthenocene group and the P atom compared to bonds to the phenyl rings due to the better electron-donating abilities of the ruthenocene group {χ_R (Rc) = 1.99, χ_R (Ph) 2.21}. The same tendency was also observed in the crystal structure of PPh$_2$Fc **(13)**.[17]

The average C-C bond length in the phenyl rings is 1.384 Å, which is comparable to the normal value (1.394 Å) for the aromatic C-C bond.[18] The average bond angle in the phenyl rings is 120.3° as expected, with the exception of the C atom attached to the P atom, which is distorted as follows: C(26)-C(21)-C(22) = 118.3°, C(12)-C(11)-C(16) =

118.2°. The average bond distance in the aromatic cyclopentadienyl rings differs for the two ruthenocenyl rings, which was also observed for the crystal structure of PPh$_2$Fc **(13)**. The C-C bonds in the top ring (1.427 Å), attached to the P atom, is on average 0.021 Å longer than the C-C bonds in the unsubstituted cyclopentadienyl ring (1.406 Å). This can be ascribed to donation of electron density towards the P atom, which increases the P-C bond length but decreases the C-C bond lengths in the ring.

The cyclopentadienyl rings were found to be in an eclipsed conformation, with the two rings approximately parallel. The dihedral angle between the planes is 0.568°. The distance between the cyclopentadienyl rings was determined at 3.6269 Å, which is comparable to, and falls between the known values for ruthenocene alone (3.68 Å)[19] and for the similar bidentate ruthenocenyl compound, Rc(PPh$_2$)$_2$ (dppr) **(17)** (3.606 Å).[20]

Table 3.25. Crystal data and structure refinement for **(65)**.

Empirical formula	C$_{22}$H$_{19}$O$_0$PRu	Theta range for data collection	2.41 to 28.00°
Formula weight	415.41	Index ranges	-18<=h<=18, -13<=k<=13, -15<=l<=15
Temperature	293(2) K	Reflections collected	50798
Wavelength	0.71073 Å	Independent reflections	4221 [R(int) = 0.0360]
Crystal system	Monoclinic	Completeness to theta = 28.00°	100.0 %
Space group	P2(1)/c	Absorption correction	None
Unit cell dimensions	a = 14.2986(7) Å b = 10.4474(5) Å c = 11.6886(6) Å α = 90° β = 91.713(3)° γ = 90°	Max. and min. transmission	0.9251 and 0.7761
Volume	1745.30(15) Å^3	Refinement method	Full-matrix least-squares on F^2
Z	4	Data / restraints / parameters	4221 / 0 / 217
Density (calculated)	1.581 Mg/m^3	Goodness-of-fit on F^2	1.072
Absorption coefficient	0.989 mm^{-1}	Final R indices [I>2sigma(I)]	R1 = 0.0275, wR2 = 0.0710
F(000)	840	R indices (all data)	R1 = 0.0320, wR2 = 0.0741
Crystal size	0.27 x 0.12 x 0.08 mm^3	Largest diff. peak and hole	1.520 and -0.498 e.Å^{-3}

Table 3.26. Bond lengths (Å) and angles (°) for **(65)**, with standard deviation given in parentheses.

Atoms	Bond	Atoms	Bond	Atoms	Bond
C(1)-C(2)	1.438(3)	C(6)-H(6)	0.9300	C(13)-H(13)	0.9300
C(1)-C(5)	1.441(3)	C(7)-C(8)	1.397(4)	C(14)-C(15)	1.385(4)
C(1)-P	1.812(3)	C(7)-Ru	2.179(2)	C(14)-H(14)	0.9300
C(1)-Ru	2.173(2)	C(7)-H(7)	0.9300	C(15)-C(16)	1.382(3)
C(2)-C(3)	1.418(4)	C(8)-C(9)	1.398(5)	C(15)-H(15)	0.9300
C(2)-Ru	2.169(2)	C(8)-Ru	2.179(3)	C(16)-H(16)	0.9300
C(2)-H(2)	0.9300	C(8)-H(8)	0.9300	C(21)-C(26)	1.376(3)
C(3)-C(4)	1.417(4)	C(9)-C(10)	1.415(5)	C(21)-C(22)	1.391(3)
C(3)-Ru	2.189(2)	C(9)-Ru	2.175(3)	C(21)-P	1.836(2)
C(3)-H(3)	0.9300	C(9)-H(9)	0.9300	C(22)-C(23)	1.393(4)
C(4)-C(5)	1.421(3)	C(10)-Ru	2.172(3)	C(22)-H(22)	0.9300
C(4)-Ru	2.183(2)	C(10)-H(10)	0.9300	C(23)-C(24)	1.374(4)
C(4)-H(4)	0.9300	C(11)-C(12)	1.387(3)	C(23)-H(23)	0.9300
C(5)-Ru	2.177(2)	C(11)-C(16)	1.393(3)	C(24)-C(25)	1.365(4)
C(5)-H(5)	0.9300	C(11)-P	1.832(2)	C(24)-H(24)	0.9300
C(6)-C(7)	1.404(4)	C(12)-C(13)	1.391(4)	C(25)-C(26)	1.396(4)
C(6)-C(10)	1.417(4)	C(12)-H(12)	0.9300	C(25)-H(25)	0.9300
C(6)-Ru	2.178(2)	C(13)-C(14)	1.370(4)	C(26)-H(26)	0.9300

Atoms	Angle	Atoms	Angle	Atoms	Angle
C(2)-C(1)-C(5)	106.4(2)	C(8)-C(9)-C(10)	108.2(3)	C(1)-P-C(11)	102.35(10)
C(2)-C(1)-P	123.50(19)	C(8)-C(9)-Ru	71.43(15)	C(1)-P-C(21)	102.46(11)
C(5)-C(1)-P	130.05(18)	C(10)-C(9)-Ru	70.91(16)	C(11)-P-C(21)	100.70(10)
C(2)-C(1)-Ru	70.53(13)	C(8)-C(9)-H(9)	125.9	C(2)-Ru-C(10)	156.76(12)
C(5)-C(1)-Ru	70.81(13)	C(10)-C(9)-H(9)	125.9	C(2)-Ru-C(1)	38.68(9)
P-C(1)-Ru	121.80(12)	Ru-C(9)-H(9)	123.4	C(10)-Ru-C(1)	123.83(11)
C(3)-C(2)-C(1)	108.6(2)	C(9)-C(10)-C(6)	107.6(3)	C(2)-Ru-C(9)	163.77(13)
C(3)-C(2)-Ru	71.77(14)	C(9)-C(10)-Ru	71.10(15)	C(10)-Ru-C(9)	37.99(12)
C(1)-C(2)-Ru	70.79(13)	C(6)-C(10)-Ru	71.21(15)	C(1)-Ru-C(9)	156.32(12)
C(3)-C(2)-H(2)	125.7	C(9)-C(10)-H(10)	126.2	C(2)-Ru-C(5)	64.07(9)
C(1)-C(2)-H(2)	125.7	C(6)-C(10)-H(10)	126.2	C(10)-Ru-C(5)	112.90(10)
Ru-C(2)-H(2)	123.4	Ru-C(10)-H(10)	123.2	C(1)-Ru-C(5)	38.69(9)
C(4)-C(3)-C(2)	108.3(2)	C(12)-C(11)-C(16)	118.2(2)	C(9)-Ru-C(5)	123.95(11)
C(4)-C(3)-Ru	70.86(14)	C(12)-C(11)-P	118.07(18)	C(2)-Ru-C(6)	124.43(11)
C(2)-C(3)-Ru	70.26(14)	C(16)-C(11)-P	123.70(18)	C(10)-Ru-C(6)	38.02(11)
C(4)-C(3)-H(3)	125.8	C(11)-C(12)-C(13)	120.9(2)	C(1)-Ru-C(6)	112.71(9)
C(2)-C(3)-H(3)	125.8	C(11)-C(12)-H(12)	119.5	C(9)-Ru-C(6)	63.34(10)
Ru-C(3)-H(3)	124.6	C(13)-C(12)-H(12)	119.5	C(5)-Ru-C(6)	130.18(9)
C(3)-C(4)-C(5)	108.1(2)	C(14)-C(13)-C(12)	120.1(2)	C(2)-Ru-C(7)	113.55(10)
C(3)-C(4)-Ru	71.31(14)	C(14)-C(13)-H(13)	120.0	C(10)-Ru-C(7)	62.95(10)
C(5)-C(4)-Ru	70.74(13)	C(12)-C(13)-H(13)	120.0	C(1)-Ru-C(7)	130.02(10)
C(3)-C(4)-H(4)	125.9	C(13)-C(14)-C(15)	119.7(2)	C(9)-Ru-C(7)	62.60(11)
C(5)-C(4)-H(4)	125.9	C(13)-C(14)-H(14)	120.1	C(5)-Ru-C(7)	165.22(10)
Ru-C(4)-H(4)	123.6	C(15)-C(14)-H(14)	120.1	C(6)-Ru-C(7)	37.60(10)
C(4)-C(5)-C(1)	108.5(2)	C(16)-C(15)-C(14)	120.3(2)	C(2)-Ru-C(8)	129.60(11)
C(4)-C(5)-Ru	71.22(13)	C(16)-C(15)-H(15)	119.9	C(10)-Ru-C(8)	63.15(11)
C(1)-C(5)-Ru	70.50(13)	C(14)-C(15)-H(15)	119.9	C(1)-Ru-C(8)	164.52(11)
C(4)-C(5)-H(5)	125.7	C(15)-C(16)-C(11)	120.7(2)	C(9)-Ru-C(8)	37.46(13)
C(1)-C(5)-H(5)	125.7	C(15)-C(16)-H(16)	119.6	C(5)-Ru-C(8)	155.69(11)
Ru-C(5)-H(5)	124.1	C(11)-C(16)-H(16)	119.6	C(6)-Ru-C(8)	63.09(10)
C(7)-C(6)-C(10)	107.3(2)	C(26)-C(21)-C(22)	118.3(2)	C(7)-Ru-C(8)	37.40(11)
C(7)-C(6)-Ru	71.23(15)	C(26)-C(21)-P	123.52(19)	C(2)-Ru-C(4)	63.75(10)
C(10)-C(6)-Ru	70.77(14)	C(22)-C(21)-P	118.01(19)	C(10)-Ru-C(4)	129.51(10)
C(7)-C(6)-H(6)	126.4	C(21)-C(22)-C(23)	120.6(3)	C(1)-Ru-C(4)	64.45(9)
C(10)-C(6)-H(6)	126.4	C(21)-C(22)-H(22)	119.7	C(9)-Ru-C(4)	112.64(10)
Ru-C(6)-H(6)	123.3	C(23)-C(22)-H(22)	119.7	C(5)-Ru-C(4)	38.04(9)
C(8)-C(7)-C(6)	108.9(2)	C(24)-C(23)-C(22)	120.2(3)	C(6)-Ru-C(4)	164.71(10)
C(8)-C(7)-Ru	71.31(15)	C(24)-C(23)-H(23)	119.9	C(7)-Ru-C(4)	155.87(10)

Table 3.26 (continued). Bond lengths (Å) and angles (°) for **(65)**, with standard deviation given in parentheses.

C(6)-C(7)-Ru	71.17(14)	C(22)-C(23)-H(23)	119.9	C(8)-Ru-C(4)	123.77(10)
C(8)-C(7)-H(7)	125.5	C(25)-C(24)-C(23)	119.5(3)	C(2)-Ru-C(3)	37.97(11)
C(6)-C(7)-H(7)	125.5	C(25)-C(24)-H(24)	120.2	C(10)-Ru-C(3)	164.01(12)
Ru-C(7)-H(7)	123.6	C(23)-C(24)-H(24)	120.2	C(1)-Ru-C(3)	64.25(9)
C(7)-C (8)-C(9)	108.0(3)	C(24)-C(25)-C(26)	120.7(3)	C(9)-Ru-C(3)	129.28(11)
C(7)-C(8)-Ru	71.30(14)	C(24)-C(25)-H(25)	119.6	C(5)-Ru-C(3)	63.52(9)
C(9)-C(8)-Ru	71.11(17)	C(26)-C(25)-H(25)	119.6	C(6)-Ru-C(3)	156.43(11)
C(7)-C(8)-H(8)	126.0	C(21)-C(26)-C(25)	120.6(2)	C(7)-Ru-C(3)	124.58(10)
C(9)-C(8)-H(8)	126.0	C(21)-C(26)-H(26)	119.7	C(8)-Ru-C(3)	113.03(10)
Ru-C(8)-H(8)	123.3	C(25)-C(26)-H(26)	119.7	C(4)-Ru-C(3)	37.83(10)

3.4.3. [Rh(FcCOCHCOCF$_3$)(CO)(PPh$_2$Fc)] (70)

Dr. A.J. Muller, from the Department of Chemistry at the University of the Free State, is acknowledged for determining and solving the single crystal structure of [Rh(FcCOCHCOCF$_3$)(CO)(PPh$_2$Fc)] **(70)**.

A perspective view of **(70)** is shown in **Figure 3.36**, showing the numbering system for atoms in the molecule. Crystal data is summarized in **Table 3.27**, and bond lengths and angles are given in **Table 3.28**.
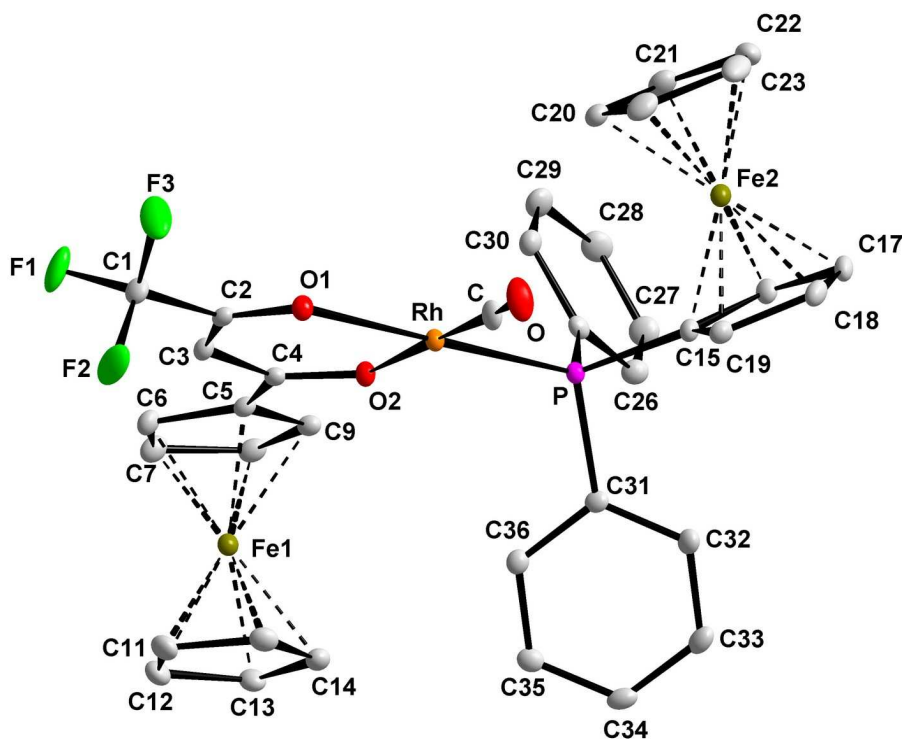
Figure 3.36. A perspective view of [Rh(FcCOCHCOCF$_3$)(CO)(PPh$_2$Fc)] **(70)**, showing atom labeling.

Coordination around the rhodium center was found to be planar, with ligand-rhodium-ligand bond angles deviating significantly from the expected 90° for a dsp^2 hybridized center: C-Rh-O(1) = 89.04(8) °, O(2)-Rh-O(1) = 89.25(6) °, C-Rh-P = 93.28(7) ° and O(2)-Rh-P = 88.49(4) °. The average C-C bond distance (1.386 Å) in the planar phenyl rings is in agreement with the normal value (1.394 Å) for the aromatic C-C bond.[18] Bond angles in the phenyl rings were found to be 120°, within experimental error (see **Table 3.28**). The phosphorus atom is surrounded by the rhodium atom and three carbon atoms of the phenyl rings and ferrocenyl group bound to it, displaying a distorted tetrahedral geometry. Bond angles around the phosphorus atom vary up to 22° from the normal 109°28' angle for a standard tetrahedron. The average distance between P and the two phenyl C atoms surrounding it is 1.826 Å, while the ferrocenyl C-P bond length is significantly shorter at 1.804 Å. This can be explained by the lower group electronegativity value of the ferrocenyl group (χ_R = 1.87) compared to that of the phenyl group (χ_R = 2.21). The ferrocenyl group is thus more electron-donating towards the P atom, compared to the phenyl-groups, leading to a shortening of the bond. This was also found to be the case for $[Rh(CH_3COCHCOCH_3)(CO)(PPh_2Fc)]$.[21] The Rh-P bond distance is 2.245 Å, which is comparable to that of similar compounds $[Rh(CH_3COCHCOCH_3)(CO)(PPh_3)]$ **(21)**,[22] $[Rh(FcCOCHCOCF_3)(CO)(PPh_3)]$ **(29)**[23] and $[Rh(CH_3COCHCOCH_3)(CO)(PPh_2Fc)]$.[21] The Rh-C-O bond angle is nearly linear, at 174°, but slightly more bent than similar compounds $[Rh(CH_3COCHCOCH_3)$ $(CO)(PPh_2Fc)]$[21] and $[Rh(FcCOCHCOCF_3)(CO)(PPh_3)]$ **(29)**,[23] with angles of 177.3° and 178.1°, respectively. The carbonyl bond distance is, however, comparable at 1.143 Å. The Rh-O bond nearest to the CF_3 group is 0.016 Å longer than the Rh-O bond nearest to the β-diketonato ferrocenyl group. The longer bond is thus *trans* to the phosphine ligand, clearly showing the large *trans* influence of the phosphine ligand compared to the carbonyl ligand. Large deviations in bond angles from the expected 120° for the sp^2 hybridized β-diketonato skeleton were observed. Angles deviated by 4° - 10°, with O(1)-C(2)-C(3) = 130.46°, C(2)-C(3)-C(4) = 124.6° and C(3)-C(4)-O(2) = 127.70°.
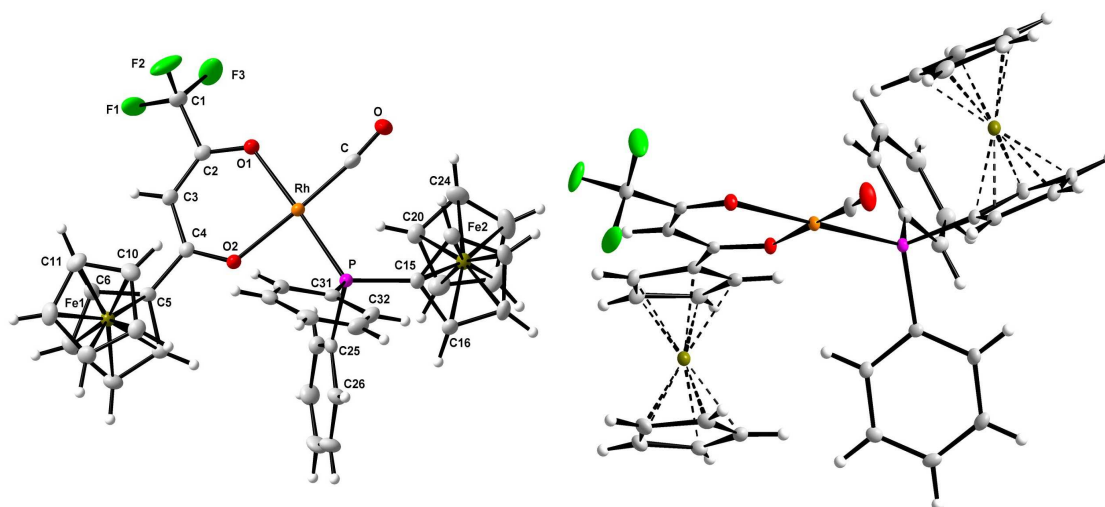
Figure 3.37. [Rh(FcCOCHCOCF₃)(CO)(PPh₂Fc)] **(70)**, showing eclipsed conformation of the cyclopentadienyl rings (left) and position of ferrocenyl-moieties with respect to each other (right).

The cyclopentadienyl rings of both ferrocenyl groups are in the eclipsed conformation, as shown in **Figure 3.37**. The distance between the cyclopentadienyl rings for the β-diketonato ferrocenyl group was determined at 3.306 Å, and 3.291 Å for the phosphine ferrocenyl group (3.32 Å in free ferrocene).[19] The larger distance for the β-diketonato ferrocenyl group indicates a higher electron density compared to that of the phosphine ferrocenyl group. This can be ascribed to delocalization over the conjugated β-diketonato rhodium ring system. It was found that the cyclopentadienyl rings of both ferrocenyl groups were slightly off-parallel, with the angle between planes for the β-diketonato ferrocenyl group at 2.20°, and 2.61° for the phosphine ferrocenyl group. The angle between the plane of the rhodium center and the β-diketonato ferrocenyl group is approximately 8.6°, while the two ferrocenyl groups are rotated 27.7°, with respect to each other, as shown in **Figure 3.37**.

Table 3.27. Crystal data and structure refinement for **(70)**.

Empirical formula	$C_{37}H_{29}F_3Fe_2O_3PRh$	Theta range for data collection	1.74 to 28.32°.
Formula weight	824.18	Index ranges	-11< = h < =13, -31< = k < =31, -18< = l < =18
Temperature	100(2) K	Reflections collected	65121
Wavelength	0.71073 Å	Independent reflections	7824 [R(int) = 0.0469]
Crystal system	Monoclinic	Completeness to theta = 28.32°	100.0 %
Space group	P 21/ n	Absorption correction	Semi-empirical from equivalents
Unit cell dimensions	a = 9.9416(2) Å b = 23.2737(5) Å c = 13.6632(3) Å α = 90° β = 96.0690(10)° γ = 90°	Max. and min. transmission	0.9001 and 0.7486
Volume	3143.64(12) Å^3	Refinement method	Full-matrix least-squares - F^2
Z	4	Data / restraints / parameters	7824 / 0 / 424
Density (calculated)	1.741 Mg/m^3	Goodness-of-fit on F^2	1.030
Absorption coefficient	1.537 mm^{-1}	Final R indices [I>2sigma(I)]	R1 = 0.0273, wR2 = 0.0581
F(000)	1656	R indices (all data)	R1 = 0.0392, wR2 = 0.0629
Crystal size	0.20 x 0.09 x 0.07 mm^3	Largest diff. peak and hole	0.574 and -0.368 e.Å^{-3}

Table 3.28. Bond lengths (Å) and angles (°) for **(70)**, with standard deviation given in parentheses.

Atoms	Bond	Atoms	Bond	Atoms	Bond
Rh-C	1.811(2)	C(9)-H(9)	0.9500	C(22)-H(22)	0.9500
Rh-O(2)	2.0565(14)	C(10)-C(14)	1.417(3)	C(23)-C(24)	1.424(4)
Rh-O(1)	2.0725(14)	C(10)-C(11)	1.422(3)	C(23)-H(23)	0.9500
Rh-P	2.2451(5)	C(10)-H(10)	0.9500	C(24)-H(24)	0.9500
P-C(15)	1.804(2)	C(11)-C(12)	1.421(3)	C(25)-C(30)	1.393(3)
P-C(31)	1.825(2)	C(11)-H(11)	0.9500	C(25)-C(26)	1.395(3)
P-C(25)	1.826(2)	C(12)-C(13)	1.415(3)	C(26)-C(27)	1.380(3)
C-O	1.143(3)	C(12)-H(12)	0.9500	C(26)-H(26)	0.9500
O(1)-C(2)	1.271(2)	C(13)- C(14)	1.416(3)	C(27)-C(28)	1.380(3)
O(2)-C(4)	1.273(2)	C(13)-H(13)	0.9500	C(27)-H(27)	0.9500
F(1)-C(1)	1.326(3)	C(14)-H(14)	0.9500	C(28)-C(29)	1.382(3)
F(2)-C(1)	1.335 (3)	C(15)-C(19)	1.435(3)	C(28)-H(28)	0.9500
F(3)-C(1)	1.312(3)	C(15)-C(16)	1.436(3)	C(29)-C(30)	1.388(3)
C(1)-C(2)	1.533(3)	C(16)-C(17)	1.418(3)	C(29)-H(29)	0.9500
C(2)-C(3)	1.369(3)	C(16)-H(16)	0.9500	C(30)-H(30)	0.9500
C(3)-C(4)	1.417(3)	C(17)-C(18)	1.409(3)	C(31)-C(32)	1.392(3)
C(3)-H(3)	0.9500	C(17)-H(17)	0.9500	C(31)-C(36)	1.393(3)
C(4)-C(5)	1.459(3)	C(18)-C(19)	1.422(3)	C(32)-C(33)	1.389(3)
C(5)-C(9)	1.435(3)	C(18)-H(18)	0.9500	C(32)-H(32)	0.9500
C(5)-C(6)	1.436(3)	C(19)-H(19)	0.9500	C(33)-C(34)	1.378(3)
C(6)-C(7)	1.415(3)	C(20)-C(21)	1.417(3)	C(33)-H(33)	0.9500
C(6)-H(6)	0.9500	C(20)-C(24)	1.418(3)	C(34)-C(35)	1.381(3)
C(7)-C(8)	1.420(3)	C(20)-H(20)	0.9500	C(34)-H(34)	0.9500
C(7)-H(7)	0.9500	C(21)-C(22)	1.412(4)	C(35)-C(36)	1.385(3)
C(8)-C(9)	1.413(3)	C(21)-H(21)	0.9500	C(35)-H(35)	0.9500
C(8)-H(8)	0.9500	C(22)-C(23)	1.405(4)	C(36)-H(36)	0.9500
Atoms	**Angle**	**Atoms**	**Angle**	**Atoms**	**Angle**
C-Rh-O(2)	176.92(8)	C(8)-C(9)-C(5)	107.69(19)	C(22)-C(23)-C(24)	108.0(2)
C-Rh-O(1)	89.04(8)	C(8)-C(9)-H(9)	126.2	C(22)-C(23)-H(23)	126.0
O(2)-Rh-O(1)	89.25(6)	C(5)-C(9)-H(9)	126.2	C(24)-C(23)-H(23)	126.0
C-Rh-P	93.28(7)	C(14)-C(10)-C(11)	107.9(2)	C(20)-C(24)-C(23)	107.7(2)
O(2)-Rh-P	88.49(4)	C(14)-C(10)-H(10)	126.1	C(20)-C(24)-H(24)	126.2
O(1)-Rh-P	177.36(4)	C(11)-C(10)-H(10)	126.1	C(23)-C(24)-H(24)	126.2

119

Table 3.28 (continued). Bond lengths (Å) and angles (°) for **(70)**, with standard deviation given in parentheses.

C(15)-P-C(31)	102.67(10)	C(12)-C(11)-C(10)	107.7(2)	C(30)-C(25)-C(26)	118.7(2)
C(15)-P-C(25)	101.20(10)	C(12)-C(11)-H(11)	126.1	C(30)-C(25)-P	119.77(16)
C(31)-P-C(25)	103.53(9)	C(10)-C(11)-H(11)	126.1	C(26)-C(25)-P	121.34(16)
C(15)-P-Rh	122.27(7)	C(13)-C(12)-C(11)	108.2(2)	C(27)-C(26)-C(25)	120.5(2)
C(31)-P-Rh	112.82(7)	C(13)-C(12)-H(12)	125.9	C(27)-C(26)-H(26)	119.8
C(25)-P-Rh	112.19(7)	C(11)-C(12)-H(12)	125.9	C(25)-C(26)-H(26)	119.8
O-C-Rh	174.0(2)	C(12)-C(13)-C(14)	108.0(2)	C(28)-C(27)-C(26)	120.3(2)
C(2)-O(1)-Rh	123.25(13)	C(12)-C(13)-H(13)	126.0	C(28)-C(27)-H(27)	119.8
C(4)-O(2)-Rh	127.70(13)	C(14)-C(13)-H(13)	126.0	C(26)-C(27)-H(27)	119.8
F(3)-C(1)-F(1)	107.29(19)	C(13)-C(14)-C(10)	108.3(2)	C(27)-C(28)-C(29)	119.9(2)
F(3)-C(1)-F(2)	106.8(2)	C(13)-C(14)-H(14)	125.9	C(27)-C(28)-H(28)	120.0
F(1)-C(1)-F(2)	105.66(19)	C(10)-C(14)-H(14)	125.9	C(29)-C(28)-H(28)	120.0
F(3)-C(1)-C(2)	112.17(18)	C(19)-C(15)-C(16)	107.21(18)	C(28)-C(29)-C(30)	120.0(2)
F(1)-C(1)-C(2)	113.89(18)	C(19)-C(15)-P	126.96(16)	C(28)-C(29)-H(29)	120.0
F(2)-C(1)-C(2)	110.56(18)	C(16)-C(15)-P	125.79(16)	C(30)-C(29)-H(29)	120.0
O(1)-C(2)-C(3)	130.46(19)	C(17)-C(16)-C(15)	107.9(2)	C(29)-C(30)-C(25)	120.5(2)
O(1)-C(2)-C(1)	111.71(18)	C(17)-C(16)-H(16)	126.0	C(29)-C(30)-H(30)	119.8
C(3)-C(2)-C(1)	117.75(19)	C(15)-C(16)-H(16)	126.0	C(25)-C(30)-H(30)	119.8
C(2)-C(3)-C(4)	124.6(2)	C(18)-C(17)-C(16)	108.52(19)	C(32)-C(31)-C(36)	119.02(19)
C(2)-C(3)-H(3)	117.7	C(18)-C(17)-H(17)	125.7	C(32)-C(31)-P	122.38(16)
C(4)-C(3)-H(3)	117.7	C(16)-C(17)-H(17)	125.7	C(36)-C(31)-P	118.60(16)
O(2)-C(4)-C(3)	124.53(19)	C(17)-C(18)-C(19)	108.52(19)	C(33)-C(32)-C(31)	120.2(2)
O(2)-C(4)-C(5)	116.40(18)	C(17)-C(18)-H(18)	125.7	C(33)-C(32)-H(32)	119.9
C(3)-C(4)-C(5)	119.02(18)	C(19)-C(18)-H(18)	125.7	C(31)-C(32)-H(32)	119.9
C(9)-C(5)-C(6)	107.38(18)	C(18)-C(19)-C(15)	107.80(19)	C(34)-C(33)-C(32)	120.1(2)
C(9)-C(5)-C(4)	124.68(19)	C(18)-C(19)-H(19)	126.1	C(34)-C(33)-H(33)	119.9
C(6)-C(5)-C(4)	127.93(19)	C(15)-C(19)-H(19)	126.1	C(32)-C(33)-H(33)	119.9
C(7)-C(6)-C(5)	108.08(19)	C(21)-C(20)-C(24)	107.9(2)	C(33)-C(34)-C(35)	120.3(2)
C(7)-C(6)-H(6)	126.0	C(21)-C(20)-H(20)	126.1	C(33)-C(34)-H(34)	119.9
C(5)-C(6)-H(6)	126.0	C(24)-C(20)-H(20)	126.1	C(35)-C(34)-H(34)	119.9
C(6)-C(7)-C(8)	108.0(2)	C(22)-C(21)-C(20)	108.0(2)	C(34)-C(35)-C(36)	119.9(2)
C(6)-C(7)-H(7)	126.0	C(22)-C(21)-H(21)	126.0	C(34)-C(35)-H(35)	120.0
C(8)-C(7)-H(7)	126.0	C(20)-C(21)-H(21)	126.0	C(36)-C(35)-H(35)	120.0
C(9)-C(8)-C(7)	108.86(19)	C(23)-C(22)-C(21)	108.4(2)	C(35)-C(36)-C(31)	120.5(2)
C(9)-C(8)-H(8)	125.6	C(23)-C(22)-H(22)	125.8	C(35)-C(36)-H(36)	119.7
C(7)-C(8)-H(8)	125.6	C(21)-C(22)-H(22)	125.8	C(31)-C(36)-H(36)	119.7

3.5.   Electrochemistry

3.5.1. Introduction

Cyclic voltammetry (CV), Oster Young square wave voltammetry (SW) and linear sweep voltammetry (LSV) were performed on all synthesized compounds (see **Goal 5** – **Chapter 1**). The discussion below is organized as follows:

a) Firstly, the electrochemistry of ferrocene (Fc), ruthenocene (Rc), osmocene (Oc) and cobaltocenium hexafluorophosphate ($Cc^+PF_6^-$) will be discussed.

b) Secondly, the electrochemistry of the phosphines $PPh_2((C_5H_4)M(C_5H_5))$ (where $M = Fe^{2+}$ (PPh_2Fc) (**13**), Co^{3+} ($PPh_2Cc^+PF_6^-$) (**67**), Os^{2+} (PPh_2Oc) (**66**) and Ru^{2+} (PPh_2Rc) (**65**)) will be presented.

c) Thirdly, the electrochemistry of rhodium complexes of the type $[Rh(FcCOCHCOR)(CO)_2]$ or $[Rh FcCOCHCOCF_3)(CO)(PPh_2Mc)]$, where R = CF_3 (**57**), Fc (**60**), Oc (**69**), Rc (**68**), and Mc = ferrocenyl (**70**) or ruthenocenyl (**71**), will be discussed. Rhodium complexes containing fluorinated phosphine ligands of the type $[Rh(FcCOCHCOCF_3)(CO)(PPh_n(C_6F_5)_{3-n})]$ (where n = 2 (**72**), 1 (**73**), 0 (**74**)), will also be discussed.

d) The electrochemistry of tetrathiafulvalene derivatives will be presented.

e) The electrochemistry of the free β-diketones ($FcCOCH_2COR$), with R as above, has been studied previously, see **Chapter 2** (**Section 2.7.3**) for a summary. However, the keto-enol isomerization kinetics of $FcCOCH_2CORc$ (**6**) has for the first time been studied electrochemically, and will be presented as the final groundbreaking result of this study.

Although electrochemically reversible one-electron redox couples are theoretically characterized by $\Delta E_p = E_{pa} - E_{pc} = 59$ mV, in this study an *experimentally* determined value of $\Delta E_p < 90$ mV will be considered small enough to imply electrochemical reversibility.[16] Quasi-reversible processes will be assigned to any process showing 90 mV $< \Delta E_p < 150$ mV, while irreversible electrochemistry will be assigned to a process showing $\Delta E_p > 150$ mV.

Peak current ratios were always calculated as $i_{p \text{ (reverse sweep)}} / i_{p \text{ (forward sweep)}}$. Formal redox potentials ($E^{o'}$), anodic peak potential (E_{pa}) and cathodic peak potentials (E_{pc}) are reported *vs* Fc/Fc$^+$ as internal standard, but were measured experimentally *vs* an in-house constructed Ag/Ag$^+$ reference electrode. Since the ferrocene wave often overlapped with signals of the compounds studied, the internal standard decamethyl ferrocene (Fc*), was employed. $E^{o'}$(Fc*/Fc^{*+}) was found to be -607 mV *vs* ferrocene, under conditions of this study. The ferrocene / ferrocenium couple, under identical conditions but in the absence of any other compounds, had $\Delta E_p = 75$ mV at 25 °C and i_{pa}/i_{pc} 0.97-1.00 at scan rates *v* =

$100 - 500$ mV s^{-1}, and E$^{o'}$ = 0.197 V vs a Ag/Ag$^+$ reference electrode in CH$_2$Cl$_2$. In this study CH$_2$Cl$_2$ and the highly non-interacting [N^{n}Bu$_4$][B(C$_6$F$_5$)$_4$] was used as solvent and supporting electrolyte system in order to limit solvent or electrolyte interaction to a minimum, either by means of solvation or ion-paring interactions.

3.5.2. Electrochemistry of Metallocenes

In order to fully understand the electrochemistry of the metallocene phosphines, and other metallocene derivatives studied during this research program, it is firstly necessary to understand the electrochemistry of the free metallocenes themselves. **Figure 3.38** (top) shows the CV of pure ruthenocene (Rc), while the CV of a solution containing simultaneously cobaltocenium hexafluorophosphate (Cc$^+$PF$_6^-$), decamethyl ferrocene (Fc*), ferrocene (Fc), osmocene (Oc) and ruthenocene (Rc) is shown at the bottom.

Decamethyl ferrocene, ferrocene and osmocene showed electrochemical reversible one-electron oxidation / reduction processes, with ΔE_p < 90 mV at a scan rate of 100 mV s^{-1} (**Table 3.29**). The reaction involved for these systems is shown in **Scheme 3.29**. Current ratios were not always 1, but this is regarded as a consequence of electrode pollution during the course of CV. To prove this, a separate CV (not shown) of each of these components in its own solution was also recorded. Peak current ratios were then found to be always better than 0.98; theoretically they should be 1.

The cobaltocenium group showed two reversible one-electron transfer waves. One is associated with the reduction of Co^{3+} to Co^{2+} at -1.3 V, the second with the reduction from Co^{2+} to Co^{1+} at -2.4 V. The complete electron transfer reaction sequence for this metallocene is shown in **Scheme 3.29**. The formation of [Co^I(C$_5$H$_5$)$_2$]$^-$ at -2.4 V occurs at the lower limit of the potential window of CH$_2$Cl$_2$ as solvent when the solution contains the mixture of all metallocenes studied, but when the Cc$^+$PF$_6^-$ and the internal standard Fc* are the only metallocenes in solution, the [Co^I(C$_5$H$_5$)$_2$]$^-$ / [Co^{II}(C$_5$H$_5$)$_2$]^0-couple is observed at significantly more positive potentials, as shown in **Figure 3.38**. Previous studies have proved that this redox couple clearly involves the Co^I centre.[24, 25] Peak current ratios and potentials for the cobaltocene couples can be found in **Table 3.29**.
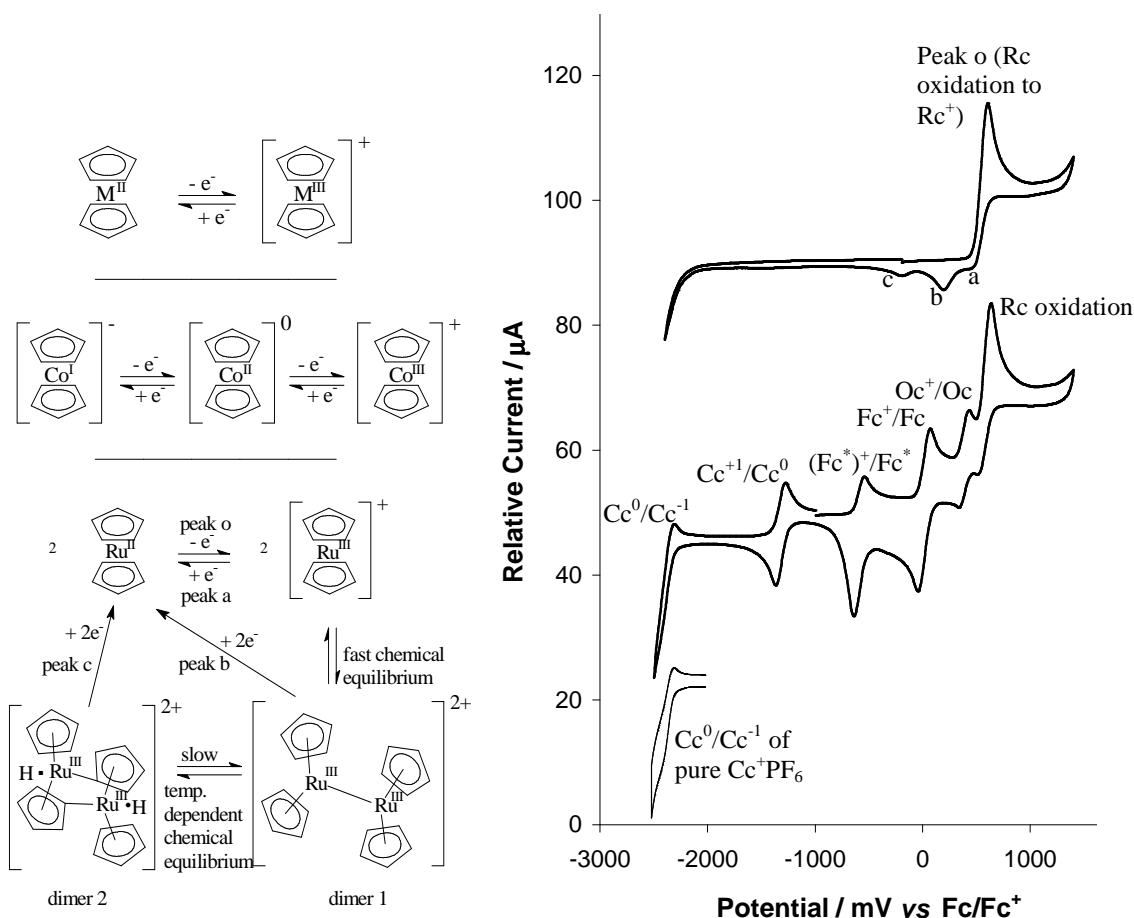
Scheme 3.29. (left) and **Figure 3.38** (right) (Note: It is an electrochemical convention to write electrochemical reactions as reduction reactions, but the above reactions are written as oxidation reactions to have the same sequence of events as the CV's in **Figure 3.38**, above right.) Top left: The reversible electron transfer reaction of metallocenes where M = Fe or Os. When M = Fe, the cyclopentadienyl ring can be either $(C_5H_5)^-$ or $(C_5Me_5)^-$. Middle left. Electron transfer reactions of cobaltocenium hexafluorophosphate. Bottom left. Electron transfer reactions associated with ruthenocene and its dimers. Right: CV's of ruthenocene (Rc) and a mixture of cobaltocenium hexafluorophosphate (Cc^+), decamethyl ferrocene (Fc^*), ferrocene (Fc), osmocene (Oc), and ruthenocene (Rc) in $CH_2Cl_2/0.1$ mol dm^{-3} $[N(^nBu_4)][B(C_6F_5)_4]$, T = 25°C, υ = 100 mV s^{-1}.

Ruthenocene electrochemistry is much more complicated. The CV, in **Figure 3.38** (top), shows an irreversible single one-electron oxidation of the ruthenium center to ruthenocenium, Rc^+, at peak o. The three reduction peaks that are observed were previously shown to be (a) the reduction of Rc^+ to Rc (peak a) and (b), the reduction of two types of dimers at peaks b and c, as shown in **Scheme 3.29** and **Figure 3.38**. The equilibrium processes involved between the Rc^+ monomer and both types of $(Rc_2)^{2+}$ dimers are very much temperature, solvent and electrolyte dependent. Dimer 1 (**Scheme 3.29**) dominates at lower temperatures (-40°C), and dimer 2 dominates at higher

123

temperatures (25°C). Reduction of the Rc^+ monomer at peak a was under the present experimental conditions poorly observed. None of the redox processes of the ruthenocene dimers are electrochemically reversible as the dimers have no oxidation peaks (it forms ruthenocene on reduction) and the peak current ratios of the Rc^+/Rc couple are never 1. Previous studies have also shown that ΔE_p for the Rc^+/Rc couple is > 100 mV when experimental conditions allow enhanced observation of peak a.

Table 3.29. Electrochemical data obtained for ruthenocene alone, as well as all metallocenes in $CH_2Cl_2/0.1$ mol dm^{-3} [N^nBu_4][$B(C_6F_5)$], at T = 25°C, potentials $vs.$ Fc/Fc^+.

| υ/mVs⁻¹	E_{pa}/mV	ΔE_p/mV	$E^{o'}$/mV	i_{pa}/μA	i_{pc}/i_{pa}	υ/mVs⁻¹	E_{pa}/mV	ΔE_p/mV	$E^{o'}$/mV	i_{pa}/μA	i_{pc}/i_{pa}
Rc – peak o / a						Rc – peak b					
100	603	155	523	2.47	-	100	194[a]	-	-	0.31[b]	-
200	627	165	545	3.43	-	200	139[a]	-	-	0.51[b]	-
300	642	177	554	3.97	-	300	104[a]	-	-	1.03[b]	-
400	648	180	558	4.39	-	400	102[a]	-	-	1.23[b]	-
500	665	195	568	4.89	-	500	83[a]	-	-	1.47[b]	-
Rc – peak c											
100	-197[a]	-	-	0.11[b]	-						
200	-250[a]	-	-	0.23[b]	-						
300	-273[a]	-	-	0.33[b]	-						
400	-278[a]	-	-	0.34[b]	-						
500	-292[a]	-	-	0.36[b]	-						
All metallocenes - Rc						All metallocenes - Oc					
100	629	-	-	1.80	-	100	428	87	385	0.74	0.78
200	647	-	-	2.62	-	200	435	99	386	1.02	0.78
300	651	-	-	3.24	-	300	440	108	386	1.33	0.64
400	677	-	-	3.80	-	400	449	121	389	1.60	0.61
500	689	-	-	4.05	-	500	454	131	389	1.74	0.61
All metallocenes - Fc						All metallocenes – Fc*					
100	54	100	0	1.06	0.99	100	-550	88	-594[d]	0.59	1.19
200	60	115	0	1.61	1.04	200	-549	91	-595[d]	0.78	1.29
300	74	146	2	2.13	1.04	300	-547	95	-595[d]	1.18	1.72
400	88	168	1	2.06	1.02	400	-535	109	-590[d]	1.43	1.98
500	100	196	3	2.72	1.30	500	-526	126	-589[d]	1.55	2.05
All metallocenes – Cc (Cc^{+1}/Cc^0)						All metallocenes – Cc (Cc^0/Cc^{-1})					
100	-1366[a]	87	-1323	0.80[b]	0.89[c]	100	-2432[a]	123	-2371	0.45[b]	0.51
200	-1370[a]	93	-1324	1.35[b]	0.89[c]	200	-2439[a]	133	-2373	0.74[b]	0.47
300	-1388[a]	123	-1327	1.73[b]	0.94[c]	300	-2453[a]	153	-2377	1.08[b]	0.47
400	-1391[a]	138	-1322	2.08[b]	0.94[c]	400	-2463[a]	169	-2379	1.59[b]	0.38
500	-1399[a]	147	-1326	2.28[b]	0.93[c]	500	-2475[a]	194	-2377	1.88[b]	0.34

(a) E_{pc}, (b) i_{pc}, (c) i_{pa}/i_{pc}, (d) -607 V in absence of other metallocenes.

3.5.3. Metallocene-containing Phosphines

In accordance with previous studies[26, 27, 28] on the electrochemistry of ferrocenyl diphenylphosphine **(13)**, CV's shown in **Figure 3.39** and associated reactions

summarized in **Scheme 3.30** show an oxidation wave for the Fe center at 0.117 V (peak 1 at 100 mV s^{-1}), followed by an irreversible oxidation wave at 1.128 V (peak 3) due to oxidation at the phosphorus center. Electrochemical data is summarized in **Table 3.30**. Since oxidation at the phosphorus atom is electrochemically irreversible, upon reduction, the ferrocene center is adjacent to an electron withdrawing, positively charged phosphorus group, causing the reduction peak of ferrocene to move to a higher potential at 0.4 V (peak 2). Due to the unstable nature of the oxidized phosphine group, it undergoes further chemical decomposition reactions at peak 4 (1.441 V), and shows no electrochemical reversibility. At slower scan rates the first oxidation wave (wave 1) becomes electrochemically reversible, with $\Delta E_p < 90$ mV. This can be attributed to the diffusion of yet unoxidised phosphine molecules from the bulk of the solution to the electrode surface (*i.e.* which have not undergone further electrochemical processes) and thus giving an electrochemically reversible ferrocenyl oxidation wave, but not chemically reversible, with i_{pc}/i_{pa} less than 1/2. If the scan is reversed prior to the oxidation reaction associated with peak 3, the redox couple associated with peak 1 becomes fully electrochemically and chemically reversible, with $E^{o'} = 78$ $\Delta E_p < 90$ mV and i_{pc}/i_{pa} larger than 0.98. When no phosphorus oxidation occurs, no further chemical decomposition reactions can occur, and the electron transfer reactions become simplified to the first step of **Scheme 3.30**. Incorporation of the ferrocenyl group as part of the phosphine ligand caused the formal reduction potential of this metallocene to be observed at a potential of 78 mV more positive than the free metallocene. Our present understanding of the electrochemical processes of PPh$_2$Fc **(13)** does not allow a clear explanation of this increase in potential. One would have expected a lowering in formal reduction potential because of the electron-donating free electron-pair on the phosphorus atom.
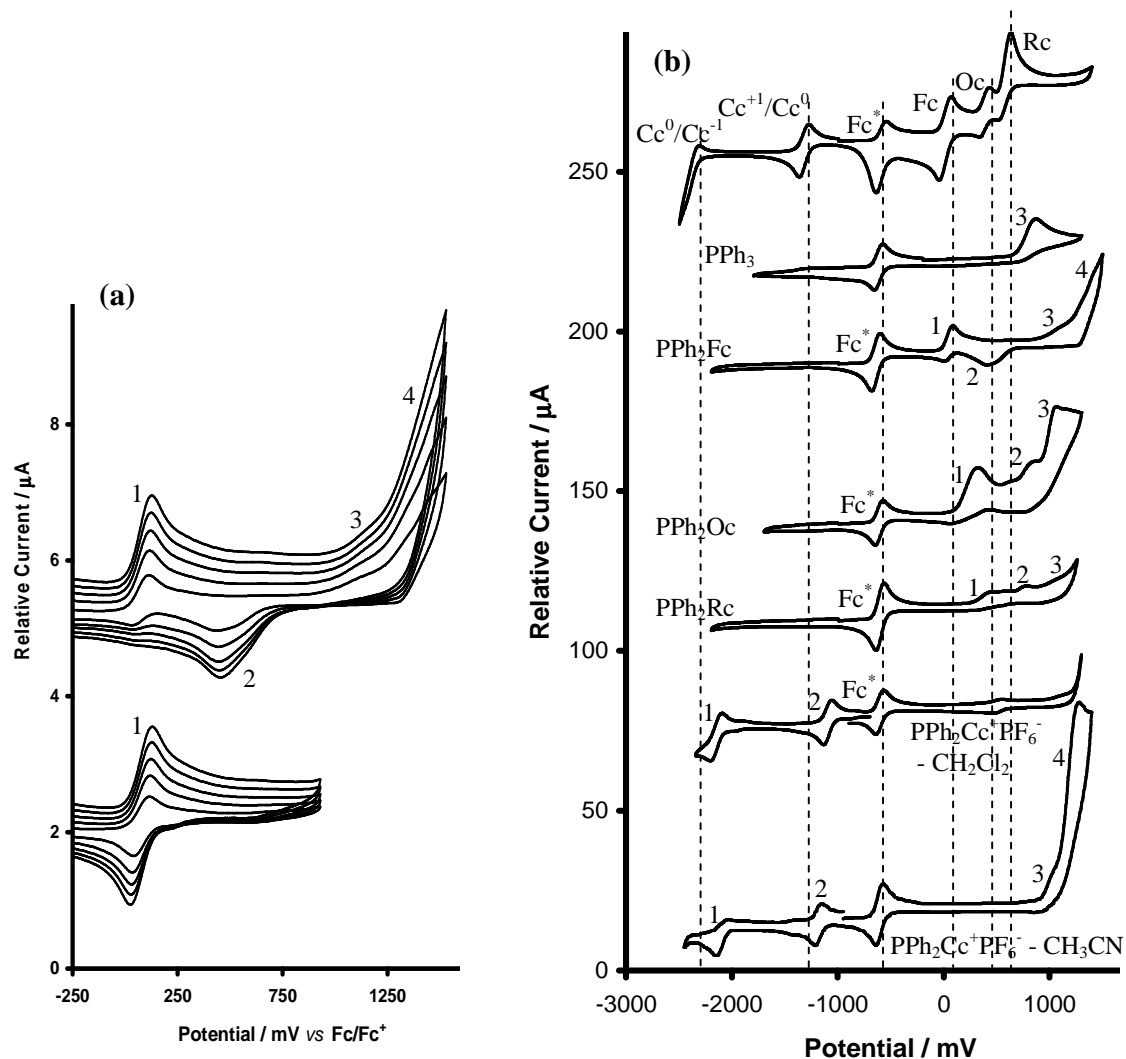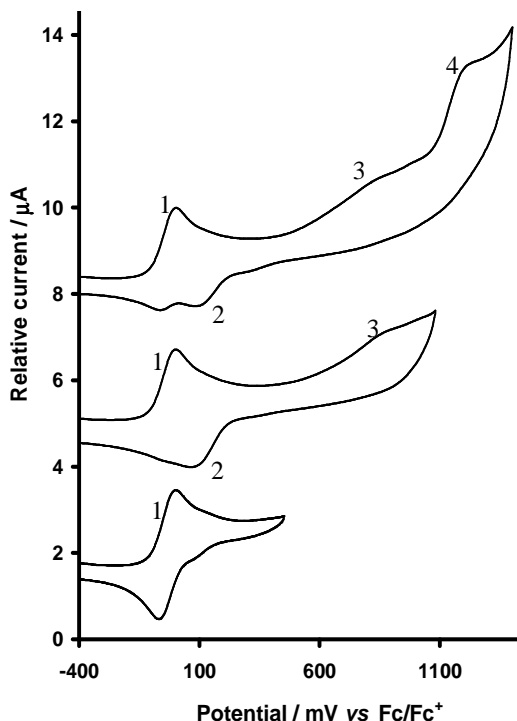
Figure 3.39. **(a)** CV's of ferrocenyl diphenylphosphine, over a wide range (top), as well as when the scan was reversed prior to peak 3 (bottom), in CH_2Cl_2/0.1 mol dm^{-3} [N($^{n}Bu_4$)][B(C_6F_5)$_4$], T = 25°C on a glassy carbon working electrode at scan rates of 100, 200, 300, 400 and 500 mV s^{-1}. **(b)** CV's of all metallocenes (top), and metallocene phosphines in CH_2Cl_2/0.1 mol dm^{-3} [NBu$_4$][B(C_6F_5)], T = 25°C, υ = 100 mV s^{-1}.
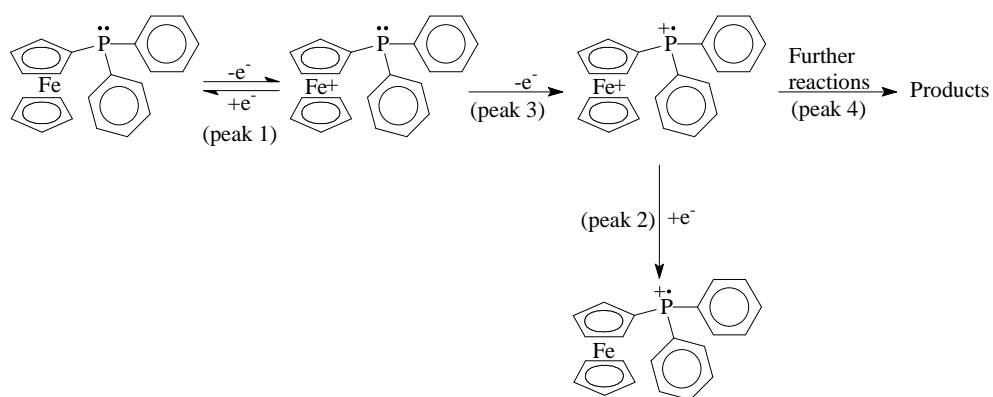
Scheme 3.30. The electron transfer reactions associated with ferrocenyldiphenylphosphine **(13)**.

126

The electrochemistry of this compound was also studied in CH_3CN and $[N(^nBu_4)][PF_6]$ as solvent and supporting electrolyte system, because CH_3CN offers an increased potential window for electrochemical studies. Peaks 3 and 4 were more clearly identified, as shown in **Figure 3.40**. The same main features as in the case of CH_2Cl_2 as solvent was observed however, *i.e.* an oxidation wave for the Fe centre at 0.006 V (peak 1, at 100 mV s^{-1}), followed by an irreversible oxidation wave at 0.852 V (peak 3) due to phosphorus oxidation, as well as an oxidation wave at 1.230 V due to further chemical decomposition reactions (peak 4). Peak 1 showed some electrochemical reversibility at slow scan rates, with $\Delta E_p < 90$ mV, due to diffusion from the bulk of the solution. The reduction wave of the Fe center was observed at a higher potential of 0.089 V (rather than the expected -0.0611 V) due to the adjacent positively charged phosphorus group, after oxidation at peak 3. Reversing the scan before peak 4 indicates that peak 4 does influence the reduction reaction of peak 2 only slightly, and consistent with the electron-transfer reactions shown in **Scheme 3.30**. Peak 1 becomes electrochemically and chemically reversible, when reversing the scan before peak 3, with $E^{o'} = -28$ $\Delta E_p < 90$ mV, and i_{pc}/i_{pa} larger than 0.98, confirming peak 3 as the oxidation peak of the phosphorus group.


Figure 3.40. CV's of ferrocenyl diphenylphosphine **(13)** over a wide range (top), reversed prior to peak 4 (middle), and reversed prior to peak 3 (bottom), in CH_3CN/0.1 mol dm^{-3} $[N(^nBu_4)][PF_6]$, T = 25°C on a glassy carbon working electrode at a scan rate of 100 mV s^{-1}.

The electrochemistry of $PPh_2Cc^+PF_6^-$ (**67**), in $CH_2Cl_2/[N(^nBu_4)][B(C_6F_5)_4]$ showed two reversible one-electron transfer waves, similar to that of the pure metallocene, as shown in **Figure 3.41**. Peak 1, being the reduction from Co^{2+} to Co^{1+} at -2.176 V at 100 mV s^{-1}, showed only quasi-reversible character, with $\Delta E_p \geq 120$ mV (**Table 3.30**) and i_{pa}/i_{pc} less than 1, due to a limiting solvent window. The second peak is much more clearly defined as the electrochemically reversible reduction of Co^{3+} to Co^{2+} at -1.105 V, with $\Delta E_p \leq 90$ mV and i_{pa}/i_{pc} approaching 1 at faster scan rates. The phosphorus oxidation falls outside of the potential window of CH_2Cl_2 as solvent. For this reason, the electrochemistry of $PPh_2Cc^+PF_6^-$ (**67**) was also studied in CH_3CN / $[N(^nBu_4)][PF_6]$ as solvent and supporting electrolyte system, enabling us to observe the phosphorus oxidation at the solvent potential limit, **Figure 3.41**. In CH_3CN, peak 1 and 2 exhibit similar results, $\Delta E_p = 0.097$ V and i_{pa}/i_{pc} values to that in CH_2Cl_2. Peak 3 and 4 is clearly visible, with peak 3, at 1 V, being a shoulder peak on peak 4, at 1.194 V at 100 mV s^{-1}. This can be interpreted in the same way as peak 3 and 4 of PPh_2Fc (**13**), with peak 3 being the one-electron oxidation reaction of the phosphorus group, and peak 4 due to further chemical decomposition reactions, **Scheme 3.31**.
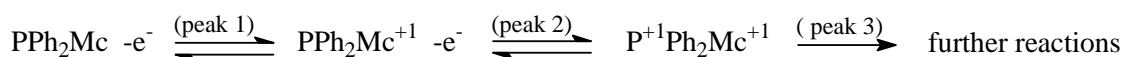
$$PPh_2Cc^{-1} \xrightarrow[\text{(peak 1)}]{-e^-} PPh_2Cc^0 \xrightarrow[\text{(peak 2)}]{-e^-} PPh_2Cc^{+1} \xrightarrow[\text{(peak 3)}]{-e^-} P^{+1}Ph_2Cc^{+1} \xrightarrow{\text{(peak 4)}} \text{further reactions}$$
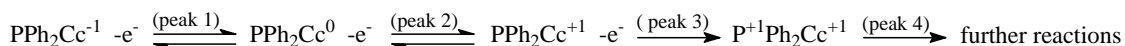
Scheme 3.31. The electron transfer reactions associated with $PPh_2Cc^+PF_6^-$ (**67**).

The LSV indicates the number of electrons transferred for peak 1, 2 and 3 to be equal, which correlates with a one-electron phosphorus oxidation, and the metal center undergoing two stepwise one-electron reductions in the same molecule. The Cc^{-1}/Cc^0 couple of $PPh_2Cc^+PF_6^-$ (**67**) in CH_3CN and CH_2Cl_2 was at -2.161 and -2.176 V *vs*. Fc/Fc^+ respectively at 100 mV s^{-1} scan rate. This is very close (within 10 mV) to each other. However, the Cc^0/Cc^{+1} couple in CH_3CN and CH_2Cl_2 was at -1.105 and -1.231 V *vs*. Fc/Fc^+ at 100 mV s^{-1} scan rate. These two potentials differ by 126 mV and is a consequence of strong CH_3CN pairing with oxidized cations. Being part of the phosphine ligand caused the Cc^{-1}/Cc^0 and Cc^0/Cc^{+1} couples in CH_2Cl_2 to be observed at potentials 195 and 223 mV larger than in the free metallocene.
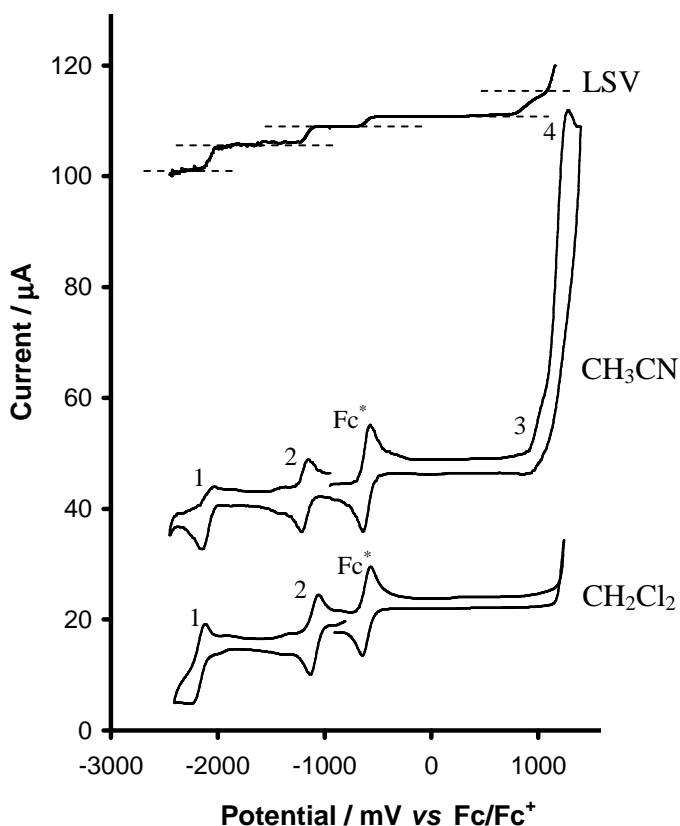
Figure 3.41. CV of diphenylphosphinocobaltocenium hexafluorophosphate **(67)**, in $CH_2Cl_2/0.1$ mol dm^{-3} $[N(^nBu_4)][B(C_6F_6)]$ (bottom), as well as in $CH_3CN/0.1$ mol dm^{-3} $[N(^nBu_4)][PF_6]$ (top), T = 25°C on a glassy carbon working electrode at a scan rate of 100 mV s^{-1}.

PPh_2Oc **(66)** and PPh_2Rc **(65)** show very similar CV's (**Figure 3.42**). Both show three irreversible oxidation peaks. The metallocene center does not show electrochemical or chemical reversibility, with $\Delta E_p > 150$ mV and i_{pa}/i_{pc} less than a half, for peak 1 (**Table 3.30**). In the case of osmocene and ruthenocene, it is possible that the electron lost upon oxidation can be replenished by internal electron transfer from the phosphine group, and thus account for a broadening of peaks observed. Peak 2 is, as in the case of PPh_2Fc, associated with oxidation on the phosphorus center, and peak 3 with further chemical reactions. The overall reaction sequence is summarized in **Scheme 3.32**.

$$PPh_2Mc \ -e^- \ \underset{}{\overset{(peak\ 1)}{\rightleftarrows}} \ PPh_2Mc^{+1} \ -e^- \ \underset{}{\overset{(peak\ 2)}{\rightleftarrows}} \ P^{+1}Ph_2Mc^{+1} \ \xrightarrow{(\ peak\ 3)} \ further\ reactions$$

Scheme 3.32. The electron transfer reactions associated with PPh_2Mc, where Mc = Rc **(65)** or Oc **(66)**.

129

The LSV indicates the number of electrons transferred for peak 1 and 2 to be equal and one, which correlates with one phosphorus group and one metal center in the same molecule being oxidized, both in a one-electron transfer process. The phosphine bound osmocenyl-group showed an E_{pa} peak at a potential of 355 mV, this is 73 mV smaller (more negative) than that of free osmocene in CH_2Cl_2 at 100 mV s^{-1}. In contrast the phosphine bound ruthenocene group was oxidized at an E_{pa} value of 127 mV more negative than the free ruthenocene. This lowering in potentials results from the electron-donating properties of the free electron-pair on the phosphorus atom.
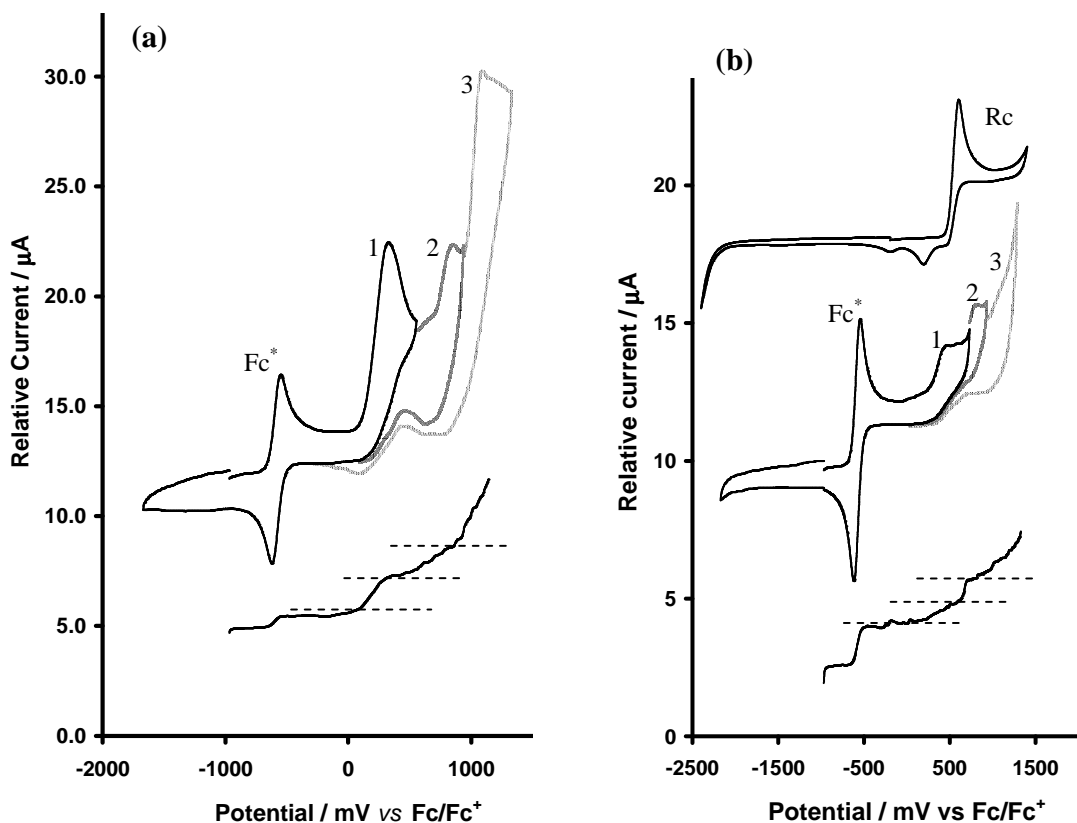
Figure 3.42. CV's and LSV's of PPh$_2$Oc (**66**) (**a**), and PPh$_2$Rc (**65**) (**b**), reversed before and after peak 2, in CH_2Cl_2/0.1 mol dm^{-3} [N(^{n}Bu$_4$)][B(C$_6$F$_6$)], T = 25°C on a glassy carbon working electrode at a scan rate of 100 mV s^{-1}.

Table 3.30. Electrochemical data obtained for all phosphines (PPh$_2$R) in either CH$_2$Cl$_2$/0.1 mol dm^{-3} [NBu$_4$][B(C$_6$F$_5$)], or CH$_3$CN/0.1 mol dm^{-3} [NBu$_4$][PF$_6$] at T = 25°C. Potentials are *vs.* Fc/Fc$^+$.

υ/mVs⁻¹	E_pa/mV	ΔE_p/mV	E°'/mV	i_pa/μA	i_pc/i_pa
Ferrocene					
100	37	75	0	5.65	0.98
Decamethylferrocene					
100	573	68	-607	4.54	0.99
PPh$_2$Fc (13) (CH$_2$Cl$_2$) – wave 1					
100	117	79	78	0.55	0.47
200	118	77	80	0.77	0.15
300	123	76	85	0.99	0.08
400	132	-	-	1.13	-
500	133	-	-	1.14	-
PPh$_2$Fc (13) (CH$_2$Cl$_2$) – wave 2					
100	377[a]	-	-	0.35[b]	-
200	438[a]	-	-	0.54[b]	-
300	443[a]	-	-	0.64[b]	-
400	444[a]	-	-	0.75[b]	-
500	452[a]	-	-	1.07[b]	-
PPh$_2$Fc (13) (CH$_2$Cl$_2$) – wave 3					
100	1128	-	-	0.25	-
200	1153	-	-	0.33	-
300	1169	-	-	0.43	-
400	1175	-	-	0.48	-
500	1193	-	-	0.53	-
PPh$_2$Fc (13) (CH$_2$Cl$_2$) – wave 4					
100	1441	0.99	-	0.56	-
200	1469	0.98	-	0.82	-
300	1488	0.96	-	1.32	-
400	1494	0.94	-	1.63	-
500	1509	0.92	-	1.90	-
PPh$_2$Fc (13) (CH$_2$Cl$_2$) – wave 1 in the absence of wave 2					
100	117	76	78	0.55	0.99
200	118	77	80	0.77	0.98
300	123	79	85	0.99	0.96
400	132	80	90	1.13	0.94
500	133	80	92	1.14	0.92
PPh$_2$Rc (65) (CH$_2$Cl$_2$) – wave 1					
100	476	229	362	0.17	0.59
200	493	227	390	0.22	0.45
300	526	229	412	0.26	0.34
400	529	228	415	0.29	0.34
500	534	227	421	0.34	0.29
PPh$_2$Rc (65) (CH$_2$Cl$_2$) – wave 2					
100	754	-	-	0.07	-
200	808	-	-	0.09	-
300	820	-	-	0.11	-
400	827	-	-	0.11	-
500	830	-	-	0.12	-

υ/mVs⁻¹	E_pa/mV	ΔE_p/mV	E°'/mV	i_pa/μA	i_pc/i_pa
PPh$_2$Fc (13) (CH$_3$CN) – wave 1					
100	6	67	-28	1.62	0.13
200	9	-	-	2.09	-
300	11	-	-	2.70	-
400	14	-	-	2.98	-
500	19	-	-	3.50	-
PPh$_2$Fc (13) (CH$_3$CN) – wave 2					
100	89[a]	-	-	0.49[b]	-
200	97[a]	-	-	1.26[b]	-
300	102[a]	-	-	2.00[b]	-
400	106[a]	-	-	2.27[b]	-
500	118[a]	-	-	2.54[b]	-
PPh$_2$Fc (13) (CH$_3$CN) – wave 3					
100	852	-	-	1.36	-
200	907	-	-	1.37	-
300	956	-	-	1.94	-
400	960	-	-	242	-
500	1001	-	-	2.83	-
PPh$_2$Fc (13) (CH$_3$CN) – wave 4					
100	1230	-	-	2.15	-
200	1311	-	-	1.55	-
300	1313	-	-	1.41	-
400	1326	-	-	1.87	-
500	1348	-	-	2.59	-
PPh$_2$Fc (13) (CH$_3$CN) – wave 1 in the absence of wave 2					
100	6	67	-28	1.64	0.99
200	9	68	-25	2.07	0.97
300	11	70	-24	2.72	0.96
400	14	72	-23	2.99	0.94
500	19	73	-21	3.49	0.93
PPh$_2$Oc (66) (CH$_2$Cl$_2$) – wave 1					
100	355	262	224	0.70	0.31
200	357	282	216	0.97	0.29
300	369	300	219	1.59	0.25
400	380	314	223	1.62	0.19
500	386	326	223	1.65	0.12
PPh$_2$Oc (66) (CH$_2$Cl$_2$) – wave 2					
100	893	-	-	0.36	-
200	928	-	-	0.51	-
300	937	-	-	0.76	-
400	943	-	-	0.79	-
500	945	-	-	0.84	-

(a) E$_{pc}$, (b) i$_{pc}$

υ/mVs^{-1}	E_{pa}/mV	ΔE_p/mV	$E^{o'}$/mV	i_{pa}/μA	i_{pc}/i_{pa}	υ/mVs^{-1}	E_{pa}/mV	ΔE_p/mV	$E^{o'}$/mV	i_{pa}/μA	i_{pc}/i_{pa}
PPh_2Rc **(65)** (CH_2Cl_2) – wave 3						PPh_2Oc **(66)** (CH_2Cl_2) – wave 3					
100	1160	-	-	0.18	-	100	1090	-	-	0.86	-
200	1173	-	-	0.21	-	200	1135	-	-	1.05	-
300	1182	-	-	0.27	-	300	1145	-	-	1.66	-
400	1190	-	-	0.30	-	400	1170	-	-	1.68	-
500	1192	-	-	0.32	-	500	1186	-	-	1.72	-
$PPh_2Cc^+PF_6^-$ **(67)** (CH_2Cl_2) – wave 1						$PPh_2Cc^+PF_6^-$ **(67)** (CH_2Cl_2) – wave 2					
100	-2176	120	-2116	0.54	0.61	100	-1105	87	-1061	0.50	0.76
200	-2184	126	-2121	0.75	0.57	200	-1115	93	-1069	0.74	0.78
300	-2188	128	-2123	0.80	0.56	300	-1115	92	-1069	0.94	0.90
400	-2199	139	-2128	1.10	0.55	400	-1120	92	-1075	1.13	0.92
500	-2203	150	-2130	1.21	0.45	500	-1126	95	-1079	1.25	0.94
$PPh_2Cc^+PF_6^-$ **(67)** (CH_3CN) – wave 1						$PPh_2Cc^+PF_6^-$ **(67)** (CH_3CN) – wave 2					
100	-2161	111	-2106	0.66	0.36	100	-1231	61	-1205	0.53	0.72
200	-2168	112	-2104	0.86	0.37	200	-1235	63	.1200	0.72	0.72
300	-2170	115	-2111	0.99	0.38	300	-1233	65	-1201	0.86	0.72
400	-2175	117	-2117	1.08	0.42	400	-1236	69	-1192	1.06	0.70
500	-2175	118	-2117	1.17	0.44	500	-1235	70	-1200	1.17	0.67
$PPh_2Cc^+PF_6^-$ **(67)** (CH_3CN) – wave 3						$PPh_2Cc^+PF_6^-$ **(67)** (CH_3CN) – wave 4					
100	977[c]	-	-	0.70[d]	-	100	1194[c]	-	-	2.43[d]	-
200	1014[c]	-	-	0.89[d]	-	200	1260[c]	-	-	3.15[d]	-
300	1022[c]	-	-	1.04[d]	-	300	1282[c]	-	-	3.57[d]	-
400	1045[c]	-	-	1.35[d]	-	400	1317[c]	-	-	4.03[d]	-
500	1069[c]	-	-	1.83[d]	-	500	1333[c]	-	-	4.33[d]	-

(c) E_{pa}, (d) i_{pa}

3.5.4. Electrochemistry of Rhodium Complexes

3.5.4.1. Rhodium Dicarbonyl Complexes

The electrochemistry of rhodium(I) dicarbonyl complexes of the type [$Rh(FcCOCHCOR)(CO)_2$] where R = CF_3 **(57)**, Fc **(60)**, Rc **(68)** and Oc **(69)**, have been studied in CH_2Cl_2 using [N^nBu_4][$B(C_6F_5)_4$] as electrolyte. In previous studies compounds **(57)** and **(60)** were investigated in CH_3CN and [N^nBu_4][PF_6].[29] CH_3CN is known to coordinate to rhodium complexes (**Chapter 2**, **Section 2.7.5.1**), and the PF_6^--anion frequently forms ion pairs of the type A^+---$(PF_6)^-$ with positively-charged (normally oxidized) species.

Under the conditions of this study, cyclic voltammetry could not resolve the redox processes of the rhodium center from that of the ferrocenyl group. In the CV's of compounds **(57)**, **(60)**, **(68)** and **(69)**, **Figure 3.43**, only the redox couples of the

ferrocenyl group of the β-diketone is observable, as well as the osmocenyl- and ruthenocenyl-species. In all cases the rhodium oxidation waves are buried under the metallocene peaks, see discussion on square wave voltammetry. Wave 1 shows the reversible one-electron redox couple for the oxidation of the ferrocenyl center of the β-diketone of all four complexes. ΔE_p was found to be larger than 90 mV at a scan rate of 100 mVs^{-1}. The second wave shows the redox couple of the second metallocene attached to the β-diketone (compounds **(60)**, **(68)** and **(69)**). Complex **(60)** shows a second reversible ferrocenyl wave ($\Delta E_p < 90$ mV) at an $E^{o'}$-value of ca. 0.49 V. Complexes **(68)** and **(69)** shows irreversible oxidation waves for the oxidation of the ruthenocenyl or osmocenyl center at E_{pa}-values of 0.83 and 0.98 V, respectively. With present knowledge, the origin of peak X in the CV of **(69)** cannot be clearly identified. Linear sweep voltammograms are also shown in **Figure 3.43**. The LSV of **(60)** shows two processes with an equal number of electrons transferred for the two ferrocenyl-signals, with the rhodium signal shared between both due to the close proximity of the two signals. The LSV's of **(68)** and **(69)** both show two electrons transferred for wave 1 and only one electron transferred for wave 2. This corresponds to the one-electron oxidation of the rhodium center being overlapped by the oxidation of the ferrocenyl group.

The redox couple of the rhodium center is buried underneath the first ferrocenyl wave – wave 1. Despite this, wave 1 still exhibits chemical reversibility for all complexes, with i_{pc}/i_{pa} approaching 1. Peak current ratios, as well as other electrochemical data are summarized in **Table 3.31**.
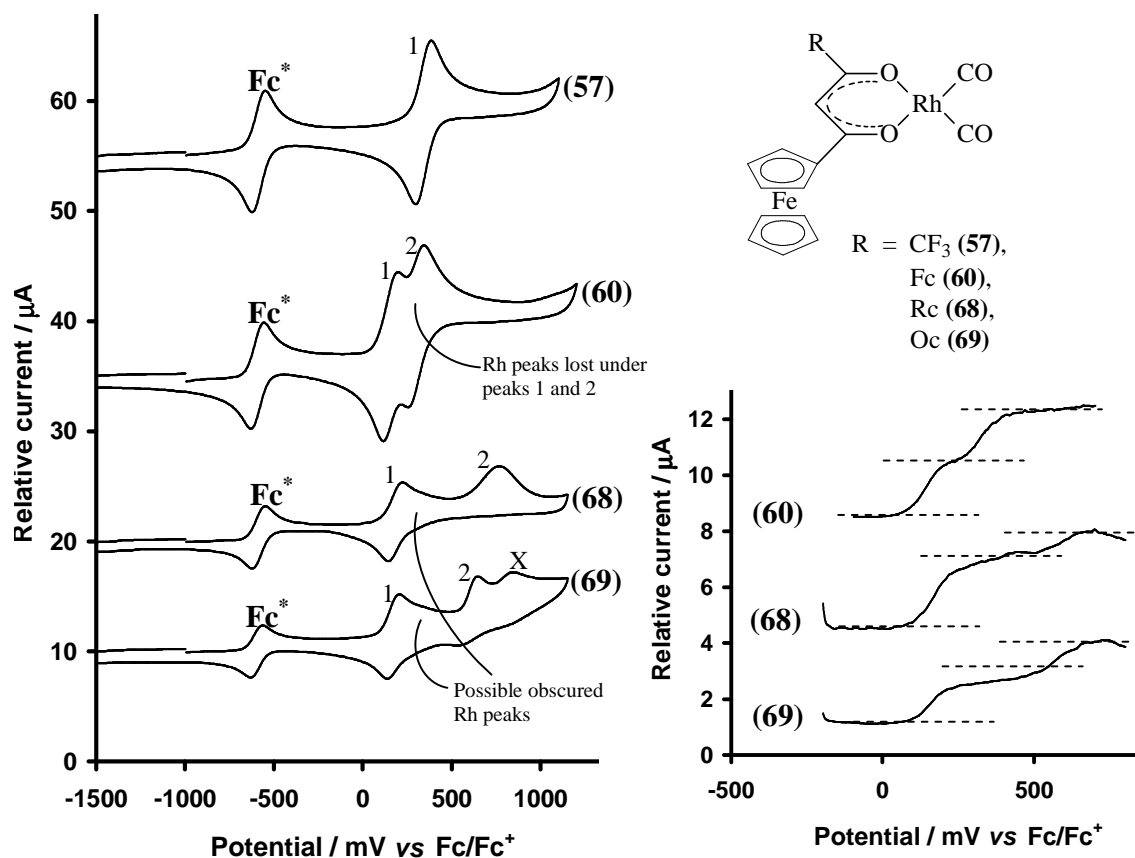
Figure 3.43. CV's (left) of rhodium(I) dicarbonyl complexes **(57)**, **(60)**, **(68)** and **(69)**, as well as LSV's (right), in CH_2Cl_2/0.1 mol dm^{-3} [N($^nBu_4$)][B(C_6F_6)], T = 25°C on a glassy carbon working electrode at a scan rate of 100 mV s^{-1}.

Square wave (SW) voltammetry has the capability to separate poorly resolved CV peaks better. This capability is enhanced if the two (or more) non-resolved electron-transfer processes take place at vastly different rates. The ferrocenyl waves normally represent electrochemical reversible (*i.e.* fast) processes. In contrast the Rh^{II}/Rh^{I} couple is often a quasi-reversible or electrochemically irreversible process (*i.e.* slow). If this is the case, SW voltammetry at high frequencies should move the Rh couple of **(57)**, **(60)**, **(68)** and **(69)** to much higher observed potentials, while the ferrocenyl formal reduction potential should be independent of SW frequency. This hypothesis was tested on **(57)**, **(60)**, **(68)** and **(69)** to see if it was possible to observe the "hidden" Rh wave. Results were exceptionally successful. **Figure 3.44** shows the SW voltammograms of all four complexes. While the rhodium(II/I) couple, which we chose to label peak 3, is buried

134

under each CV, the SW voltammograms at 50 Hz clearly showed peak 3 to the right of peak 1. Peak 2 is that of the second metallocene group on **(60)**, **(68)** and **(69)**.
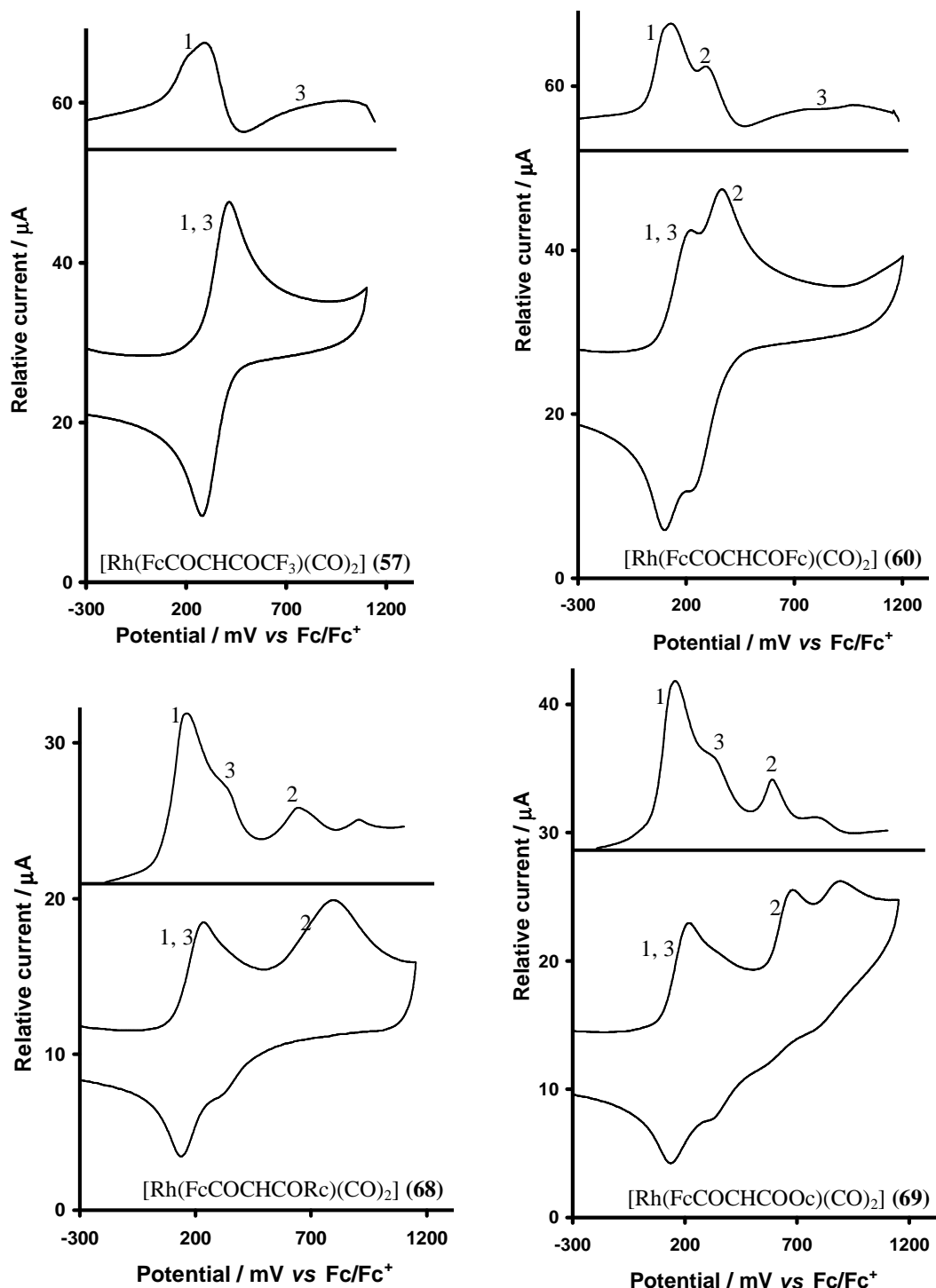
Figure 3.44. CV's (bottom part of each diagram) and SW's (top) of rhodium(I) dicarbonyl complexes **(57)**, **(60)**, **(68)** and **(69)**, in $CH_2Cl_2/0.1$ mol dm^{-3} [N($^nBu_4$)][B(C_6F_6)], T = 25°C on a glassy carbon working electrode measured at a CV scan rate of 100 mV s^{-1}, and SW measured at a frequency of 50 Hz.

Table 3.31. Data obtained for all rhodium(I) dicarbonyl complexes [Rh(FcCOCHCOR)(CO)$_2$] in CH$_2$Cl$_2$/0.1 mol dm^{-3} [N^{n}Bu$_4$][B(C$_6$F$_5$)], at T = 25°C.

υ/mVs^{-1}	E_{pa}/mV	ΔE_p/mV	$E^{o'}$/mV	i_{pa}/μA	i_{pc}/i_{pa}	υ/mVs^{-1}	E_{pa}/mV	ΔE_p/mV	$E^{o'}$/mV	i_{pa}/μA	i_{pc}/i_{pa}
[Rh(FcCOCHCOCF$_3$)(CO)$_2$] **(57)**											
100	583	87	540	0.750	0.99						
200	596	107	543	1.196	0.98						
300	603	115	546	1.491	0.97						
400	610	128	546	1.740	0.93						
500	617	139	547	1.966	0.92						
[Rh(FcCOCHCOFc)(CO)$_2$] **(60)** – wave 1						[Rh(FcCOCHCOFc)(CO)$_2$] **(60)** – wave 2					
100	385	75	348	0.794	0.98	100	529	85	487	0.787	0.98
200	400	96	352	0.861	0.93	200	549	114	492	0.842	0.97
300	407	103	356	1.109	0.92	300	558	126	495	1.009	0.91
400	412	112	357	1.270	0.89	400	562	138	494	1.215	0.88
500	421	120	360	1.405	0.85	500	571	145	499	1.345	0.85
[Rh(FcCOCHCOOc)(CO)$_2$] **(68)** – wave 1						[Rh(FcCOCHCOOc)(CO)$_2$] **(68)** – wave 2					
100	388	60	358	0.358	0.96	100	827	89	783	0.344	0.22
200	413	77	375	0.491	0.94	200	866	107	806	0.472	0.21
300	414	78	376	0.650	0.88	300	877	116	819	0.554	0.17
400	421	80	380	0.806	0.84	400	882	121	829	0.675	0.15
500	426	90	381	0.866	0.81	500	897	122	837	0.854	0.11
[Rh(FcCOCHCORc)(CO)$_2$] **(69)** – wave 1						[Rh(FcCOCHCORc)(CO)$_2$] **(69)** – wave 2					
100	430	82	383	0.317	0.97	100	975	-	-	0.249	-
200	432	95	386	0.502	0.93	200	984	-	-	0.345	-
300	438	104	387	0.627	0.91	300	993	-	-	0.450	-
400	444	114	389	0.729	0.89	400	1010	-	-	0.519	-
500	450	115	393	0.888	0.85	500	1033	-	-	0.562	-

Group electronegativities (χ_R) are useful quantities to predict reactivity with. This study use χ_R-values on the Gordy scale. An increase in formal reduction potentials ($E^{o'}$) of the ferrocenyl peak (wave 1) was observed along with an increase in group electronegativities of the varying β-diketonato substituents in [Rh(FcCOCHCOR)(CO)$_2$]. This could be used to construct a calibration curve of χ_R *vs.* $E^{o'}$. From the calibration curve, the unknown χ_R-value for the osmocenyl group was read off, and found to be 1.90. The known data that was used, as well as the value determined for the osmocene group, is tabulated in **Table 3.32**, and the plot is shown in **Figure 3.45**.

R	χ_R	$E^{o'}$ / mV
CF₃ (57)	3.01	540
Fc (60)	1.87	348
Rc (68)	1.99	383
Oc (69)	1.90	358
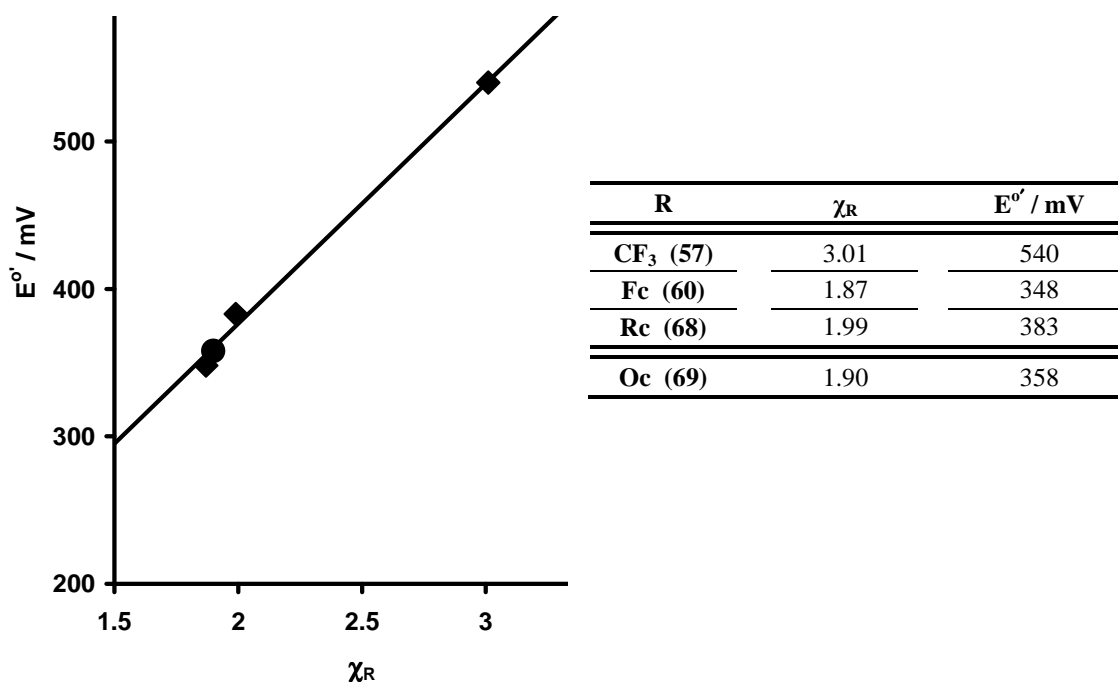
Figure 3.45 & Table 3.32. Calibration curve of known of $E^{o'}$-values *vs.* Gordy scale group electronegativities (χ_R) for rhodium(I) dicarbonyl complexes, [Rh(FcCOCHCOR)(CO)₂], with values used tabulated as shown.

To further study the rhodium(I) redox couple being overlapped by the ferrocenyl redox couple, spectro-electrochemistry was performed. IR-spectra were taken of the dicarbonyl complex as the applied potential was increased in 0.1 V increments, utilizing an Ottle-cell, as described in **Chapter 4** (**Section 4.6.1**). By focusing on the IR carbonyl peaks, it is possible to show changes in the redox state of the rhodium center as the potential is increased.

IR-spectra obtained from spectro-electrochemistry of rhodium(I) dicarbonyl complexes **(57)**, **(60)**, **(68)** and **(69)** are shown in **Figure 3.46**. At a resting potential of 0 V, two carbonyl peaks, A_1 and B_1, of the original species are observable. As the potential is increased, these two carbonyl peaks disappear, together with the appearance of two new carbonyl peaks, A_2 and B_2. The newly formed peaks reach a maximum in size at a potential just larger than that of wave 1, as observed by CV. These two new peaks can be attributed to the Rh(II) species formed upon oxidation at wave 1. As the potential is increased even further, the Rh(II) carbonyl peaks disappear at a potential of above 1.6 V,

indicating decomposition of the rhodium complex, due to loss of the carbonyl ligands. IR-peak values of the Rh(I) and the oxidized Rh(II) carbonyl peaks, as well as the potential of maximum Rh(II) IR-peak values are listed in **Table 3.33**.
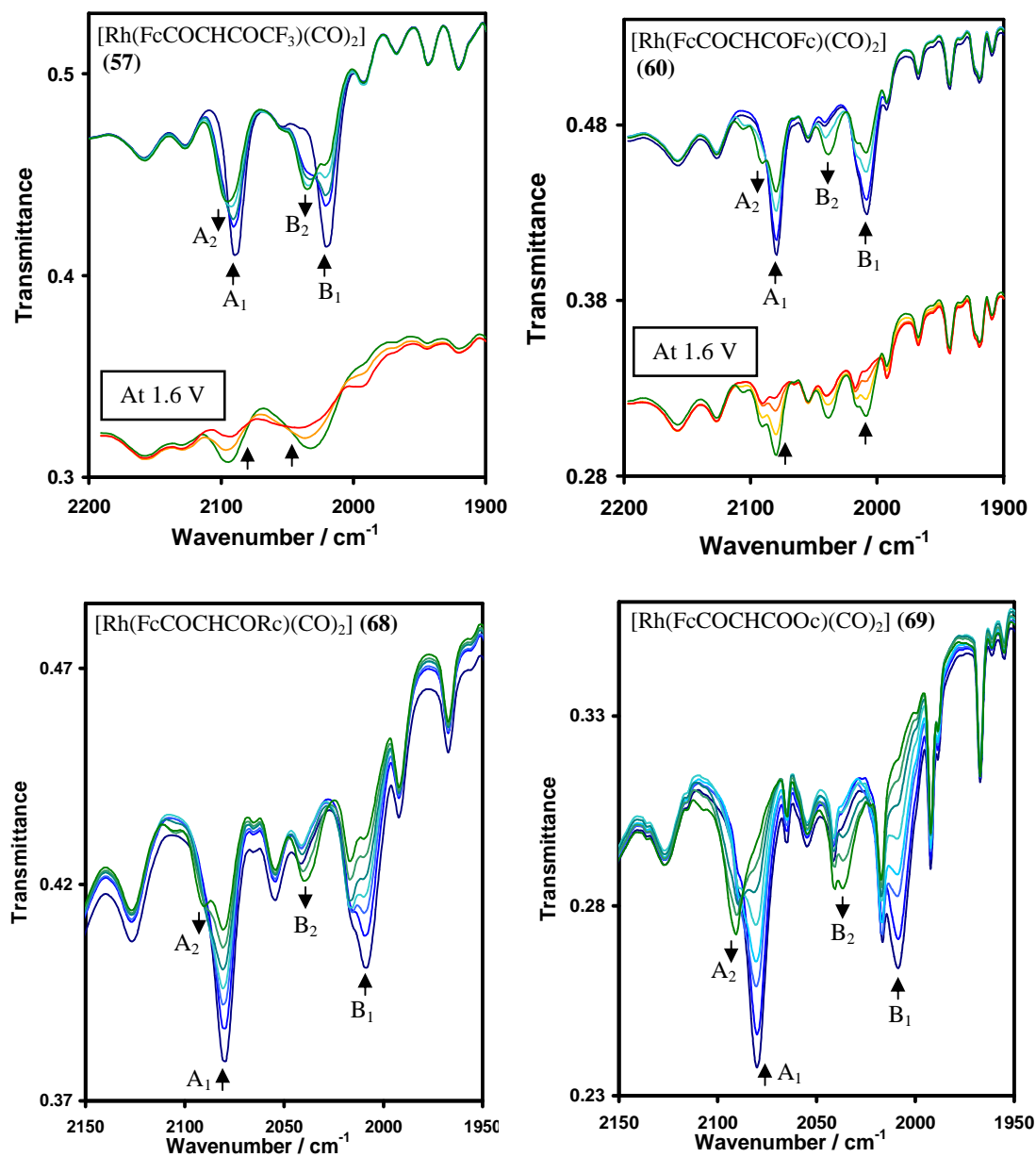
Figure 3.46. IR-spectra of rhodium(I) dicarbonyl complexes **(57)**, **(60)**, **(68)** and **(69)** at a concentration of 0.003 mol dm^{-3}, at regular potential increases, in CH$_2$Cl$_2$/0.3 mol dm^{-3} [N(^{n}Bu$_4$)][B(C$_6$F$_6$)], T = 25°C. No changes in IR-spectra were observed at wavenumbers below 1950 cm^{-1}.

Table 3.33. Spectro-electrochemical date obtained for 0.003 mol dm^{-3} rhodium(I) dicarbonyl complexes [Rh(FcCOCHCOR)(CO)$_2$] in CH$_2$Cl$_2$/0.3 mol dm^{-3} [N^{n}Bu$_4$][B(C$_6$F$_5$)], at T = 25°C.

R	Rh(I) υ(CO) / cm^{-1}		Rh(II) Potential / V	Rh(II) υ(CO) / cm^{-1}	
	A$_1$	B$_1$		A$_2$	B$_2$
CF$_3$ (57)	2086	2021	1.00	2098	2037
Fc (60)	2079	2010	1.05	2089	2037
Rc (68)	2077	2008	0.80	2094	2091
Oc (69)	2079	2008	0.80	2090	2036

Spectro-electrochemistry thus gives further proof of the rhodium center undergoing oxidation at wave 1, and is overlapped by the β-diketonato ferrocenyl group. The electrochemistry of rhodium(I) dicarbonyl complexes can be summarized schematically, as shown in **Scheme 3.33**.

[Rh^I(FcCOCHCOCF$_3$)(CO)$_2$] $\quad\xrightarrow[\;+2 \text{ x } (1e^-)\;]{\;-2 \text{ x } (1e^-)\;}\quad$ [Rh^{II}(Fc$^+$COCHCOCF$_3$)(CO)$_2$]

(57) $\qquad\qquad\qquad$ Peaks
$\qquad\qquad\qquad\qquad$ unresolved

[Rh^I(FcCOCHCOMc)(CO)$_2$] $\quad\xrightarrow[\;+2 \text{ x } (1e^-)\;]{\;-2 \text{ x } (1e^-)\;}\quad$ [Rh^{II}(Fc$^+$COCHCOMc)(CO)$_2$] $\quad\xrightarrow[\;+\;e^-\;]{\;-\;e^-\;}\quad$ [Rh^{II}(Fc$^+$COCHCOMc$^+$)(CO)$_2$]

$\qquad\qquad\qquad\qquad$ Peaks
$\qquad\qquad\qquad\qquad$ unresolved
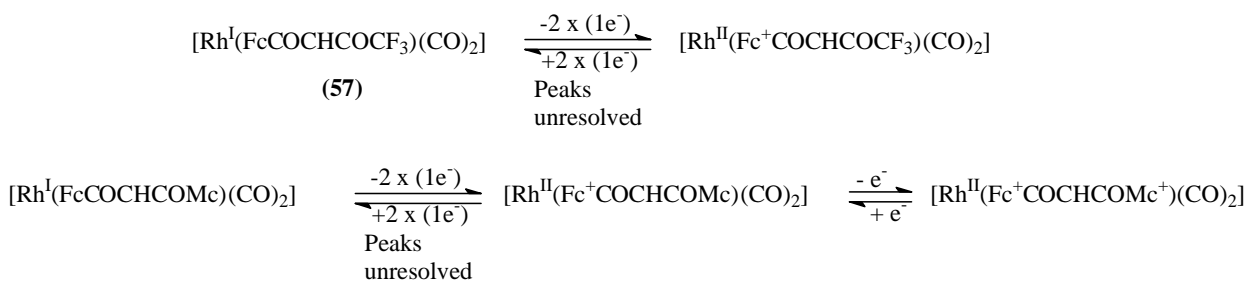
Mc = Fc (60), Rc (68), Oc (69)
with Fc = (C5H4)Fe^{II}(C$_5$H$_5$); Rc = (C$_5$H$_4$)Ru^{II}(C$_5$H$_5$); Oc = (C$_5$H$_4$)Os^{II}(C$_5$H$_5$)

Scheme 3.33. The electron transfer reactions associated with rhodium(I) dicarbonyl complexes.

3.5.4.2. Metallocene-Containing Rhodium(I) Phosphine Complexes

To date, very little is known about the electrochemistry of rhodium phosphine complexes containing ferrocenyl groups. No reports are available on rhodium(I) complexes coordinated to metallocene-containing phosphines. This study is the first to do so. Newly synthesized rhodium(I) metallocene-containing phosphine complexes of the type [Rh(FcCOCHCOCF$_3$)(CO)(PPh$_2$R)] where R = Fc **(70)** and Rc **(71)** have been studied in CH$_2$Cl$_2$ / 0.1 mol dm^{-3} [N^{n}Bu$_4$][B(C$_6$F$_5$)$_4$]. However, peak resolution was again very poor. Here it was decided necessary to also study the electrochemistry of [Rh(CH$_3$COCHCOCH$_3$)(CO)(PPh$_3$)] **(21)** and [Rh(FcCOCHCOCF$_3$)(CO)(PPh$_3$)] **(29)** under the same experimental conditions to observe the rhodium center with less interference (peak overlapping) from other metallocene groups.
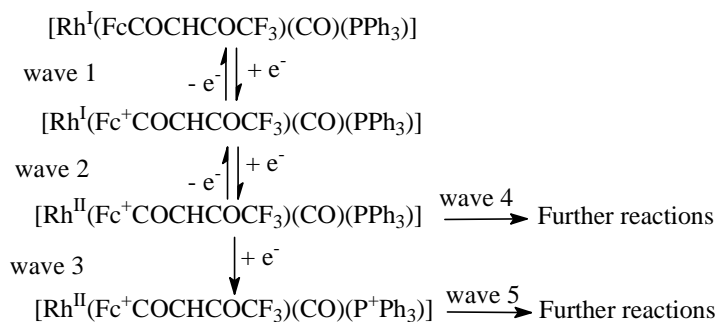
The CV of [Rh(CH$_3$COCHCOCH$_3$)(CO)(PPh$_3$)] **(21)**, **Figure 3.47**, shows two waves. The first wave 1 at an E$^{o'}$-value of ca. 0.5 V (**Table 3.34**) represents an electrochemically irreversible electron-transfer process, and is assigned to the Rh(II)/Rh(I) redox couple. ΔE_p-values of more than 150 mV and i_{pc}/i_{pa}-values of less than 0.5 highlight the electrochemical and chemical irreversibility of the rhodium(I) / rhodium(II) redox couple, although a significant amount of Rh(II) reduction can be observed if the turn-around potential is chosen to exclude the phosphine oxidation wave labeled 2. The second oxidation wave, wave 2, represents an irreversible oxidation at 1.4 V, at the edge of the solvent window. This is assigned to a phosphorus oxidation, similar to that observed for the free, uncoordinated phosphine ligands, as discussed in **Section 3.5.3**. In the reverse cathodic (reduction) cycle, two reduction peaks, wave 3 and 4, can be observed at ca. -0.9 V and ca. -0.3 V, respectively. In analogy to previous studies, both are assigned Rh reduction. When reversing the scan direction before the second oxidation wave is reached, reduction wave 4 is absent. This indicates that wave 4 is a rhodium reduction wave associated with a species that contains an oxidized phosphines group, linked to wave 2. Wave 3 is associated with the rhodium redox couple at wave 1 having no oxidized phosphines group. The weak intensity of peaks 3 and 4 is attributed to product diffusion away from the surface of the electrode during the time required for the potentiostat to scan the potentials during the reduction cycle from wave 1 (or 2) till waves 3 (and 4). Electrochemical data are summarized in **Table 3.34**.
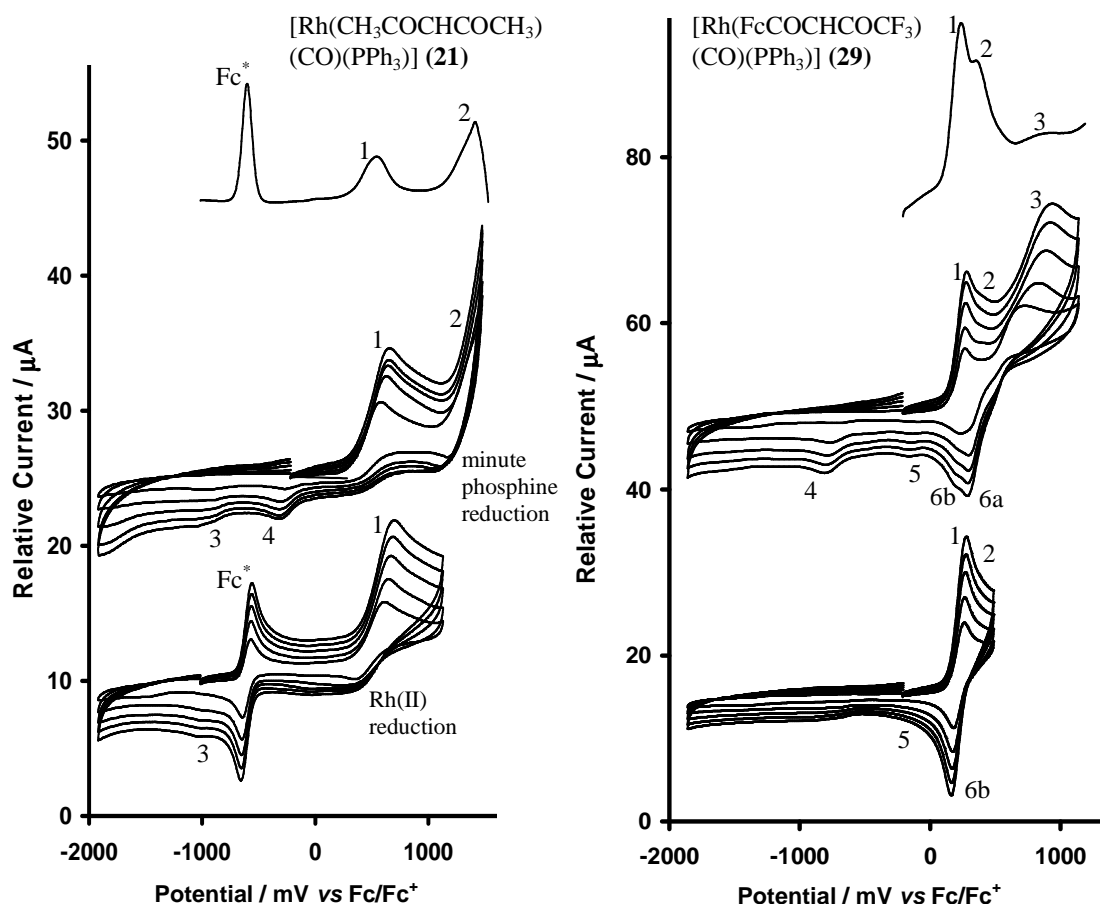
Figure 3.47. CV's of rhodium phosphine complexes **(21)** and **(29)** at scan rates from 100 - 500 mV s^{-1}, in CH$_2$Cl$_2$/0.1 mol dm^{-3} [N(^{n}Bu$_4$)][B(C$_6$F$_6$)], T = 25°C on a glassy carbon working electrode, as well as SW's (top) at a frequency of 90 Hz.

The CV of [Rh(FcCOCHCOCF$_3$)(CO)(PPh$_3$)] **(29)**, also shown in **Figure 3.47**, shows similar redox behavior to **(21)**, but with the addition of the ferrocenyl electron transfer process to the voltammogram. Wave 1, at 0.26 V can be attributed to the ferrocenyl oxidation wave. Similar to the rhodium dicarbonyl compounds, discussed in **Section 3.5.4.1**, overlapping of the ferrocenyl and rhodium peaks are observed. In this case, however, wave 2 is clearly observable as a quasi-reversible rhodium(II/I) redox couple, with ΔE$_p$ value of smaller than 150 mV. Clearer distinction between wave 1 and 2 can be made by SW, **Figure 3.47**. Wave 3 can again be considered an irreversible phosphine oxidation at ca. 0.8 V. Again, two rhodium reduction waves are observed at approximately -0.7 V (wave 4) and 0.1 V (wave 5), respectively. Wave 4 disappears when the scan is reversed prior to the phosphine oxidation at wave 3, indicating wave 4

141

involves reduction of a rhodium species still containing an oxidized phosphine ligand. Wave 5 is associated with rhodium reduction of a species bearing no oxidized phosphines group (*i.e.* generation of **(29)** itself). The ferrocenyl peak at wave 1 shows two reduction waves, 6a and 6b, when the CV scan is wide enough to include wave 3. When the scan is reversed prior to the phosphorus oxidation at wave 3, the ferrocenyl peak becomes chemically and electrochemically reversible, with $\Delta E_p < 90$ mV, and i_{pc}/i_{pa} larger than 0.98, together with the disappearance of wave 6a. This can be considered similar to the ferrocenyl wave of PPh_2Fc **(13)**, as discussed in **Section 3.5.3**. When phosphorus oxidation occurs at wave 3 and the potential is again decreased in the reverse cathodic cycle, reduction does not take place at the phosphorus center. Reduction of the ferrocenyl group associated with the electrochemically generated species at wave 3 thus takes place at a higher potential under the influence of the adjacent positively-charged phosphorus group. Wave 6b is associated with ferrocenium reduction of a species containing no oxidized phosphine ligand. This was proved as follows: When the scan is reversed prior to wave 3 and no phosphorus oxidation takes place, oxidation wave 1 and reduction wave 6b of the ferrocene group takes place completely reversible as expected. The electrochemistry of **(29)** can be summarized as shown in **Scheme 3.34**.

$[Rh^I(FcCOCHCOCF_3)(CO)(PPh_3)]$

wave 1 $-e^-$ $\uparrow$ $\downarrow$ $+e^-$

$[Rh^I(Fc^+COCHCOCF_3)(CO)(PPh_3)]$

wave 2 $-e^-$ $\uparrow$ $\downarrow$ $+e^-$

$[Rh^{II}(Fc^+COCHCOCF_3)(CO)(PPh_3)]$ $\xrightarrow{\text{wave 4}}$ Further reactions

wave 3 $\downarrow$ $+e^-$

$[Rh^{II}(Fc^+COCHCOCF_3)(CO)(P^+Ph_3)]$ $\xrightarrow{\text{wave 5}}$ Further reactions

Scheme 3.34. Electron transfer reactions associated with $[Rh(FcCOCHCOCF_3)(CO)(PPh_3)]$ **(29)**, with Fc $= (C_5H_4)Fe^{II}(C_5H_5)$.

The CV of $[Rh(FcCOCHCOCF_3)(CO)(PPh_2Fc)]$ **(70)**, shown in **Figure 3.48**, shows similar redox behavior to **(29)**, with the addition of the electrochemical fingerprint of an additional phosphine-bound ferrocene group. Wave 1, at ca. 0.3 V can be attributed to the electrochemically quasi-reversible rhodium oxidation wave, with ΔE_p-value of smaller than 150 mV. Overlapping again occurs with the first ferrocenyl peak, wave 2,

but can be separated by SW, as shown in **Figure 3.48**. The reduction peak, wave 7, associated with the ferrocenyl group is again observed to a higher potential than expected, at 0.32 V (at 100 mV s^{-1}, **Table 3.34**), under the influence of the positively-charged phosphorus group after oxidation thereof. When the scan is reversed prior to the phosphorus oxidation (wave 4), the ferrocene group gives a chemically and electrochemically reversible redox-couple. Wave 3 shows a quasi-reversible redox couple of the second phosphine-bound ferrocenyl-group, with peak current ratios of 0.9 or more, indicating chemical reversibility. Phosphorus oxidation takes place at 0.913 V, wave 4. A rhodium reduction wave associated with a species containing oxidized phosphines group (wave 5) is observed at -0.715 V. This wave disappears when the scan is reversed prior to the phosphorus oxidation at wave 4. A second reduction wave is also observed at ca. -0.4 V (wave 6), which is associated with rhodium reduction of a species bearing no oxidized phosphine group.

The CV of [Rh(FcCOCHCOCF$_3$)(CO)(PPh$_2$Rc)] **(71)**, also shown in **Figure 3.48**, shows similar redox behavior to **(70)**, with a phosphine-bound ruthenocenyl peak replacing the equivalent ferrocenyl peak in **(70)**. Wave 1, at E$_{pa}$ = 0.257 V is attributed to the electrochemically quasi-reversible β-diketonato ferrocene oxidation wave, with the peak-shape resembling that of pure ferrocene. Overlapping again occurs with the rhodium redox couple, wave 2, which shows electrochemical reversibility, with ΔE$_p$-values between 70 and 85 mV, but chemical irreversibility, with i$_{pc}$/i$_{pa}$ smaller than 0.9. Distinction between wave 1 and 2 can clearly be made by SW, as shown in **Figure 3.48**. Wave 3 shows a quasi-reversible redox couple of the ruthenocenyl group, with peak current ratios of 0.9 or more, indicating chemical reversibility. Phosphorus oxidation takes place at 1.106 V, wave 4. A rhodium reduction wave (wave 5) is observed at -0.368 V, which disappears when the scan is reversed prior to the phosphorus oxidation at wave 3. Hence, wave 5 is associated with a species still containing an oxidized phosphines group. Wave 6 at 0.103 V is associated with rhodium reduction of a species bearing no oxidized phosphines group.
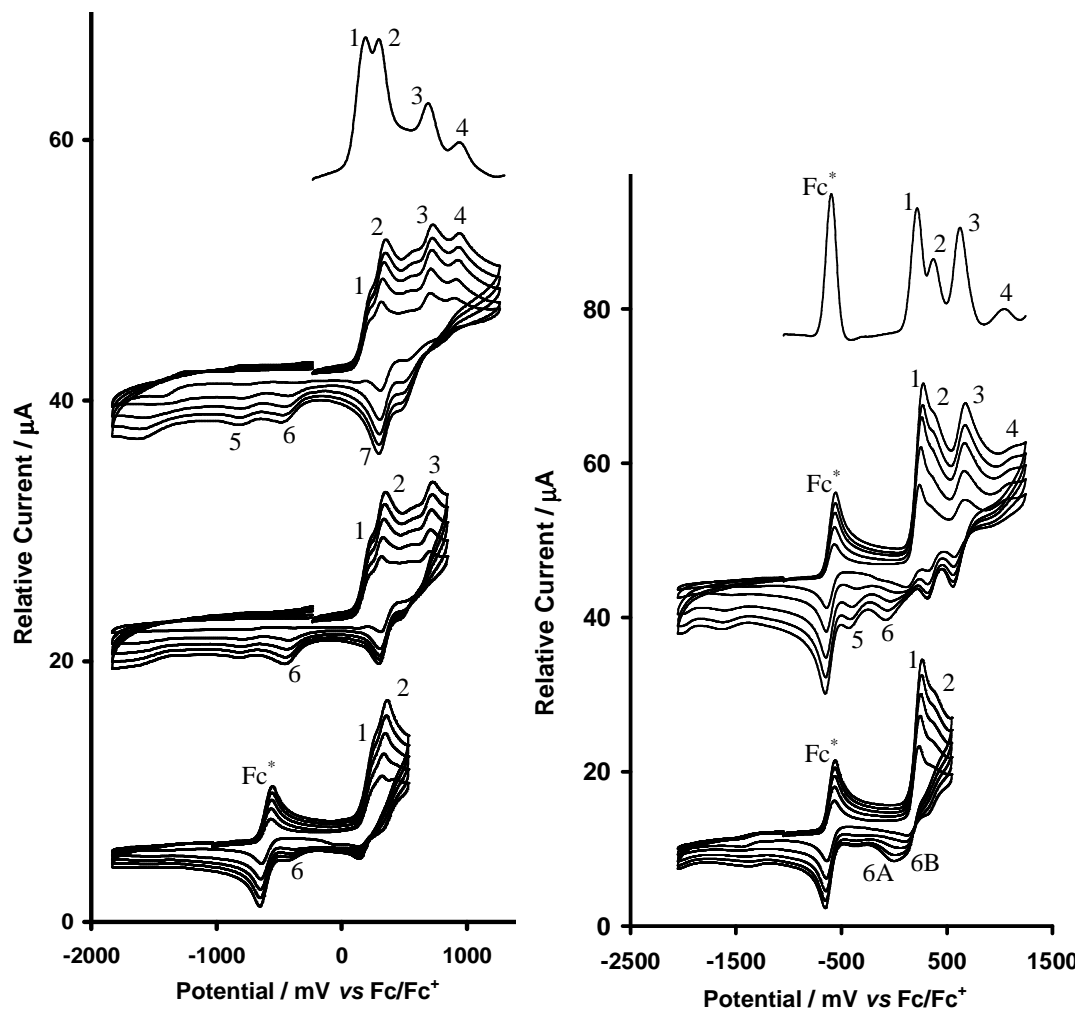
Figure 3.48. CV's of rhodium phosphine complexes **(70)** and **(71)**, with the scan direction reversed at different potentials, and with scan rates from 100 - 500 mV s^{-1}, in CH$_2$Cl$_2$/0.1 mol dm^{-3} [N(^{n}Bu$_4$)][B(C$_6$F$_6$)], T = 25°C on a glassy carbon working electrode. SW's (top), at a frequency of 90 Hz, are also shown.

144

Table 3.34. Data obtained for rhodium(I) phosphine complexes (21), (29), (70) and (71) in CH_2Cl_2/0.1 mol dm^{-3} [N^nBu_4][$B(C_6F_5)$], at T = 25°C.

υ/mVs^{-1}	E_{pa}/mV	ΔE_p/mV	$E^{o'}$/mV	i_{pa}/μA	i_{pc}/i_{pa}	υ/mVs^{-1}	E_{pa}/mV	ΔE_p/mV	$E^{o'}$/mV	i_{pa}/μA	i_{pc}/i_{pa}
[Rh(CH₃COCHCOCH₃)(CO)(PPh₃)] (21) – wave 1											
100	580	217	472	4.89	0.41	100	1402	-	-	5.86	-
200	649	295	502	6.49	0.27	200	1437	-	-	6.99	-
300	652	317	494	6.76	0.22	300	1441	-	-	7.99	-
400	655	325	493	6.88	0.20	400	1444	-	-	8.05	-
500	658	344	486	6.75	0.19	500	1446	-	-	8.43	-
100	-893[a]	-	-	0.18[b]	-	100	-258[a]	-	-	0.37[b]	-
200	-923[a]	-	-	0.21[b]	-	200	-303[a]	-	-	0.86[b]	-
300	-954[a]	-	-	0.27[b]	-	300	-308[a]	-	-	0.89[b]	-
400	-968[a]	-	-	0.30[b]	-	400	-312[a]	-	-	1.01[b]	-
500	-1033[a]	-	-	0.39[b]	-	500	-314[a]	-	-	1.03[b]	-
100	260	-	-	3.86	-	100	338	113	282	5.56	0.31
200	270	-	-	6.45	-	200	370	168	286	7.00	0.38
300	271	-	-	7.69	-	300	383	183	292	8.40	0.39
400	273	-	-	8.69	-	400	385	188	291	9.86	0.58
500	290	-	-	9.60	-	500	388	198	189	11.12	0.70
100	719	-	-	6.44	-	100	-686[a]	-	-	0.25[b]	-
200	839	-	-	7.30	-	200	-739[a]	-	-	0.91[b]	-
300	898	-	-	9.46	-	300	-754[a]	-	-	1.29[b]	-
400	927	-	-	11.12	-	400	-778[a]	-	-	1.52[b]	-
500	953	-	-	11.78	-	500	-798[a]	-	-	1.69[b]	-
100	-103[a]	-	-	0.08[b]	-	100	298[a]	-	-	3.35[b]	-
200	-138[a]	-	-	0.25[b]	-	200	292[a]	-	-	5.99[b]	-
300	-143[a]	-	-	0.28[b]	-	300	288[a]	-	-	7.18[b]	-
400	-161[a]	-	-	0.30[b]	-	400	285[a]	-	-	8.15[b]	-
500	-172[a]	-	-	0.54[b]	-	500	282[a]	-	-	9.09[b]	-
100	245	102	194	3.90	0.12	100	320	-	-	2.31	-
200	248	128	184	4.54	0.14	200	329	-	-	3.43	-
300	252	138	183	5.00	0.17	300	345	-	-	3.78	-
400	262	165	180	5.13	0.18	400	350	-	-	4.71	-
500	264	180	174	5.59	0.20	500	356	-	-	4.67	-
100	720	177	632	1.95	0.89	100	913	-	-	0.78	-
200	721	220	611	2.15	0.91	200	936	-	-	1.1	-
300	722	249	599	2.38	0.93	300	942	-	-	1.42	-
400	725	260	595	2.41	0.94	400	951	-	-	1.36	-
500	728	272	592	2.56	0.95	500	965	-	-	1.43	-
100	-715[a]	-	-	0.12[b]	-	100	-362[a]	-	-	0.13[b]	-
200	-775[a]	-	-	0.21[b]	-	200	-418[a]	-	-	0.39[b]	-
300	-793[a]	-	-	0.52[b]	-	300	-452[a]	-	-	0.78[b]	-
400	-806[a]	-	-	0.78[b]	-	400	-466[a]	-	-	1.10[b]	-
500	-817[a]	-	-	0.91[b]	-	500	-480[a]	-	-	1.24[b]	-

Section headers within the table:

[Rh(CH₃COCHCOCH₃)(CO)(PPh₃)] (21) – wave 1 ; [Rh(CH₃COCHCOCH₃)(CO)(PPh₃)] (21) – wave 2

[Rh(CH₃COCHCOCH₃)(CO)(PPh₃)] (21) – wave 3 ; [Rh(CH₃COCHCOCH₃)(CO)(PPh₃)] (21) – wave 4

[Rh(FcCOCHCOCF₃)(CO)(PPh₃)] (29) – wave 1 ; [Rh(FcCOCHCOCF₃)(CO)(PPh₃)] (29) – wave 2

[Rh(FcCOCHCOCF₃)(CO)(PPh₃)] (29) – wave 3 ; [Rh(FcCOCHCOCF₃)(CO)(PPh₃)] (29) – wave 4

[Rh(FcCOCHCOCF₃)(CO)(PPh₃)] (29) – wave 5 ; [Rh(FcCOCHCOCF₃)(CO)(PPh₃)] (29) – wave 6

[Rh(FcCOCHCOCF₃)(CO)(PPh₂Fc)] (70) – wave 1 ; [Rh(FcCOCHCOCF₃)(CO)(PPh₂Fc)] (70) – wave 2

[Rh(FcCOCHCOCF₃)(CO)(PPh₂Fc)] (70) – wave 3 ; [Rh(FcCOCHCOCF₃)(CO)(PPh₂Fc)] (70) – wave 4

[Rh(FcCOCHCOCF₃)(CO)(PPh₂Fc)] (70) – wave 5 ; [Rh(FcCOCHCOCF₃)(CO)(PPh₂Fc)] (70) – wave 6

Table 3.34. (continued) Data obtained for rhodium(I) phosphine complexes **(21)**, **(29)**, **(70)** and **(71)** in CH$_2$Cl$_2$/0.1 mol dm^{-3} [NBu$_4$][B(C$_6$F$_5$)], at T = 25°C.

υ/mVs^{-1}	E$_{pa}$/mV	ΔE$_p$/mV	E$^{o'}$/mV	i$_{pa}$/μA	i$_{pc}$/i$_{pa}$	υ/mVs^{-1}	E$_{pa}$/mV	ΔE$_p$/mV	E$^{o'}$/mV	i$_{pa}$/μA	i$_{pc}$/i$_{pa}$
[Rh(FcCOCHCOCF$_3$)(CO)(PPh$_2$Fc)] (70) – wave 7											
100	320^a	-	-	2.05^b	-						
200	304^a	-	-	3.37^b	-						
300	302^a	-	-	3.47^b	-						
400	297^a	-	-	4.48^b	-						
500	295^a	-	-	4.52^b	-						
[Rh(FcCOCHCOCF$_3$)(CO)(PPh$_2$Rc)] (71) – wave 1						**[Rh(FcCOCHCOCF$_3$)(CO)(PPh$_2$Rc)] (71) – wave 2**					
100	257	127	194	10.09	0.24	100	358	70	323	1.54	0.67
200	266	183	175	12.49	0.22	200	368	74	333	2.57	0.74
300	269	211	164	14.43	0.19	300	371	78	334	3.36	0.79
400	287	261	157	17.81	0.17	400	378	81	338	3.87	0.81
500	289	176	151	18.68	0.15	500	384	85	342	4.06	0.85
[Rh(FcCOCHCOCF$_3$)(CO)(PPh$_2$Rc)] (71) – wave 3						**[Rh(FcCOCHCOCF$_3$)(CO)(PPh$_2$Rc)] (71) – wave 4**					
100	656	102	605	2.80	0.90	100	1106	-	-	2.10	-
200	665	104	612	4.14	0.92	200	1114	-	-	1.82	-
300	670	110	615	4.96	0.96	300	1135	-	-	1.96	-
400	676	113	618	6.12	0.97	400	1151	-	-	1.54	-
500	689	114	631	6.84	0.98	500	1165	-	-	1.12	-
[Rh(FcCOCHCOCF$_3$)(CO)(PPh$_2$Rc)] (71) – wave 5						**[Rh(FcCOCHCOCF$_3$)(CO)(PPh$_2$Rc)] (71) – wave 6**					
100	-368^a	-	-	0.28^b	-	100	103^a	-	-	0.56^b	-
200	-369^a	-	-	0.42^b	-	200	38^a	-	-	0.76^b	-
300	-397^a	-	-	0.83^b	-	300	-15^a	-	-	1.23^b	-
400	-413^a	-	-	1.05^b	-	400	-68^a	-	-	1.98^b	-
500	-446^a	-	-	1.40^b	-	500	-82^a	-	-	2.52^b	-

(a) E$_{pc}$, (b) i$_{pc}$

Spectro-electrochemistry was also performed on the rhodium(I) phosphine complexes [Rh(CH$_3$COCHCOCH$_3$)(CO)(PPh$_3$)] **(21)**, [Rh(FcCOCHCOCF$_3$)(CO)(PPh$_3$)] **(29)**, [Rh(FcCOCHCOCF$_3$)(CO)(PPh$_2$Fc)] **(70)** and [Rh(FcCOCHCOCF$_3$)(CO)(PPh$_2$Rc)] **(71)**. IR-spectra obtained from spectro-electrochemistry of these complexes are shown in **Figure 3.49**. At a resting potential of 0 V, one carbonyl peak (labeled A), of the mother species is observable. As the potential is increased in 0.1V increments, no changes in the IR-spectra are observed, even when potentials are reached corresponding to the oxidation of Rh(I) to Rh(II). This does not indicate however that no changes take place at the rhodium-center at these potentials, but only that changes taking place do not have a significant influence on the IR-spectra. As the potential is increased even further, the carbonyl-peak decreases and finally disappears, but only at potentials higher than 1.6 V, corresponding to reaching the end of the solvent window.
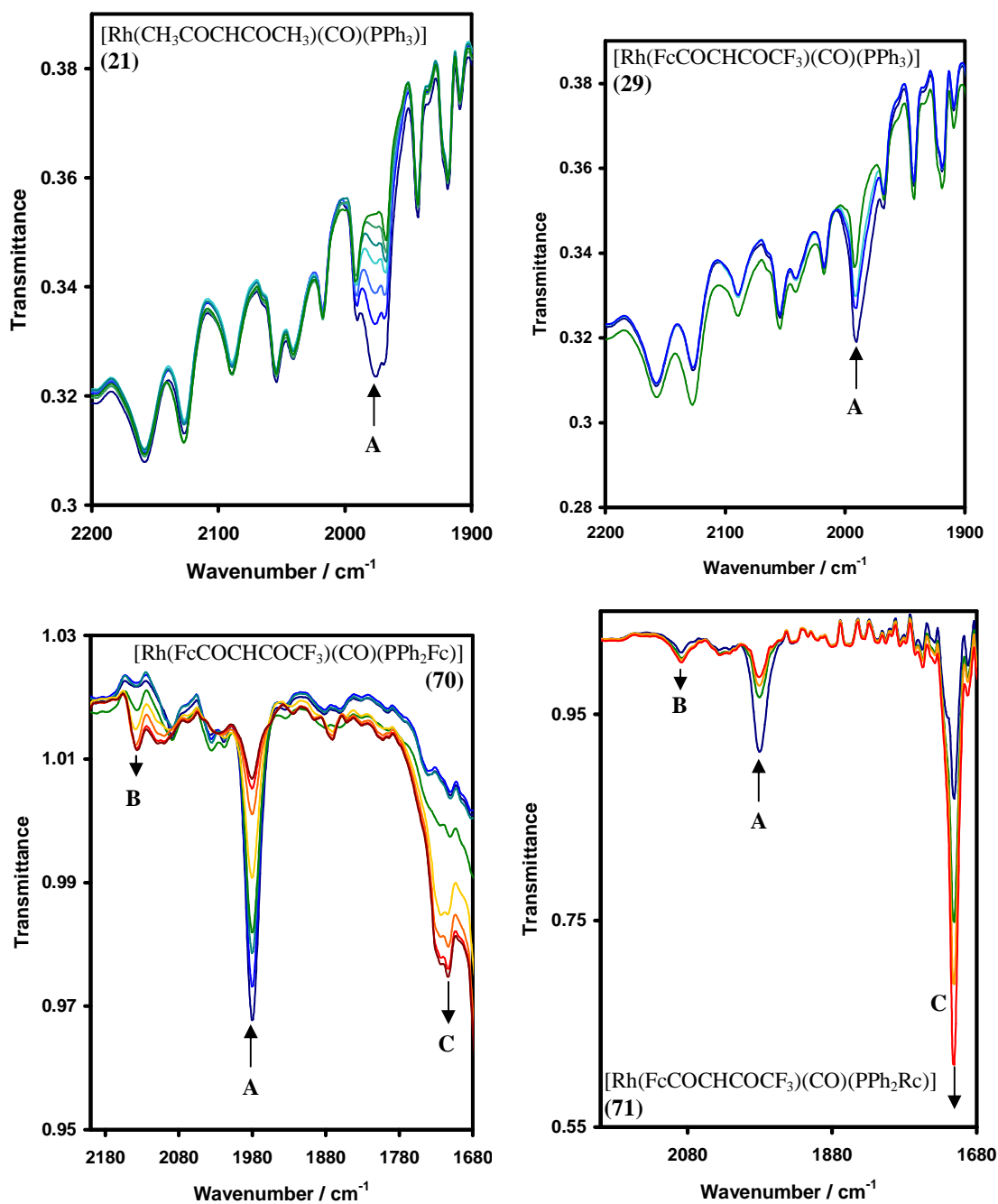
Figure 3.49. IR-spectra of rhodium(I) phosphine complexes **(21)**, **(29)**, **(70)** and **(71)** at a concentration of 0.003 mol dm^{-3}, at regular potential increases, in CH$_2$Cl$_2$/0.3 mol dm^{-3} [N(^{n}Bu$_4$)][B(C$_6$F$_6$)], T = 25°C. No further observations were made for **(21)** and **(29)** between 1600 and 1900 cm^{-1}.

An interesting observation was made with complexes **(70)** and **(71)** when the potential is increased above 1.6 V. Together with the disappearance of the carbonyl peak, two new carbonyl peaks formed to higher (2100 cm^{-1}, peak B) and lower (1700 cm^{-1} peak C)

147

wavenumbers, resembling Rh(III) alkyl and Rh(III) acyl species, as formed after oxidative addition. This is explained as the oxidative addition of the solvent, dichloromethane, to the rhodium complex. To confirm this, another experiment was carried out, with methyl iodide added to the electrolytic solution, and the potential increased as previously. Clear distinction could be made between oxidative addition products of CH_3I and oxidative addition products of CH_2Cl_2, and as the potential is increased, switched from the methyl iodide products (dominant at low potential) to dichloromethane products (dominant at high potentials). **Figure 3.50** shows IR-spectra of the Rh(I) starting complex without methyl iodide added and at resting potential (a), as well as at increased potential, forming the dichloromethane oxidative addition products (b), and finally with methyl iodide added and at an increased potential, forming the methyl iodide oxidative addition products. Wavenumbers of oxidative addition products are listed in **Table 3.35**.
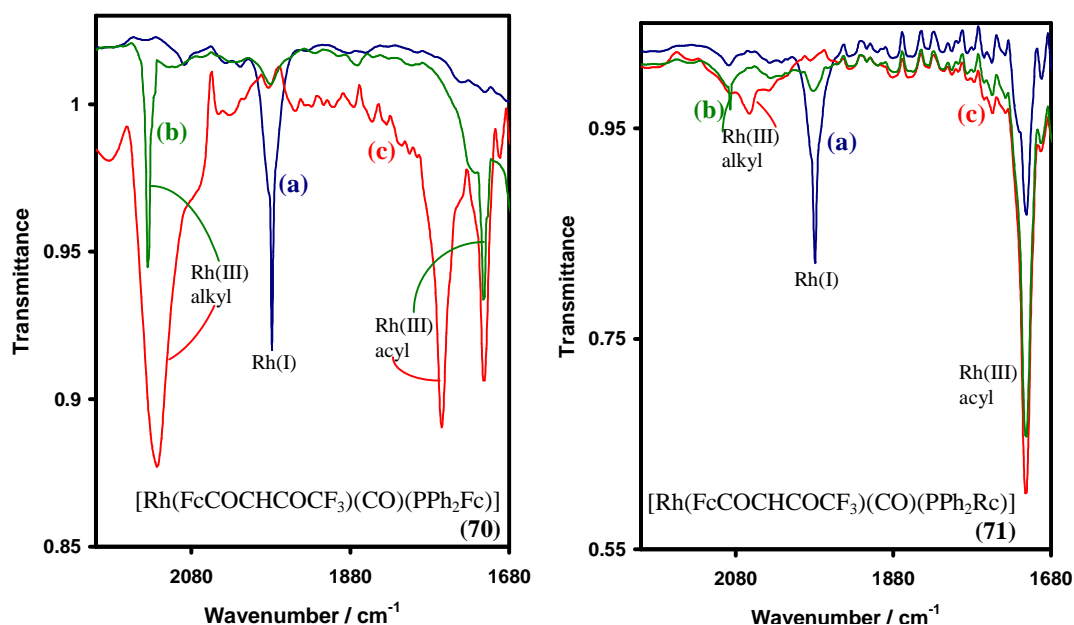
Figure 3.50. IR-spectra of rhodium(I) phosphine complexes **(70)** and **(71)** at a resting potential of 0 V(**a**), and at a potential of more than 1.6 V (**b**). IR-spectra of complexes **(70)** and **(71)** with the addition of MeI and increased potential are indicated in (**c**). Rhodium concentration of 0.003 mol dm^{-3} in CH_2Cl_2/0.3 mol dm^{-3} [N(^{n}Bu$_4$)][B(C$_6$F$_6$)], T = 25°C were used.

148

Table 3.35. Spectro-electrochemical date obtained for 0.003 mol dm^{-3} rhodium(I) phosphine complexes [Rh(FcCOCHCOCF$_3$)(CO)(PPh$_2$R)] in CH$_2$Cl$_2$/0.3 mol dm^{-3} [NBu$_4$][B(C$_6$F$_5$)], at T = 25°C.

R	Rh(I) υ(CO) / cm^{-1}	Rh(III) CH$_3$I oxidative addition / cm^{-1}		Rh(III) CHCl$_3$ oxidative addition / cm^{-1}	
		Alkyl	Acyl	Alkyl	Acyl
Fc (70)	1979	2135	1712	2122	1765
Rc (71)	1978	2087	1711	2060	1712

3.5.4.3. Rhodium(I) Complexes Containing Fluorinated Phosphines

The electrochemistry of the new rhodium(I) complexes containing fluorinated phosphines that eminated from this study, [Rh(FcCOCHCOCF$_3$)(CO)(PPh$_n$(C$_6$F$_5$)$_{3-n}$] with n = 2 **(72)**, 1 **(73)**, or 0 **(74)**, have been investigated in CH$_2$Cl$_2$ / 0.1 mol dm^{-3} [N^{n}Bu$_4$][B(C$_6$F$_5$)$_4$].

The CV's of complexes **(72)**, **(73)** and **(74)** are shown in **Figure 3.51**. All exhibit similar electrochemical behavior. Three redox couples are observable. Wave 1 at potentials between 0.27 V and 0.34 V (**Table 3.36**) for compounds **(72)** – **(74)**, represents a redox process associated with the β-diketonato ferrocenyl group. Since ΔE_p values are smaller than 90 mV at a scan rate of 100 mV s^{-1}, the process is electrochemically reversible. Peak current ratios of better than 0.9 were also found, indicating chemical reversibility. Again, the rhodium-based redox process associated with wave 2 is found to be submerged underneath the ferrocenyl redox couple. SW voltammetry, **Figure 3.51**, could not clearly resolve waves 1 and 2. From the CV traces, wave 2 represents a quasi-reversible process at E$^{o'}$ values approximately 0.37 V – 0.39 V, and ΔE_p values between 90 mV and 150 mV, and i$_{pc}$/i$_{pa}$ values smaller than 0.8. The large deviations from unity for the current ratios indicate poor chemical reversibility. Electrochemically irreversible oxidation of the phosphine-group was observed at wave 3, between 1.0 V and 1.5 V. A reduction peak, wave 4, is also observed at approximately 0.58 V – 0.61 V, and probably corresponds to reduction of freshly oxidized phosphines groups. The reduction wave 5, at approximately -0.5 V, were absent if the switching potential was small enough to exclude wave 3, and is at present assigned to an unidentified decomposition product after phosphines oxidation takes place. Electrochemical data are summarized in **Table 3.36**.
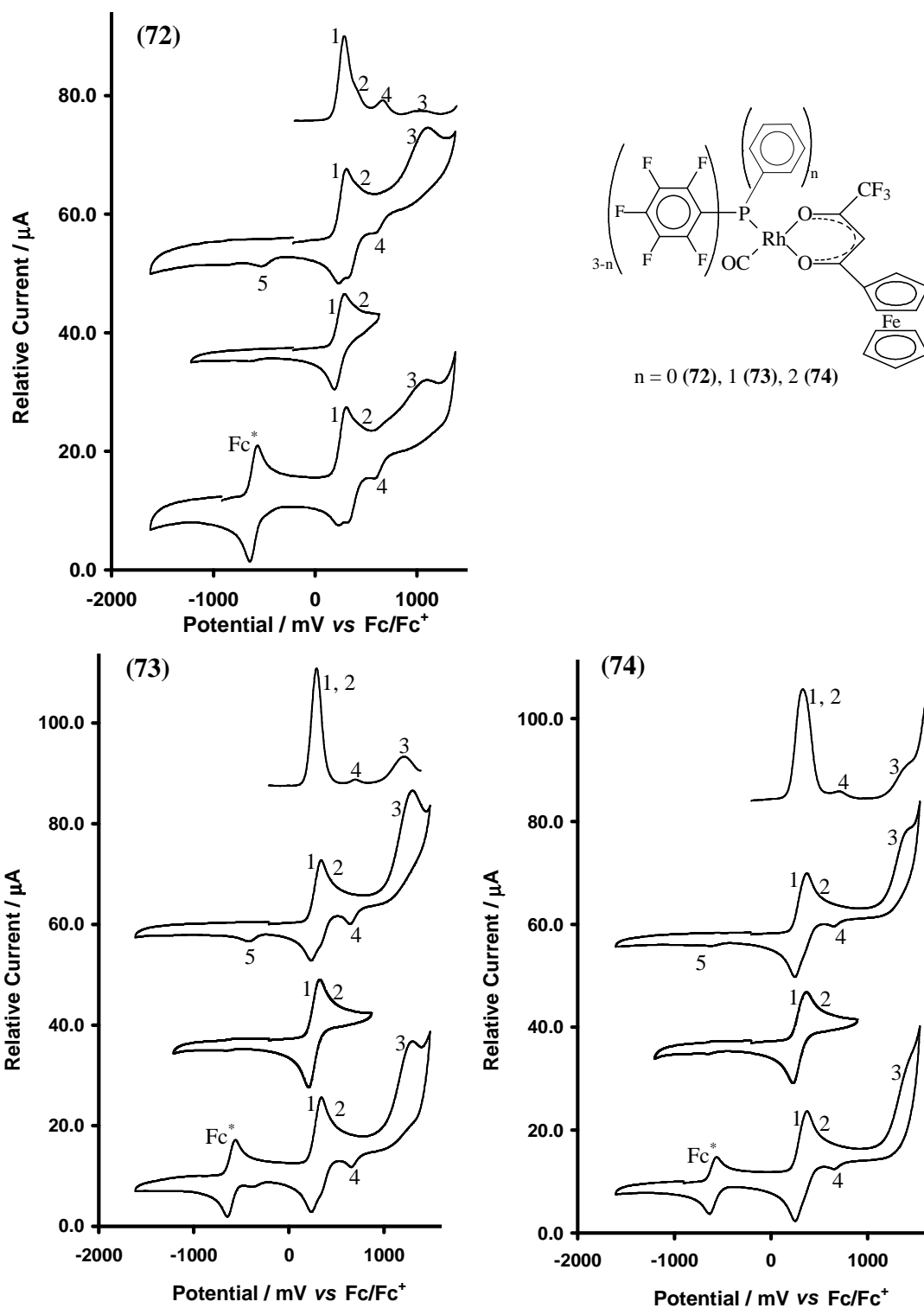
Figure 3.51. CV's of rhodium phosphine complexes **(72)**, **(73)** and **(74)**, with scan rates of 200 mV s⁻¹, in CH₂Cl₂/0.1 mol dm⁻³ [N(ⁿBu₄)][B(C₆F₆)], T = 25°C on a glassy carbon working electrode. SW's (top for each complex) at a frequency of 50 Hz is also shown.

A general increase in potential was observed for waves 1 and 3, as the number of fluorinated rings on the phosphine ligand is increased. Thus as the total group electronegativity ($\chi_{PR'R''R'''}$) on the phosphine increases as more fluorinated rings are added, oxidation becomes more difficult. A large dependence exists between phosphine group electronegativity and E_{pa} values for phosphine oxidation. The β-diketonato ferrocenyl-group formal reduction potential was much less dependent on changes in phosphine group electronegativity. Both relationships are quantified mathematically by the following equations:

Wave 1: $E^{o'} = 132\ \chi_{PR'R''R'''} - 644.5$

Wave 3: $E_{pa} = 848\ \chi_{PR'R''R'''} - 4810$

This dependence is illustrated graphically in **Figure 3.52**. From **Figure 3.52** it is clear that the PPh$_2$Fc **(70)** and PPh$_2$Rc **(71)** complexes do not fit the dependency predicted for wave 3, probably because when the phosphorus atom is oxidized, the Fc and Rc groups are already oxidized to the *charged* ferrocenium and ruthenocenium species. All the other phosphines are neutral ligands when the P atom is oxidized. No significant influence on the position of rhodium oxidation was observed.
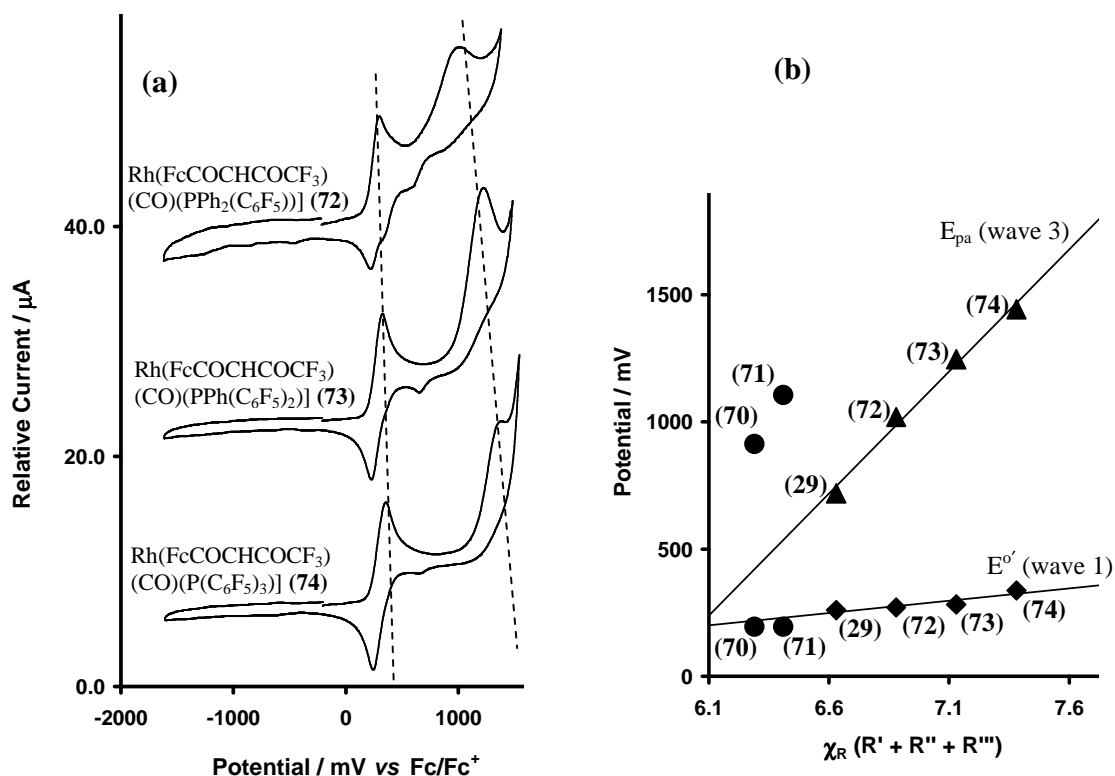
Figure 3.52. (a) CV's of rhodium phosphine complexes **(72)**, **(73)** and **(74)** at a scan rate of 100 mV s^{-1}, in CH$_2$Cl$_2$/0.1 mol dm^{-3} [N(^{n}Bu$_4$)][B(C$_6$F$_6$)], T = 25°C on a glassy carbon working electrode. **(b)** Graph of E$_{pa}$ (for wave 3) or E$^{o'}$ (for wave 1) *vs.* total group electronegativity (χ_R) of the phosphine substituents, showing a linear relationship between $\chi_{PR'R''R'''}$ ($\chi_{R'} + \chi_{R''} + \chi_{R'''}$) and the oxidation potential.

Table 3.36. Data obtained for rhodium(I) phosphine complexes **(72)**, **(73)**, and **(74)** in CH$_2$Cl$_2$/0.1 mol dm^{-3} [NBu$_4$][B(C$_6$F$_5$)], at T = 25°C.

υ/mVs^{-1}	E$_{pa}$/mV	ΔE$_p$/mV	E$^{o'}$/mV	i$_{pa}$/µA	i$_{pc}$/i$_{pa}$	υ/mVs^{-1}	E$_{pa}$/mV	ΔE$_p$/mV	E$^{o'}$/mV	i$_{pa}$/µA	i$_{pc}$/i$_{pa}$
[Rh(FcCOCHCOCF$_3$)(CO)(PPh$_2$(C6F5))] **(72)** – wave 1						[Rh(FcCOCHCOCF$_3$)(CO)(PPh$_2$(C6F5))] **(72)** – wave 2					
100	302	62	271	2.03	0.95	100	419	96	371	0.60	0.75
200	321	83	280	2.67	0.94	200	424	104	372	0.86	0.73
300	332	96	284	3.39	0.93	300	437	117	379	1.05	0.68
400	340	106	287	3.80	0.91	400	448	129	384	1.67	0.65
500	342	108	288	4.15	0.89	500	452	134	385	1.86	0.62
[Rh(FcCOCHCOCF$_3$)(CO)(PPh$_2$(C6F5))] **(72)** – wave 3						[Rh(FcCOCHCOCF$_3$)(CO)(PPh$_2$(C6F5))] **(72)** – wave 4					
100	1019	-	-	1.74	-	100	-459[a]	-	-	0.07[b]	-
200	1131	-	-	2.24	-	200	-514[a]	-	-	0.47[b]	-
300	1160	-	-	3.37	-	300	-544[a]	-	-	0.48[b]	-
400	1180	-	-	3.46	-	400	-573[a]	-	-	0.50[b]	-
500	1194	-	-	4.02	-	500	-581[a]	-	-	0.56[b]	-
[Rh(FcCOCHCOCF$_3$)(CO)(PPh(C6F5)$_2$)] **(73)** – wave 1						[Rh(FcCOCHCOCF$_3$)(CO)(PPh(C6F5)$_2$)] **(73)** – wave 2					
100	325	86	282	6.53	0.94	100	399	81	359	3.13	0.76
200	334	100	284	11.97	0.91	200	404	90	359	3.76	0.73
300	350	119	291	14.88	0.87	300	416	105	364	4.05	0.69
400	353	124	291	17.07	0.85	400	422	113	366	4.89	0.65
500	358	130	293	19.92	0.83	500	430	125	368	5.49	0.61

Table 3.36. (continued) Data obtained for rhodium(I) phosphine complexes **(72)**, **(73)**, and **(74)** in CH_2Cl_2/0.1 mol dm^{-3} [NBu_4][$B(C_6F_5)$], at T = 25°C.

υ/mVs^{-1}	E_{pa}/mV	ΔE_p/mV	$E^{o'}$/mV	i_{pa}/μA	i_{pc}/i_{pa}	υ/mVs^{-1}	E_{pa}/mV	ΔE_p/mV	$E^{o'}$/mV	i_{pa}/μA	i_{pc}/i_{pa}
[Rh(FcCOCHCOCF$_3$)(CO)(PPh(C6F5)$_2$)] **(73) – wave 3**						[Rh(FcCOCHCOCF$_3$)(CO)(PPh(C6F5)$_2$)] **(73) – wave 4**					
100	1247	-	-	5.40	-	100	-378^a	-	-	0.15^b	-
200	1313	-	-	10.67	-	200	-418^a	-	-	1.34^b	-
300	1345	-	-	18.23	-	300	-451^a	-	-	2.41^b	-
400	1356	-	-	23.40	-	400	-459^a	-	-	2.91^b	-
500	1381	-	-	28.18	-	500	-466^a	-	-	3.07^b	-
[Rh(FcCOCHCOCF$_3$)(CO)(P(C6F5)$_3$)] **(74) – wave 1**						[Rh(FcCOCHCOCF$_3$)(CO)(P(C6F5)$_3$)] **(74) – wave 2**					
100	380	82	337	8.33	0.95	100	441	123	380	5.32	0.78
200	384	92	338	11.13	0.91	200	453	142	382	6.05	0.75
300	394	111	339	14.10	0.87	300	461	153	385	7.54	0.69
400	401	124	339	15.89	0.84	400	469	164	387	8.34	0.67
500	409	139	340	17.40	0.81	500	478	177	390	9.01	0.65
[Rh(FcCOCHCOCF$_3$)(CO)(P(C6F5)$_3$)] **(74) – wave 3**						[Rh(FcCOCHCOCF$_3$)(CO)(P(C6F5)$_3$)] **(74) – wave 4**					
100	1443	-	-	11.22	-	100	-613^a	-	-	0.17^b	-
200	1446	-	-	15.20	-	200	-621^a	-	-	0.43^b	-
300	1458	-	-	18.58	-	300	-626^a	-	-	0.67^b	-
400	1486	-	-	20.14	-	400	-636^a	-	-	08.4^b	-
500	1546	-	-	23.18	-	500	-667^a	-	-	0.94^b	-

(a) E_{pc}, (b) i_{pc}

3.5.5. Electrochemistry of Tetrathiafulvalene-Containing Complexes

The tetrathiafulvalene (TTF) core is a known electroactive group.[30] It has previously been shown by the Lorcy group that the TTF group undergoes two completely reversible stepwise one-electron redox processes, as shown in **Scheme 3.35**, due to the delocalization capabilities of this group.[31] Their study used CH_2Cl_2 as solvent and [NBu_4][PF_6] as supporting electrolyte.
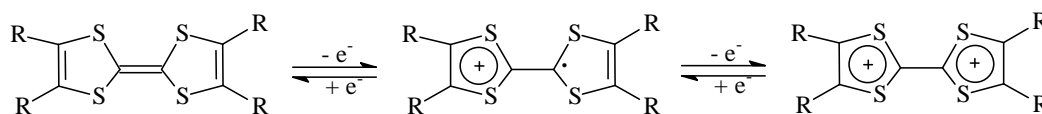
Scheme 3.35. Redox processes of the TTF-core.

In this study, we investigated the electrochemistry of the TTF-containing ligands, α-TTF-Sacac **(39)** and β-TTF-Sacac **(88)**, in CH_2Cl_2 and [N^nBu_4][$B(C_6F_5)_4$] as solvent and supporting electrolyte. Both compounds showed the expected two one-electron redox couples from the TTF core, as shown in **Figure 3.53**. Wave 1 was observed at $E^{o'}$ values of 22 mV and -111 mV, for **(39)** and **(88)**, respectively, while $E^{o'}$ values for wave 2 was

630 mV and 677 mV, respectively (**Table 3.37**). ΔE_p values of smaller than 90 mV were observed for waves 1 and 2, at scan rates of 100 mVs^{-1}, indicating electrochemical reversibility (**Table 3.37**). Both compounds **(39)** and **(88)** also showed chemical reversibility for both redox couples, with peak current ratios of 0.90 to 0.99. Linear sweep voltammetry was also performed, **Figure 3.53**, and it indicated that an equal number of electrons are associated with waves 1 and 2. This is concurrent with two one-electron redox processes as illustrated in **Scheme 3.35**. It is interesting to note that $E^{o'}$-wave 2 - $E^{o'}$-wave 1 = 608 mV for **(39)**, but 788 mV for **(88)**. This clearly shows that **(88)** is much more efficient in delocalizing charged intermediates than **(39)**, probably because the substitution pattern of **(88)** allows less steric hindrance than **(39)**.
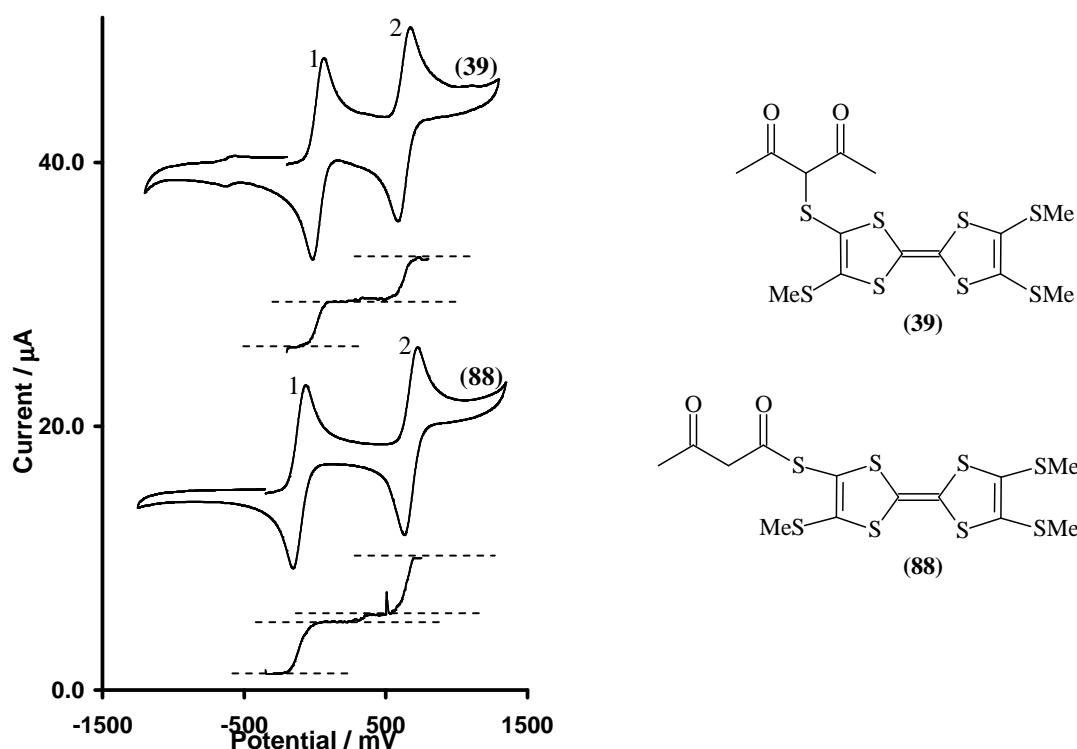
Figure 3.53. CV's, of TTF-containing compounds **(39)** and **(88)**, at a scan rate of 100 mV s^{-1}, as well as LSV's, in CH_2Cl_2/0.1 mol dm^{-3} [N(^{n}Bu$_4$)][B(C$_6$F$_6$)], T = 25°C on a glassy carbon working electrode.

The electrochemistry of rhodium(I) tetrathiafulvalene complexes **(75)** and **(76)** was then explored in CH_2Cl_2 / 0.1 mol dm^{-3} [N^{n}Bu$_4$][B(C$_6$F$_5$)$_4$]. Voltammograms are shown in **Figure 3.54**, and data is summarized in **Table 3.37**. Each complex shows two redox couples belonging to the TTF core, as well as a rhodium redox couple. In the case of

154

(75), wave 1 and 2 shows quasi-reversible one-electron processes at 0.08 V and 0.66V, with $\Delta E_p \approx 130 - 140$ mV at 100 mVs^{-1}. Peak current ratios were found to be approaching 1, indicating chemical reversibility.

Oxidation of the rhodium center from Rh(I) to Rh(II) was observed at 0.89 V (wave 3), with ΔE_p values of between 90 and 150 mV. This indicated electrochemical quasi-reversibility. The rhodium redox couple was found not be chemically reversible, with peak current ratios smaller than 0.8. A property of **(75)** is that both TTF-based redox processes are completed *before* the rhodium center is oxidized. As the scan rate is increased from 100 to 500 mVs^{-1}, a decrease is observed in the peak current ratios i_{pc}/i_{pa} of the rhodium redox couple, wave 3. However, due to the uncertainty and inaccuracy of the measured currents, because of poor peak resolution, this drift in current ratio was not interpreted. Complex **(76)** also showed three one-electron transfer processes. Waves 1 and 3 represent quasi-reversible one-electron redox-couples associated with the TTF core, at -0.17 V and 0.70 V, and ΔE_p values smaller than 150 mV. Peak current ratios were found to be approaching 1, indicating chemical reversibility. For complex **(75)**, oxidation of the rhodium center was observed at 0.51 V (wave 2, *i.e.* between the TTF processes and not after them), with ΔE_p values of between 90 and 150 mV, indicating electrochemical quasi-reversibility. The rhodium redox-couple was found not be chemically reversible, with peak current ratios smaller than 0.5. SW's and LSV's are also shown in **Figure 3.54**. The LSV of both complexes **(75)** and **(76)** show the number of electrons involved to be equal for waves 1, 2, and 3. This confirms all three to be one-electron processes, giving further proof for the oxidation of Rh(I) to Rh(II).
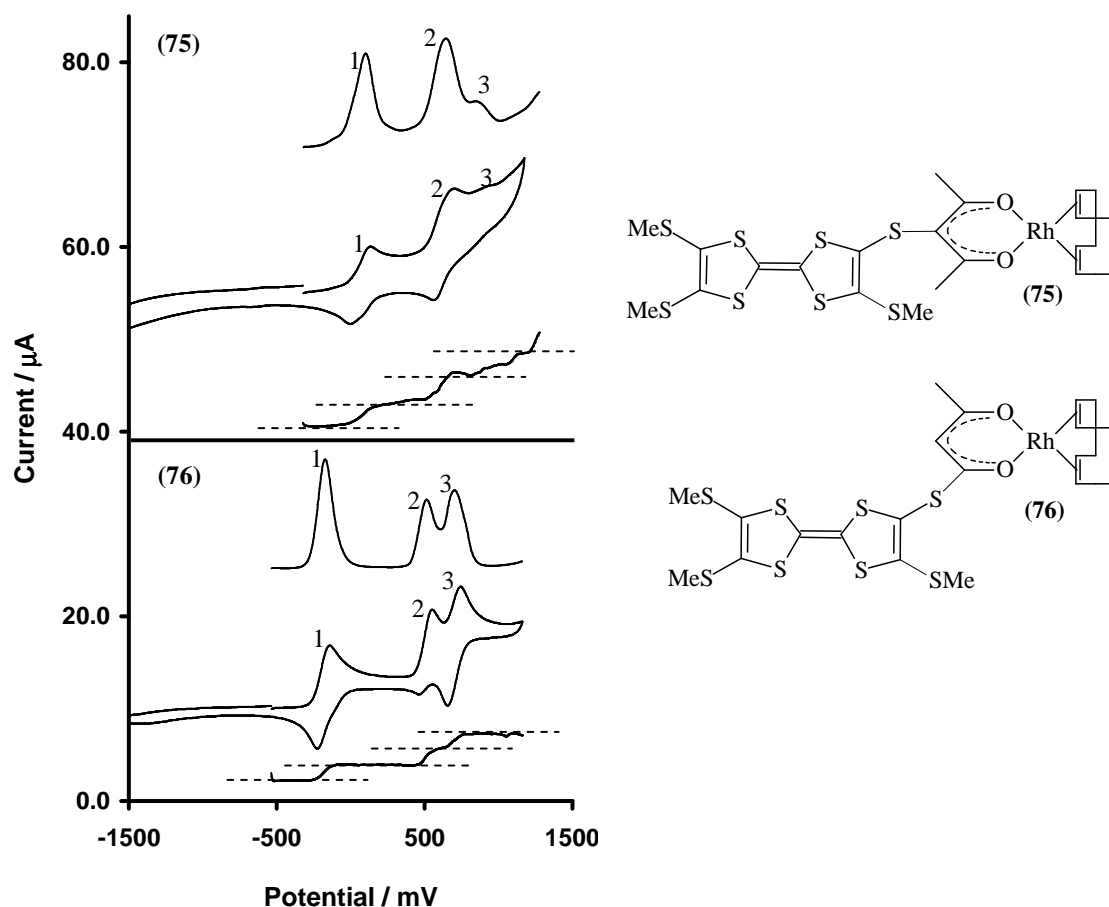
Figure 3.54. CV's, of TTF-containing rhodium(I) complexes **(75)** and **(76)**, at a scan rate of 100 mV s^{-1}, in CH$_2$Cl$_2$/0.1 mol dm^{-3} [N(^{n}Bu$_4$)][B(C$_6$F$_6$)], T = 25°C on a glassy carbon working electrode. SW's (top of each figure) at a frequency of 10 Hz, as well as LSV's (bottom of each figure) are also shown for each complex.

Despite complexes **(75)** and **(76)** possessing similar electronic properties, with only differences in the substitution pattern, a large difference with respect to the rhodium position in the sequence of redox processes were observed. In the case of **(75)**, oxidation of Rh(I) takes place at 0.89 V, and after TTF oxidation. This contrasts the formal reduction potential of 0.51 V for complex **(76)**. The rhodium center of complex **(76)** is thus easier to oxidize, indicating that the TTF group in **(76)** is much better orientated to donate electron density towards the rhodium center. When considering the spatial orientation of the TTF group in both complexes, it can be assumed that due to steric influences of two methyl groups in complex **(75)**, the TTF group is rotated out of the plane of the rhodium center. In the case of complex **(76)**, no such interaction is taking place and the TTF group is orientated to form a flat plane with the rhodium center. This

156

makes donation of electron density much more efficient, forming an overall conjugated system, and thus lowering the oxidation potential of the rhodium center in **(76)**.

Table 3.37. Data obtained for TTF-containing compounds **(39)**, **(88)**, **(75)** and **(76)** in CH_2Cl_2/0.1 mol dm^{-3} [NBu$_4$][B(C$_6$F$_5$)], at T = 25°C.

υ/mVs^{-1}	E_{pa}/mV	ΔE_p/mV	$E^{o'}$/mV	i_{pa}/μA	i_{pc}/i_{pa}	υ/mVs^{-1}	E_{pa}/mV	ΔE_p/mV	$E^{o'}$/mV	i_{pa}/μA	i_{pc}/i_{pa}
α-TTF-Sacac **(39)** – wave 1						α-TTF-Sacac **(39)** – wave 2					
100	64	84	22	5.79	0.97	100	675	90	630	5.36	0.96
200	69	90	24	7.89	0.97	200	679	103	623	7.24	0.94
300	70	101	20	9.55	0.96	300	683	109	629	8.81	0.94
400	71	103	20	11.05	0.94	400	685	114	628	9.93	0.93
500	79	114	22	11.96	0.93	500	686	116	628	10.93	0.93
β-TTF-Sacac **(88)** – wave 1						β-TTF-Sacac **(88)** – wave 2					
100	-68	86	-111	7.46	0.99	100	723	93	677	7.32	0.98
200	-42	115	-100	10.60	0.97	200	746	120	686	10.09	0.96
300	-36	129	-101	13.07	0.94	300	753	128	689	12.31	0.94
400	-35	134	-102	14.93	0.94	400	755	132	689	14.06	0.93
500	-34	138	-103	16.74	0.93	500	758	138	689	15.62	0.90
[Rh(α-TTF-Sacac)(cod)] **(75)** – wave 1						[Rh(α-TTF-Sacac)(cod)] **(75)** – wave 2					
100	151	139	82	1.68	0.95	100	726	134	659	2.15	0.96
200	159	149	85	2.30	0.93	200	738	141	668	2.27	0.94
300	161	157	83	2.85	0.87	300	739	141	669	2.83	0.90
400	169	171	84	3.25	0.86	400	750	149	676	3.25	0.89
500	176	180	86	3.45	0.85	500	758	154	681	3.63	0.87
[Rh(α-TTF-Sacac)(cod)] **(75)** – wave 3						[Rh(β-TTF-Sacac)(cod)] **(76)** – wave 1					
100	931	86	888	0.30	0.80	100	-136	88	-172	6.48	0.95
200	933	91	889	0.49	0.78	200	-126	85	-169	8.92	0.94
300	949	111	892	0.79	0.71	300	-123	86	-166	10.87	0.93
400	958	125	894	0.84	0.64	400	-118	88	-162	12.03	0.91
500	960	137	896	0.87	0.58	500	-112	92	-158	13.80	0.90
[Rh(β-TTF-Sacac)(cod)] **(76)** – wave 2						[Rh(β-TTF-Sacac)(cod)] **(76)** – wave 3					
100	555	90	510	5.25	0.34	100	746	86	703	5.51	0.94
200	585	116	527	6.58	0.29	200	763	110	708	7.97	0.93
300	591	119	532	7.48	0.25	300	765	117	707	9.56	0.91
400	603	120	543	8.91	0.22	400	771	125	709	9.98	0.89
500	620	131	555	10.34	0.19	500	776	131	711	10.38	0.88

(a) E_{pc}, (b) i_{pc}

3.5.6. Electrochemical Isomerization Kinetics

3.5.6.1.   Introduction

A fellow researcher, Christian Kemp, studied the electrochemistry of β-diketone **(6)**, FcCOCH$_2$CORc. It was found that distinction could be made by CV between keto and enol signals of the equilibrium associated with the β-diketone FcCOCH$_2$CORc **(6)**, as shown in **Scheme 3.36**. It was also found that when samples are stored for extended

periods of time (larger than three months) the sample converted quantitatively to the enol isomer. When such a sample was then dissolved, its conversion to a solution having equilibrium concentrations of both enol and keto isomers could be followed by ^{1}H NMR. Rate constants for this enol to keto conversion was thus determined by ^{1}H NMR. The first-order rate constant of enol to keto conversionin deuterated acetonitrile was found to be 0.000039 s^{-1} and in deuterated dichloromethane it was found to be 0.000736 s^{-1}.

The ferrocenyl center of (**6**) showed reversible electrochemistry, in acetonitrile at a glassy carbon working electrode in the presence of 0.1 mol dm^{-3} [N(^{n}Bu)$_4$][PF$_6$] supporting electrolyte. Formal reduction potentials for the ferrocenyl group of the enol and keto species of (**6**) were estimated, $E^{o'}$ = 0.213 and 0.244 V *vs.* Fc/Fc$^+$, respectively. Relevant CV parameters are summarized in **Table 3.38**.

On the other hand, irreversible electrochemistry was found for the ruthenocenyl center of (**6**) in acetonitrile and only peak anodic potentials, E_{pa}, *vs.* Fc/Fc$^+$ in the potential range 0.38 V < E_{pa} < 0.67 V were observed in its CV, **Figure 3.55**. Oxidation of the ruthenocenyl center takes place after the ferrocenyl group is first oxidized to ferrocenium during CV scans. This leads to oxidation of the ruthenocenyl center at a higher potential than expected since it is under the influence of the positively charged ferrocenium species having a group electronegativity (χ_R) of 2.82.
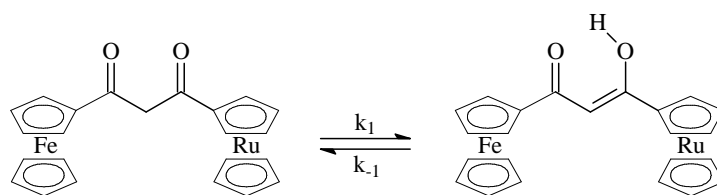
Scheme 3.36. Equilibrium between keto and enol tautomers of FcCOCH$_2$CORc (**6**).

In this study, the electrochemistry of (**6**) (FcCOCH$_2$CORc) was reinvestigated in CH$_2$Cl$_2$ / [(^{n}Bu$_4$N)(B(C$_6$F$_5$)$_4$], and potentials are summarized in **Table 3.38**. Potentials associated with the keto and enol isomers of (**6**) are summarized in **Table 3.38**.

158
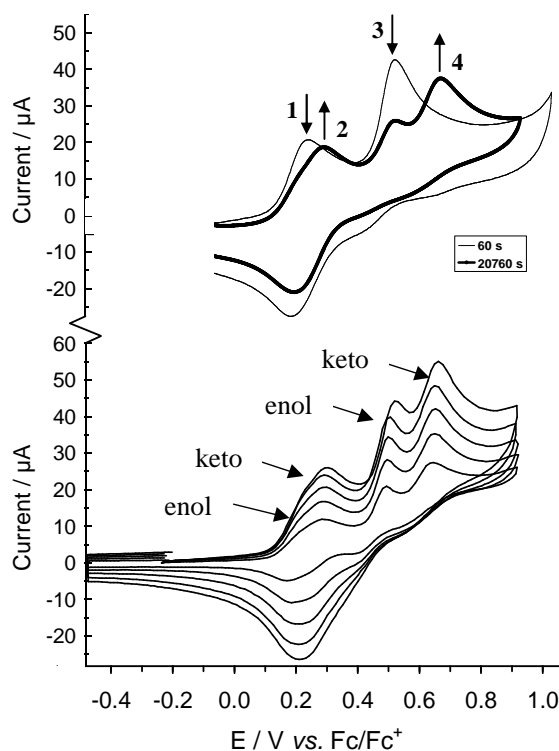
Figure 3.55. *Top*: CV's of a 2.0 mmol dm^{-3} enol solution, and of a near-equilibrium solution (bold line) of FcCOCHCORc **(6)** in CH$_3$CN/ 0.1 mol dm^{-3} [N(^{n}Bu)$_4$][PF$_6$] at 20 °C utilizing a glassy carbon electrode and scan rate of 100 mV s^{-1} recorded at the indicated times after dissolving the sample. *Bottom*: CV's of an equilibrium CH$_3$CN solution of **(6)** at scan rates of 50 (smallest current), 100, 150, 200 and 250 mV s^{-1}.

Table 3.38. Peak anodic potentials *vs.* Fc/Fc$^+$ and peak anodic currents for FcCOCHCORc **(6)**, in CH$_3$CN/ 0.1 mol dm^{-3} [N(^{n}Bu)$_4$][PF$_6$], as well as data for **(6)** in CH$_2$Cl$_2$ / 0.1 M [N(^{n}Bu)$_4$][B(C$_6$F$_5$)$_4$].

% enol [a]	E$_{pa1}$ / mV	i$_{pa1}$ / µA	E$_{pa2}$ / mV	i$_{pa2}$ / µA
CH$_3$CN				
	enol		keto	
42.5	Fc (wave 1) 0.250	- [b]	Fc (wave 2) 0.281	- [b]
(χ_{Fc}=1.87, χ_{Fc+}=2.82)	Rc (wave 3) 0.484[c]	20.0	Rc (wave 4) 0.636[c]	25.8
CH$_2$Cl$_2$				
50.1	Fc (wave 1) 0.265	- [b]	Fc (wave 2) 0.314	- [b]
(dimer,[d] E$_{pc}$= 0.515)	Rc (wave 3) 0.802[c]	- [b]	Rc (wave 4) 0.883[c]	- [b]

(a) By ^{1}H NMR in CDCl$_3$ at equilibrium. (b) Poor peak resolution disallowed peak current measurement. (c) E$_{pa3}$, the ruthenocenyl oxidation potential of the enol form, and E$_{pa4}$, that of the keto form of **(6)** after the ferrocenyl group has *already* been oxidized to ferrocenium. (d) In CH$_2$Cl$_2$, a weak reduction potential was observed which is consistent with dimerization of a Ru^{III} species in analogy with what was found for free ruthenocene.

3.5.6.2. CH$_3$CN as Solvent

The good resolution between keto and enol peaks of **Figure 3.55** suggests that it must in principle be possible to follow the kinetics of isomerization for **(6)** electrochemically, because the keto content at equilibrium approaches 50 %, and because peak current, i$_p$, is

directly proportional to concentration, C, according to the Randles-Sevcik equation, $i_p = (2.69 \times 10^5)n^{3/2}AD^{1/2}Cv$.[32]   Several problems are associated with CV and SW measurements that normally would disqualify these techniques as useful methods in kinetic studies.   The most serious of these is electrode fouling (polluting) that may occur during the extended periods of time required for slow kinetic changes.   For (6), electrode fouling led to

   i) a loss of peak resolution especially for waves 1 and 2,

   ii) a ruthenocenyl-based E_{pa} potential drift of more than 120 mV to more positive values, and

   iii) a slow systematic decrease in current intensity as the electrode surface was compromised.

These problems were overcome by replacing measured i_p values with % keto content relative to an internal standard, free ferrocene, as described in the experimental section. Thus, time based CV experiments on (6) led to rate constants that only scattered between $(8\text{-}14) \times 10^{-5}$ s^{-1} by measuring how the enol wave 3 (**Figure 3.55**) for keto to enol conversions of an enol enriched solution of (6) decreased with time.   Poor peak resolution between peaks 1 and 2 disallowed following this reaction by utilizing the ferrocenyl wave of (6).   Attempts to follow the kinetics in CH_3CN with square wave voltammetry were also unsuccessful.

3.5.6.3. CH_2Cl_2 as Solvent

In an attempt to prove the existence of a $[(C_5H_5)Ru^{III}(C_5H_4R)]^+/ [(C_5H_5)Ru^{II}(C_5H_4R)]$ couple during the electrochemical investigation, the electrochemical kinetic study of enol to keto conversion of (6) were re-investigated in a non-coordinative $CH_2Cl_2/0.1$ mol dm^{-3} $[N(^nBu)_4][B(C_6F_5)_4]$ solvent and supporting electrolyte system. From ^1H NMR data (the temperature study) it was found that isomerization kinetics in CH_2Cl_2 is almost 20 times faster than in CH_3CN, which gives less time for electrode pollution.   In CH_2Cl_2, the resolution of ferrocenyl waves 1 and 2 were markedly improved, especially in the presence of free ferrocene as internal standard. However, the two ruthenocenyl waves at peaks 3 (E_{pa} = 0.802 V) and 4 (E_{pa} = 0.883 V) became much *less* resolved than was found in CH_3CN (**Table 3.38**).   Clear evidence of a $[(C_5H_5)Ru^{III}(C_5H_4R)]^+$ species was also

found, since a cathodic current for the ruthenocenyl group during the reverse sweep could clearly be seen, as shown in **Figure 3.56**.
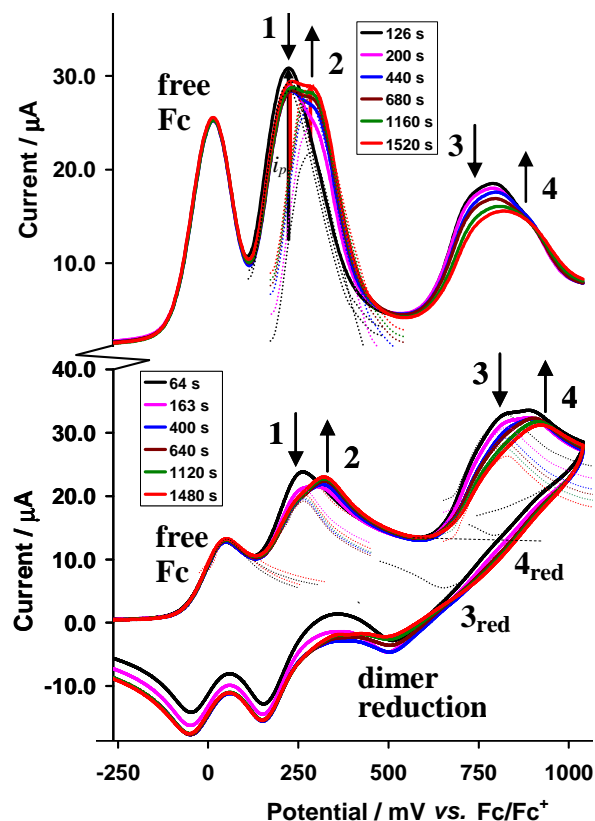
Figure 3.56. Sample square wave voltammograms (top, at 50 Hz) and cyclic voltammograms (bottom at scan rate 200 mV s^{-1}) in CH$_2$Cl$_2$ at 20 $^{\circ}$C showing how the enol form (peaks 1 and 3) becomes less prominent while the keto form becomes more prominent (peaks 2 and 4) as an enol enriched solution of **(6)** approaches equilibrium. For the CV, dotted lines show anticipated decay curves. For the SW's, the dotted lines show the peaks of waves 1 and 2 independent of the influence of each other.

When potentials are not referenced against the experimentally used Ag/Ag$^+$ reference electrode, but rather versus an internal standard, here Fc/Fc$^+$, as first suggested by Gagny,[33] direct potential comparisons between the CH$_3$CN and CH$_2$Cl$_2$ solvent systems become possible. The key result from this treatment is that, although formal reduction potentials *versus* Fc/Fc$^+$ for ferrocenyl-based waves 1 and 2 of **(6)** are for all practical purposes the same in both solvents, potentials associated with ruthenocenyl waves 3 and 4 of **(6)** were shifted to much more positive potentials in CH$_2$Cl$_2$, as shown in **Table 3.38**. Different ruthenocene oxidation products appear to form in CH$_3$CN and CH$_2$Cl$_2$. The ruthenocenyl fragment oxidation product in CH$_3$CN is probably the Ru^{IV} species

$[(C_5H_4R)(Cp)Ru^{IV}\cdot CH_3CN]^{2+}$ while in CH_2Cl_2, the labile Ru^{III} species $[(C_5H_5)Ru^{III}(C_5H_4R)]^+$ is first formed during oxidation. Contrasting this, in both solvents ferrocene oxidation only gave the Fe^{III} species $[(C_5H_5Fe^{III}(C_5H_4R)]^+$. These results highlight different substrate-solvent interactions (CH_3CN contrasting CH_2Cl_2). In particular it shows that strong CH_3CN association occurs with the oxidized ruthenocenyl fragment of (**6**), but that CH_3CN association with the oxidized ferrocenyl fragment of the same molecule are so weak that for all practical purposes it can be neglected.

The i_{pc}/i_{pa} current ratio for waves 3 (the Rc enol wave of (**6**)) and 4 (the Rc keto wave of (**6**)) deviate substantially from unity in CH_2Cl_2. Results therefore are consistent with unstable, i.e quickly decomposing $[(C_5H_5)Ru^{III}(C_5H_4R)]^+$ fragments forming during the oxidation of the ruthenocenyl group of (**6**) at 20 °C. The position of the most prominent $(C_5H_5)Ru^{III}(C_5H_4R)$ fragments reduction wave at E = ca. 0.515 V *vs.* Fc/Fc$^+$ at 20 °C in CH_2Cl_2 (**Figure 3.56**) is consistent with a two-electron Ru^{III} dimer reduction in analogy to free ruthenocene, because it is found at a potential ca. 290 mV lower than $E_{pa,peak\ 3}$ = 802 mV. This peak potential difference is too large to be associated with a simple $(C_5H_5)Ru^{III}(C_5H_4R)]^+$ / $[(C_5H_5)Ru^{II}(C_5H_4R)$ couple. However, weak peak shoulders 3_{red} and 4_{red} are observed at $E_{cathodic}$ = ca. 671 and 777 mV respectively (**Figure 3.56**). Despite the weakness of shoulders 3_{red} and 4_{red} that obviously hampers Ru^{III} reduction peak assignments, key information can be extracted from them. The estimated $\Delta E_p = E_{pa,\ peak\ i} - E_{pc,shoulder\ i}$ values of *ca.* 131 and 106 mV for peak / shoulder pairs 3 and 4 allow them to be associated with reversible to quasi reversible one-electron transfer processes. They are consistent with simple $(C_5H_5)Ru^{III}(C_5H_4R)]^+$ / $[(C_5H_5)Ru^{II}(C_5H_4R)$ couples.

Table 3.39 summarizes sets of time based currents that was collected during the conversion of an enol enriched solution of (**6**) to a solution having the equilibrium content of keto and enol isomers. These data sets were utilized to obtain isomerization rate constants from three different electrochemical sets of kinetic experiments performed in CH_2Cl_2. Time-based plots showing how the % keto isomer increase as the equilibrium position is approached from the enol side for all three electrochemical experimental approaches are shown in **Figure 3.57**. The insert highlights the validity of a first-order

162

treatment of ferrocenyl-based square wave obtained kinetic data. Rate constants $k_{obs} = k_1 + k_{-1}$ for all three techniques approached 3×10^{-3} s^{-1}. This corresponded well with the ^{1}H NMR experimental result giving $k_{obs} = 1.47 \times 10^{-3}$ s^{-1} that was obtained by Kemp[34] earlier.
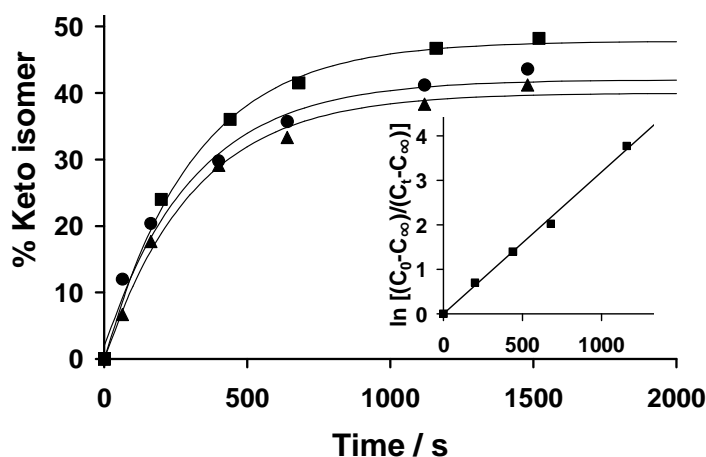
Figure 3.57. Time trace showing the formation of % keto isomer as determined by ferrocenyl-based square wave (■, top), ruthenocenyl-based cyclic (●, middle) and ferrocenyl-based cyclic (▲, bottom) voltammetry for **(6)** at 25°C in CH$_2$Cl$_2$. *Insert*: a kinetic plot of ferrocenyl-based square wave data from **Table 3.39** for this isomerization. The slope of this graph gives the first order rate constant $k_{obs} = k_1 + k_{-1}$ =0.0031 s^{-1} (C = % keto isomer).

Table 3.39. Cyclic voltammetry data of ferrocenyl waves 1 and 2 (labeled as Fc-CV) and ruthenocenyl waves 3 and 4 (Rc-CV) collected with time for the conversion of enol to keto isomers of RcCOCH$_2$COFc **(6)** in CH$_2$Cl$_2$ at 20°C. Values in brackets corresponds to square wave data of ferrocenyl waves 1 and 2 (Fc-SW).

Measurement time / s Fc CV / Rc CV (Fc SW)	i_{pa}, enol / μA Fc CV / Rc CV (Fc SW)	i_{pa}, keto / μA Fc CV / Rc CV (Fc SW)	% keto [a] Fc CV / Rc CV (Fc SW)	$\ln \dfrac{(\%\,keto)_0 - (\%\,keto)_\infty}{(\%\,keto)_t - (\%\,keto)_\infty}$ Fc CV / Rc CV (Fc SW)
0 / 0 (0)	-[b] / -[b] (-)[b]	-[b] / -[b] (-)[b]	0[c] / 0[c] (0)[c]	0[c] / 0[c] (0)[c]
64 / 64 (200)	41.5 / 49 (44)	3 / 6.7 (14)	6.7 / 12.0 (24.1)	0.183 / 0.288 (0.702)
163 / 163 (440)	38 / 43 (34)	8.2 / 11 (19)	17.7 / 20.4 (35.9)	0.584 / 0.616 (1.391)
400 / 400 (680)	34 / 40 (31)	14 / 17 (22)	29.1 / 29.8 (41.5)	1.300 / 1.236 (2.027)
640 / 640 (1160)	32 / 36 (30)	16 / 21 (24)	33.3 / 36.8 (46.7)	1.787 / 2.089 (3.712)
1120 / 1120 (1520)	29 / 34 (29)	18 / 23.4 (27)	38.3 / 40.8 (48.2)	3.158 / 3.555 (-)[d]
t = ∞	-[b] / -[b] (-)[b]	-[b] / -[b] (-)[b]	40[c] / 42[c] (47.8)[c]	- - -

(a) $\%\,keto = \dfrac{i_{pa},\,keto}{i_{pa},\,keto + i_{pa},\,enol} \times 100$. (b) Not measured due to the time required for dissolving analytes. (c) Values not measured but obtained from a non-linear least squares MINSQ fit. (d) Because the measured i_p value is larger than the calculated t_∞ value, this data point was not calculated.

Finally, the % keto isomer at equilibrium in CH$_2$Cl$_2$ as obtained by the Fc-CV, Rc-CV and Fc-SW experiments are 40, 42 and 47.8 % respectively (**Table 3.39**). The

equilibrium constant $K_c = k_1 / k_{-1}$ applicable to **Scheme 3.36** were also determined as 1.50 from Fc – CV experiments, **Table 3.39**, 1.38 from Rc – CV experiments and 1.09 from Fc – SW measurements. The average K_c value is thus 1.32.

By simultaneously solving the equations $K_c = k_1 / k_{-1}$ and $k_{obs} = k_1 + k_{-1} = 3 \times 10^{-3}$ s^{-1}, the rate constants k_1 and k_{-1} applicable to the equilibrium keto **(6)** $\underset{k_{-1}}{\overset{k_1}{\rightleftharpoons}}$ enol **(6)** (**Scheme 3.36**) could be calculated as $k_1 = 0.00172$ s^{-1} and $k_{-1} = 0.00131$ s^{-1}. By ^{1}H NMR measurements k_1 and k_{-1} were found to be 0.00074 s^{-1} and 0.00073 s^{-1}. The close agreement of the electrochemical and ^{1}H NMR methods of determining rate constants of slow isomerisation kinetic processes are extremely satisfying. This study represents the first study to successfully utilise electrochemical measurements (CV and SW) to obtain kinetic data of isomerisation processes involving redox active compounds.

3.6. Anti-Cancer Studies on Metal-Containing Complexes

The purpose of the synthesis of all the described complexes of this study was to investigate their physical properties, as well as investigate their possible application in terms of cancer treatment. This was considered appropriate, since it has been found that complexes of rhodium(I)[35], as well as ferrocene-containing compounds[36] show promising anti-tumor activity, with only marginal toxicity, as discussed in **Chapter 2** (**Section 2.8**). The effectivity of all new synthesized compounds in terms of cancer treatment was probed by determining their cytotoxicity against cancer cells. The type of cancer cells used in this study was HeLa, a human cervix epitheloid cancer cell line. Selected compounds were also probed against CoLo (a human colorectal cell line). Prof. C.E.J. Medlen, from the Department of Pharmacology at the University of Pretoria is acknowledged for performing these tests. Cytotoxicity is presented as IC$_{50}$-values, and indicate the drug dose required to kill 50 % of cancer cells. Tests were also performed on cisplatin **(63)** for benchmarking.

3.6.1. Metallocene-containing and Fluorinated Phosphines

The metallocene-containing phosphine ligands PPh$_2$Fc **(13)**, PPh$_2$Rc **(65)** and PPh$_2$Oc **(66)** were all tested for cytotoxicity, in order to determine the influence of the different

metallocene centers on the compounds anti-tumor activity, as well as to be able to compare the results to that of the rhodium(I) compounds complexed with these phosphines. Data obtained are listed in **Table 3.40**.

Table 3.40. IC_{50}-values for HeLa cell lines after treatment with phosphines of the type PPh_2R. Group electronegativities (χ_R) of the R-group are also shown.

R	χ_R	IC_{50} for HeLa cell line / μmol.dm^{-3}
Fc (13)	1.87	21(3)
Rc (65)	1.99	33.1(5)
Oc (66)	1.90	>50
Cisplatin (63)	-	0.5(1)

No clear trend, with respect to a relationship between IC_{50}-values and group electronegativity, could be observed from the results obtained. It is clear, however, that the ferrocenyl-containing compound **(13)** is the most effective in this series. Still, none of the metallocene-containing compounds exhibited anti-tumor activity comparable to that of cisplatin **(63)**. It is expected that, when these ligands are coordinated to a metal center possessing anti-tumor activity, significant increases in IC_{50}-values would be observed due to synergistic effects.

Phosphine ligands containing pentafluorophenyl rings, $PPh_2(C_6F_5)$ **(90)**, $PPh(C_6F_5)_2$ **(91)** and $P(C_6F_5)_3$ **(92)**, were also tested for their cytotoxicity in order to be able to compare the results to that of the rhodium(I) compounds complexed with these phosphines. Data obtained are listed in **Table 3.41**.

Table 3.41. IC_{50}-values for HeLa and CoLo cell lines after treatment with phosphines of the type $PPh_n(C_6F_5)_{3-n}$. Total group electronegativities (χ_R) of the phosphine substituents are also shown {χ_R = 2.21 for Ph, χ_R = 2.46 for (C_6F_5)}.

Compound	χ_R (R' + R" + R''')	IC_{50} for HeLa cell line / μmol.dm^{-3}	IC_{50} for CoLo cell line / μmol.dm^{-3}
$PPh_2(C_6F_5)$ (90)	6.88	37.2(8)	-
$PPh(C_6F_5)_2$ (91)	7.13	35(4)	-
$P(C_6F_5)_3$ (92)	7.38	6(2)	7(1)
Cisplatin (63)	-	0.5(1)	1.6(3)

Results obtained showed significant anti-tumor activity for the highest fluorinated phosphine **(92)**. Comparable IC_{50}-values were obtained for **(90)** and **(91)**. The HeLa cell survival curve for **(92)** is shown in **Figure 3.58**.
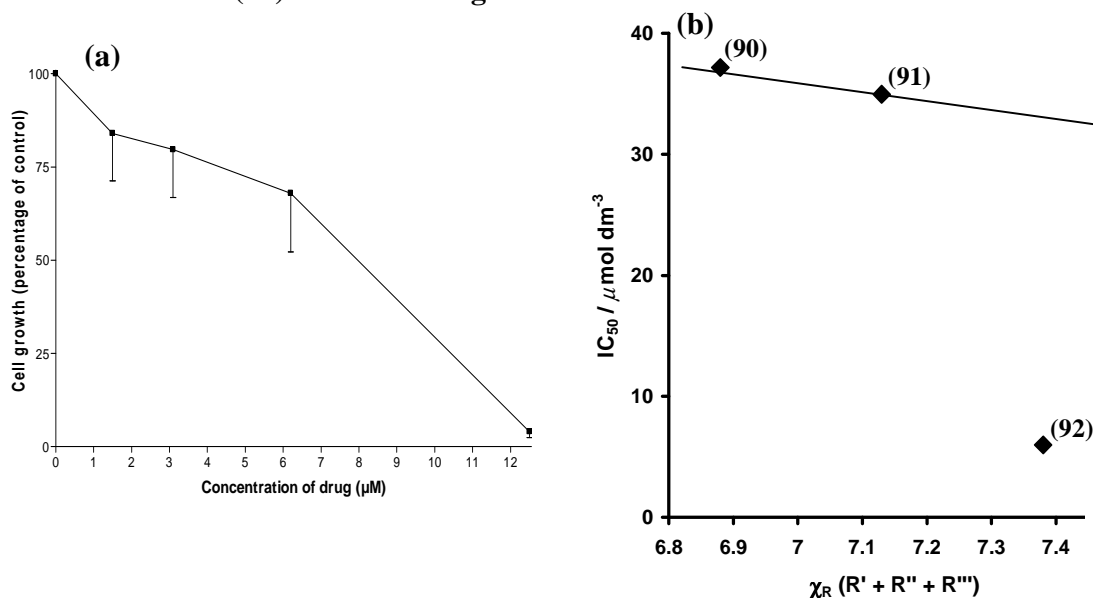
Figure 3.58. (a) Plot of percentage survival CoLo cells against concentration (μmol dm^{-3}) of P(C$_6$F$_5$)$_3$ **(92)**. **(b)** Graph of HeLa IC_{50}-values *vs*. the total group electronegativity of the phosphorus substituents for phosphines PPh$_n$(C$_6$F$_5$)$_{3-n}$, where n = 0 **(90)**, 1 **(91)**, 2 **(92)**.

3.6.2. Rhodium(I) Phosphine Complexes

Rhodium(I) complexes containing metallocenyl phosphine ligands of the type [Rh(FcCOCHCOCF$_3$)(CO)(PPh$_2$Mc)] where Mc = Fc **(70)** and Rc **(71)**, were tested for their cytotoxicity. For reasons of comparison the rhodium(I) complex with triphenylphosphine, [Rh(FcCOCHCOCF$_3$)(CO)(PPh$_3$)] **(29)**, as well as the parent rhodium(I) dicarbonyl complex [Rh(FcCOCHCOCF$_3$)(CO)$_2$] **(57)** were also tested for their anti-tumor properties. Data obtained are listed in **Table 3.42**.

Table 3.42. IC_{50}-values for HeLa and CoLo cell lines after treatment with rhodium(I) phosphine complexes of the type [Rh(FcCOCHCOCF$_3$)(CO)(L)]. Group electronegativities (χ_R) of the varying phosphine substituent are also shown.

L	χ_R	IC_{50} for HeLa cell line / μmol.dm^{-3}	IC_{50} for CoLo cell line / μmol.dm^{-3}
CO **(57)**	-	21.2(1)	-
PPh$_3$ **(29)**	2.21	10.9(5)	20(1)
PPh$_2$Fc **(70)**	1.87	19(3)	-
PPh$_2$Rc **(71)**	1.99	16(1)	-
Cisplatin **(63)**	-	0.5(1)	1.6(3)

The results obtained showed that all phosphine-containing complexes exhibited better cytotoxic properties than that of the dicarbonyl complex **(57)**. When phosphine ligands are present a linear decrease in IC_{50}-values is observed as the group electronegativity (χ_R) of the varying phosphine substituent increases, with **(29)** possessing the lowest IC_{50}-value. This trend is shown in **Figure 3.59**, and indicates that in this series of compounds, the χ_R-value (*i.e.* electron richness) is an important factor controlling cytotoxicity. However, presence of an additional metallocene on the phosphine ligand does not add to the cytotoxic properties of the drug in a synergistic way. The anti-tumor activity of **(29)** was also tested *vs*. CoLo cells, but showed significant reduced anti-tumor activity. The survival curve for **(29)** *vs*. CoLo cells are shown in **Figure 3.59**.
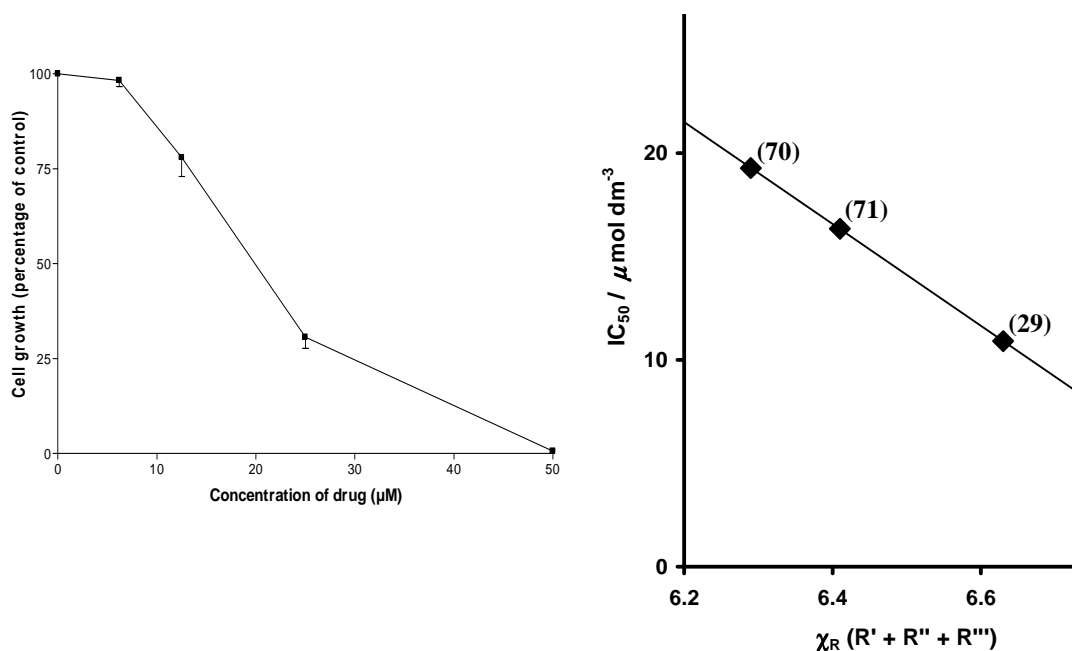
Figure 3.59. (a) Plot of percentage survival CoLo cells against concentration (μmol dm^{-3}) of [Rh(FcCOCHCOCF$_3$)(CO)(PPh$_3$)] **(29)**. **(b)** Graph of IC_{50}-values *vs*. the total group electronegativity of the phosphorus substituents for rhodium(I) complexes [Rh(FcCOCHCOCF$_3$)(CO)(PPh$_2$R)], with R = Ph **(29)**, Fc **(70)** and Rc **(71)**.

Rhodium(I) complexes containing fluorinated phosphine ligands of the type [Rh(FcCOCHCOCF$_3$)(CO)(PPh$_n$(C$_6$F$_5$)$_{3-n}$)], with n = 0 **(72)**, 1 **(73)** and 2 **(74)**, were also tested for their cytotoxicity. Data obtained are listed in **Table 3.43**, as well as that obtained for [Rh(FcCOCHCOCF$_3$)(CO)(PPh$_3$)] **(29)**, and the parent rhodium(I) dicarbonyl complex [Rh(FcCOCHCOCF$_3$)(CO)$_2$] **(57)**.

167

Table 3.43. IC$_{50}$-values for HeLa and CoLo cell lines after treatment with rhodium(I) complexes containing fluorinated phosphines of the type [Rh(FcCOCHCOCF$_3$)(CO)(L)]. Total group electronegativities (χ_R) of the phosphine substituents are also shown {χ_R = 2.21 for Ph, χ_R = 2.46 for (C$_6$F$_5$)}.

L	χ_R (R' + R" + R''')	IC$_{50}$ for HeLa cell line / μmol.dm^{-3}	IC$_{50}$ for CoLo cell line / μmol.dm^{-3}
CO (57)	-	21.2(1)	-
PPh$_3$ (29)	6.63	10.9(5)	20(1)
PPh$_2$(C$_6$F$_5$) (72)	6.88	11(4)	7(1)
PPh(C$_6$F$_5$)$_2$ (73)	7.13	13(2)	29(4)
P(C$_6$F$_5$)$_3$ (74)	7.38	2.4(6)	19(1)
Cisplatin (63)	-	0.5(1)	1.6(3)

The results obtained showed that all phosphine-containing complexes exhibited better cytotoxic properties than that of the dicarbonyl complex **(57)**. When phosphine ligands are present, comparable IC$_{50}$-values were obtained for **(29)**, **(72)** and **(73)**, but dramatically lower values were found for **(74)** when tested against HeLa cells. This indicates that for the fluorinated phosphines complexes, no significant relationship exists between the group electronegativity (χ_R) of the phosphine ligands and the cytotoxic properties, as can be seen from **Figure 3.60**. All fluorine-containing complexes showed better anti-tumor activity than metallocene-containing complexes. Similar to the observations made when investigating the pure phosphine ligands, a dramatic increase in cytotoxic properties is observed for the compound containing three pentafluorophenyl rings **(74)**. IC$_{50}$-values obtained for all the fluorinated phosphine-containing rhodium(I) complexes possessed the overall best cytotoxic properties. This indicates that the pentafluorophenyl ring plays a key role in determining cytotoxic activity. When present in high quantities, as in **(74)**, it becomes the dominant drug fragment operating synergistically with the rhodium(I) nucleus. The anti-tumor activities of all complexes were also tested *vs.* CoLo cells, but no clear trend could be observed. Survival curves for CoLo cells against complexes **(72)**, **(73)** and **(74)** are shown in **Figure 3.60**.
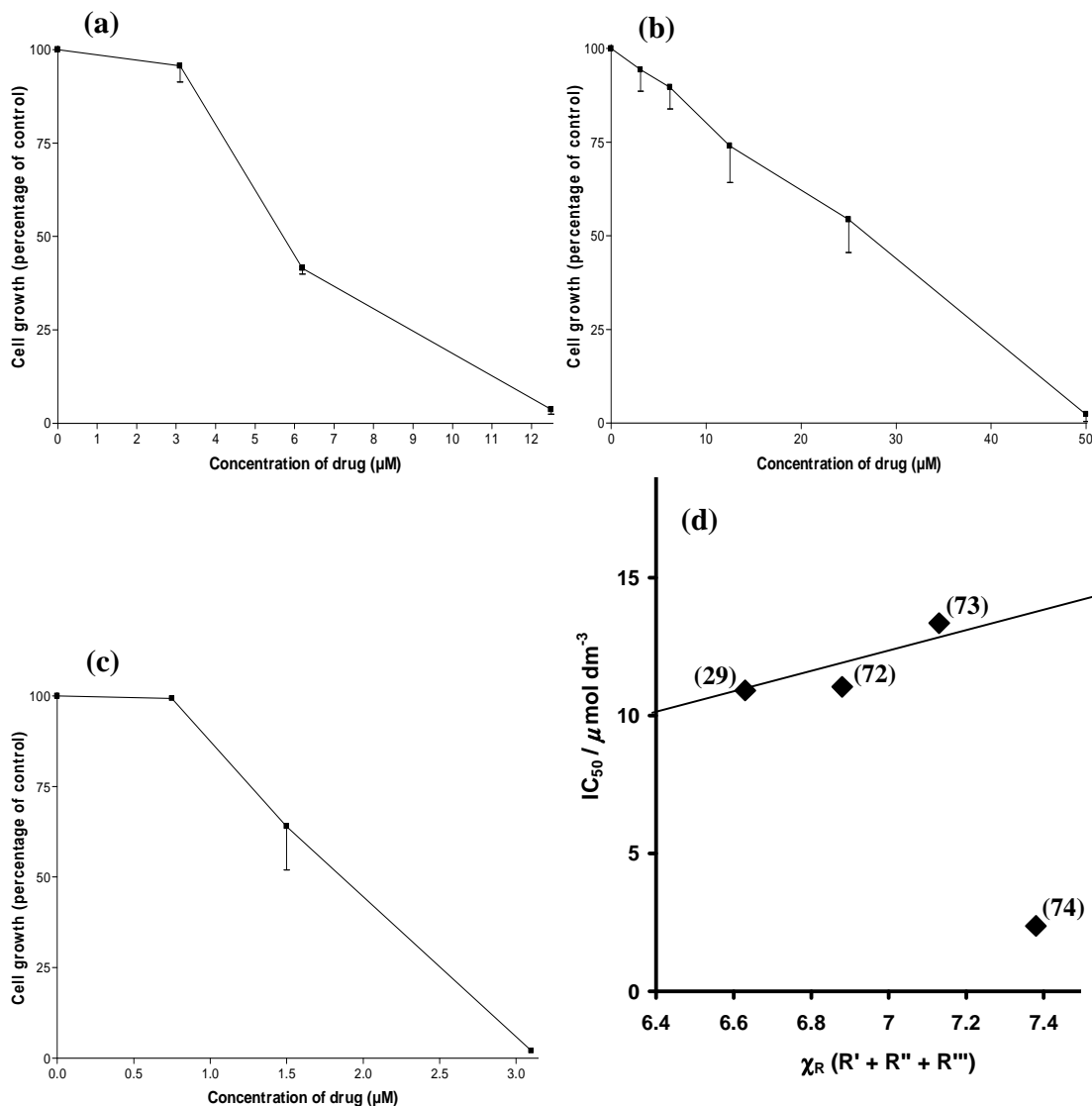
Figure 3.60. Plots of percentage survival CoLo cells against concentration (μmol dm^{-3}) for rhodium(I) phosphine complexes of the type [Rh(FcCOCHCOCF$_3$)(CO)(PPh$_n$(C$_6$F$_5$)$_{3-n}$)], where n = 2 **(72) (a)**, 1 **(73)** **(b)** and 0 **(74) (c)**. **(d)** Graph of IC$_{50}$-values *vs*. the total group electronegativity of the phosphorus substituents for rhodium(I) complexes containing fluorinated phosphines.

3.6.3. Tetrathiafulvalene-Containing Compounds

Tetrathiafulvalene (TTF) containing rhodium(I) complexes, [Rh(α-TTF-Sacac)(cod)] **(75)** and [Rh(α-TTF-Sacac)(cod)] **(76)**, and the free TTF-containing ligands, (α-TTF-Sacac) **(39)** and (β-TTF-Sacac) **(88)** were the last compounds tested for anti-tumor activity. Results obtained are listed in **Table 3.44**.

Table 3.44. IC$_{50}$-values for HeLa and CoLo cell lines after treatment with TTF-containing complexes.

Compound	IC$_{50}$ for HeLa cell line / μmol.dm^{-3}	IC$_{50}$ for CoLo cell line / μmol.dm^{-3}
(α-TTF-Sacac) (39)	16(1)	1.7(2)
(β-TTF-Sacac) (88)	19.5(5)	-
[Rh(α-TTF-Sacac)(cod)] (75)	>50	-
[Rh(β-TTF-Sacac)(cod)] (76)	-[a]	-
Cisplatin (63)	0.5(1)	1.6(3)

(a) Not soluble in test medium to perform experiments.

The rhodium(I) complex containing the TTF-group on the terminal position of the β-diketone **(76)** did not dissolve in appropriate concentrations in the test medium, and could not be used in these assays. The other rhodium(I) complex containing the TTF-group on the central α-position of the β-diketone **(75)**, showed no observable anti-tumor activity within the tested range. However, both TTF-containing ligands **(39)** and **(88)**, showed significant and comparable IC$_{50}$-values. Survival curves for compounds **(39)** and **(88)** are shown in **Figure 3.61**. This indicates that the TTF-group is a cytotoxically active fragment, but activity is lost when complexed with Rh(I), and no synergistic effects are observed.
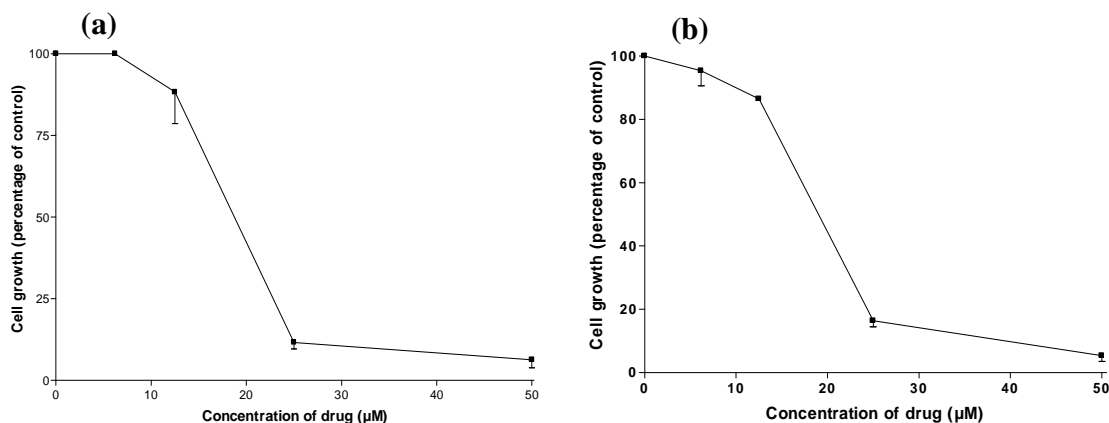
Figure 3.61. (a) Plot of percentage survival CoLo cells against concentration (μmol dm^{-3}) for (α-TTF-Sacac) **(39)**. **(b)** Plot of percentage survival HeLa cells against concentration (μmol dm^{-3}) for (β-TTF-Sacac) **(88)**.

[1] B.S. Furniss, A.J. Hannaford, P.W.G. Smith, A.R. Tatchell, *Vogel's Textbook of Practical Organic Chemistry*, 5th ed., Pearson Education Limited, Harlow, England, **1989**, pp. 693-695.

[2] G.P. Sollot, H.E. Mertwoy, S. Portnoy, J.L. Snead, *J. Org. Chem*, 1962, **28**, 1090-1092.

[3] A.W. Rudie, D. W. Lichtenberg, M.L. Katcher, A. Davison, *Inorganic Chemistry*, 1978, **17**, 2859-2863.

[4] E.C. Steynberg, G.J. Lamprecht, J.G. Leipoldt, *Inorg. Chim. Acta*, 1987, **133**, 33-37.

[5] J. Conradie, G.J. Lamprecht, S. Otto, J.C. Swarts, *Inorg. Chim. Acta*, 2002, **328**, 191

[6] D.E. Bublitz, K.L. Rinehart, *Organic Reactions*, 1969, **17**, 76.

[7] P.J. Swarts, M. Immelman, G.J. Lamprecht, S.E. Greyling, J.C. Swarts, *S. Afr. J. Chem.*, 1997, **50**, 208.

[8] J. Conradie, Ph.D. Study, *Chemical kinetics, electrochemistry and structural aspects of ferrocene-containing betadiketonato complexes of rhodium(I) and iridium(I)*, University of the Free State, R.S.A., 1999.

[9] D. Vagedes, G. Erker, G. Kehr, K. Bergander, O. Kataeva, R. Fröhlich, S. Grimme, C. Mück-Lichtenfeld, *J. Chem. Soc. Dalton Trans.*, 2003, 1337-1344.

[10] J.L. Davidson, B. Holz, P.C. Leverd, W.E. Lindsell, N.J. Simpson, *J. Chem. Soc. Dalton Trans.*, 1994, 3527-3532.

[11] M. Ozcesxmeci, E. Hamuryudan, *Dyes and Pigments*, 2008, **77**, 457-461.

[12] N. Bellec, J. Massue, T. Roisnel, D. Lorcy, *Inorg. Chem. Comm.*, 2007, **10**, 1172-1176.

[13] J. Conradie, G.J. Lamprecht, A. Roodt, J.C. Swarts, *Polyhedron*, 2007, **26**, 5075-5087.

[14] G.M. Barrow, *Physical Chemistry*, 6th edition, McGraw-Hill Companies, Inc., New York, 1996, pp. 801-803.

[15] W.C. du Plessis, J.J.C. Erasmus, G.J. Lamprecht, J. Conradie, T.S. Cameron, A.S. Aquino, J.C. Swarts, *Can. J. Chem.*, 1999, **77**, 378-386.

[16] A. Auger, J.C. Swarts, *Organometallics*, 2007, **26**, 102-109.

[17] J.A. Adeleke, L.K. Liu, *Acta Cryst*, 1993, **C49**, 680-682.

[18] L.E. Sutin, *Tables of Interatomic Distances and Configuration in Molecules and Ions, Supplement 1956-1959*, The Chemical Society, London, p. S16s.

[19] T. Hayashi, A. Ohno, S. Lu, Y. Matsumoto, E. Fukuyo, K. Yanagi, *J. Am. Chem. Soc.*, 1994, **116**, 4221-4226.

[20] S. Li, B. Wei, P.M.N. Low, H.K. lee, T.S.A. Hor, F. Xue, T.C.W. Mak, *J. Chem. Soc., Dalton Trans.*, 1997, 1289-1293.

[21] S. Otto, A. Roodt, J.J.C. Erasmus, J.C. Swarts, *Polyhedron*, 1998, **17**, 2447-2453.

[22] J.G. Leipoldt, S.S. Basson, L.D.C. Bok, T.I.A. Gerber, *Inorg. Chim. Acta*, 1978, L35-L37.

[23] G.J. Lamprecht, J.C. Swarts, J. Conradie, J.G. Leipoldt, *Acta Cryst. C*, 1993, **49**, 82.

[24] N.E. Murr, *Transition Met. Chem.*, 1981, **6**, 321-324.

[25] J.C. Swarts, D. Laws, W.E. Geiger, *Organometallics*, 2005, **24**, 341-343.

[26] J.C. Kotz, C.L. Nivert, *J. Organomet. Chem.*, 1973, **52**, 387-406.

[27] A. Gref, P. Diter, D. Guillaneux, H.B. Kagan, *New J. Chem.*, 1997, **21**, 1353-1358.

[28] F. Barrière, R.U. Kirss, W.E. Geiger, *Organometallics*, 2005, **24**, 48-52.

[29] J. Conradie, T.S. Cameron, M.A.S. Aquino, G.J. Lamprecht, J.C. Swarts, *Inorg. Chim. Acta*, 2005, **358**, 2530-2542.

[30] J. Massue, N. Bellec, S. Chopin, E. Levillain, T. Roisnel, R. Clérac, D. Lorcy, *Inorg. Chem.*, 2005, **44**, 8740-8748.

[31] E. Sezer, F. Turksoy, U. Tunca, T. Ozturk, *J. Electroanalytical Chem.*, 2004, **570**, 101-105.

[32] P.T Kissinger, W.R. Heineman, In *Laboratory techniques in electroanalytical chemistry*, Marcel Dekker, Inc., New York, 1984, p. 82.

[33] R.R. Gagne, C.A. Koval, G.C. Lisensky, *Inorg. Chem.* 1980, **19**, 2855.

[34] K.C. Kemp, M.Sc. Study, *Syntesis, electrochemical, kinetic and thermodynamic studies of new ruthenocene-containing betadiketonato rhodium(I) complexes with biomedical applications*, University of the Free State, R.S.A., 2004.

[35] Sava, S. Zorzet, L. Perissin, G. Mestroni, G. Zassinovich, A. Bontempi, *Inorg. Chim. Acta*, 1987, **137**, 69-71.

[36] E.W. Neuse, F. Kanzawa, *Applied Organomet. Chem.*, 1990, **4**, 19-26.

Chapter 4

Experimental

4.1. Introduction

This chapter describes all experimental procedures, reaction conditions and techniques for the synthesis of all compounds, as well as all kinetics, electrochemistry and cytotoxic testing.

4.2. Materials

Solid reagents (Merck and Aldrich) were used without further purification. Liquid reagents and solvents were distilled prior to use, and water was double distilled. Organic solvents were dried according to published methods.[1] Chromatography was performed on SiO_2 (Merck Kieselgel 60, grain size 0.040 – 0.063 mm) as solid phase. Melting points (m.p.) were determined with an Olympus BX 51 microscope equipped with a Linkam THMS 600 heating apparatus and are uncorrected.

4.3. Spectroscopic Measurements

NMR measurements were recorded on either a Bruker Advance DPX 300 NMR spectrometer or a Bruker Advance II 600 NMR spectrometer. Chemical shifts were reported relative to $SiMe_4$ at 0.00 ppm, utilizing the solvent peak as internal standard. IR spectra were recorded on a Digilab 2000 Fourier transform spectrometer utilizing a He-Ne laser at 633 nm. UV spectra were recorded on a Cary 50 Probe UV/Visible spectrophotometer. Temperature was controlled using a water bath to within $\pm\, 0.1\ °C$.

4.4. Synthesis

4.4.1. Ruthenocene (93)

(93)
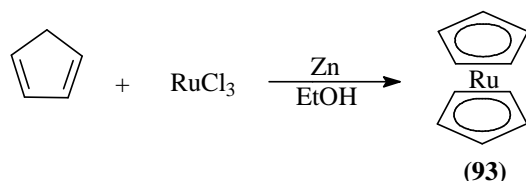
Ruthenium trichloride (5 g, 24.1 mmol) was added to a stirred solution of dried ethanol (140 ml) and freshly cracked cyclopentadiene (140 ml, 72.3 mmol, 3 eq.), under N_2. Zinc-dust (50 g, 36.2 mmol, 1.5 eq.) was slowly added, and the suspension stirred for 2 h. The solution was filtered and the precipitate washed with ether (200 ml). The combined organic layers were washed with water (3 x 100 ml). It was filtered, at reduced pressure, through silica gel, and the silica gel washed with ether (200 ml). The solvent was removed under reduced pressure, and the product recrystallized from hexane and ether. Yield 79 % (4.38 g). Melting point = 198 °C. δ_H (300 MHz, $CDCl_3$)/ppm: 4.58 (s; 10H; 2 x (C_5H_5)), **Spectrum 1**.

4.4.2. Acetyl Ferrocene (94)

(94)
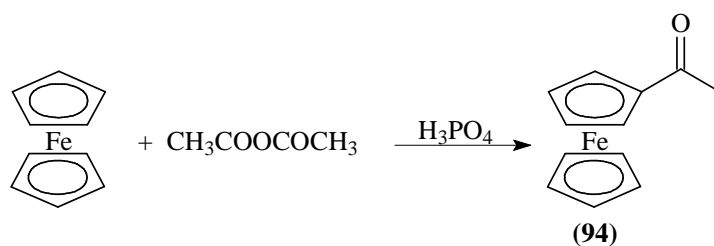
Ferrocene (5 g, 26.9 mmol) was dissolved in acetic anhydride (25 ml, 266 mmol, 10 eq.) and, while stirring, 85 % phosphoric acid (2.5 ml, 22.0 mmol, 0.8 eq.) was added slowly. The mixture was heated to 90 °C for 10 min. Ice was added and the mixture neutralized with a saturated $NaHCO_3$ solution. It was directly filtered and the precipitate washed with water (100 ml). Column chromatography, using hexane : ether (1:1) (R_f = 0.38) was used to purify the product. Yield 60 % (2.85 g). Melting point = 85 °C. υ(C=O) = 1661 cm^{-1}. δ_H (300 MHz, $CDCl_3$)/ppm: 4.80 (t; 2H; 0.5 x C_5H_4); 4.53 (t; 2H; 0.5 x C_5H_4); 4.23 (s; 5H; C_5H_5); 2.42 (s; 3H; CH_3), **Spectrum 2**.

4.4.3. Acetyl Ruthenocene (95)

(93) + CH$_3$COOCOCH$_3$ $\xrightarrow[\text{DCM}]{\text{AlCl}_3}$ **(95)**
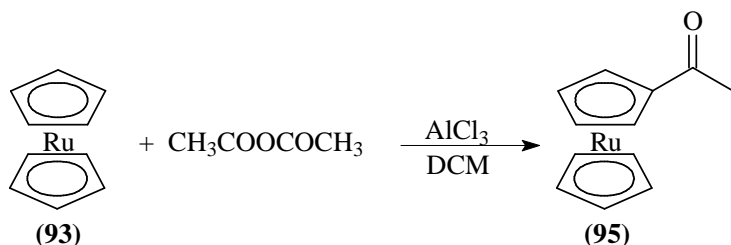
A solution of ruthenocene (1.5 g, 6.5 mmol) and aluminum trichloride (1.9 g, 14.3 mmol, 2.2 eq.) in CH$_2$Cl$_2$ (135 ml) was brought to reflux, under N$_2$. Acetic anhydride (0.6 ml, 6.5 mmol, 1 eq.), in CH$_2$Cl$_2$ (30 ml) was slowly added to the mixture, all under N$_2$. The reaction mixture was refluxed for a further hour, water (135 ml) was added, and refluxing continued for another 20 minutes. The layers were separated and the organic layer washed with water (3 x 100 ml), dried over sodium sulphate, and the solvent evaporated under reduced pressure. The product was purified with column chromatography, using hexane : ether (1:1) (R$_f$ = 0.42). Yield 55 % (0.98 g). Melting point = 112 °C. υ(C=O) = 1652 cm^{-1}. δ_H (300 MHz, CDCl$_3$)/ppm: 5.11 (t; 2H; 0.5 x C$_5$H$_4$); 4.80 (t; 2H; 0.5 x C$_5$H$_4$); 4.61 (s; 5H; C$_5$H$_5$); 2.32 (s; 3H; CH$_3$), **Spectrum 3**.

4.4.4. Acetyl Osmocene (96)

+ CH$_3$COOCOCH$_3$ $\xrightarrow{\text{H}_3\text{PO}_4}$ **(96)**
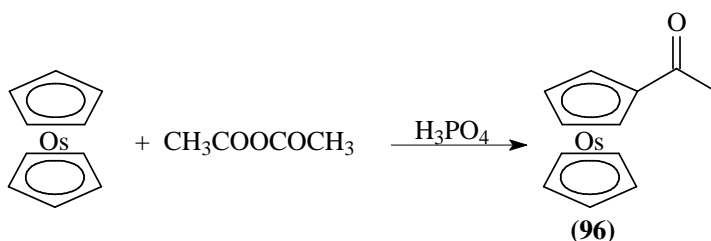
85 % Phosphoric acid (3 ml, 2.6 mmol, 4.0 eq.) was added to acetic anhydride (10 ml, 0.1 mol, 40 eq.) at 0 °C and degassed under Ar for 1 hour. Osmocene was added at 0 °C, then heated to 80 °C for 4 hours. After cooling the mixture completely, on ice, aqueous sodium carbonate with ice was added until neutralized. Products were extracted with CH$_2$Cl$_2$ (3 x 50 ml), and the organic layer washed with water (3 x 50 ml). The product was purified with column chromatography, using hexane : ether (1:1) (R$_f$ = 0.49). Yield 55 % (0.98 g). Melting point = 131 °C. υ(C=O) = 1668 cm^{-1}. δ_H (300 MHz,

175

CDCl$_3$/ppm: 5.25 (t; 2H; 0.5 x C$_5$H$_4$); 4.97 (t; 2H; 0.5 x C$_5$H$_4$); 4.82 (s; 5H; C$_5$H$_5$); 2.24 (s; 3H; CH$_3$), **Spectrum 4**.

4.4.5. 1-Ferrocenyl-4,4,4-trifluorobutane-1,3-dione (1)
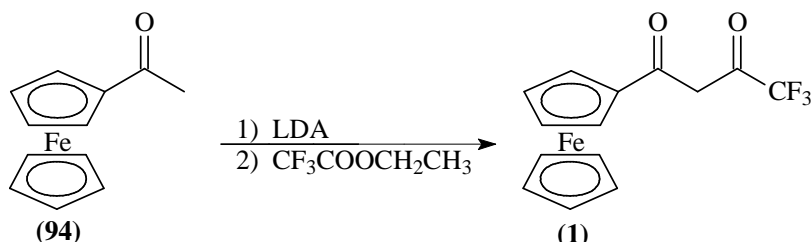
Acetyl ferrocene (1 g, 4.6 mmol) was dissolved in the minimum dry THF (10 ml) and degassed with N$_2$. It was cooled to 0 °C, lithium diisoproplyamine (LDA) (3.3 ml of 1.8 M, 5.9 mmol, 1.2 eq.) was added under N$_2$, and stirred for 20 minutes. Ethyl trifluoroacetate (0.71 ml, 4.6 mmol, 1 eq.) was added to the ice cold reaction mixture under N$_2$. The reaction mixture was then allowed to warm to room temperature and stirred overnight. Ether (50 ml) was added until a precipitate of the lithium salt of **(1)** immediately formed, and filtered. The precipitate was suspended in ice cold 1 M HCl (100 ml) and extracted with ether. The organic layer was dried over anhydrous Na$_2$SO$_4$ and evaporated under reduced pressure to yield the pure product. Yield 59 % (0.85 g). Melting point = 102 °C. υ(C=O) = 1621 cm^{-1}. δ_H (300 MHz, CDCl$_3$)/ppm: 6.10 (s; 1H; CH); 4.89 (t; 2H; 0.5 x C$_5$H$_4$); 4.71 (t; 2H; 0.5 x C$_5$H$_4$); 4.26 (s; 5H; C$_5$H$_5$), **Spectrum 5**.

4.4.6. 1,3-Diferrocenylpropane-1,3-dione (5)
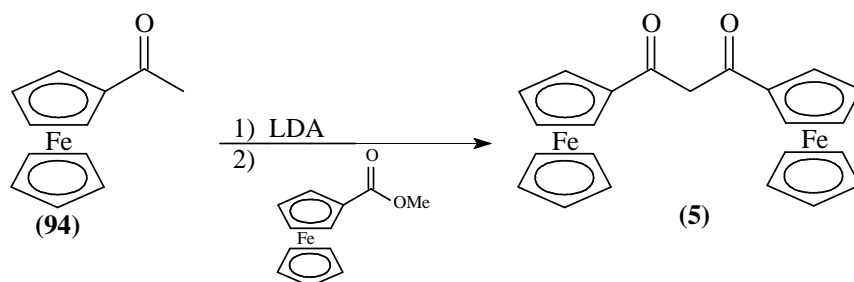
Acetyl ferrocene (0.5 g, 2.3 mmol) was dissolved in the minimum dry THF (4.5 ml) and degassed with N$_2$. The solution was cooled to 0 °C, LDA (1.5 ml of 1.8 M, 2.8 mmol, 1.2 eq.) added under N$_2$, and stirred for 20 minutes. Methyl ferrocenoate (0.54 g, 2.3

mmol, 1 eq.) was added and the reaction mixture under N_2. The reaction mixture was allowed to warm to room temperature and stirred overnight. Ether (30 ml) was added until a precipitate was formed. The precipitate was filtered, suspended in 1 M HCl (50 ml) and extracted with ether. The organic layer was dried over anhydrous Na_2SO_4 and evaporated under reduced pressure to yield the pure product. Yield 62 % (0.60 g). Melting point = 157 °C. υ(C=O) = 1641 cm^{-1}. δ_H (300 MHz, CDCl$_3$)/ppm: 5.99 (s; 1H; enol CH); 4.95 (t; 2H; enol 0.5 x C$_5$H$_4$); 4.85 (t; 2H; keto 0.5 x C$_5$H$_4$); 4.59 (t; 2H; enol 0.5 x C$_5$H$_4$); 4.54 (t; 2H; keto 0.5 x C$_5$H$_4$); 4.23 (s; 5H; keto C$_5$H$_5$); 4.21 (s; 5H; enol C$_5$H$_5$); 4.11 (s; 2H; keto CH$_2$), **Spectrum 6**.

4.4.7. 1-Ferrocenyl-3-ruthenocenylpropane-1,3-dione (6)
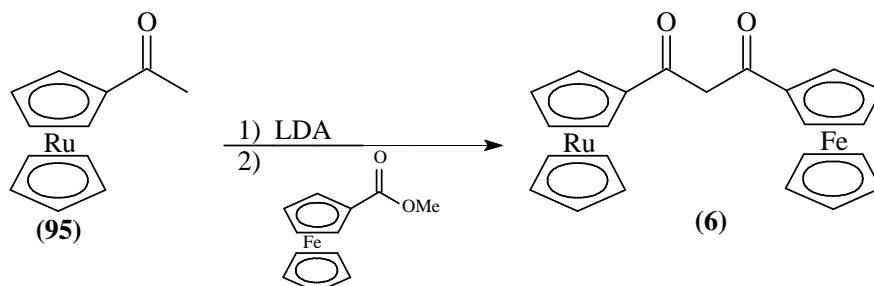
Acetyl ferrocene (0.3 g, 1.1 mmol) was dissolved in the minimum dry THF (2.0 ml) and degassed with N_2. It was cooled to 0 °C, LDA (0.6 ml of 1.8 M, 1.1 mmol, 1 eq.) added under N_2, and stirred for 20 minutes. Methyl ferrocenoate (0.26 g, 1.1 mmol, 1 eq.) was added to the reaction mixture under N_2. The reaction mixture was allowed to warm to room temperature and stirred overnight. Ether (45 ml) was added until a precipitate was formed, and filtered. The precipitate was then suspended in 1 M HCl (75 ml) and extracted with ether. The organic layer was dried over anhydrous Na_2SO_4 and evaporated under reduced pressure to yield the pure product. Yield 29 % (0.15 g). Melting point = 178 °C. υ(C=O) = 1632 cm^{-1}. δ_H (300 MHz, CDCl$_3$)/ppm: 5.91 (s; 1H; enol CH); 5.23 (t; 2H; keto 0.5 x C$_5$H$_4$; Rc); 5.20 (t; 2H; enol 0.5 x C$_5$H$_4$; Rc); 4.93 (t; 2H; keto 0.5 x C$_5$H$_4$; Fc); 4.83 (m; 6H; enol 0.5 x C$_5$H$_4$; Fc; keto 0.5 x C$_5$H$_4$; Rc; enol 0.5 x C$_5$H$_4$; Rc); 4.61 (s; 5H; enol C$_5$H$_5$; Rc); 4.60 (t; 2H; enol 0.5 x C$_5$H$_4$; Fc); 4.58 (s; 5H; ketol C$_5$H$_5$; Rc); 4.54 (t; 2H; keto 0.5 x C$_5$H$_4$; Fc); 4.23 (s; 5H; keto C$_5$H$_5$; Fc); 4.20 (s; 5H; enol C$_5$H$_5$; Fc); 3.89 (s; 2H; keto CH$_2$), **Spectrum 7**.

4.4.8. 1-Ferrocenyl-3-osmocenylpropane-1,3-dione (7)
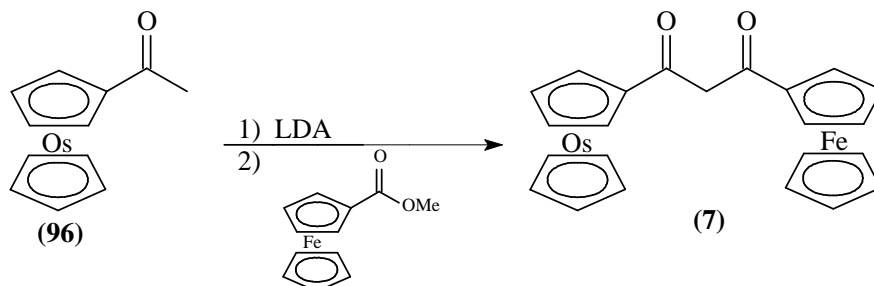
Acetyl osmocene (0.25 g, 0.71 mmol) was dissolved in the minimum dry THF (1.5 ml) and degassed with N_2. It was cooled to 0 °C, LDA (0.4 ml of 1.8 M, 0.71 mmol, 1 eq.) added under N_2, and stirred for 30 minutes. Methyl ferrocenoate (0.17 g, 0.71 mmol, 1 eq.) was added to the reaction mixture under N_2. The reaction mixture was allowed to warm to room temperature and stirred overnight. Ether (30 ml) was added until a precipitate was formed, and filtered. The precipitate was suspended in 1 M HCl (50 ml) and extracted with ether. The organic layer was dried over anhydrous Na_2SO_4 and evaporated under reduced pressure to yield the pure product. Yield 31 % (0.12 g). Melting point = 194 °C. $\upsilon(C=O) = 1652$ cm^{-1}. δ_H (300 MHz, CDCl$_3$)/ppm: 5.83 (s; 1H; enol CH); 5.37 (t; 2H; keto 0.5 x C_5H_4; Oc); 5.35 (t; 2H; enol 0.5 x C_5H_4; Oc); 5.00 (m; 4H; keto 0.5 x C_5H_4; Oc; enol 0.5 x C_5H_4); 4.92 (t; 2H; enol 0.5 x C_5H_4; Fc); 4.81 (s; 5H; keto C_5H_5; Oc); 4.78 (t; 2H; keto 0.5 x C_5H_4; Fc); 4.74 (s; 5H; enol C_5H_5; Oc); 4.58 (t; 2H; keto 0.5 x C_5H_4; Fc); 4.50 (t; 2H; enol 0.5 x C_5H_4; Fc); 4.24 (s; 5H; keto C_5H_5; Fc); 4.16 (s; 5H; enol C_5H_5; Fc); 3.89 (s; 2H; keto CH$_2$), **Spectrum 8**.

4.4.9. Cobaltocenium (97), Methylcobaltocenium (98) and 1,1'-Dimethylcobaltocenium (99) Hexafluorophosphate
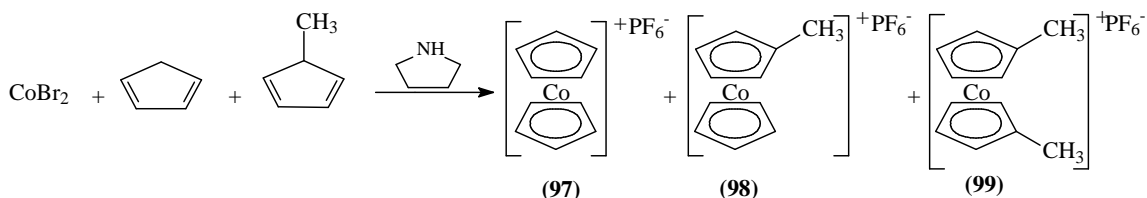
Anhydrous cobalt(II) bromide (20 g, 91.4 mmol) was added in small portions to a solution of freshly cracked methyl cyclopentadiene (18.3 g, 229 mmol, 2.5 eq.) and

cyclopentadiene (15.1 g, 229 mmol, 2.5 eq.) in dry pyrrolidine (90 ml), under N_2 at 0 °C. The solution was warmed to room temperature and stirred overnight. The solvent was evaporated under reduced pressure and the residue washed with hot water (500 ml). The aqueous phase was extracted with ether to remove starting materials, and clarified with charcoal. The mixture of products was precipitated as hexafluorophosphate salts by careful addition of sodium hexafluorophosphate (12-15 g in 35 ml water), filtered and dried. It was not possible to separate the components from each other. Yield 20 % (6 g). δ_H (300 MHz, CD_3CN)/ppm: The NMR of the crude mixture is shown in **Spectrum 9**, but the unresolved mixture of peaks not assigned.

Cracking of cyclopentadiene.

Liquid paraffin (200 ml) was placed in a 500 ml three-necked round-bottomed flask, fitted with a dropping funnel, a thermometer dipping into the paraffin and a Vigreux column attached to a distillation head carrying a thermometer and a condenser. The liquid paraffin was heated to 200 – 240 °C, and dicyclopentadiene was added very slowly *via* the dropping funnel. Cyclopentadiene, distilling at 40 – 42 °C, was collected in a cooled receiver until a sufficient amount was obtained. The diene dimerises readily at room temperature and was thus stored in a freezer and used as soon as possible.

Cracking of methyl cyclopentadiene.

Similarly to the cracking of cyclopentadiene, liquid paraffin (200 ml) was placed in a 500 ml three-necked round-bottomed flask, fitted with a dropping funnel, a thermometer dipping into the paraffin and a Vigreux column attached to a distillation head carrying a thermometer and a condenser. The liquid paraffin was heated to 240 – 260 °C and methyl dicyclopentadiene was added very slowly *via* the dropping funnel. Methyl cyclopentadiene, distilling at 60 – 62 °C, was collected in a cooled receiver until a sufficient amount was obtained. The diene dimerises readily at room temperature, and was thus stored in a freezer and used as soon as possible.

4.4.10. Carboxycobaltocenium hexafluorophosphate (100)
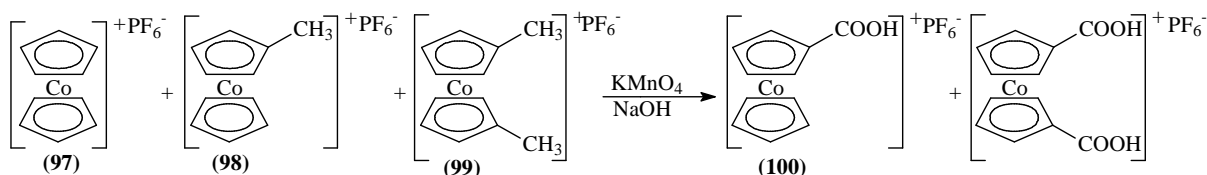
A solution of potassium permanganate (9.3 g, 58.6 mmol, 3.4 eq.), sodium hydroxide (1.24 g, 31.0 mmol, 1.8 eq.) and the mixture of cobaltocenium reagents **(97)**, **(98)** and **(99)** (6 g, 17.2 mmol) in water (140 ml), was refluxed for 3 hours. The hot solution was filtered through celite to remove the generated manganese dioxide. Sodium hexafluorophosphate (3.5 g) was added and the solution chilled and filtered to isolate unsubstituted cobaltocenium hexafluorophosphate **(97)**. 6 M HCl was added dropwise to the filtrate to precipitate a mixture of mono- and di-carboxylated cobaltoceniums. The mono-carboxilated cobaltocenium was extracted by washing the precipitate with hot acetone. This gave carboxycobaltocenium hexafluorophosphate in 28 % yield (1.8 g). The remaining solid was pure 1,1'-dicarboxycobaltocenium hexafluorophosphate. Yield 25 % (1.6 g). Warning note: It is possible to over-extract the mixture of **(100)** and 1,1'-dicarboxycobaltocenium hexafluorophosphate, as the latter is slightly soluble in hot acetone. Carboxycobaltocenium hexafluorophosphate melting point = 198 °C. υ(C=O) = 1706 cm^{-1}. δ_H (300 MHz, CD$_3$CN)/ppm: 6.11 (t; 2H; 0.5 x C$_5$H$_4$); 5.82 (t; 2H; 0.5 x C$_5$H$_4$); 5.77 (s; 5H; C$_5$H$_5$), **Spectrum 10**.

4.4.11. Chlorocarbonylcobaltocenium salt (101)
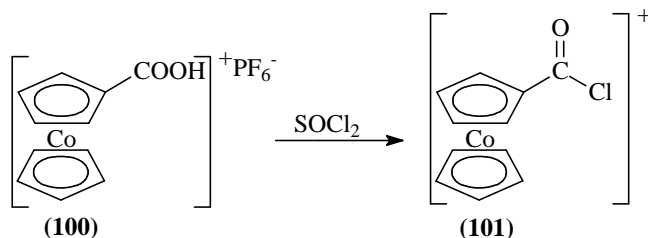
Carboxycobaltocenium hexafluorophosphate (1 g, 2.7 mmol) was refluxed in thionyl chloride (5 ml, large excess) for 48 hours. The solution was concentrated, under reduced pressure, to approximately 1.5 ml and chilled to 0 °C. The yellow precipitate was filtered

off and washed with dry ether and stored in a desiccator. Yield 94 % (0.98 g). Melting point = 187 °C. $\upsilon(C=O) = 1728$ cm^{-1}. δ_H (300 MHz, CD$_3$CN)/ppm: 6.58 (t; 2H; 0.5 x C$_5$H$_4$); 6.30 (t; 2H; 0.5 x C$_5$H$_4$); 6.22 (s; 5H; C$_5$H$_5$), **Spectrum 11**.

4.4.12. Propanoylferrocene (79)

(79)
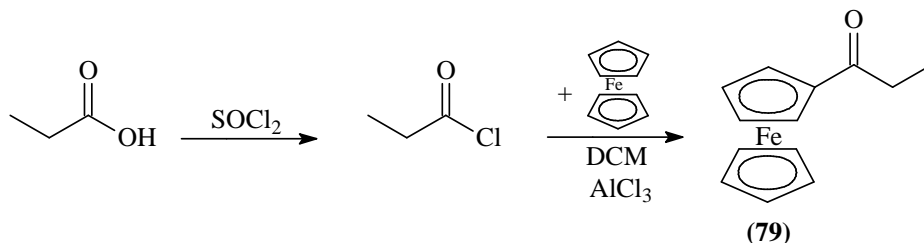
Propanoic acid (0.97 ml, 12.9 mmol) was refluxed in thionyl chloride (0.94 ml, 12.9 mmol, 1 eq.) for 2 hours, then cooled to room temperature. The crude product mixture was added to a solution of ferrocene (2 g, 10.75 mmol, 0.8 eq.) and aluminum trichloride (1.72 g, 12.9 mmol, 1 eq.) in dry CH$_2$Cl$_2$ (50 ml) under N$_2$. The mixture was refluxed for 3 hours and quenched with saturated NaHCO$_3$. Following extraction of the mixture with CH$_2$Cl$_2$ (3 x 50 ml), the organic layers were washed with water (3 x 50 ml) and dried over Na$_2$SO$_4$, filtered and the solvent removed under reduced pressure. The product was purified by column chromatography, using hexane : ether (1:1) (R$_f$ = 0.54). The compound is a liquid at room temperature. Yield 85 % (2.48 g). $\upsilon(C=O) = 1653$ cm^{-1}. δ_H (300 MHz, CDCl$_3$)/ppm: 4.79 (t; 2H; 0.5 x C$_5$H$_4$); 4.49 (t; 2H; 0.5 x C$_5$H$_4$); 4.19 (s; 5H; C$_5$H$_5$); 2.74 (q; 2H; CH$_2$); 1.20 (t; 3H; CH$_3$), **Spectrum 12**.

4.4.13. Ferrocenoic Anhydride (77)

(77)
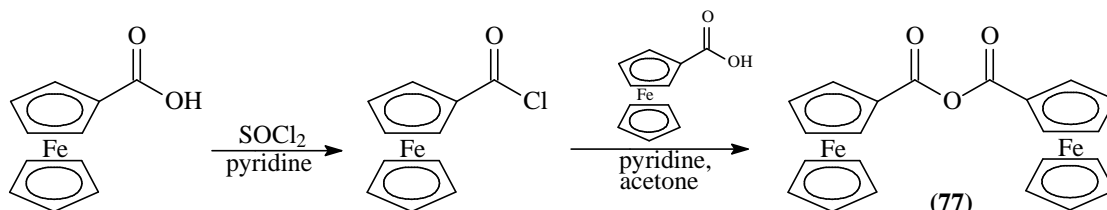
To a mixture of ferrocene carboxylic acid (0.4 g, 1.83 mmol) and pyridine (5 ml), thionyl chloride (0.13 ml, 1.83 mmol, 1 eq.) was slowly added. The mixture was refluxed for 30 minutes and cooled on ice. The crude mixture was added very slowly to a solution of

181

ferrocene carboxylic acid (0.41 g, 1.73 mmol, 0.95 eq.) and pyridine (0.3 ml, 3.65 mmol, 2 eq.) in dry acetone (20 ml), under N_2, with a rise in temperature. The mixture was refluxed for a further 2 hours and cooled on ice. The product precipitated and was filtered off and washed with dry ether. It was dried and stored in a desiccator. Yield 56 % (0.44 g). $\upsilon(C=O) = 1650$ cm^{-1}. δ_H (300 MHz, CDCl$_3$)/ppm: 4.89 (t; 4H; 0.5 x 2 C$_5$H$_4$); 4.66 (t; 4H; 0.5 x 2 C$_5$H$_4$); 4.28 (s; 10H; 2 C$_5$H$_5$), **Spectrum 13**.

The ferrocene carboxylic acid was provided by Prof. J.C. Swarts from the University of the Free State. δ_H (300 MHz, CDCl$_3$)/ppm: 4.87 (t; 4H; 0.5 x 2 C$_5$H$_4$); 4.48 (t; 4H; 0.5 x 2 C$_5$H$_4$); 4.27 (s; 10H; 2 C$_5$H$_5$), **Spectrum 14**.

4.4.14. Cobaltocenoic anhydride hexafluorophosphate (78)
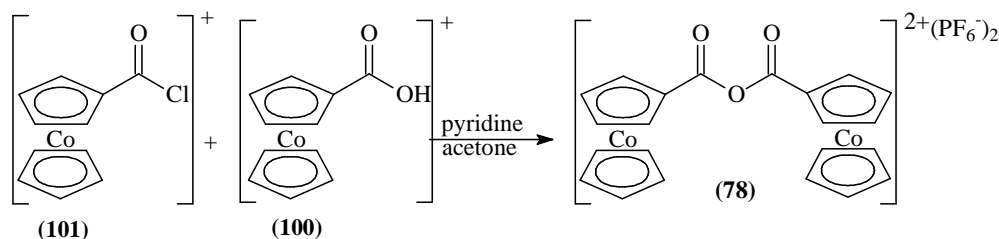
Chlorocarbonylcobaltocenium salt (0.10 g, 0.25 mmol) was slowly added to a solution of carboxycobaltocenium hexafluorophosphate (0.10 g, 0.25 mmol, 1 eq.) and pyridine (0.04 ml, 0.50 mmol, 2 eq.) in dry acetone (5 ml), under N_2, with a rise in temperature. The mixture was refluxed for a further 2 hours and cooled on ice. Sodium hexafluorophosphate (0.5 g) was added to precipitate the product. It was filtered off and washed with dry ether, dried and stored in a desiccator. Yield 59 % (0.12 g). Melting point = 175 °C. δ_H (300 MHz, CD$_3$CN)/ppm: 6.35 (t; 4H; 0.5 x 2 C$_5$H$_4$); 6.11 (t; 4H; 0.5 x 2 C$_5$H$_4$); 6.06 (s; 10H; 2 C$_5$H$_5$), **Spectrum 15**.

4.4.15. Attempted β-Diketone Synthesis utilizing BF₃.

(79)

$R = CH_3, CF_3, Fc, Cc^+PF_6^-$

(80)
Sole Product

Yield 0 %
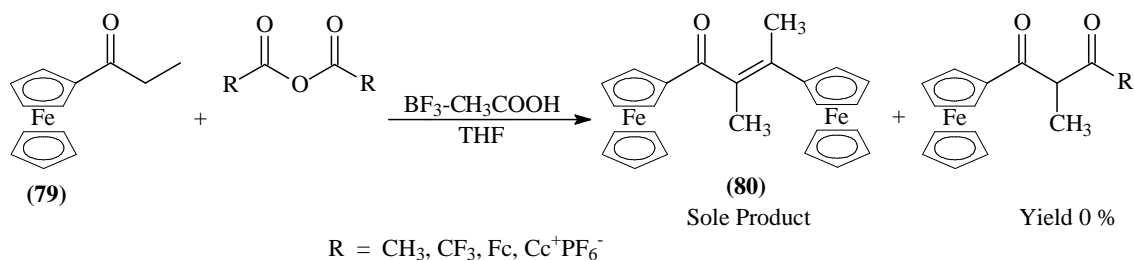
The reaction procedure afforded no β-diketone. In all cases only the aldol product **(80)** could be isolated.

A solution of propanoylferrocene (0.02 g, 0.08 mmol), the appropriate anhydride (0.15 mmol, 2 eq.) and p-toluene sulfonic acid (0.001 g, 0.003 mmol, 0.02 eq.), in THF (10), is stirred at room temperature for 30 minutes. Boron trifluoride acetic acid complex (0.02 ml, 0.15 mmol, 2 eq.) is slowly added and the mixture stirred overnight. A solution of sodium acetate (2 ml of 4 M) is added, a condenser fitted, and the mixture refluxed for 3 hours. The mixture is cooled to room temperature and extracted with ether (3 x 50 ml). The organic layer is washed with aqueous $NaHCO_3$ (20 ml) and water (3 x 50 ml), dried over Na_2SO_4, and evaporated under reduced pressure to liberate **(80)** in up to 34 % yield. Melting point =187 °C. δ_H (300 MHz, $CDCl_3$)/ppm: 4.85 (t; 2H; 0.5 x C_5H_4); 4.64 (t; 4H; 0.5 x C_5H_4); 4.53 (t; 2H; 0.5 x C_5H_4); 4.47 (t; 4H; 0.5 x C_5H_4); 4.23 (s; 5H; C_5H_5)); 4.20 (s; 5H; C_5H_5); 2.80 (s; 3H; CH_3); 2.60 (s; 3H; CH_3), **Spectrum 16**.

4.4.16. Ferrocenyldiphenylphosphine (13)

(13)
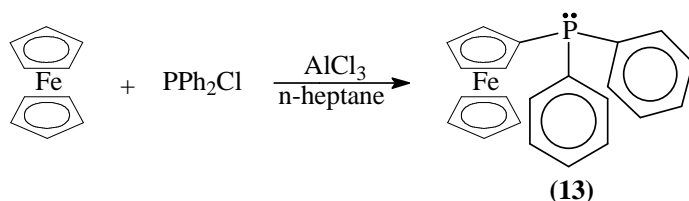
Anhydrous aluminum trichloride (1.43 g, 10.8 mmol, 1 eq.) was stirred with a suspension of ferrocene (2 g, 10.8 mmol) in n-heptane (35 ml), and allowed to cool after an initial spontaneous exothermic reaction onset. A solution of chlorodiphenylphosphine (2. 92 ml, 10.8 mmol, 1 eq.) in n-heptane was slowly added over a 20 minute period. The mixture was heated to reflux for a further 20 hours. After cooling, the solution was

decanted through filter paper. The remaining solids were washed with hot n-heptane (20 ml) and added to the first n-heptane phase, to yield unreacted ferrocene. The solids were washed with hot water (20 ml) in portions, followed by hot toluene (80 ml) in portions. The combined toluene solution was evaporated. The product was purified by recrystalization from ethanol. Yield 36 % (1.44 g). Melting point =122 °C. δ_H (300 MHz, CDCl$_3$)/ppm: 7.37 (m; 10H; 2 x C$_6$H$_5$), 4.40 (t; 2H; 0.5 x C$_5$H$_4$); 4.13 (t; 4H; 0.5 x C$_5$H$_4$); 4.10 (s; 5H; C$_5$H$_5$), **Spectrum 17**.

4.4.17. Ruthenocenyldiphenylphosphine (65)

(93)   **(65)**
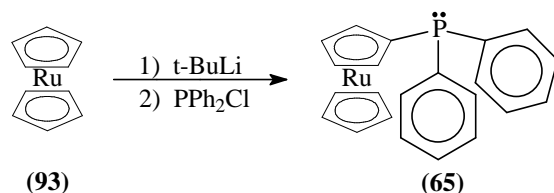
Ruthenocene (1 g, 4.3 mmol) was dissolved in dry THF (15 ml) and the system degassed under Ar for 30 minutes. The solution was cooled to -78 °C and t-butyl lithium (2.55 ml, 4.3 mmol, 1 eq. warning: very flammable upon air exposure) was added dropwise to the solution under Ar. The solution was allowed to warm to room temperature and stirred for 2 hours. It was again cooled to -78 °C and chlorodiphenylphosphine (2.34 ml, 13.0 mmol, 3 eq.) was slowly added under Ar. The solution was allowed to warm to room temperature and stirred for a further 2 days. The reaction mixture was quenched with saturated sodium bicarbonate and extracted with CH$_2$Cl$_2$. The products were separated by column chromatography, using hexane : ether (1:1) (R$_f$ = 0.81). Yield 19 % (0.34 g). Melting point = 127 °C. δ_H (300 MHz, CDCl$_3$)/ppm: 7.36 (m; 10H; 2 x C$_6$H$_5$), 4.73 (t; 2H; 0.5 x C$_5$H$_4$); 4.50 (t; 2H; 0.5 x C$_5$H$_4$); 4.47 (s; 5H; C$_5$H$_5$), **Spectrum 18**.

4.4.18. Osmocenyldiphenylphosphine (66)

(66)
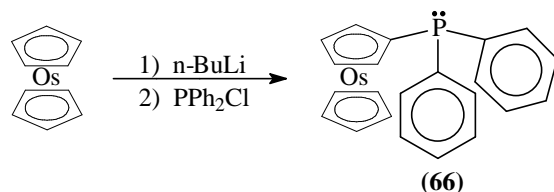
Osmocene (0.3 g, 0.94 mmol) was dissolved in dry ether (6 ml) and the system degassed under Ar for 30 minutes. The solution was cooled to -78 °C and n-butyl lithium (0.6 ml, 1.1 mmol, 1.2 eq.) was added dropwise to the solution under Ar. The solution was allowed to warm to room temperature and stirred overnight. It was again cooled to -78 °C and chlorodiphenylphosphine (1.0 ml, 5.7 mmol, 5 eq.) was slowly added under Ar. The solution was allowed to warm to room temperature and stirred for a further 2 days. The reaction mixture was quenched with saturated sodium bicarbonate and extracted with CH_2Cl_2. The products were separated by column chromatography, using hexane : ether (1:1) (R_f = 0.79). Yield 13 % (0.062 g). Melting point = 141 °C. δ_H (300 MHz, $CDCl_3$)/ppm: 7.38 (m; 10H; 2 x C_6H_5), 4.91 (t; 2H; 0.5 x C_5H_4); 4.65 (m; 7H; 0.5 x C_5H_4, C_5H_5), **Spectrum 19**.

4.4.19. Diphenylphosphinocobaltocenium Hexafluorophosphate (67)
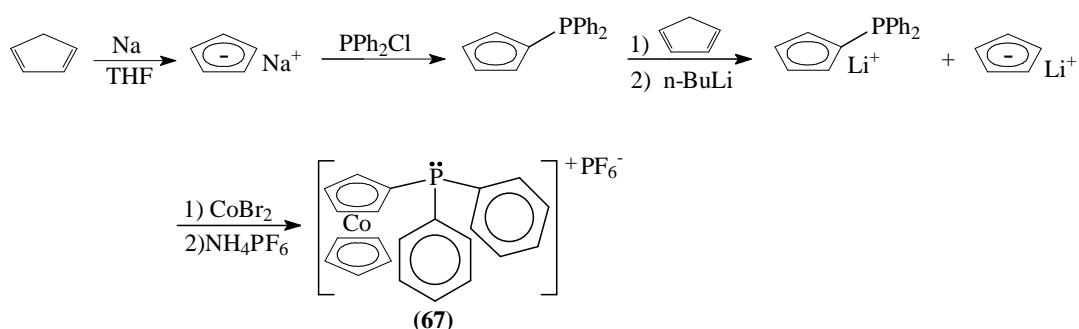
To a slurry of finely cut sodium wire (0.56 g, 24.4 mmol, 1 eq.) in THF (200 ml) at 0 °C and under N_2, freshly cracked cyclopentadiene (2 ml, 24.4 mmol, 1 eq. See **Procedure 4.4.1.9**) was slowly added, and the mixture stirred until all the sodium was consumed. The pink solution was cooled to -78 °C and chlorodiphenylphosphine (4.4 ml, 24.4 mmol, 1 eq.) was slowly added. The solution was allowed to warm to room temperature and stirred for 30 minutes. It was again cooled to -78 °C and again cyclopentadiene (2 ml, 24.4 mmol, 1 eq.) was added, followed by n-butyl lithium (24.3 ml, 48.7 mmol, 2 eq.). After 15 minutes of stirring, cobalt bromide (5.32 g, 24.4 mmol) was added under a counter stream of N_2. The mixture was allowed to warm to room temperature and stirred for 16 hours. Acetic acid (1.4 ml, 24.4 mmol, 1 eq.) was added and the mixture stirred in an open vessel for 15 minutes. The mixture was filtered, NH_4PF_6 was added to the filtrate and the solvent evaporated. The brown sludge was washed with warm n-hexane

and the product crystallized from this n-hexane solution. Yield 58 % (7.3 g). Melting point = 207 °C. δ_H (300 MHz, CDCl$_3$)/ppm: 7.69 (m; 10H; 2 x C$_6$H$_5$), 6.13 (t; 2H; 0.5 x C$_5$H$_4$); 5.91 (t; 2H; 0.5 x C$_5$H$_4$), 5.73 (s; 5H; C$_5$H$_5$), **Spectrum 20**.

4.4.20.Di-μ-chloro-bis[(1,2,5,6-η)1,5-cyclooctadiene]rhodium (84)
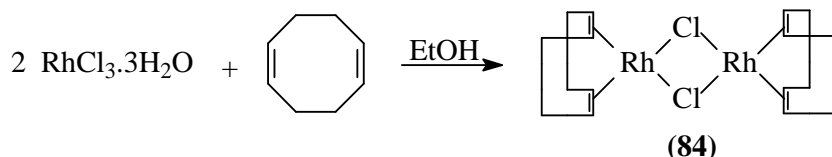
In a fumehood, rhodium trichloride (1 g, 4.8 mmol) and cyclooctadiene (2 ml, 4.8 mmol, 1 eq.) was dissolved in ethanol (30 ml). The mixture was refluxed, while stirring, for 3 hours. The reaction mixture was cooled on ice and the precipitate was filtered off and washed with ethanol. Yield 26 % (0.6 g). (Previous reports have obtained yields of up to 80 %.)[2] Melting point = 243 °C. δ_H (300 MHz, CDCl$_3$)/ppm: 4.25 (m; 4H; 4CH), 2.52 (m; 4H; 0.5 x 4CH$_2$); 1.77 (m; 4H; 0.5 x CH$_2$), **Spectrum 21**.

4.4.21.[Rh(FcCOCHCOCF$_3$)(cod)] (47)
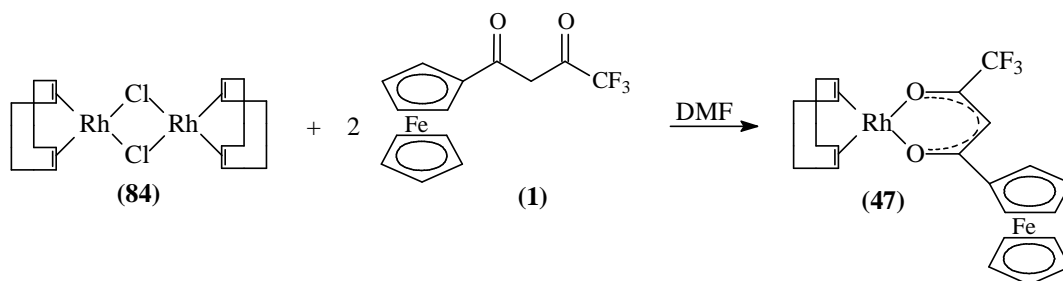
Solid β-diketone (0.39 g, 1.2 mmol, 2 eq.) was added to a solution of [Rh$_2$Cl$_2$(cod)$_2$] (0.3 g, 0.61 mmol) in DMF (4 ml). The mixture was stirred for 5 minutes and the product precipitated with an excess of water. The product was filtered off, dissolved in ether and the organic layer washed with water. The ether was dried over Na$_2$SO$_4$ and evaporated under reduced pressure. Yield 88 % (0.56 g). Melting point = 186 °C. δ_H (300 MHz, CDCl$_3$)/ppm: 5.96 (s; 1H; CH), 4.71 (t; 2H; 0.5 x C$_5$H$_4$); 4.49 (t; 2H; 0.5 x C$_5$H$_4$), 4.20 (m; 9H; C$_5$H$_5$, 4CH), 2.53 (m; 4H; 0.5 x 4CH$_2$), 1.89 (m; 4H; 0.5 x 4CH$_2$), **Spectrum 22**.

4.4.22.[Rh(FcCOCHCOFc)(cod)] (51)
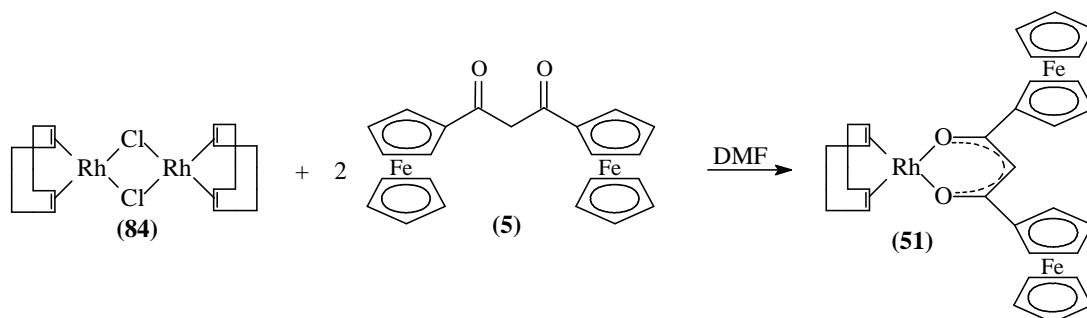
Solid β-diketone (0.45 g, 1.02 mmol, 2 eq.) was added to a solution of [Rh$_2$Cl$_2$(cod)$_2$] (0.25 g, 0.51 mmol) in DMF (4 ml). The mixture was stirred for 1 hour and the product precipitated with an excess of water. The product was filtered off, dissolved in ether and the organic layer washed with water. The ether was dried over Na$_2$SO$_4$ and evaporated under reduced pressure. Yield 91 % (0.30 g). Melting point = 246 °C. δ$_H$ (300 MHz, CDCl$_3$)/ppm: 5.95 (s; 1H; CH), 4.71 (t; 4H; 0.5 x 2C$_5$H$_4$); 4.37 (t; 4H; 0.5 x 2C$_5$H$_4$), 4.25 (m; 4H; 4CH), 4.18 (s; 10H; 2C$_5$H$_5$); 1.90 (m; 4H; 0.5 x 4CH$_2$), 1.77 (m; 4H; 0.5 x 4CH$_2$), **Spectrum 23**.

4.4.23.[Rh(FcCOCHCORc)(cod)] (81)
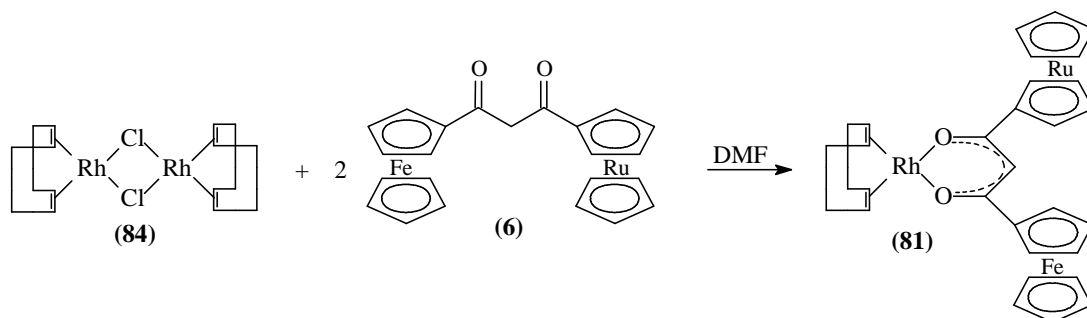
Solid β-diketone (0.09 g, 0.18 mmol, 2 eq.) was added to a solution of [Rh$_2$Cl$_2$(cod)$_2$] (0.04 g, 0.09 mmol) in DMF (1 ml). The mixture was stirred for 1 hour and the product precipitated with an excess of water. The product was filtered off, dissolved in ether and the organic layer washed with water. The ether was dried over Na$_2$SO$_4$ and evaporated under reduced pressure. Yield 87 % (0.06 g). Melting point = 176 °C. δ$_H$ (300 MHz, CDCl$_3$)/ppm: 5.88 (s; 1H; CH), 5.06 (t; 2H; 0.5 x C$_5$H$_4$, Rc), 4.68 (t; 2H; 0.5 x C$_5$H$_4$, Rc), 4.65 (t; 2H; 0.5 x C$_5$H$_4$, Fc), 4.58 (s; 5H; C$_5$H$_5$, Rc), 4.34 (t; 2H; 0.5 x C$_5$H$_4$, Fc),

187

4.25 (m; 4H; 4CH), 4.16 (s; 5H; C_5H_5, Fc); 2.52 (m; 4H; 0.5 x $4CH_2$), 1.77 (m; 4H; 0.5 x $4CH_2$), **Spectrum 24**.

4.4.24. [Rh(FcCOCHCOOc)(cod)] (82)
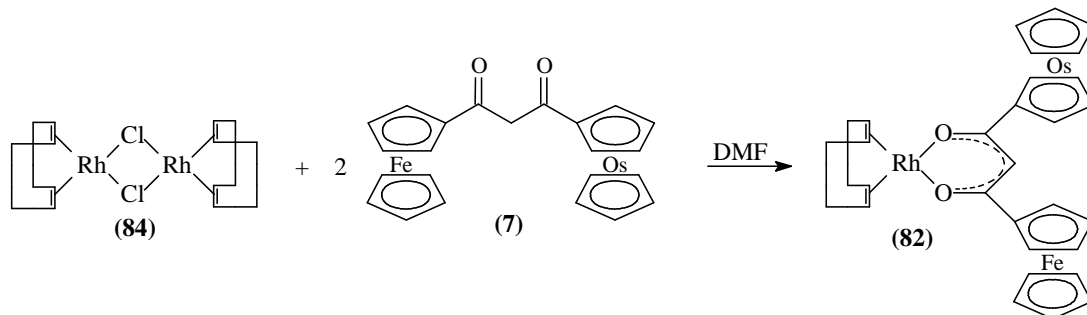
Solid β-diketone (0.1 g, 0.17 mmol, 2 eq.) was added to a solution of $[Rh_2Cl_2(cod)_2]$ (0.04 g, 0.09 mmol) in DMF (1 ml). The mixture was stirred for 2 hours and the product precipitated with an excess of water. The product was filtered off, dissolved in ether and the organic layer washed with water. The ether was dried over Na_2SO_4 and evaporated under reduced pressure. Yield 77 % (0.05 g). Melting point = 183 °C. δ_H (300 MHz, $CDCl_3$)/ppm: 5.80 (s; 1H; CH), 5.21 (t; 2H; 0.5 x C_5H_4, Oc); 4.87 (t; 2H; 0.5 x C_5H_4, Oc), 4.77 (s; 5H; C_5H_5, Oc), 4.63 (t; 2H; 0.5 x C_5H_4, Fc), 4.33 (t; 2H; 0.5 x C_5H_4, Fc); 4.15 (s; 5H; C_5H_5, Fc), 4.08 (m; 4H; 4CH), 2.52 (m; 4H; 0.5 x $4CH_2$), 1.87 (m; 4H; 0.5 x $4CH_2$), **Spectrum 25**.

4.4.25. [Rh(FcCOCHCOCF$_3$)(CO)$_2$] (57)
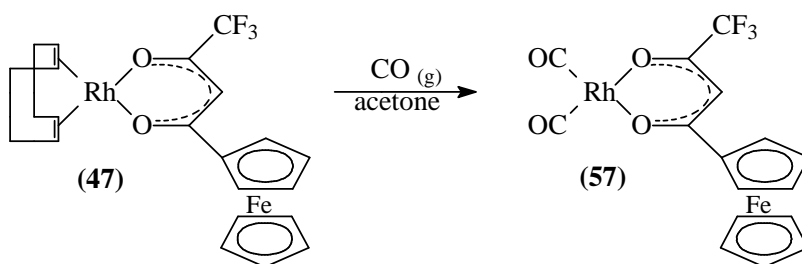
[Rh(FcCOCHCOCF$_3$)(cod)] (0.3 g, 0.56 mmol) was dissolved in acetone (140 ml). Carbon monoxide gas was bubbled through the solution by passing it through a sintered glass tube. The CO (g) pressure was maintained at approximately 1 cm above atmospheric pressure for 25 minutes. Cold water (170 ml) was added to precipitate the

product, and the mixture stirred for a further 15 minutes, then centrifuged. The precipitate was washed with water, with care being taken not to allow liberated cod to get in contact with the precipitate, filtered and dried in a desiccator. Yield 97 % (0.26 g). Melting point = 219 °C. υ(C=O) = 2075 and 2021 cm^{-1}. δ_H (300 MHz, CDCl$_3$)/ppm: 6.21 (s; 1H; CH), 4.86 (t; 2H; 0.5 x C$_5$H$_4$); 4.64 (t; 2H; 0.5 x C$_5$H$_4$), 4.21 (s; 5H; C$_5$H$_5$), **Spectrum 26**.

4.4.26.[Rh(FcCOCHCOFc)(CO)$_2$] (60)
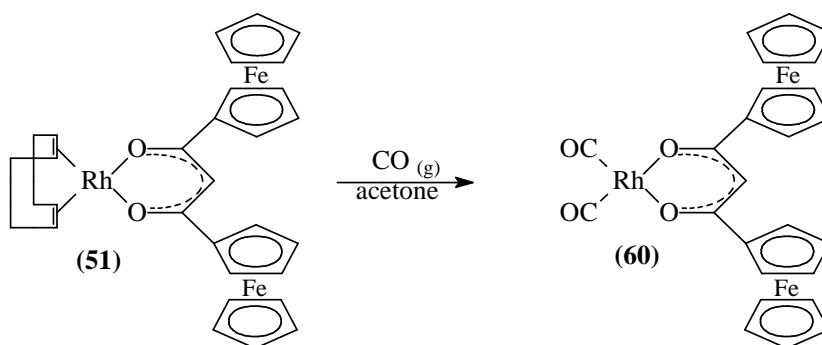
[Rh(FcCOCHCOFc)(cod)] (0.38 g, 0.58 mmol) was dissolved in acetone (100 ml). Carbon monoxide gas was bubbled through the solution, by passing it through a sintered glass tube. The CO (g) pressure was maintained at approximately 1 cm above atmospheric pressure for 30 minutes. Cold water (140 ml) was added to precipitate the product, and the mixture stirred for a further 15 minutes, then centrifuged. The precipitate was washed with water, with care being taken not to allow liberated cod to get in contact with the precipitate, filtered and dried in a desiccator. Yield 74 % (0.21 g). Melting point = 247 °C. υ(C=O) = 2074 and 2018 cm^{-1}. δ_H (300 MHz, CDCl$_3$)/ppm: 6.18 (s; 1H; CH), 4.83 (t; 4H; 0.5 x 2C$_5$H$_4$); 4.48 (t; 4H; 0.5 x 2C$_5$H$_4$), 4.18 (s; 10H; 2C$_5$H$_5$), **Spectrum 27**.

4.4.27. [Rh(FcCOCHCORc)(CO)$_2$] (68)
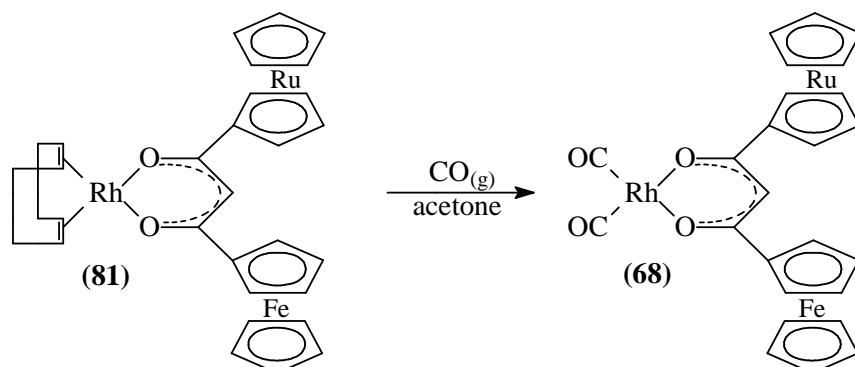
[Rh(FcCOCHCORc)(cod)] (0.2 g, 0.29 mmol) was dissolved in acetone (80 ml). Carbon monoxide gas was bubbled through the solution by passing it through a sintered glass tube. The CO (g) pressure was maintained at approximately 1 cm above atmospheric pressure for 30 minutes. Cold water (120 ml) was added to precipitate the product, and the mixture stirred for a further 15 minutes, then centrifuged. The precipitate was washed with water, with care being taken not to allow liberated cod to get in contact with the precipitate, filtered and dried in a desiccator. Yield 85 % (0.12 g). Melting point = 185 °C. υ(C=O) = 2068 and 2006 cm^{-1}. δ_H (300 MHz, CDCl$_3$)/ppm: 6.10 (s; 1H; CH), 5.18 (t; 2H; 0.5 x C$_5$H$_4$, Rc); 4.77 (m; 4H; 0.5 x C$_5$H$_4$, Rc; 0.5 x C$_5$H$_4$, Fc), 4.57 (s; 5H; C$_5$H$_5$, Rc) 4.45 (t, 2H, 0.5 x C$_5$H$_4$, Fc), 4.16 (s; 5H; C$_5$H$_5$, Fc), **Spectrum 28**.

4.4.28. [Rh(FcCOCHCOOc)(CO)$_2$] (69)
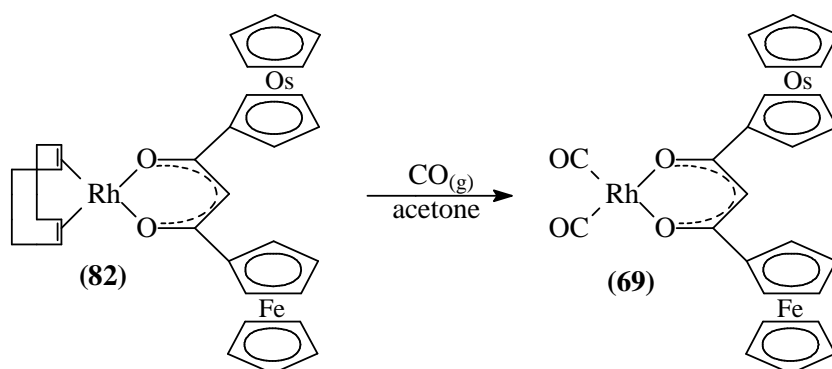
[Rh(FcCOCHCOOc)(cod)] (0.1 g, 0.13 mmol) was dissolved in acetone (40 ml). Carbon monoxide gas was bubbled through the solution by passing it through a sintered glass tube. The CO (g) pressure was maintained at approximately 1 cm above atmospheric

pressure for 30 minutes. Cold water (60 ml) was added to precipitate the product, and the mixture stirred for a further 15 minutes, then centrifuged. The precipitate was washed with water, with care being taken not to allow liberated cod to get in contact with the precipitate, filtered and dried in a desiccator. Yield 81 % (0.08 g). Melting point = 191 °C. υ(C=O) = 2069 and 2006 cm^{-1}. δ_H (300 MHz, CDCl$_3$)/ppm: 6.02 (s; 1H; CH), 5.33 (t; 2H; 0.5 x C$_5$H$_4$, Oc); 4.95 (t; 2H; 0.5 x C$_5$H$_4$, Oc), 4.78 (s; 5H; C$_5$H$_5$, Oc), 4.76 (t; 2H; 0.5 x C$_5$H$_4$, Fc), 4.44 (t; 2H; 0.5 x C$_5$H$_4$, Fc), 4.15 (s; 5H; C$_5$H$_5$, Fc), **Spectrum 29**.

4.4.29.[Rh(CF$_3$COCHCOCH$_3$)(CO)$_2$] (83)
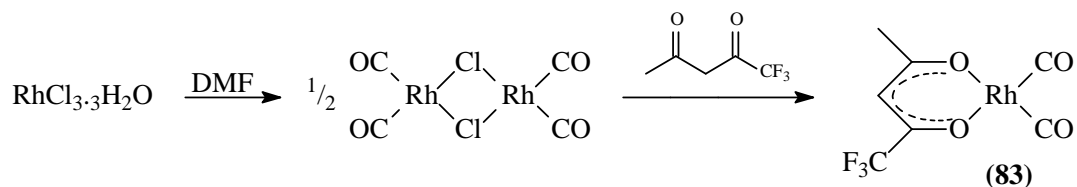
Compound **(83)** was synthesized as a less electronegative rhodium(I) dicarbonyl reagent, to react with PPh$_2$Oc **(66)**, since attempts to react **(66)** with metallocene-containing rhodium(I) dicarbonyl compounds [Rh(FcCOCHCOCF$_3$)(CO)$_2$] **(57)** and [Rh(FcCOCHCOOc)(CO)$_2$] **(69)** failed to yield a pure product.

DMF (20 ml) was refluxed in a round bottomed flask for 15 minutes, and then discarded. Rhodium trichloride (0.1 g, 0.48 mmol) was added to the warmed flask and dissolved in the minimum water (4 drops). With stirring DMF (4 ml) was added and the solution was heated to reflux for 25 minutes. The solution was cooled on ice and solid β-diketone (0.05 ml, 0.48 mmol, 1 eq.) was added. The reaction mixture was warmed to room temperature and stirred for a further 30 minutes. Addition of cold water (30 ml) precipitated the product. It was filtered, washed with water and dried in a desiccator. Yield 40 % (0.06 g). Melting point = 198 °C. υ(C=O) = 2078 and 2023 cm^{-1}. δ_H (300 MHz, CDCl$_3$)/ppm: 6.07 (s; 1H; CH), 4.15 (s; 3H; CH$_3$), **Spectrum 30**.

4.4.30. [Rh(FcCOCHCOCF$_3$)(CO)(PPh$_3$)] (29)
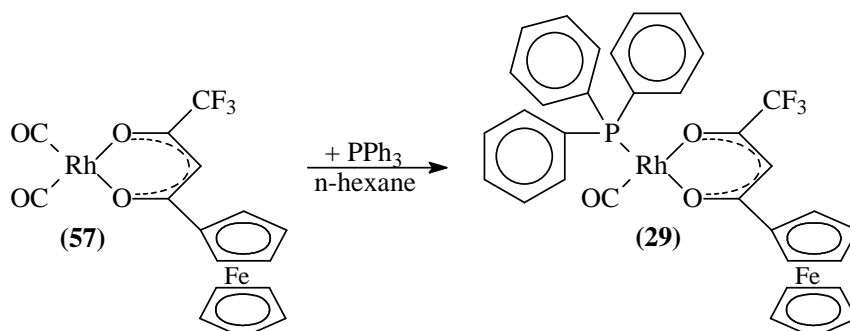
Solid triphenylphosphine (0.07 g, 0. 25 mmol, 1 eq.) was added to an oxygen-free solution of [Rh(FcCOCHCOCF$_3$)(CO)$_2$] (0.12 g, 0.25 mmol) in n-hexane (100 ml). The mixture was heated to 45 °C and stirred overnight, for approximately 16 hours. The warm solution was filtered and evaporated slowly to form the crystalline product as two inseparable isomers. Yield 81 % (0.15 g). Melting point = 178 °C. υ(C=O) = 1987 cm^{-1}. δ_H (300 MHz, CDCl$_3$)/ppm: 7.52 (m; 6H; 0.6 x 2C$_6$H$_5$), 7.49 (m; 4H; 0.4 x 2C$_6$H$_5$), 6.09 (s; 1H; CH, isomer 2), 6.08 (s; 1H; CH, isomer 1), 4.86 (t; 2H; 0.5 x C$_5$H$_4$, Fc, isomer 1), 4.52 (t; 2H; 0.5 x C$_5$H$_4$, Fc, isomer 1), 4.29 (t; 2H; 0.5 x C$_5$H$_4$, Fc, isomer 2), 4.22 (s, 5H; C$_5$H$_5$, Fc, isomer 1), 4.11 (t; 2H; 0.5 x C$_5$H$_4$, Fc, isomer 2), 3.96 (s; 5H; C$_5$H$_5$, Fc, isomer 2), **Spectrum 31**.

4.4.31. [Rh(FcCOCHCOCF$_3$)(CO)(PPh$_2$Fc)] (70)
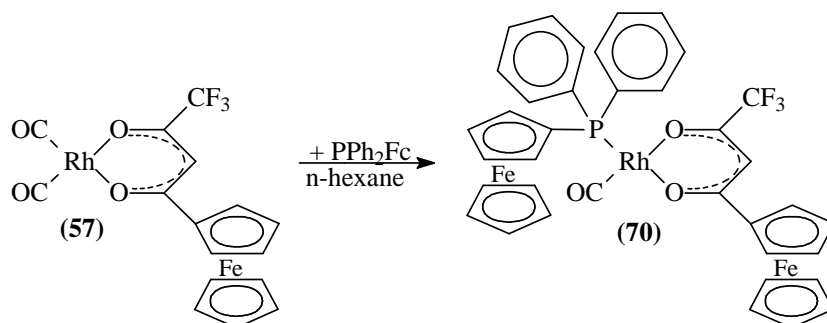
Solid ferrocenyldiphenylphosphine (0.08 g, 0.21 mmol, 1 eq.) was added to an oxygen-free solution of [Rh(FcCOCHCOCF$_3$)(CO)$_2$] (0.10 g, 0.21 mmol) in n-hexane (90 ml). The mixture was heated to 45 °C and stirred overnight. The warm solution was filtered and evaporated slowly to form the crystalline product as two inseparable isomers. Yield 73 % (0.13 g). Melting point = 186°C. υ(C=O) = 1975 cm^{-1}. δ_H (300 MHz,

CDCl$_3$)/ppm: 7.69 (m; 6H; 0.6 x 2C$_6$H$_5$), 7.44 (m; 4H; 0.4 x 2C$_6$H$_5$), 6.12 (s; 1H; CH, isomer 1), 6.10 (s; 1H; CH, isomer 2), 4.90 (t; 2H; 0.5 x C$_5$H$_4$, PPh$_2$Fc, isomer 1), 4.54 (t; 2H; 0.5 x C$_5$H$_4$, PPh$_2$Fc, isomer 1), 4.50 (m; 4H; 0.5 x C$_5$H$_4$, β-Fc, isomer 1; 0.5 x C$_5$H$_4$, PPh$_2$Fc, isomer 2), 4.39 (m, 7H; 0.5 x C$_5$H$_4$, β-Fc, isomer 1; C$_5$H$_5$, PPh$_2$Fc, isomer 2), 4.33 (s; 5H; C$_5$H$_5$, PPh$_2$Fc, isomer 1), 4.29 (t; 2H; 0.5 x C$_5$H$_4$, β-Fc, isomer 2), 4.27 (t; 2H; 0.5 x C$_5$H$_4$, β-Fc, isomer 2), 4.23 (s; 5H; C$_5$H$_5$, β-Fc, isomer 1), 4.02 (m; 7H; 0.5 x C$_5$H$_4$, β-Fc, isomer 2; C$_5$H$_5$, β-Fc, isomer 2), **Spectrum 32**.

4.4.32.[Rh(FcCOCHCOCF$_3$)(CO)(PPh$_2$Rc)] (71)
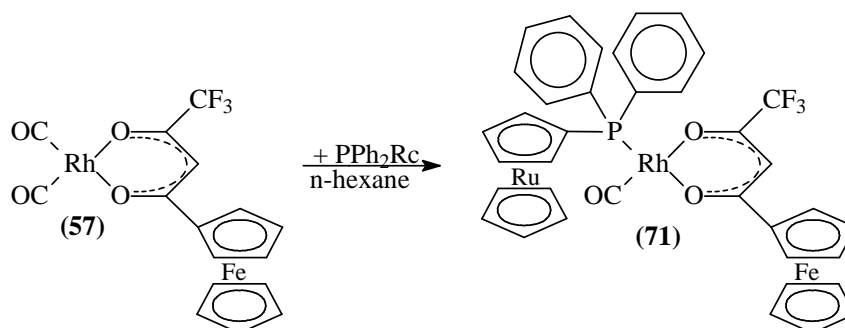
Solid ruthenocenyldiphenylphosphine (0.03 g, 0.07 mmol, 1 eq.) was added to an oxygen-free solution of [Rh(FcCOCHCOCF$_3$)(CO)$_2$] (0.03 g, 0.07 mmol) in n-hexane (20 ml). The mixture was heated to 45 °C and stirred overnight. The warm solution was filtered and evaporated slowly to form the crystalline product as two inseparable isomers. Yield 77 % (0.05 g). Melting point = 134 °C. υ(C=O) = 1978 cm^{-1}. δ$_H$ (300 MHz, CDCl$_3$)/ppm: 7.73 (m; 6H; 0.6 x 2C$_6$H$_5$), 7.44 (m; 4H; 0.4 x 2C$_6$H$_5$), 6.08 (s; 1H; CH, isomer 1), 6.06 (s; 1H; CH, isomer 2), 4.87 (t; 2H; 0.5 x C$_5$H$_4$, Rc, isomer 1), 4.81 (m; 4H; 0.5 x C$_5$H$_4$, Rc, isomer 1; 0.5 x C$_5$H$_4$, Rc, isomer 2), 4.75 (t; 2H; 0.5 x C$_5$H$_4$, Fc, isomer 1), 4.67 (m, 7H; 0.5 x C$_5$H$_4$, Rc, isomer 2; C$_5$H$_5$, Rc, isomer 2), 4.63 (s; 5H; C$_5$H$_5$, Rc, isomer 1), 4.53 (t; 2H; 0.5 x C$_5$H$_4$, Fc, isomer 1), 4.29 (t; 2H; 0.5 x C$_5$H$_4$, Fc, isomer 2), 4.22 (s; 5H; C$_5$H$_5$, Fc, isomer 1), 4.03 (t; 2H; 0.5 x C$_5$H$_4$, Fc, isomer 2), 4.00 (s; 5H; C$_5$H$_5$, Fc, isomer 2), **Spectrum 33**.

## 4.4.33. Attempted Synthesis of Rhodium(I) Osmocenyldiphenyl phosphine compounds (85), (86) and (87)

(83) R = CH$_3$, R' = CF$_3$
(57) R = Fc, R' = CF$_3$
(69) R = Fc, R' = Oc

(85) R = CH$_3$, R' = CF$_3$
(86) R = Fc, R' = CF$_3$
(87) R = Fc, R' = Oc
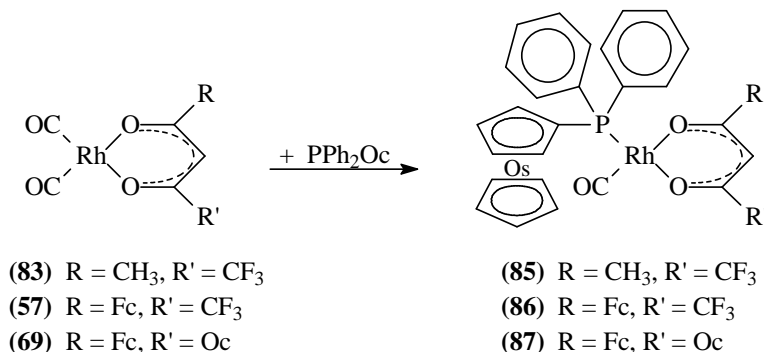
Solid osmocenyldiphenylphosphine (1 eq.) was added to an oxygen-free solution of the appropriate rhodium(I) dicarbonyl compound **(83)**, **(57)** or **(69)** (1 eq.) in n-hexane (20 ml per 0.1 mol reagent). The mixture was heated to 45 °C and stirred overnight. The warm solution was filtered and evaporated slowly to precipitate the product. In all cases the mixture was shown by NMR to contain both starting materials as well as the desired product, as discussed in **Chapter 3**, **Section 3.2.5.1**. Both flash chromatography (n-hexane : ether, 1:1) and recrystallisation (n-hexane, CH$_2$Cl$_2$) were unsuccessful in separating the crude mixture.

4.4.34. [Rh(FcCOCHCOCF$_3$)(CO)(PPh$_2$(C$_6$F$_5$))] (72)
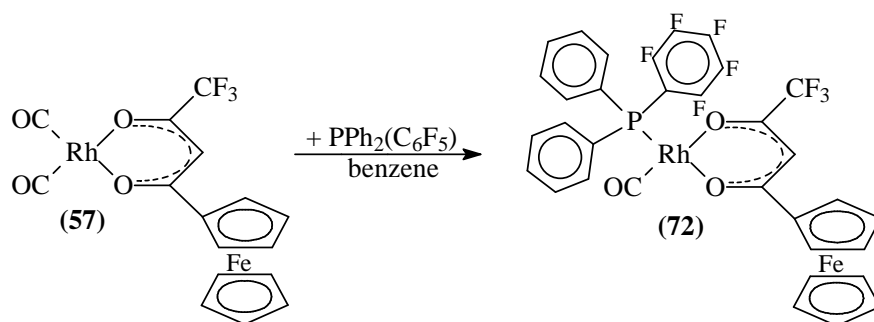
Solid phosphine (0.02 g, 0.06 mmol, 1 eq.) was added to an oxygen-free solution of [Rh(FcCOCHCOCF$_3$)(CO)$_2$] (0.03 g, 0.06 mmol) in benzene (5 ml), Bubbling was observed. The solution was stirred for 2 hours and the warm solution filtered and evaporated slowly to precipitate the product as two inseparable isomers. Yield 79 %

(0.04 g). Melting point = 105 °C. υ(C=O) = 1986 cm^{-1}. δ_H (300 MHz, CDCl$_3$)/ppm:
7.96 (m; 6H; 0.6 x 2C$_6$H$_5$), 7.51 (m; 4H; 0.4 x 2C$_6$H$_5$), 6.14 (s; 1H; CH, isomer 2), 6.11
(s; 1H; CH, isomer 1), 4.89 (t; 2H; 0.5 x C$_5$H$_4$, Fc, isomer 1), 4.57 (t; 2H; 0.5 x C$_5$H$_4$, Fc,
isomer 1), 4.37 (t; 2H; 0.5 x C$_5$H$_4$, Fc, isomer 2), 4.26 (s, 5H; C$_5$H$_5$, Fc, isomer 1), 4.19
(t; 2H; 0.5 x C$_5$H$_4$, Fc, isomer 2), 4.04 (s; 5H; C$_5$H$_5$, Fc, isomer 2), **Spectrum 34**.

4.4.35.[Rh(FcCOCHCOCF$_3$)(CO)(PPh(C$_6$F$_5$)$_2$)] (73)
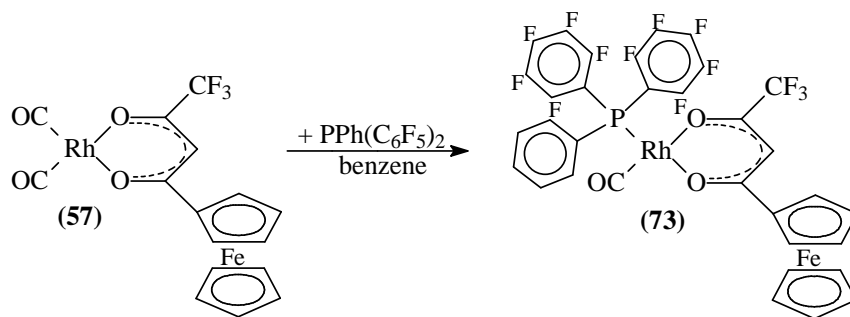
Solid phosphine (0.04 g, 0.08 mmol, 1 eq.) was added to an oxygen-free solution of
[Rh(FcCOCHCOCF$_3$)(CO)$_2$] (0.04 g, 0.08 mmol) in benzene (10 ml), Bubbling was
observed. The solution was stirred for 2 hours and the warm solution filtered and
evaporated slowly to precipitate the product as two inseparable isomers. Yield 75 %
(0.06 g). Melting point = 87 °C. υ(C=O) = 1991 cm^{-1}. δ_H (300 MHz, CDCl$_3$)/ppm: 7.99
(m; 6H; 0.6 x 2C$_6$H$_5$), 7.54 (m; 4H; 0.4 x 2C$_6$H$_5$), 6.14 (s; 1H; CH, isomer 2), 6.11 (s; 1H;
CH, isomer 1), 4.87 (t; 2H; 0.5 x C$_5$H$_4$, Fc, isomer 1), 4.58 (t; 2H; 0.5 x C$_5$H$_4$, Fc, isomer
1), 4.45 (t; 2H; 0.5 x C$_5$H$_4$, Fc, isomer 2), 4.26 (t; 2H; 0.5 x C$_5$H$_4$, Fc, isomer 2), 4.24 (s,
5H; C$_5$H$_5$, Fc, isomer 1), 4.11 (s; 5H; C$_5$H$_5$, Fc, isomer 2), **Spectrum 35**.

4.4.36.[Rh(FcCOCHCOCF$_3$)(CO)(P(C$_6$F$_5$)$_3$)] (74)
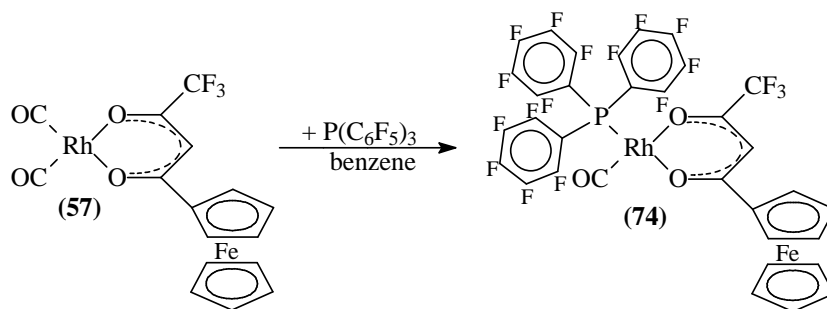
Solid phosphine (0.04 g, 0.08 mmol, 1 eq.) was added to an oxygen-free solution of [Rh(FcCOCHCOCF$_3$)(CO)$_2$] (0.04 g, 0.08 mmol) in benzene (10 ml), Bubbling was observed. The solution was stirred for 2 hours and the warm solution filtered and evaporated slowly to precipitate the product as two inseparable isomers. Yield 79 % (0.07 g). Melting point = 79 °C. υ(C=O) = 1998 cm^{-1}. δ_H (300 MHz, CDCl$_3$)/ppm: 7.99 (m; 6H; 0.6 x 2C$_6$H$_5$), 7.54 (m; 4H; 0.4 x 2C$_6$H$_5$), 6.13 (s; 1H; CH, isomer 2), 6.09 (s; 1H; CH, isomer 1), 4.85 (t; 2H; 0.5 x C$_5$H$_4$, Fc, isomer 1), 4.59 (t; 2H; 0.5 x C$_5$H$_4$, Fc, isomer 1), 4.50 (t; 2H; 0.5 x C$_5$H$_4$, Fc, isomer 2), 4.31 (t; 2H; 0.5 x C$_5$H$_4$, Fc, isomer 2), 4.23 (s, 5H; C$_5$H$_5$, Fc, isomer 1), 4.13 (s; 5H; C$_5$H$_5$, Fc, isomer 2), **Spectrum 36**.

4.4.37. Attempted Synthesis of [Rh(FcCOCHCOCF$_3$)(CO) (PPh$_2$Cc$^+$)] (PF$_6^-$) (102)
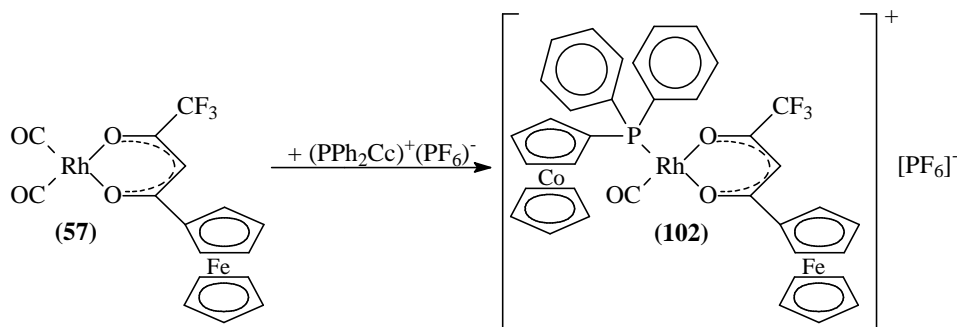
Solid phosphine (1 eq.) was added to an oxygen-free solution of [Rh(FcCOCHCOCF$_3$) (CO)$_2$] (1 eq) in either n-hexane, dried acetone or a mixture of n-hexane and THF (1:1) (20 ml per 0.1 mol reagent). The solution was stirred overnight, filtered and slowly evaporated to precipitate the product. In all cases, only starting materials could be isolated in 70 – 90 % yields.

4.4.38. Attempted Synthesis of [Rh(FcCOCHCOR)(CO)(PPh₂Fc)] (103), (104) and (105)
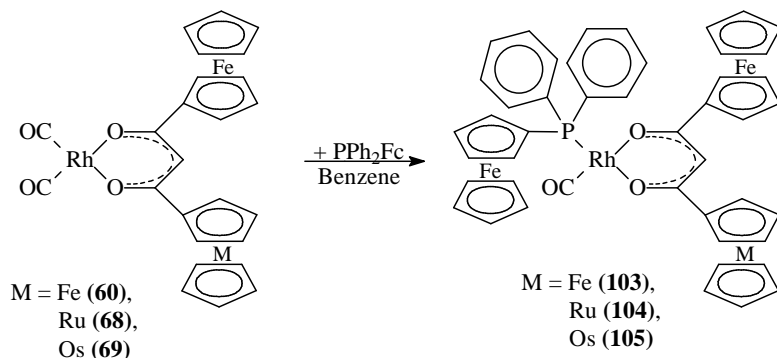
Solid ferrocenyldiphenylphosphine (1 eq.) was added to an oxygen-free solution of the appropriate dicarbonyl complex, **(60)**, **(68)** or **(69)** (1 eq.), in n-hexane (20 ml per 0.1 mol reagent). The mixture was stirred overnight at 45 °C, filtered and evaporated slowly to precipitate the product. In all cases the mixture was shown by NMR to contain both starting materials as well as the desired product, but any attempt to separate the crude reaction mixture failed to liberate a pure product.

4.4.39. Attempted Synthesis of [Rh(FcCOCHCOR)(CO)(PPh₂Rc)] (106), (107) and (108)
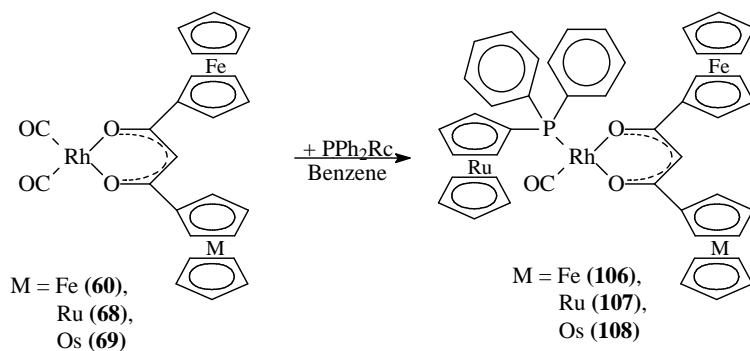
Solid ruthenocenyldiphenylphosphine (1 eq.) was added to an oxygen-free solution of the appropriate dicarbonyl complex **(60), (68) or (69)** (1 eq.) in benzene (minimum). The mixture was stirred overnight, filtered and evaporated slowly to precipitate the product. In all cases NMR showed the crude reaction mixture to contain both starting materials as well as the desired product.

4.4.40.[Rh(α-TTF-Sacac)(cod)] (75)
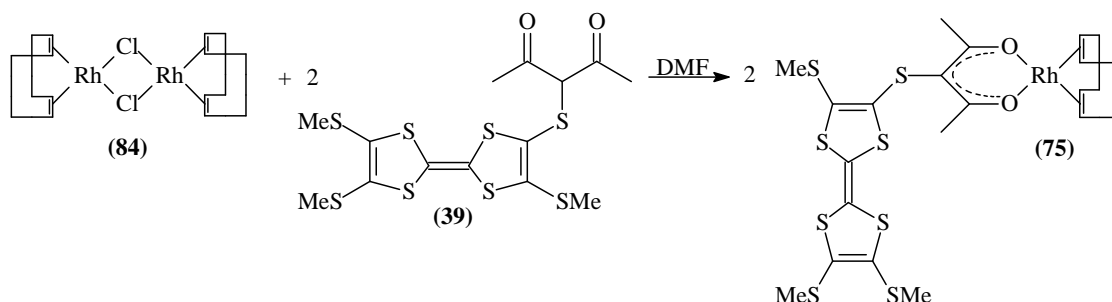
The β-diketone ligand (39) was provided by Dr. D Lorcy from the University of Rennes, France.

Solid β-diketone (0.05 g, 0.11 mmol, 2 eq.) was added to a solution of [Rh$_2$Cl$_2$(cod)$_2$] (0.03 g, 0.05 mmol) in DMF (2 ml). The mixture was stirred for 1 hour and the product precipitated with an excess of water. The product was filtered off, dissolved in ether and the organic layer washed with water. The ether was dried over Na$_2$SO$_4$ and evaporated under reduced pressure. Yield 72 % (0.06 g). Melting point = 179 °C. δ$_H$ (300 MHz, CDCl$_3$)/ppm: 4.13 (m; 4H; 4CH), 2.52 (m; 4H; 0.5 x 4CH$_2$), 2.48 (s; 3H; CH$_3$), 2.54 (s; 3H; CH$_3$), 2.44 (s; 3H; CH$_3$), 2.39 (m; 6H; 3SMe), 1.86 (m; 4H; 0.5 x 4CH$_2$), **Spectrum 37**.

4.4.41.[Rh(γ-TTF-Sacac)(cod)] (76)
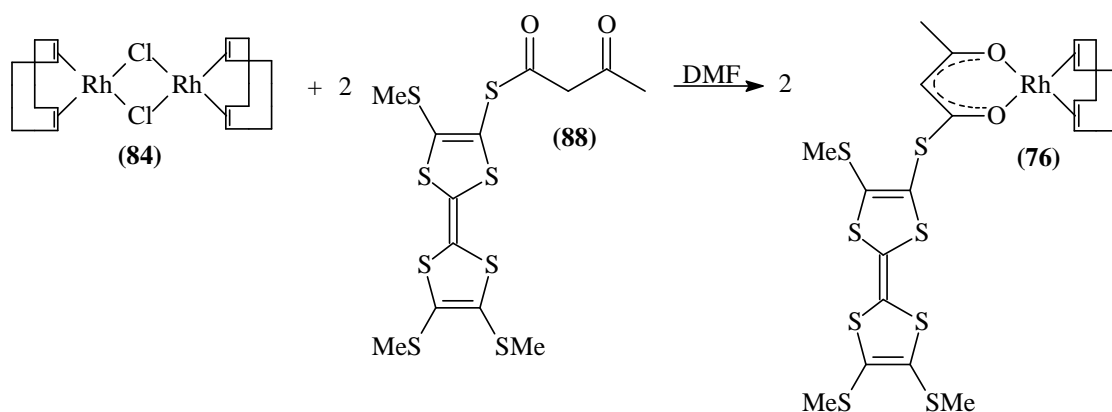
The β-diketone ligand (88) was provided by Dr. D Lorcy from the University of Rennes, France.

Solid β-diketone (0.10 g, 0.21 mmol, 2 eq.) was added to a solution of [Rh$_2$Cl$_2$(cod)$_2$] (0.06 g, 0.11 mmol) in DMF (4 ml). The mixture was stirred for 1 hour and the product

precipitated with an excess of water. The product was filtered off, dissolved in ether and the organic layer washed with water. The ether was dried over Na_2SO_4 and evaporated under reduced pressure. Yield 78 % (0.12 g). Melting point = 203 °C. δ_H (300 MHz, $CDCl_3$)/ppm: 5.46 (s; 1H; CH), 4.12 (m; 4H; 4CH), 2.49 (m; 4H; 0.5 x 4CH$_2$), 2.19 (s; 3H; CH$_3$), 2.02 (s; 3H; SMe), 1.95 (s; 6H; SMe), 1.85 (m; 4H; 0.5 x 4CH$_2$), **Spectrum 38**.

4.5.   Kinetics

4.5.1. Oxidative Addition Kinetics

NMR kinetic measurements were recorded on either a Bruker Advance DPX 300 NMR spectrometer for ^{1}H NMR kinetics, with chemical shifts relative to SiMe$_4$ at 0.00 ppm, utilizing the solvent peak as internal standard. ^{31}P and ^{19}F NMR measurements were recorded on a Bruker Advance II 600 NMR spectrometer, with chemical shifts relative to CFCl$_3$ at 0 ppm, using C$_6$H$_5$F as standard at -113.15 ppm for ^{19}F spectra, and chemical shifts relative to 85 % H$_3$PO$_4$ (0 ppm) for the ^{31}P spectra. IR kinetics were recorded on a Digilab 2000 Fourier transform spectrometer utilizing a He-Ne laser at 633 nm and UV/vis spectra on a Cary 50 Probe UV/visible spectrophotometer.

All kinetic measurements were monitored under pseudo first-order conditions, with [CH$_3$I] between 10 and 1 000 times that of rhodium(I) phosphine complexes. At least five different concentrations within this range were utilized. The concentration of rhodium(I) phosphine complexes were ≤ 0.0004 mol dm^{-3} for UV/vis measurements, and ≤ 0.01 mol dm^{-3} for IR and NMR measurements. The activation parameters, ΔH^* and ΔS^*, were obtained from kinetic experiments between 5.0 and 41.0 °C. Unless otherwise stated, five temperatures, held constant within 0.1 °C, were employed to establish the temperature dependence. The observed first-order rate constants were obtained from least-squares fits of absorbance *vs.* time data utilizing the fitting program MINSQ.[3]

4.5.2. Substitution Kinetics

A computer-controlled Applied Photophysics SX.18MV stopped-flow instrument was used to collect kinetic data. Observed rate constants were determined using the associated Applied Photophysics software. The temperature was controlled using a water bath to within 0.1 °C. The UV/vis-spectra of the [Rh(TTF-Sacac)(cod)] complexes, as well as the product of substitution [Rh(phen)(cod)]$^+$, were determined in methanol at 25 °C, on a Cary 50 Probe UV/visible spectrophotometer. From these spectra the wavelengths were determined where the reaction was followed kinetically. All substitution reactions were performed in freshly distilled methanol under pseudo first-order conditions, with the 1,10-phenanthroline concentrations between 10 and 500 times in excess. At least five different concentrations in this range were utilized for each complex. The activation parameters, ΔH^* and ΔS^*, were obtained from kinetic runs between 5 °C and 41 °C, with five different temperatures employed to establish the temperature dependence for each substitution reaction.

4.6. Structure Determinations

4.6.1. FcCOCH$_2$COOc (7)

The author acknowledges Mr. J.M. Janse van Rensburg from the Department of Chemistry, University of the Free State, for determining the crystal structure.

Red needle crystals of (7) were obtained by recrystallization from CH$_2$Cl$_2$ and n-heptane, by slow evaporation of the solvent. Data was collected on a Bruker X8 ApexII 4K Kappa CCD diffractometer, using Mo-K$_\alpha$ radiation.

4.6.2. PPh$_2$Rc (65)

The author acknowledges Mr. J.M. Janse van Rensburg from the Department of Chemistry, University of the Free State, for determining and solving the crystal structure.

Crystals of **(65)** were obtained by recrystallization from CH_2Cl_2 and n-hexane, by slow evaporation of the solvent. A colourless needle crystal, of dimensions 0.27 x 0.12 x 0.08 mm^3, was used for data collection on a Bruker X8 ApexII 4K Kappa CCD diffractometer, using Mo-K$_\alpha$ radiation. Cell constants and an orientation matrix for data collection were obtained from the least-squares refinement using the setting angles of 50 798 reflections in the range $2.41° < \theta < 28°$. Data were corrected for Lorentz and polarization effects. The structure was solved by direct methods and expanded using Fourier techniques. The non-hydrogen atoms were refined anisotropically. Hydrogen atoms were included but not refined.

4.6.3. [Rh(FcCOCHCOCF$_3$)(CO)(PPh$_2$Fc)] (70)

The author acknowledges Dr. A.J. Muller from the Department of Chemistry, University of the Free State, for determining and solving the crystal structure.

Crystals of **(70)** were obtained by recrystallization from warm n-hexane, by slowly allowing the reaction mixture to cool. A red needle crystal, of dimensions 0.20 x 0.09 x 0.07 mm^3, was used for data collection on a Bruker X8 ApexII 4K Kappa CCD diffractometer, using Mo-K$_\alpha$ radiation. Cell constants and an orientation matrix for data collection were obtained from the least-squares refinement using the setting angles of 65 121 reflections in the range $1.74° < \theta < 28.32°$. Data were corrected for Lorentz and polarization effects. The structure was solved by direct methods and expanded using Fourier techniques. The non-hydrogen atoms were refined anisotropically. Hydrogen atoms were included but not refined.

4.7.   Electrochemistry

Measurements on ca. 1.0 mmol.dm^{-3} solutions of the complexes in dry, air free dichloromethane containing 0.10 mol.dm^{-3} tetrabutylammonium tetrakis (pentafluorophenyl)borate as supporting electrolyte, were conducted under a blanket of purified argon at 25 °C utilizing a BAS 100 B/W electrochemical workstation interfaced with a personal computer. A three-electrode cell, which utilized a Pt auxiliary electrode, a glassy carbon working electrode (surface area 0.0707 cm^2) and an in house constructed

Ag/Ag$^+$ (0.01 mol.dm^{-3} AgNO$_3$) reference electrode mounted on a Luggin capillary was used. Successive experiments under the same experimental conditions showed that all formal reduction and oxidation potentials were reproducible within 5 mV. Results are referenced against ferrocene, utilizing decamethyl ferrocene (Fc*) as internal standard. To achieve this, each experiment was first performed in the absence of ferrocene and decamethyl ferrocene, and then repeated in the presence of $<$ 1 mmol.dm^{-3} decamethyl ferrocene. A separate experiment containing only ferrocene and decamethyl ferrocene was also performed. Data was then manipulated on a Microsoft Excel worksheet to set the formal reduction potentials of the Fc/Fc$^+$ couple to 0 V. Under our conditions the Fc*/Fc^{*+} couple was at -607 mV vs. Fc/Fc$^+$, while the Fc/Fc$^+$ couple was at 220 mV vs. Ag/Ag$^+$.

4.7.1. Spectral Electrochemistry

Spectral electrochemistry was performed with an Omni Cell Specac P/N 1800 (shown in **Figure 4.1**), attached to a BAS CV-27 electrochemical workstation interfaced with a personal computer. The Ottel cell was placed inside a Bruker Tensor 27 Fourier transform IR in order to obtain IR-spectra. Measurements were carried out on ca. 3.0 mmol.dm^{-3} solutions of the complexes in dry dichloromethane, containing 0.30 mol.dm^{-3} tetrabutylammonium tetrakis(penta fluorophenyl)borate as supporting electrolyte, at 25 °C. IR-spectra were taken at regular intervals, as the potential was increased in 0.05 V - 0.1 V increments, from 0 V till *ca*. 1.6 V.
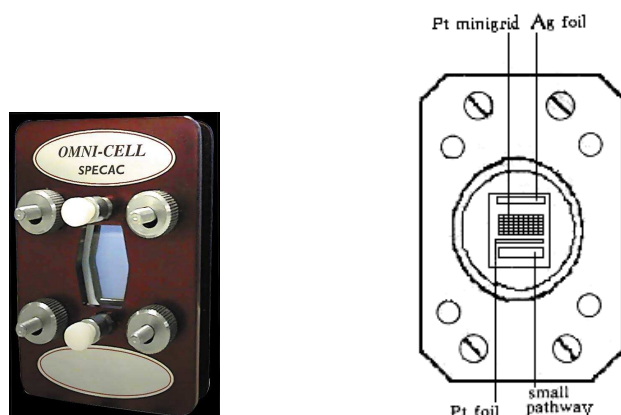
Figure 4.1. Picture and schematic representation of an Omni cell.

4.7.2. Electrochemical Isomerization Kinetics

Time-based CV and SW voltammograms of 2.0 mmol dm^{-3} enol-enriched solutions of FcCOCH$_2$CORc (6) in CH$_3$CN as well as in CH$_2$Cl$_2$ were recorded at a scan rate of 200 mV s^{-1} and frequency of 50 Hz. To overcome electrode fouling problems, manual adjustment of the amplitude of the internal standard, free ferrocene, or the ferrocenyl wave of (6), to identical peak current levels for each time-based run, and conversion of the amended time-based peak currents to percentage keto isomer, allowed collection of good kinetic interpretable data.

Solid β-diketone samples older than 3 months were quickly dissolved and CV's and SW's recorded at appropriate times at 298 K until an equilibrium set in. The percentage keto isomer at each time interval was determined from **Equation 4.1**. From the time-based keto percentage data fitted to **Equation 4.2**,[4] observed rate constant k_{obs} could be calculated.

$$\% \text{ keto isomer} = \frac{i_p \text{ of keto signal}}{i_p \text{ of keto signal} + i_p \text{ of enol signal}} \times 100$$

Equation 4.1

$$\ln\left[\frac{(\text{initial \% keto isomer}) - (\text{\% keto isomer at infinite time})}{(\text{\% keto isomer at time t}) - (\text{\% keto isomer at infinite time})}\right]$$

Equation 4.2

$$= (k_1 + k_{-1})t = k_{obs}t$$

The percentage keto isomer at infinite time is that of K_c, while k_1 and k_{-1} relates to **Equation 4.3**.

$$\text{Rc-CO-CH}_2\text{-CO-R} \underset{k_{-1}}{\overset{k_1}{\rightleftharpoons}} \text{Rc-CO-CH=C(OH)-R}$$
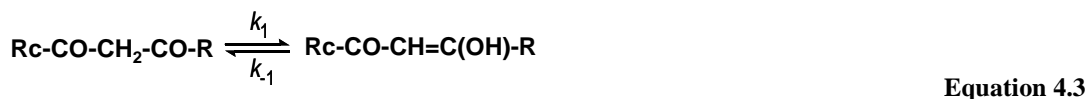
Equation 4.3

The individual rate constants k_1 and k_{-1} were obtained by simultaneously solving the equations $K_c = k_1/k_{-1}$ and $k_{obs} = k_1 + k_{-1}$.

4.8. Cytotoxic Tests

The author acknowledges Prof. C.E.J. Medlen, from the Department of Pharmacology, University of Pretoria, for performing the experiments.

Compounds were dissolved in DMSO to give stock concentrations of 10 mg cm^{-3} and diluted in the appropriate growth medium (EMEM+), which contains components such as essential amino acids, vitamins, inorganic salts, hormones, metabolites and nutrients) supplemented with fetal calf serum (FCS) to give final DMSO concentrations not exceeding 0.5 % and drug concentrations of 1 – 3000 μg cm^{-3} prior to cell experiments.

Human cervix epitheloid cancer cell line, HeLa (ATCC CCI-2), was grown as a monolayer culture in MEM. Human colorectal cell line, CoLo DM320 (ATCC CCL-220), was grown as a suspended culture in RPMI 1640. Growth medium was incubated at 37 °C under 5 % CO_2 and fortified with 10 % FCS and 1 % penicillin and streptomycin. Appropriate solvent control systems were included. Cells were seeded at 500 cells / well for 7 days incubation experiments and in 96 well microtiter plates in a final volume of 200 μl of growth medium in the presence or absence of different concentrations of experimental drugs. Wells without cells and with cells but without drugs were included as controls. After incubation at 37 °C for 7 days, cell survival was measured by means of the colometric 3-(4,5-dimethylthiazol-2-yl)-diphenyl tetrasodium bromide (MMT) assay.

---

[1] B.S. Furniss, A.J. Hannaford, P.W.G. Smith, A.R. Tatchell, *Vogel's Textbook of Practical Organic Chemistry*, 5th ed., Pearson Education Limited, Harlow, England, **1989**, pp. 395-412.

[2] W.C. du Plessis, T.G. Vosloo, J.C. Swarts, *J. Chem. Soc., Dalton Trans.*, 1998 2507-2514.

[3] MINSQ, Least Squares Parameter Estimation, Version 3.12, MicroMath, 1990.

[4] J.E. House, In *Principles of Chemical Kinetics*, W. C. Brown Publishers: Dubuque, 1997, p. 46-51.

Chapter 5

Summary and Future Perspectives

In this study, metallocene-containing ligands, as well as their rhodium(I) complexes, were synthesized and their physical properties examined. Four known metallocene-containing β-diketones, FcCOCH$_2$COR with R = CF$_3$, ferrocenyl (Fc), ruthenocenyl (Rc) and osmocenyl (Oc), were synthesized. Attempts were made to synthesize positively-charged cobaltocenium-containing β-diketones, utilizing BF$_3$ as catalyst. However, all attempts were unsuccessful, due to the competing aldol condensation side reaction dominating over the expected Claisen condensation, β-diketone-forming reaction. A range of metallocene-containing phosphine ligands were synthesized by various methods, including the known PPh$_2$Fc, and the new ligands PPh$_2$Rc, PPh$_2$Oc and the positively-charged (PPh$_2$Cc$^+$)(PF$_6^-$) ligand. The crystal structure of PPh$_2$Rc was determined. This compound crystallized in a monoclinic crystal system having a P2(1)/c space group, Z = 4, a = 14.2986(7) Å, b = 10.4474(5) Å, c = 11.6886(6) Å, α = γ = 90°, β = 91.713(3)°.

Rhodium(I) phosphine complexes were synthesized, by first synthesizing a series of four new rhodium(I) dicarbonyl complexes, [Rh(FcCOCHCOR)(CO)$_2$], where R = CF$_3$, Fc, Rc and Oc. Two new electron-rich metallocenyl-phosphine rhodium complexes of the type [Rh(FcCOCHCOCF$_3$)(CO)(PPh$_2$Mc)], where Mc = Fc and Rc, were then synthesized. The known complex, [Rh(FcCOCHCOCF$_3$)(CO)(PPh$_3$)], was also synthesized for comparison purposes. ^{1}H and ^{31}P NMR studies showed the existence of at least two isomers, the *cis-* and *trans*-isomers, in solution. The crystal structure of [Rh(FcCOCHCOCF$_3$)(CO)(PPh$_2$Fc)] was solved, indicating that the *cis*-isomer (where the phosphine ligand is next to the β-diketonato oxygen closest to the ferrocenyl group) forms in the crystal state. This is the opposite isomer than electronic considerations predict, and it shows clearly that crystallization energy plays a more dominant role than steric or electronic influences during crystallization. [Rh(FcCOCHCOCF$_3$)(CO)(PPh$_2$Fc)] crystallized in a monoclinic crystal system having a P2(1)/n space group, Z = 4, a = 9.9416(2) Å, b = 23.2737(5) Å, c = 13.6632(3) Å, α = γ = 90°, β = 96.069(1)°.

A series of three new electron-poor rhodium(I) complexes containing pentafluorophenyl-rings substituted on the phosphine ligands of the type [Rh(FcCOCHCOCF$_3$)(CO){PPh$_n$(C$_6$F$_5$)$_{3-n}$}] with n = 0, 1 and 2, was also synthesized. ^{1}H and ^{19}F NMR studies were carried out, also indicating the existence of a *cis*- and *trans*-isomer in solution.

Oxidative addition (the first step of the Monsanto process towards commercial acetic acid synthesis) of methyl iodide to all the above mentioned rhodium(I) phosphine complexes was studied kinetically by UV, FT-IR, ^{1}H NMR, ^{31}P NMR and ^{19}F NMR. Results obtained by different methods were in excellent agreement. To our knowledge, this was the first time that ^{19}F was used to elucidate oxidative addition reactions. NMR Results showed that oxidative addition proceeded by up to three consecutive reaction steps, involving two Rh(III) alkyl and two Rh(III) acyl species. NMR results also showed the existence of at least two isomers of each alkyl and acyl species in the reaction mixture. Long reaction times and background noise during the third step made it difficult to identify the second acyl species clearly. The mechanism was found to follow the general reaction mechanism below (**Scheme 5.1**). Large variations in rate constant were observed. It is known that the rates of reaction for oxidative addition reactions increase with an increase in electron density on the metal center. Despite this, the rate of reaction for [Rh(FcCOCHCOCF$_3$)(CO)(PPh$_2$Rc)] {χ_R(Rc) =1.99; k_1 = 0.015 dm^{3}mol^{-1}s^{-1}} was found to be about double that of [Rh(FcCOCHCOCF$_3$)(CO)(PPh$_2$Fc)] {χ_R(Fc) =1.87; k_1 = 0.0075 dm^{3}mol^{-1}s^{-1}}, with [Rh(FcCOCHCOCF$_3$)(CO)(PPh$_3$)] {χ_R(Ph) =2.21; k_1 = 0.006 dm^{3}mol^{-1}s^{-1}} reacting slightly slower. Rates of reaction for fluorinated compounds were dramatically slower, due to the highly electron-withdrawing pentafluorophenyl groups attached. [Rh (FcCOCHCOCF$_3$)(CO){PPh$_2$(C$_6$F$_5$)}] (k_1 = 0.0003 dm^{3}mol^{-1}s^{-1}) showed rates of reaction of up to 20x slower than that of [Rh(FcCOCHCOCF$_3$)(CO)(PPh$_3$)], with [Rh(FcCOCHCOCF$_3$)(CO){PPh(C$_6$F$_5$)$_2$}] (k_1 = 0.000010 dm^{3}mol^{-1}s^{-1}) showing rates of reactions 600x slower and [Rh(FcCOCHCOCF$_3$)(CO){P(C$_6$F$_5$)$_3$}] not undergoing oxidative addition at all (*i.e.* k_1 = 0 dm^{3}mol^{-1}s^{-1}). The fluorinated complexes were also

only involved in the first step involving rate constants k_2 and k_{-2} of the mechanism shown in **Scheme 5.1**, implying that $k_3 = k_4 = 0$ s^{-1}.

$$
\begin{bmatrix} [Rh^I(fctfa)(CO)(PPh_3)]_A \\ \Updownarrow K_{c1} \\ [Rh^I(fctfa)(CO)(PPh_3)]_B \end{bmatrix} + CH_3I \underset{k_{-1}}{\overset{k_1}{\rightleftharpoons}} \begin{bmatrix} [Rh^{III}\text{-alkyl1A}] & [Rh^{III}\text{-acyl1A}] \\ \Updownarrow K_{c2} \quad K_2=k_2/k_{-2} \quad \Updownarrow K_{c3} \\ [Rh^{III}\text{-alkyl1B}] & [Rh^{III}\text{-acyl1B}] \end{bmatrix} \underset{k_{-3}}{\overset{k_3}{\rightleftharpoons}} \begin{bmatrix} [Rh^{III}\text{-alkyl2A}] \\ \Updownarrow K_{c4} \\ [Rh^{III}\text{-alkyl2B}] \end{bmatrix} \underset{k_{-4}}{\overset{k_4}{\rightleftharpoons}} \begin{bmatrix} [Rh^{III}\text{-acyl2A}] \\ \Updownarrow K_{c5} \\ [Rh^{III}\text{-acyl2B}] \end{bmatrix}
$$

First set of reactions   *Second set of reactions*   *Third set of reactions*
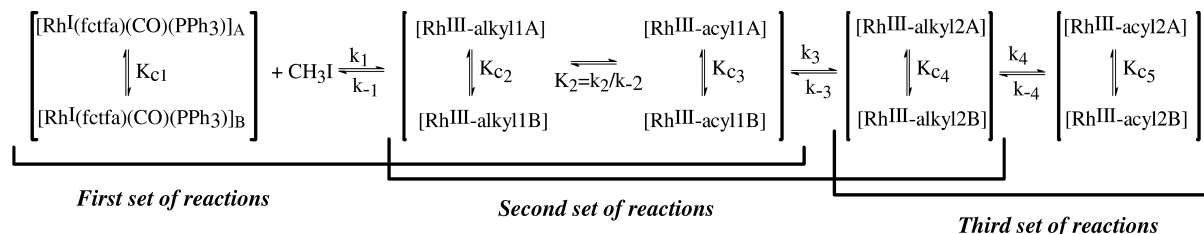
Scheme 5. 1. Proposed mechanism for oxidative addition of CH_3I to rhodium β-diketonato complexes.

Rhodium(I) cyclooctadiene complexes containing acetylacetonato ligands substituted with a tetrathiafulvalene (TTF) group in either the α- or the β-position were also synthesized. The substitution reaction of the TTF-containing β-diketonato ligand with 1,10-phenanthroline was investigated by stopped-flow methods due to the extremely fast rate of reaction for these compounds. Second-order rate constants were found to be in the order of 1×10^3 dm^3 mol^{-1} s^{-1}. The β-diketonato group was found to be displaced by 1,10-phenanthroline. The rate of reaction doubled when the bulky TTF group was substituted on the β-position, instead of the α-position. This clearly shows the significant role the position of side-groups play on the rate of reaction, despite identical electronic properties.

The electrochemistry of all synthesized complexes were studied in CH_2Cl_2 and the highly non-interacting $[N^nBu_4][B(C_6F_5)_4]$ as supporting electrolyte. The CV's of the metallocene-containing phosphines showed the regular redox couples associated with the metallocenes; one one-electron transfer process for ferrocene, osmocene and ruthenocene and two one-electron processes for cobaltocene. A single electrochemical irreversible, one-electron oxidation at the phosphorus center at potentials above 1 V was also observed. Oxidation of the phosphorus center forms a highly unstable phosphorus radical, which is followed by further decomposition reactions.

The electrochemistry of rhodium(I) complexes showed an additional quasi-reversible one-electron oxidation at the rhodium center to form an unstable rhodium(II) species. In the case of the rhodium(I) dicarbonyl complexes, $[Rh(FcCOCHCOR)(CO)_2]$ with R =

207

CF$_3$, Fc, Rc and Oc, the rhodium-based electron-transfer process was buried underneath the ferrocene redox couple. Square wave voltammetry was, however, successful to resolve the two separate peaks. Spectro-electrochemistry coupled to Fourier transform IR gave further proof of the oxidation of rhodium(I). The CV's of rhodium(I) phosphine complexes [Rh(FcCOCHCOCF$_3$)(CO)(*phosphine*)] showed the redox couples of the β-diketonato ferrocenyl groups at potentials ranging from 0.25 V to 0.4 V. Some overlapping between the ferrocene redox couple and rhodium redox couple was again observed, but was well resolved by SW. Oxidation of the phosphorus center was also observed at potentials ranging from 0.9 V to 1.4 V. An additional metallocene redox couple is also observed for complexes with metallocene-containing phosphine ligands. Spectro-electrochemistry was able to detect oxidative addition of the solvent, CH$_2$Cl$_2$ to the rhodium(I) center at high potentials (E$_{applied}$ > 1.4 V *vs*. Fc/Fc$^+$).

The electrochemistry of rhodium(I)-cod complexes containing tetrathiafulvalene-substituted acetylacetonato groups showed three redox processes, two of which belonged to the redox-active tetrathiafulvalene group. The redox-couple of the rhodium center were observed at 0.89 V and 0.51 V for the complexes substituted in the α- and β-positions respectively. Rotation of the α-substituted tetrathiafulvalene group out of the rhodium plane severely hampers conjugation, while, in the case of the β-substituted complex, conjugation between the highly electron-donating tetrathiafulvalene group and the rhodium center takes place. When a conjugated system is formed, the rhodium center becomes more electron-rich and oxidation takes place at a lower potential.

All newly synthesized compounds were tested for anti-tumor activity. It was found that the metallocene-containing phosphine ligands alone show little anti-tumor activity, although phosphines with a high fluorine-content showed significant activity. For rhodium(I) phosphine complexes, anti-tumor activity was observed to increase linearly with an increase in group electronegativity (χ$_R$) of the phosphine substituents, irrespective of the presence of additional metallocene groups. The pentafluorophenyl-group was identified as a powerful anti-tumor fragment. Tetrathiafulvalene-containing ligands also

showed significant activity, but their rhodium(I) complexes showed no significant cytotoxicity.

The present investigation can be considered the augural study of a vast research program to follow. [Rh(FcCOCHCOCF$_3$)(CO)(PPh$_2$Rc)] was identified as the most effective compound capable of undergoing oxidative addition, with an oxidative addition half-life of 39 s. However, no attention has been focused on any possible catalytic activity of the present series of compounds. A fine balance exists between oxidative addition and reductive elimination, in the overall Monsanto catalytic cycle. Increasing the rate of oxidative addition usually slows down the reductive elimination. A study to determine the rate of reductive elimination must be initiated, in order to establish the overall potential of the present series of compounds as possible catalysts. A study to determine the effect of the present compounds in catalysis under industrial high pressure CO conditions and high temperatures, conditions under which catalyst stability is crucial, must also be performed.

The electron-rich metallocene-containing phosphine ligands synthesized in this study proved very successful to accelerate the rate of oxidative addition to rhodium complexes. Extending this series of phosphines holds many interesting possibilities. The effect of inserting an alkyl spacer between the metallocene and the phosphorus-atom {PPh$_2$-(CH$_2$)$_n$-Mc} on the group electronegativity of the phosphine ligand will allow fine tuning of the rate of oxidative addition. A completely new class of ligands consisting of mixed phosphites, where the metallocene group is attached *via* an oxygen atom to the phosphorous atom {PPh$_2$-O-(CH$_2$)$_n$-Mc} can be synthesized. The effect it has on oxidative addition reactions when co-ordinated to rhodium can be researched. Varying the number of such phosphite substituents {PPh$_n$-(O-(CH$_2$)-Mc)$_{3-n}$} may offer higher catalytic activity. Investigating the electrochemistry of such new phosphine and phosphite ligands would be essential and offer great insight into phosphorus electrochemistry.

Attempts during this study to expand the metallocene-containing β-diketonato series to include cobaltocenium were unsuccessful, mostly due to the positive charge on the cobaltocenium group $\{(C_5H_4)Co^{III}(C_5H_5)\}^+$. Synthetic routes used for other metallocenes (ferrocene, ruthenocene and osmocene) can be utilized if the cobaltocene group can be manipulated in the reduced form $\{(C_5H_4)Co^{II}(C_5H_5)\}$. The neutral $(C_5H_4)Co^{II}(C_5H_5)$ species is, however, highly unstable (air sensitive), and must be handled in an inert atmosphere. With the appropriate apparatus, and by taking the necessary care, this is a viable option towards cobaltocenium complexes which should also contribute to the development of good and new synthetic skills.

The tetrathiafulvalene group of ligands also offers a vast range of projects for future research. Many more TTF-containing ligands have been synthesized, including TTF-containing phosphine ligands. To date, very few of these have been complexed with metals. These ligands can thus be complexed with rhodium, and their physical properties, as well as catalytic applications investigated.

Appendix 1

NMR Spectra

Spectrum 1. Ruthenocene (93)
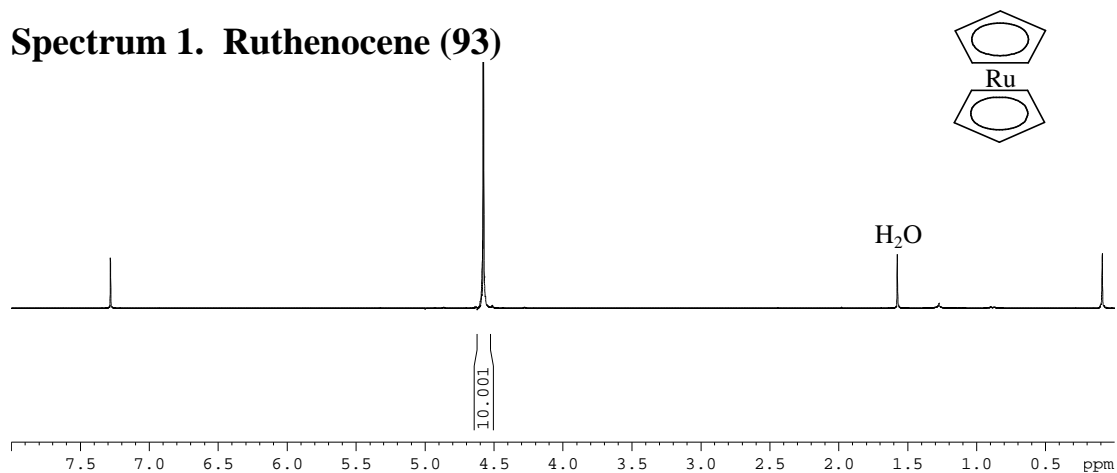
Spectrum 2. Acetyl Ferrocene (94)
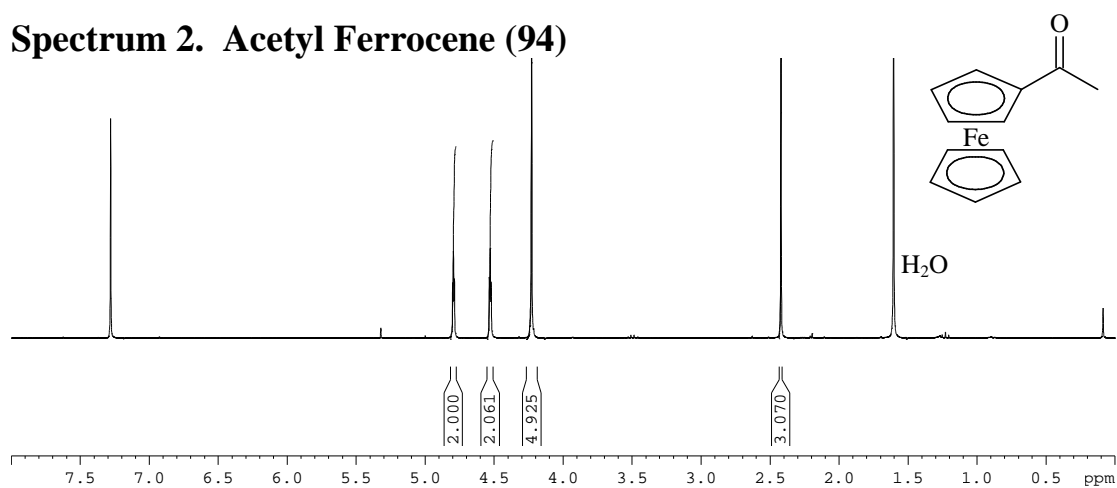
Spectrum 3. Acetyl Ruthenocene (95)
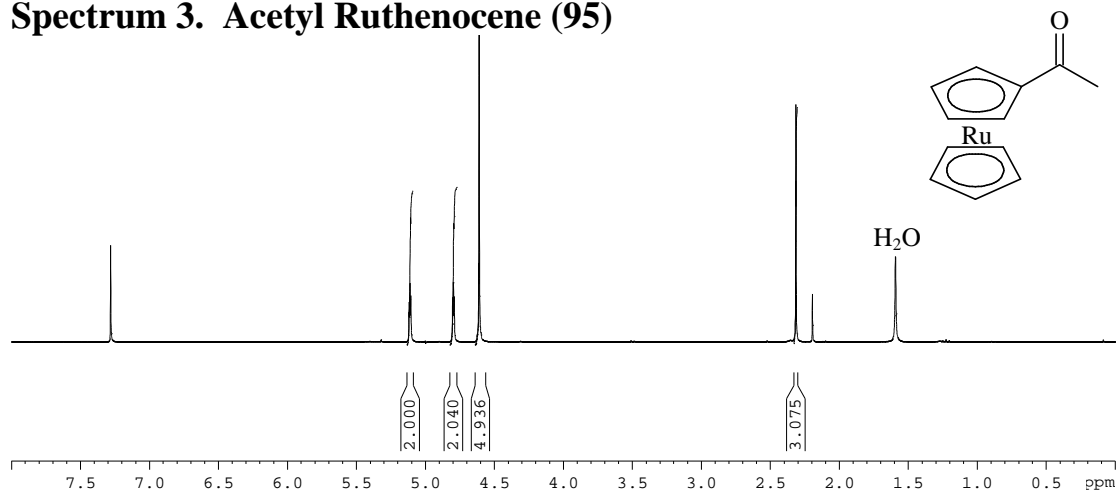
Spectrum 4. Acetyl Osmocene (96)
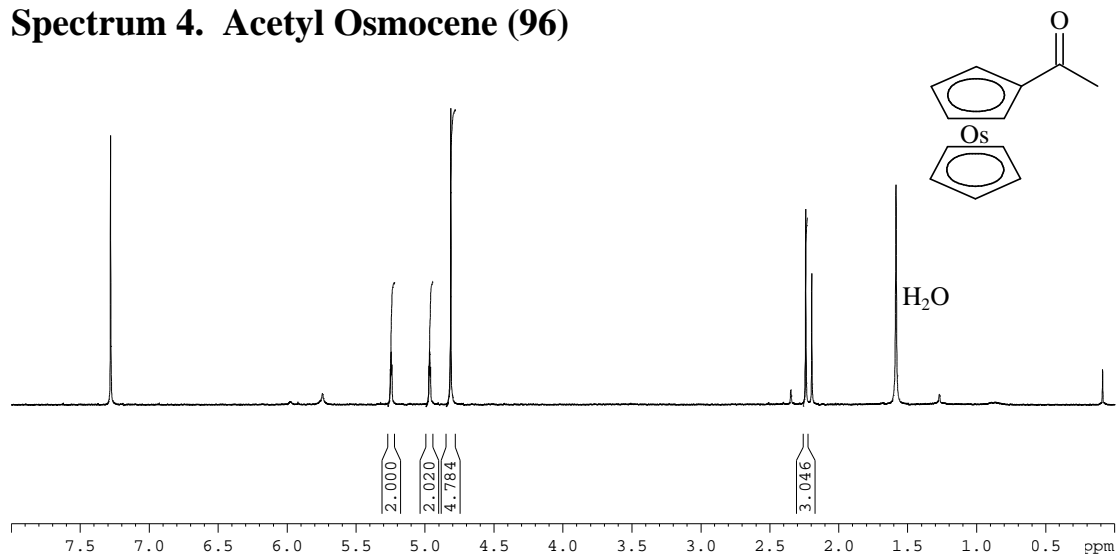
Spectrum 5. 1-Ferrocenyl-4,4,4-trifluorobutane-1,3-dione (1)
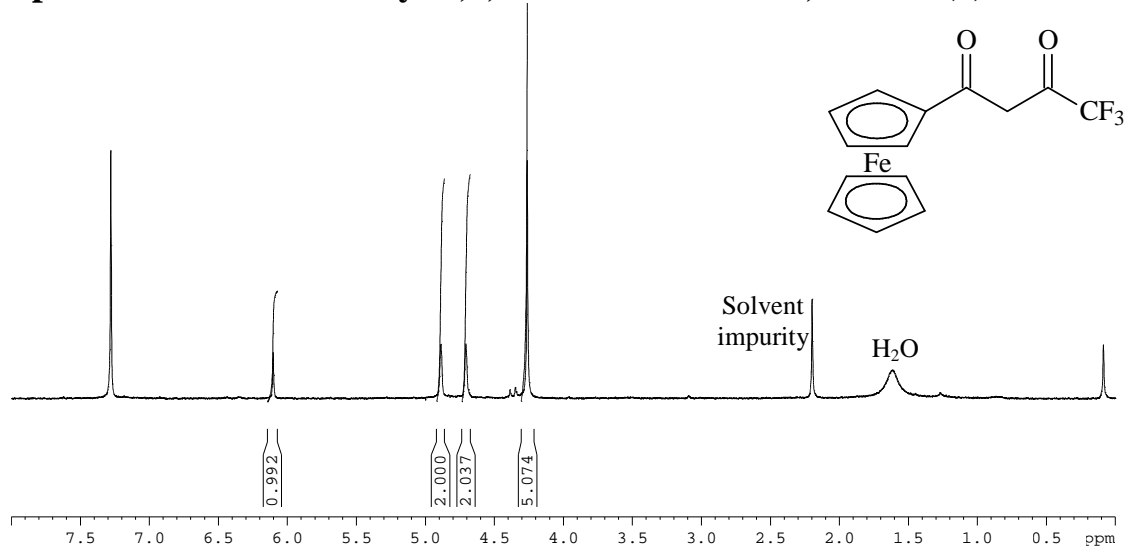
Spectrum 6. 1,3-Diferrocenylpropane-1,3-dione (5)
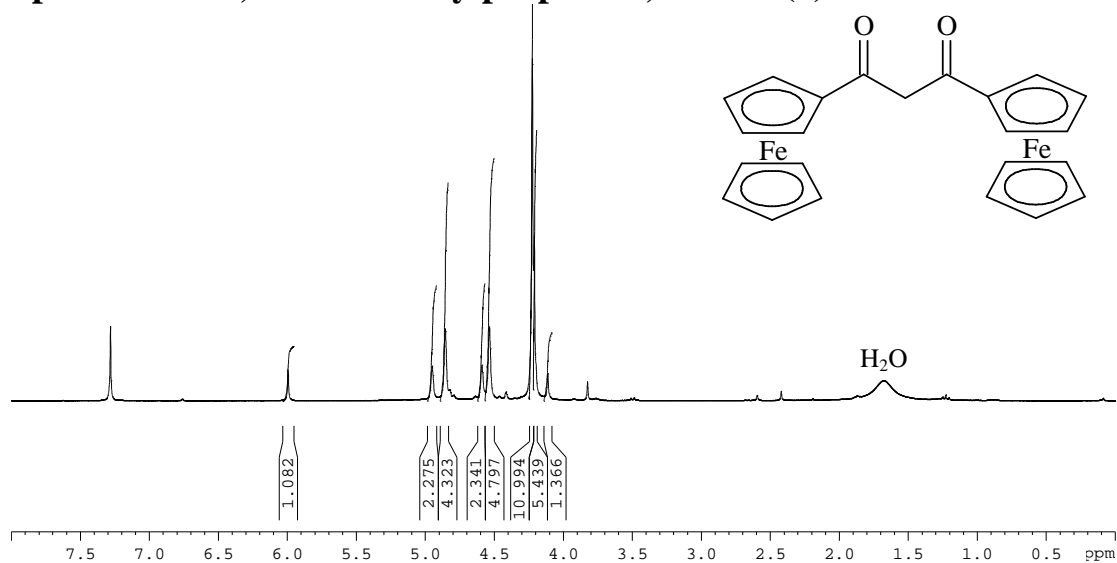
Spectrum 7. 1-Ferrocenyl-3-ruthenocenylpropane-1,3-dione (6)

Solvent impurity

H_2O
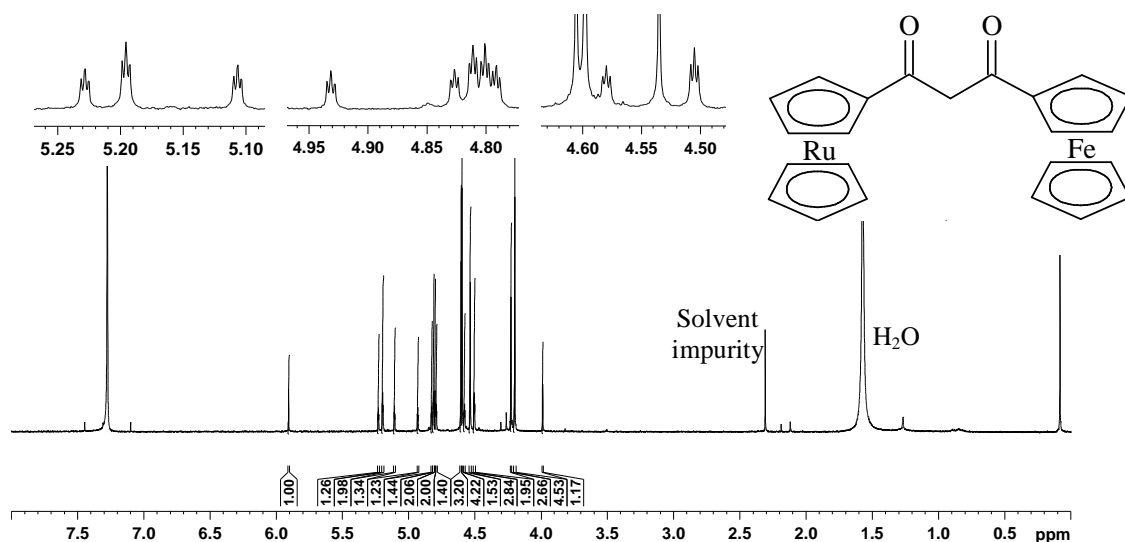
Spectrum 8. 1-Ferrocenyl-3-osmocenylpropane-1,3-dione (7)

H_2O
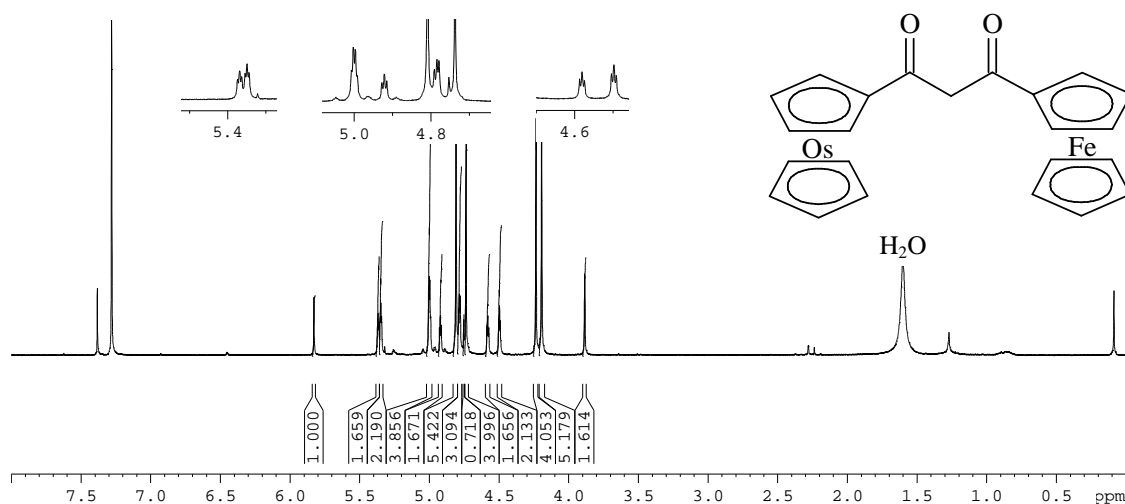
Spectrum 9. Non-isolatable Cobaltocenium (97), Methylcobaltocenium (98) and 1,1'-Dimethylcobaltocenium (99) Hexafluorophosphate Mixture
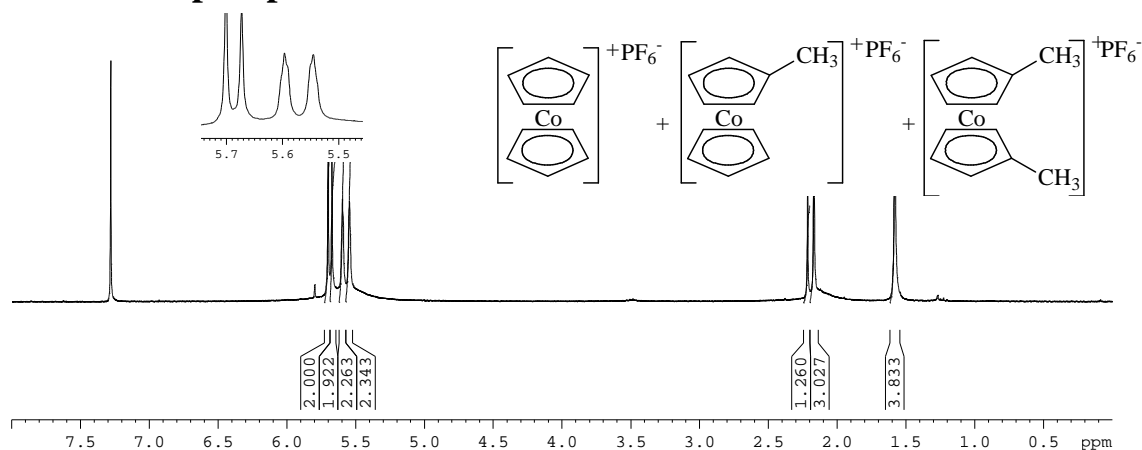
Spectrum 10. Carboxycobaltocenium hexafluorophosphate (100)
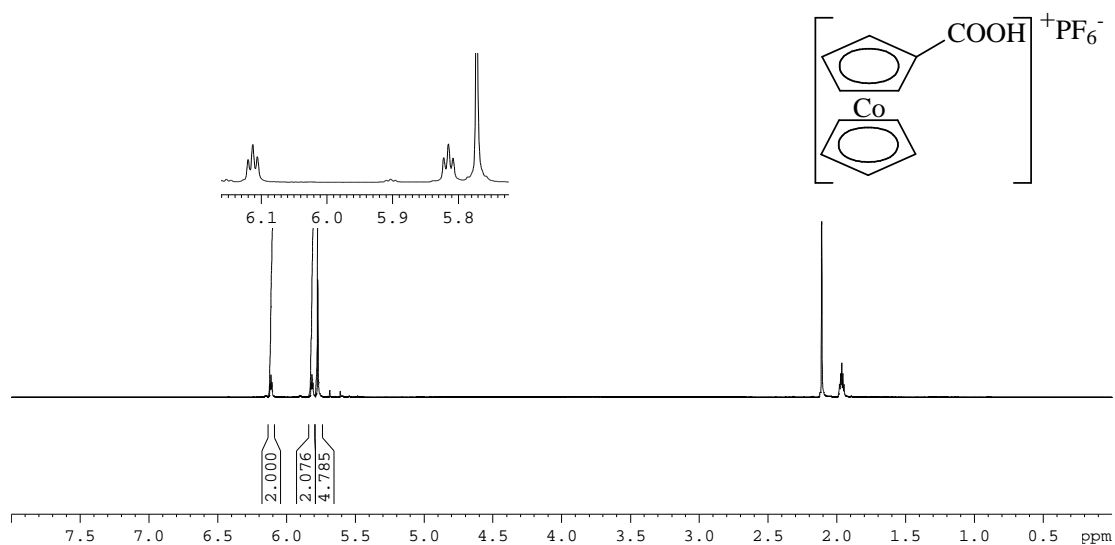
Spectrum 11. Chlorocarbonylcobaltocenium salt (101)
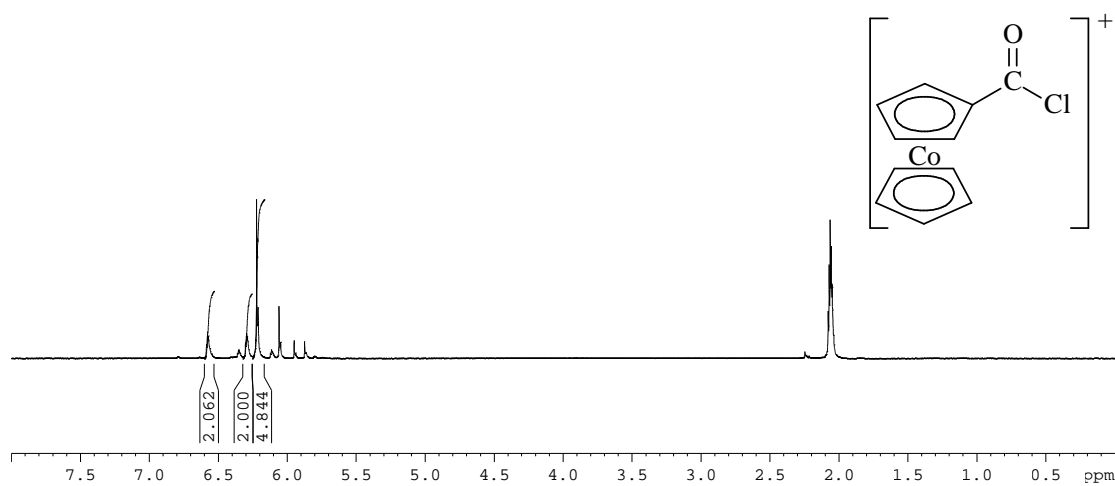
Spectrum 12. Propanoylferrocene (79)
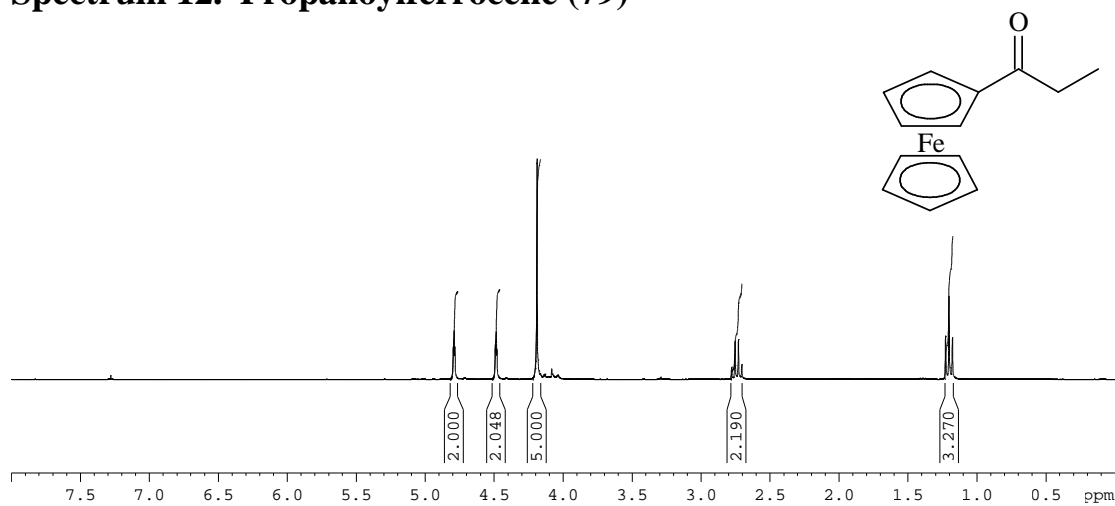
Spectrum 13. Ferrocenic Anhydride (77)
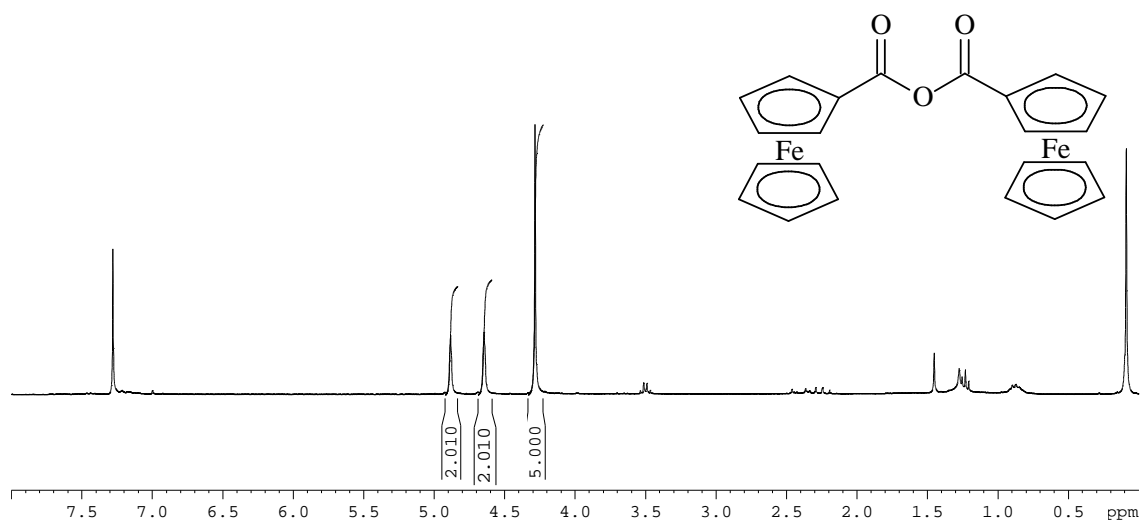
Spectrum 14. Ferrocene Carboxylic acid
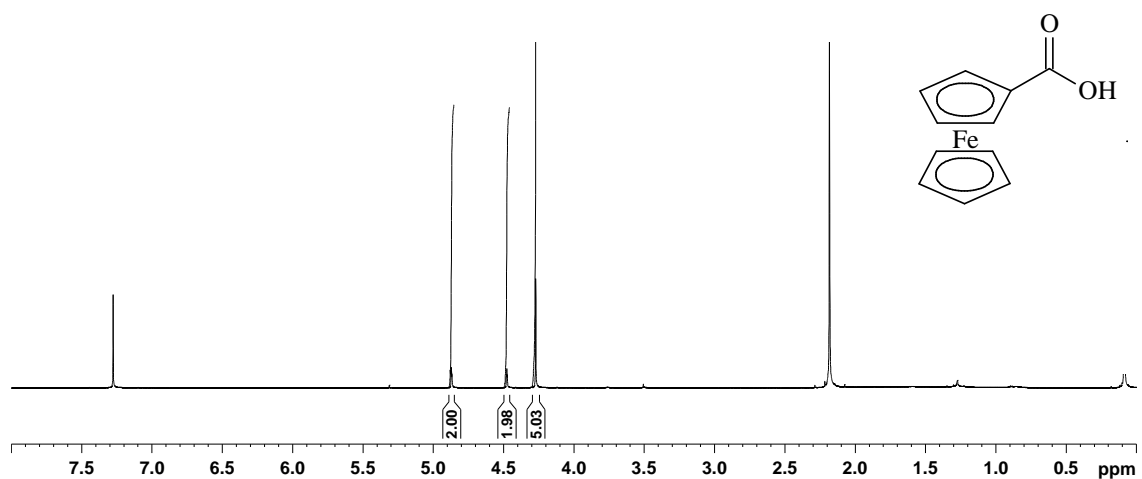
Spectrum 15. Cobaltocenium anhydride hexafluorophosphate (78)
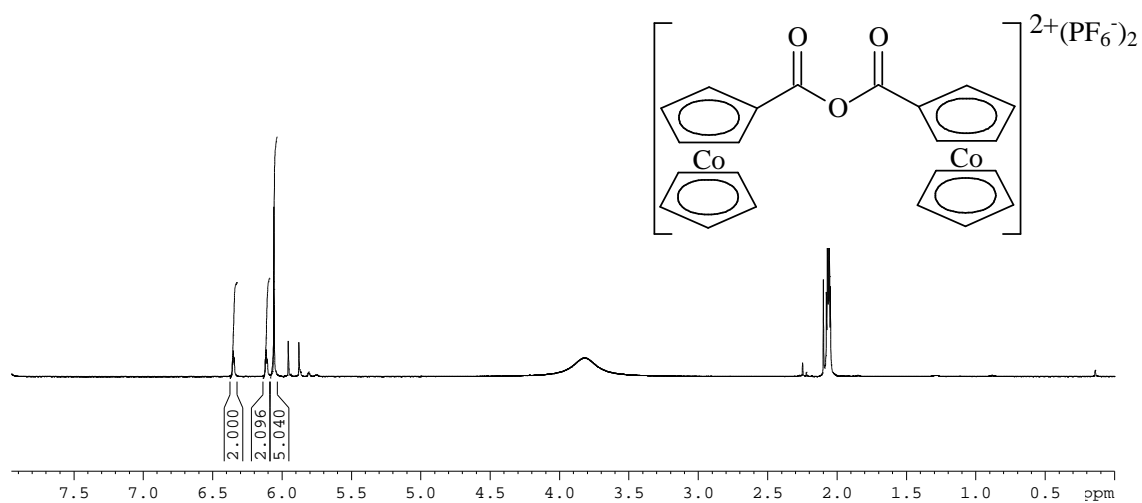
Spectrum 16. Aldol Product (from BF₃-Synthesis) (80)
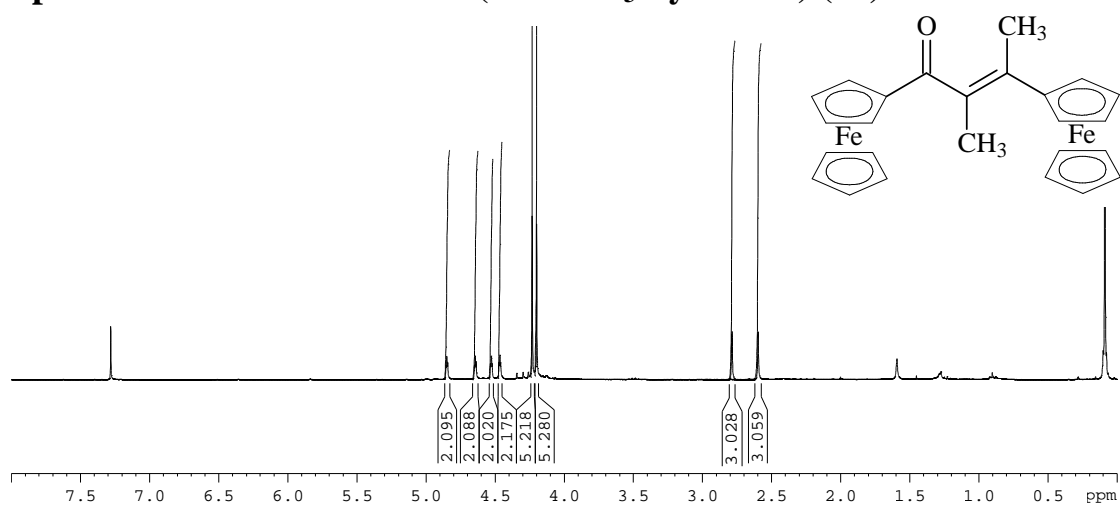
Spectrum 17. Ferrocenyl Diphenylphosphine (13)
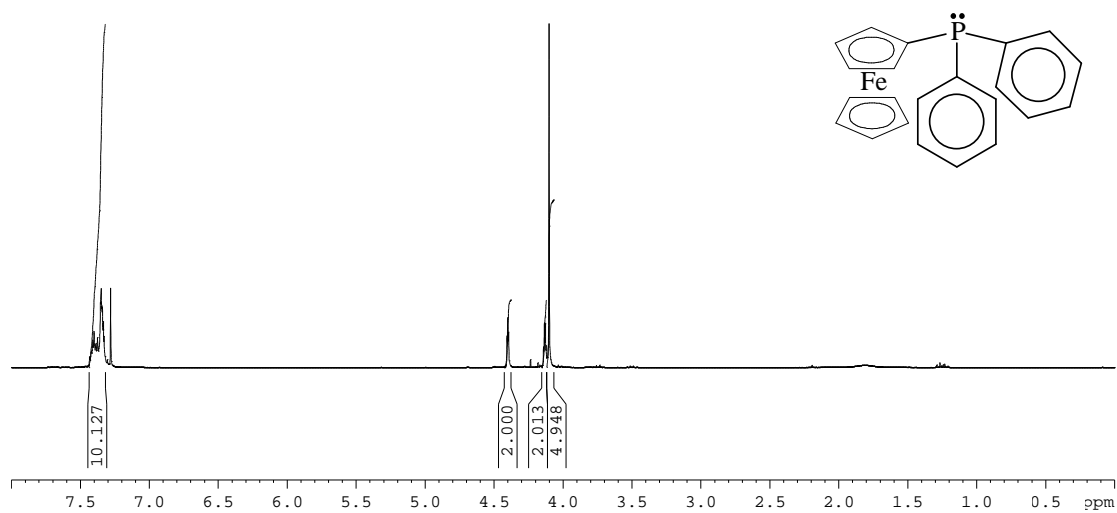
Spectrum 18. Ruthenocenyl Diphenylphosphine (65)
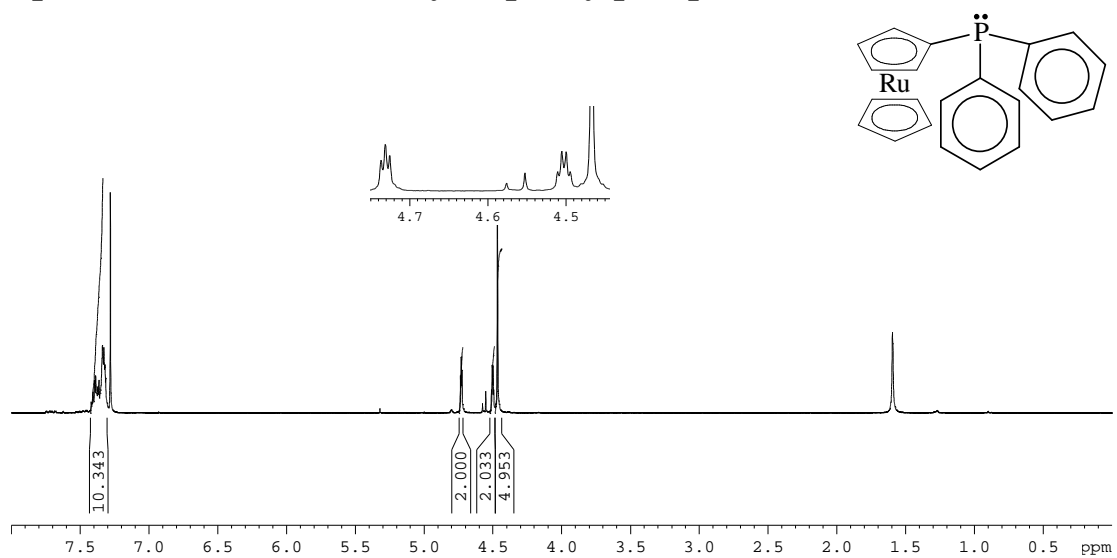
Spectrum 19. Osmocenyl Diphenylphosphine (66)
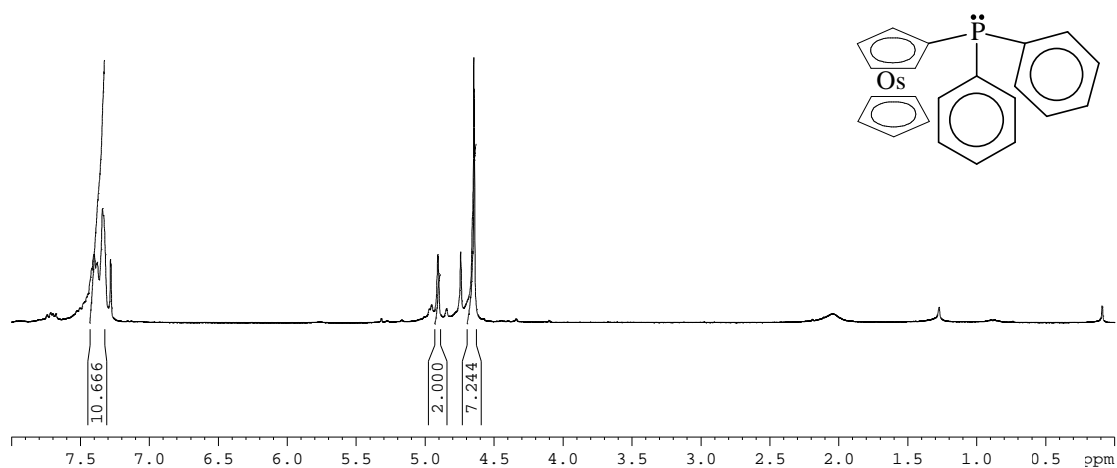
Spectrum 20. Diphenylphosphinocobaltocenium hexafluorophosphate (67)
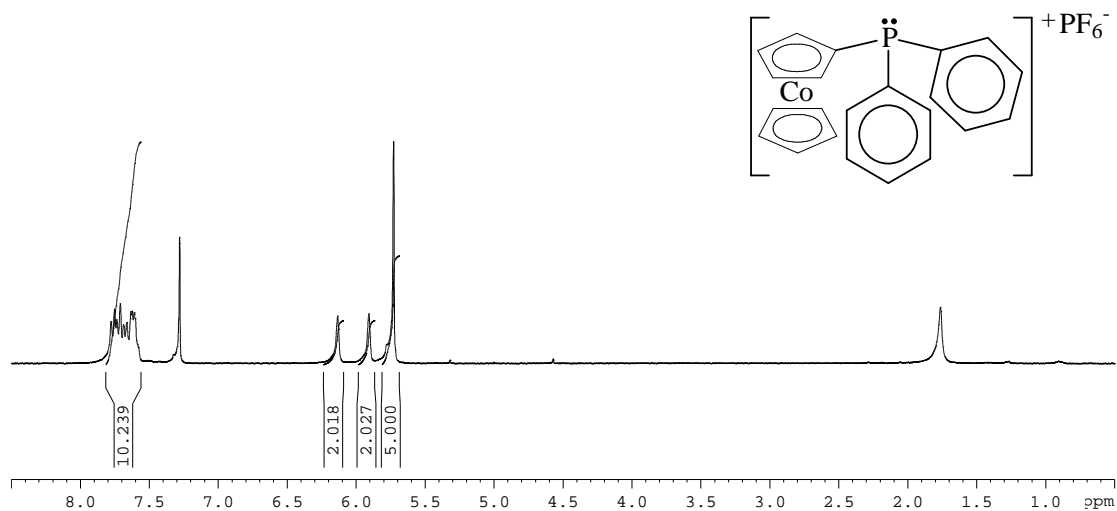
Spectrum 21. Di-μ-chloro-bis[(1,2,5,6-η)1,5-cyclooctadiene]rhodium (84)
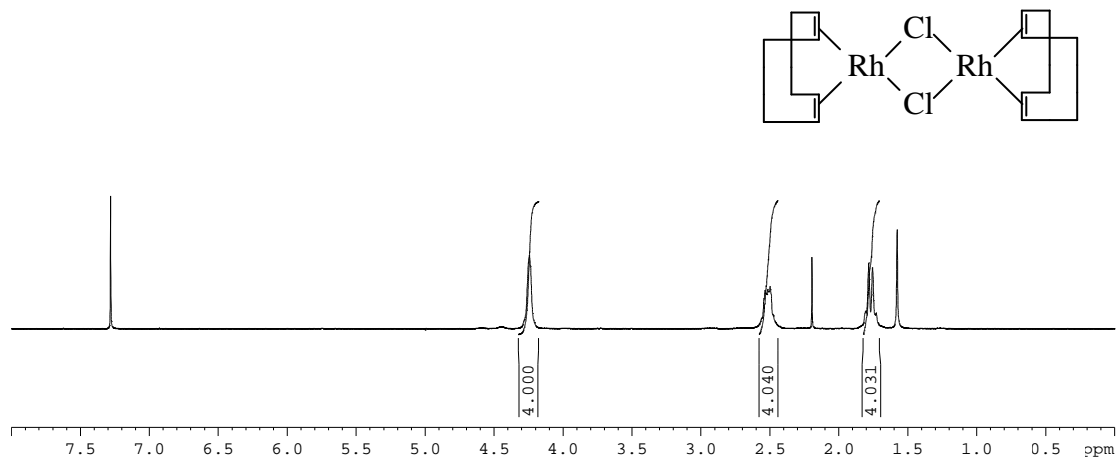
Spectrum 22. [Rh(FcCOCHCOCF₃)(cod)] (47)
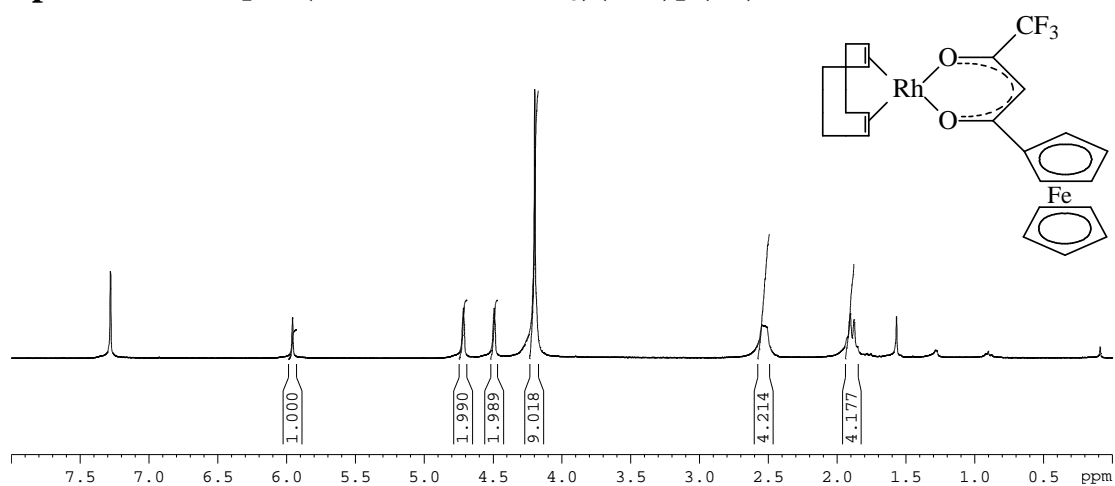
Spectrum 23. [Rh(FcCOCHCOFc)(cod)] (51)
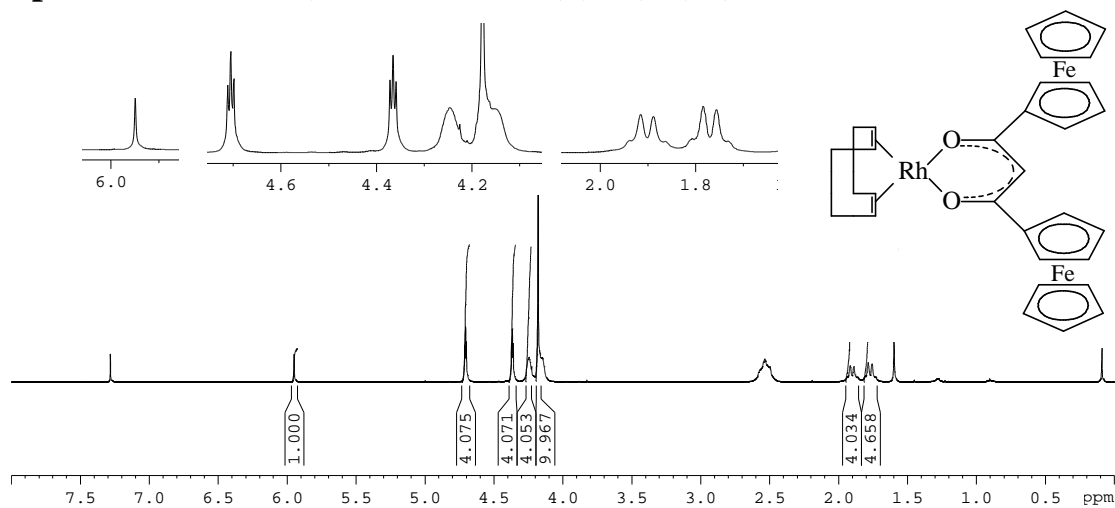
Spectrum 24. [Rh(FcCOCHCORc)(cod)] (81)
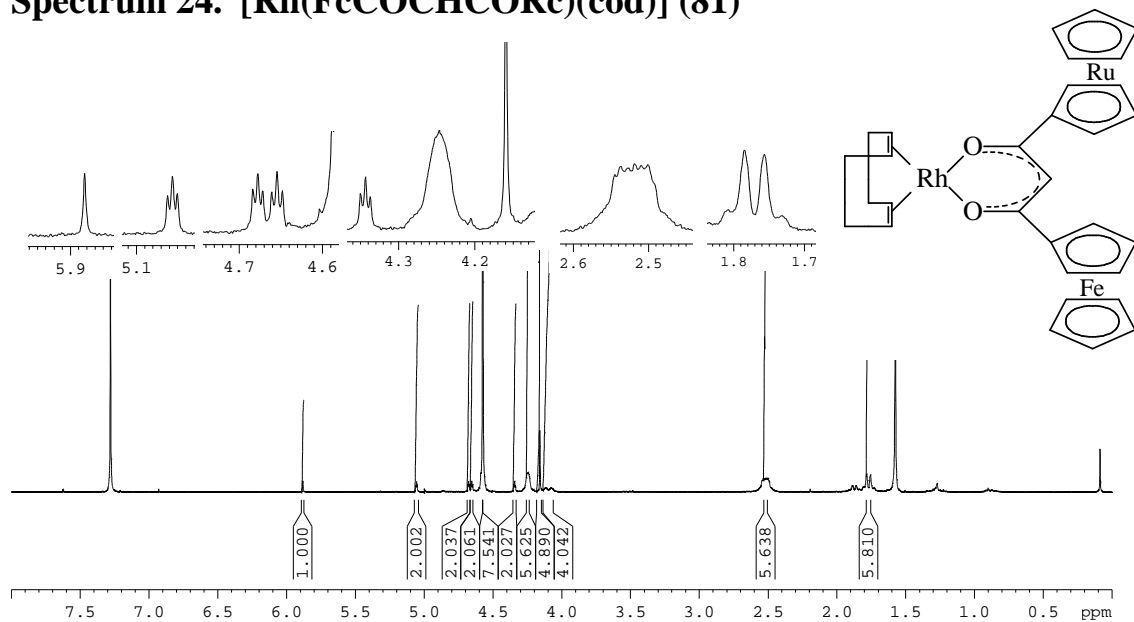
Spectrum 25. [Rh(FcCOCHCOOc)(cod)] (82)
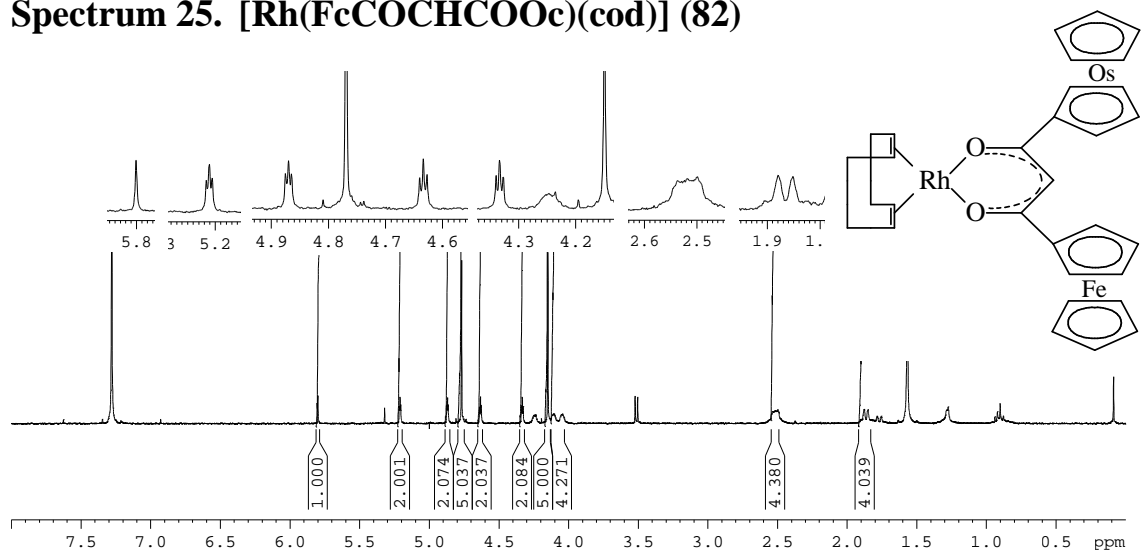
Spectrum 26. [Rh(FcCOCHCOCF₃)(CO)₂] (57)
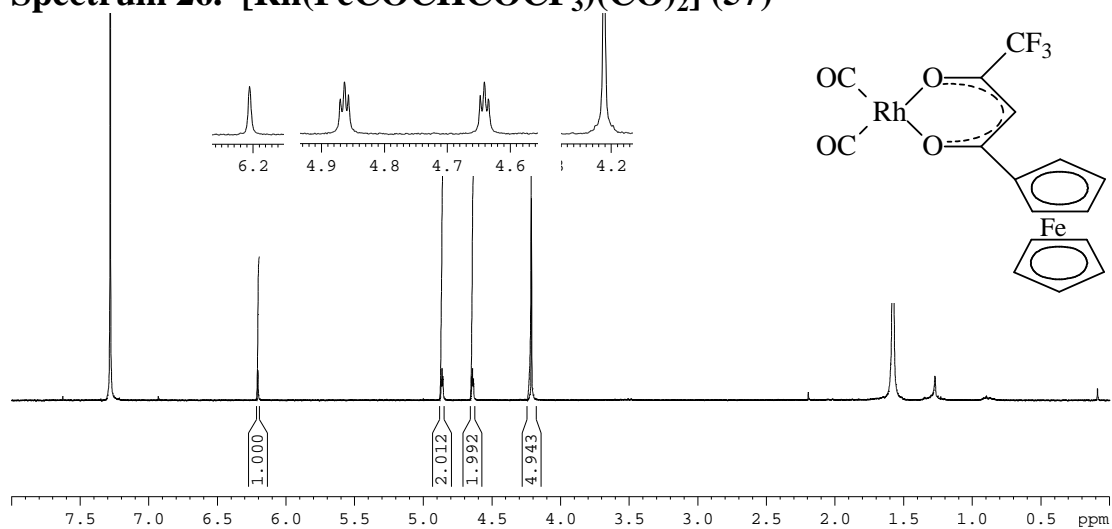
Spectrum 27. [Rh(FcCOCHCOFc)(CO)₂] (60)
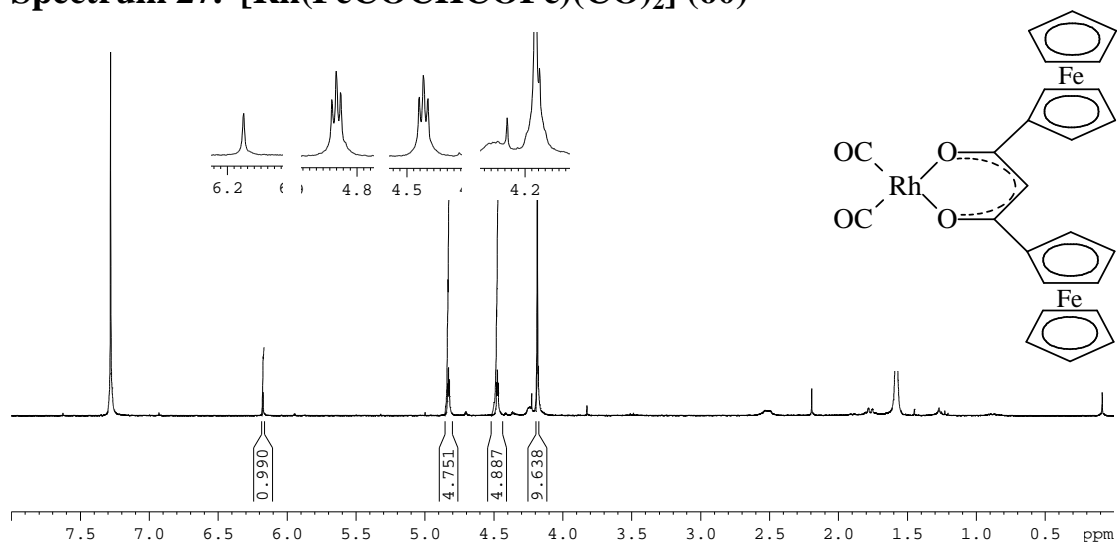
Spectrum 28. [Rh(FcCOCHCORc)(CO)₂] (68)
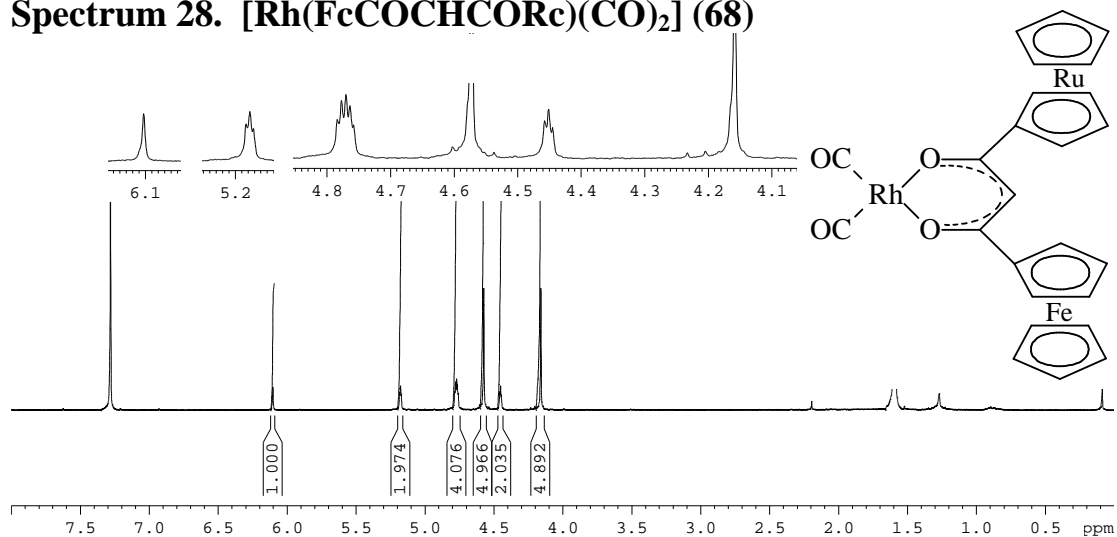
Spectrum 29. [Rh(FcCOCHCOOc)(CO)₂] (69)
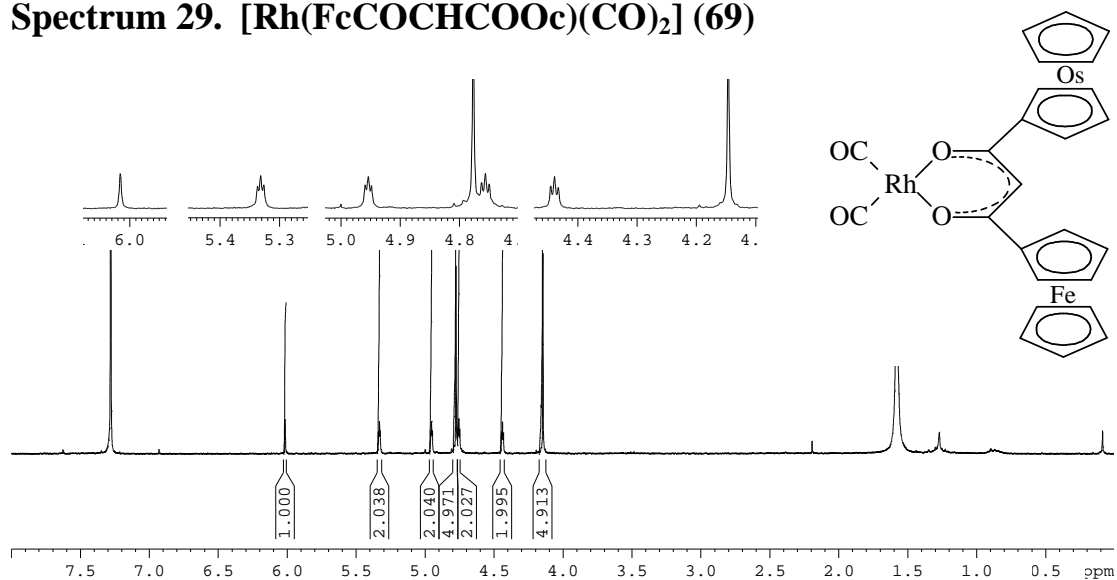
Spectrum 30. [Rh(CF₃COCHCOCH₃)(CO)₂] (83)
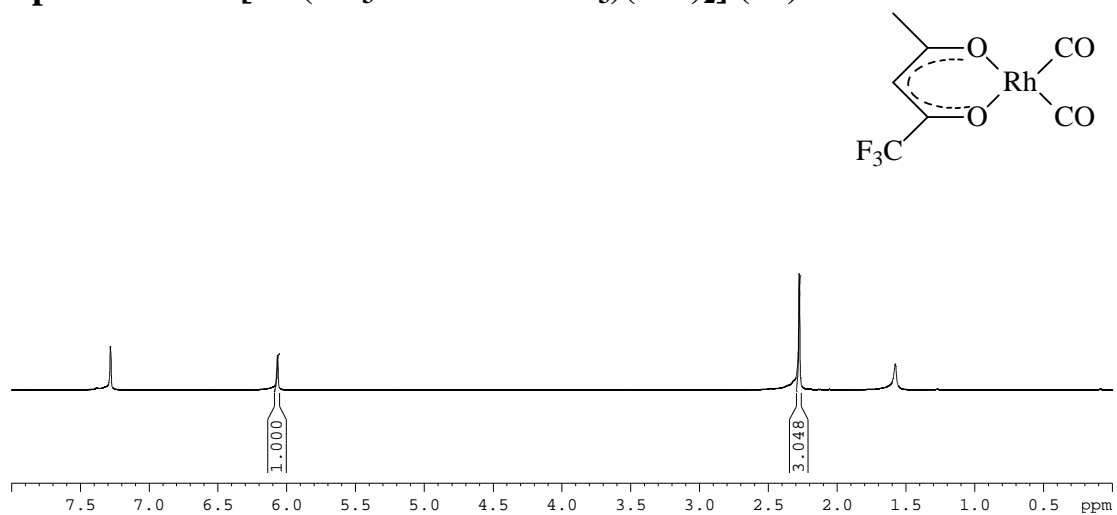
Spectrum 31. [Rh(FcCOCHCOCF₃)(CO)(PPh₃)] (29)
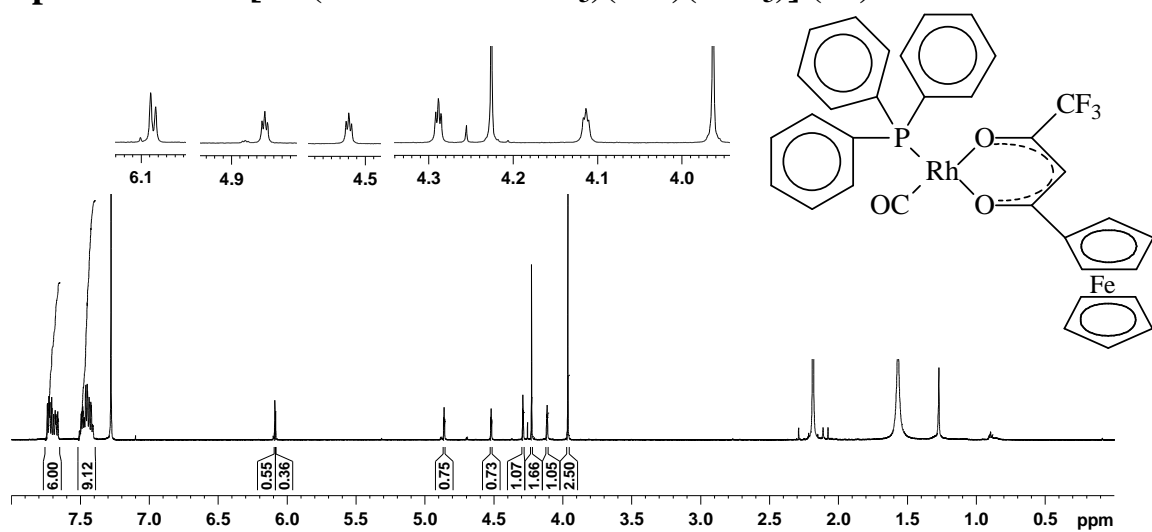
Spectrum 32. [Rh(FcCOCHCOCF₃)(CO)(PPh₂Fc)] (70)
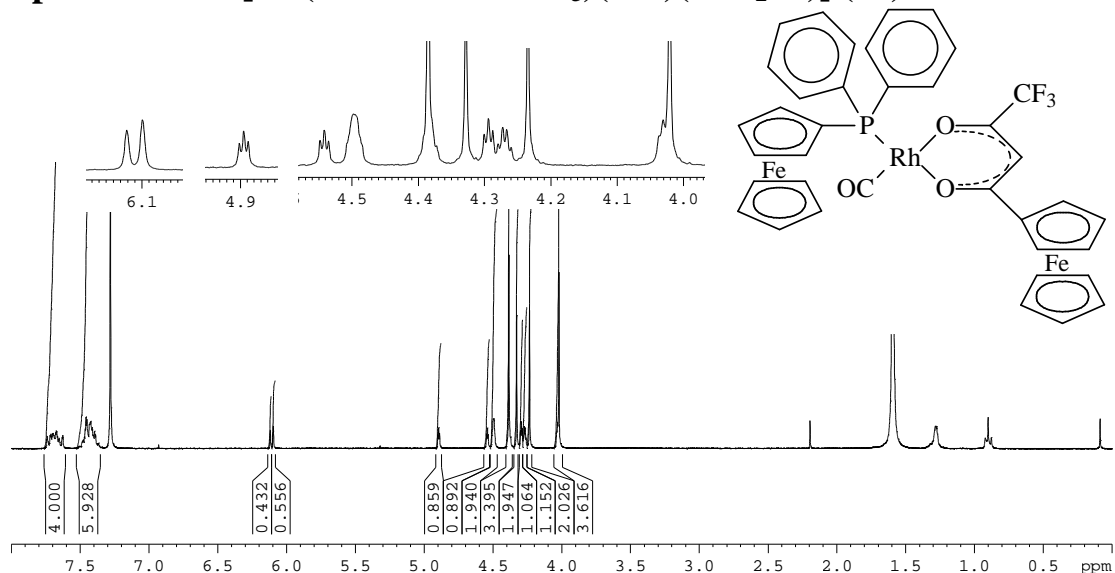
Spectrum 33. [Rh(FcCOCHCOCF₃)(CO)(PPh₂Rc)] (71)
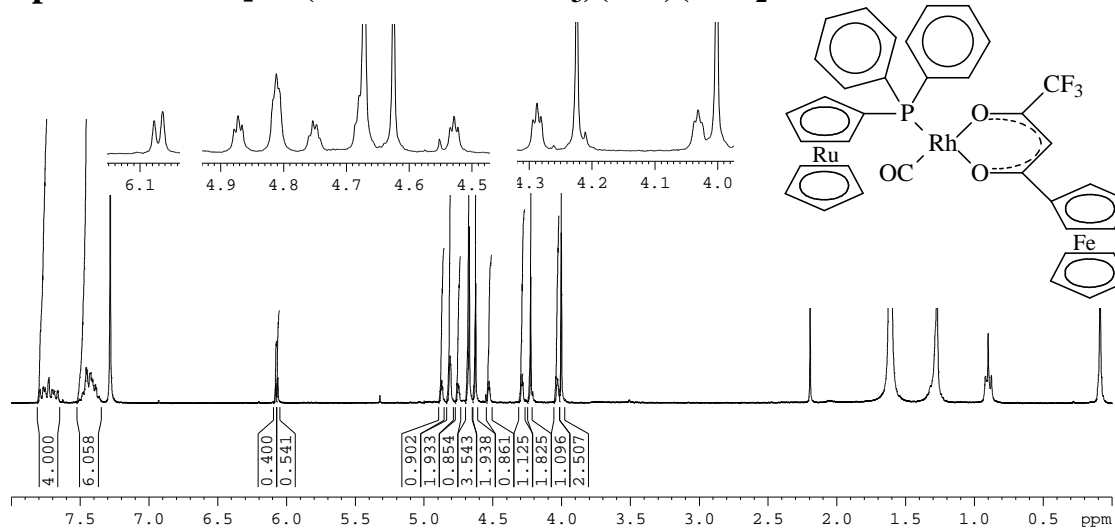
Spectrum 34. [Rh(FcCOCHCOCF₃)(CO)(PPh₂(C₆F₅))] (72)
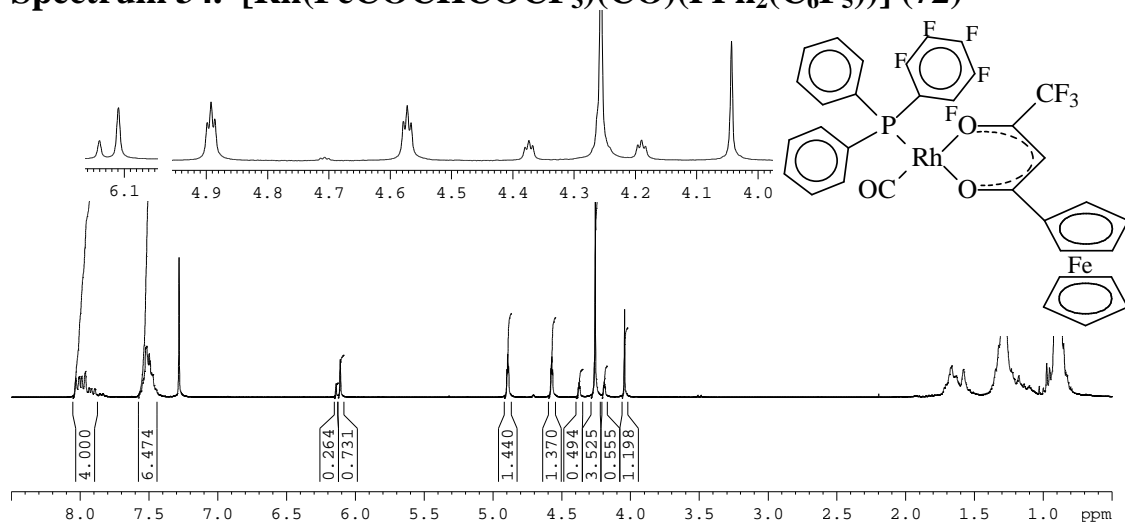
Spectrum 35. [Rh(FcCOCHCOCF₃)(CO)(PPh(C₆F₅)₂)] (73)
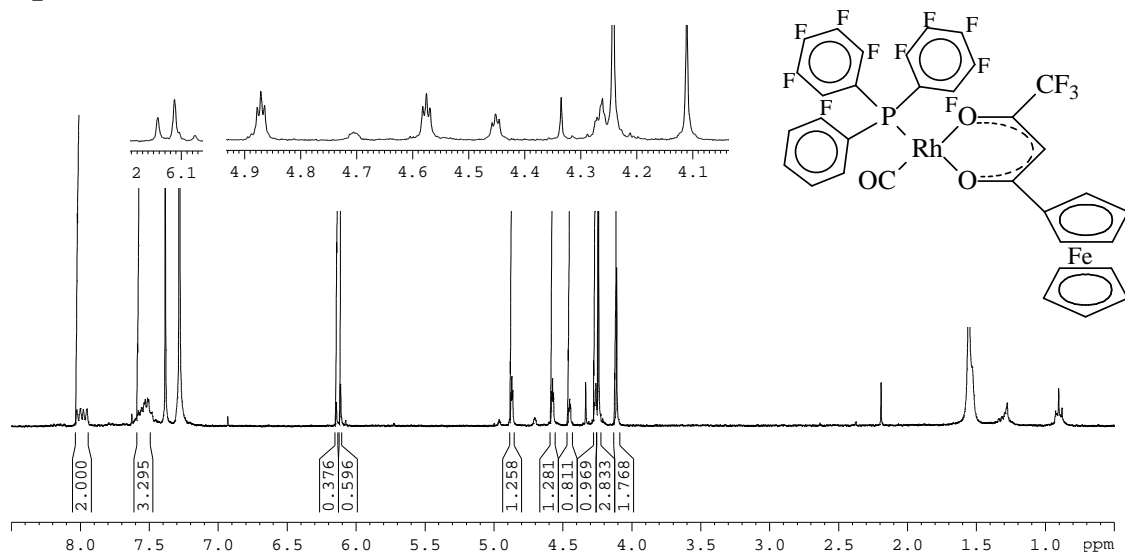
Spectrum 36. [Rh(FcCOCHCOCF₃)(CO)(P(C₆F₅)₃)] (74)

Spectrum 37. [Rh(α-TTF-Sacac)(cod)] (75)

7.5 7.0 6.5 6.0 5.5 5.0 4.5 4.0 3.5 3.0 2.5 2.0 1.5 1.0 0.5 ppm

4.003 3.941 3.110 2.958 6.526 4.091

Spectrum 38. [Rh(γ-TTF-Sacac)(cod)] (76)

7.5 7.0 6.5 6.0 5.5 5.0 4.5 4.0 3.5 3.0 2.5 2.0 1.5 1.0 0.5 ppm

1.001 4.176 4.168 3.283 3.055 6.379 4.222
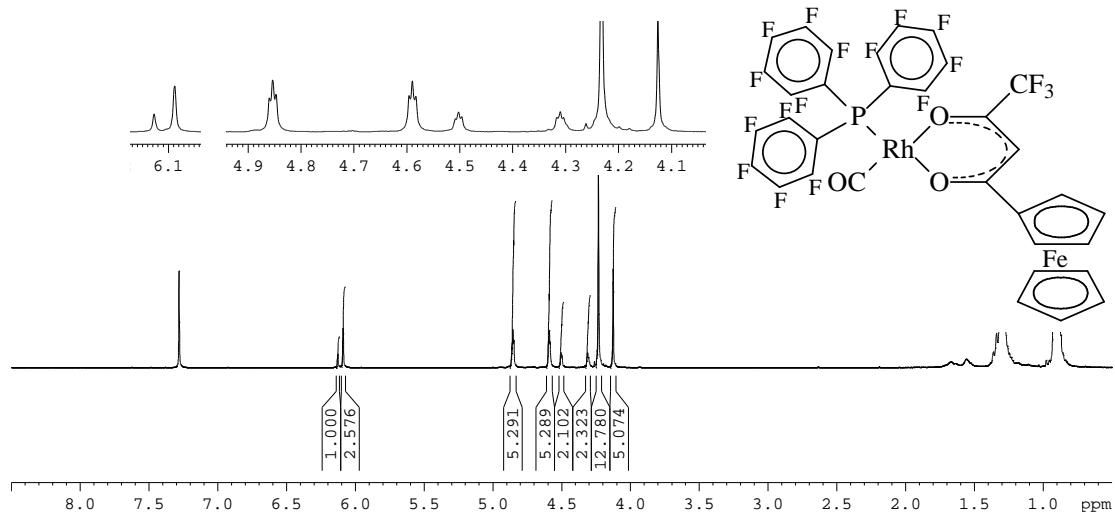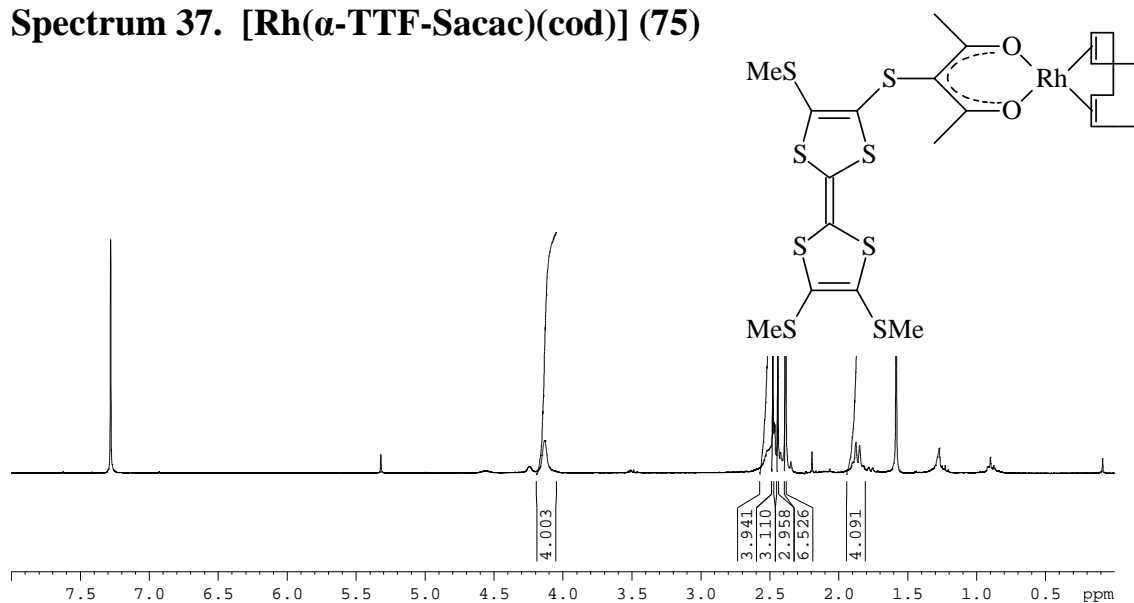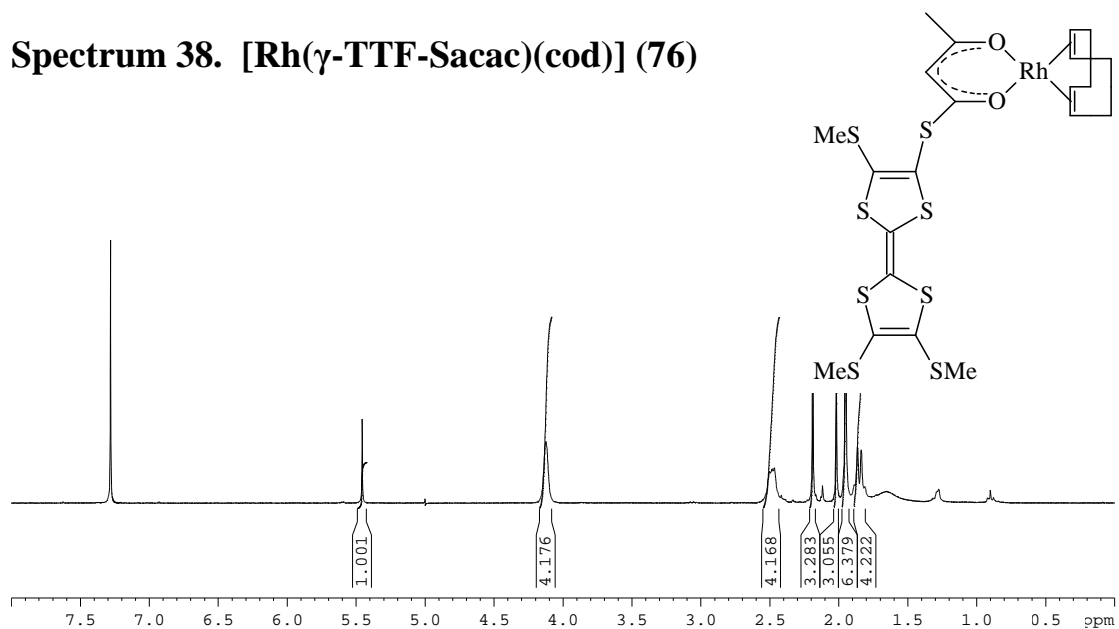
Abstract

Metallocene-containing ligands, as well as their rhodium(I) complexes, were synthesized and their physical properties examined. Four known metallocene-containing β-diketones, $FcCOCH_2COR$ with R = CF_3, Fc, Rc and Oc, were synthesized, as well as a range of metallocene-containing phosphine ligands, including the known PPh_2Fc, and the new ligands PPh_2Rc, PPh_2Oc and the positively-charged $(PPh_2Cc^+)(PF_6^-)$. The new rhodium(I) dicarbonyl complexes $[Rh(FcCOCHCOR)(CO)_2]$, where R = CF_3, Fc, Rc and Oc, were synthesized as starting materials for rhodium(I) phosphine complexes. Electron-rich phosphine complexes, containing metallocenyl-phosphines of the type $[Rh(FcCOCHCOCF_3)(CO)(PPh_2Mc)]$, where Mc = Fc and Rc, as well as the known complex $[Rh(FcCOCHCOCF_3)(CO)(PPh_3)]$, were synthesized. A series of electron-poor phosphine complexes containing pentafluorophenyl rings substituted on the phosphine ligand of the type $[Rh(FcCOCHCOCF_3)(CO)\{PPh_n(C_6F_5)_{3-n}\}]$, with n = 0, 1 and 2, were also synthesized. Crystal structures of $FcCOCH_2COOc$, PPh_2Rc and $[Rh(FcCOCHCOCF_3)(CO)(PPh_2Fc)]$ were solved.

The oxidative addition (the first, rate determining step of the Monsanto process to form acetic acid) of methyl iodide to above mentioned rhodium(I) phosphine complexes were followed kinetically by UV, FT-IR, ^1H NMR, ^{31}P NMR and ^{19}F NMR. Results showed that oxidative addition proceeded by up to three consecutive reaction steps, involving two Rh(III) alkyl and two Rh(III) acyl species. NMR results also showed the existence of at least two isomers of each Rh(III) alkyl and acyl species in the reaction mixture. Large variations in rate constant were observed. The rate of reaction for $[Rh(FcCOCHCOCF_3)(CO)(PPh_2Rc)]$ $\{\chi_R(Rc) = 1.99, k_1 = 0.015$ dm^3 mol^{-1} $s^{-1}\}$ was found to be about double that of $[Rh(FcCOCHCOCF_3)(CO)(PPh_2Fc)]$ $\{\chi_R(Fc) = 1.87, k_1 = 0.0075$ dm^3 mol^{-1} $s^{-1}\}$, with $[Rh(FcCOCHCOCF_3)(CO)(PPh_3)]$ $\{\chi_R(Ph) = 2.21, k_1 = 0.006$ dm^3 mol^{-1} $s^{-1}\}$ slightly slower. Rates of reaction for fluorinated compounds were dramatically slower, due to the highly electron-withdrawing pentafluorophenyl groups attached. $[Rh(FcCOCHCOCF_3)(CO)\{PPh_2(C_6F_5)\}]$ ($k_2 = 0.0003$ dm^3 mol^{-1} s^{-1}) showed rates of reaction of up to 20x slower than that of $[Rh(FcCOCHCOCF_3)(CO)(PPh_3)]$, with

[Rh(FcCOCHCOCF$_3$)(CO){PPh(C$_6$F$_5$)$_2$}] (k$_2$ = 0.000010 dm^3 mol^{-1} s^{-1}) showing rates of reaction 600x slower. [Rh(FcCOCHCOCF$_3$)(CO){P(C$_6$F$_5$)$_3$}] did not undergo oxidative addition at all.

Acetylacetonato ligands substituted with a tetrathiafulvalene group in either the α- or the β-position of the β-diketone were complexed with rhodium(I) cyclooctadiene complexes to form [Rh(cod)(β-diketone)]. The substitution reaction of the TTF-containing β-diketonato ligand with 1,10-phenanthroline was investigated by stopped-flow methods due to the high rate of reaction for these compounds (k$_2$ = 1 x 10^3 dm^3 mol^{-1} s^{-1}).

A full electrochemical study was carried out on all synthesized complexes in CH$_2$Cl$_2$ / 0.1 mol dm^{-3} [N^{n}Bu$_4$][B(C$_6$F$_5$)$_4$] as solvent and supporting electrolyte. Where appropriate, spectro-electrochemical investigations were also performed. This study was also the first to develop techniques able to investigate slow kinetics electrochemically. The reaction used to develop these techniques was the isomerization from enol to keto form of the β-diketone RcCOCH$_2$COFc.

All newly synthesized compounds were tested for anti-tumor activity. It was found that the pentafluorophenyl group is a powerful anti-tumor fragment with significant synergism in [Rh(FcCOCHCOCF$_3$)(CO){P(C$_6$F$_5$)$_3$}]. Group electronegativity (χ_R) is the determining factor for cytotoxicity, in the absence of synergistic effects. An increase in group electronegativity leads to an increase in cytotoxicity. TTF-containing ligands also showed significant activity, but rhodium(I) complexes thereof had no effect.

Keywords: Rhodium(I), ferrocene, phosphine, β-diketone, oxidative addition, substitution kinetics, electrochemistry, group electronegativity.

Opsomming

Metalloseenbevattende ligande, sowel as hul rodium(I)-komplekse, is gesintetiseer en hul fisiese eienskappe bestudeer. Vier bekende metalloseenbevattende β-diketone, FcCOCH$_2$COR met R = CF$_3$, Fc, Rc en Oc, is gesintetiseer, sowel as die reeks PPh$_2$Fc, PPh$_2$Rc, PPh$_2$Oc en die positief gelaaide (PPh$_2$Cc$^+$)(PF$_6^-$) metalloseenbevattende fosfien ligande. Die voorheen onbekende rodium(I)-dikarbonielkomplekse [Rh(FcCOCHCOR)(CO)$_2$], met R = CF$_3$, Fc, Rc en Oc, is gesintetiseer as uitgangstof vir die sintese van rodium(I)-fosfienkomplekse. Nuwe elektronryk metalloseen-bevattende fosfienkomplekse, [Rh(FcCOCHCOCF$_3$)(CO) (PPh$_2$Mc)], met Mc = Fc en Rc, sowel as die bekende [Rh(FcCOCHCOCF$_3$)(CO)(PPh$_3$)], is gesintetiseer. 'n Reeks elektronarm komplekse, wat pentafluoorfenielringe op die fosfienligande bevat, [Rh (FcCOCHCOCF$_3$)(CO){PPh$_n$(C$_6$F$_5$)$_{3-n}$}] met n = 0, 1 en 2, is ook gesintetiseer. Die kristalstrukture van FcCOCH$_2$COOc, PPh$_2$Rc en [Rh(FcCOCHCOCF$_3$)(CO)(PPh$_2$Fc)] is opgelos.

Die oksidatiewe addisiereaksie (die snelheidsbepalende eerste stap van die Monsanto-proses vir die sintese van asynsuur) van metieljodied aan die bogenoemde rodium(I)-fosfienkomplekse is bestudeer met behulp van UV, FT-IR, ^{1}H KMR, ^{31}P KMR en ^{19}F KMR. Resultate het gewys dat oksidatiewe addisie tot drie opeenvolgende stappe behels. Twee Rh(III)-alkiel- en twee Rh(III)-asielspesies is waargeneem. KMR-data het verder minstens twee isomere van elke Rh(I)-alkiel en -asielspesie geïdentifiseer. Groot verskille in die oksidatiewe addisiereaksiesnelhede is waargeneem. Die reaksietempo vir [Rh(FcCOCHCOCF$_3$)(CO)(PPh$_2$Rc)] {χ$_R$(Rc) = 1.99, k$_1$ = 0.015 dm^3 mol^{-1} s^{-1}} is ongeveer dubbel die van [Rh(FcCOCHCOCF$_3$)(CO)(PPh$_2$Fc)] {χ$_R$(Fc) = 1.87, k$_1$ = 0.0075 dm^3 mol^{-1} s^{-1}}, met [Rh(FcCOCHCOCF$_3$)(CO)(PPh$_3$)] {χ$_R$(Ph) = 2.21, k$_1$ = 0.006 dm^3 mol^{-1} s^{-1}} se snelheid effens stadiger. Die reaksietempo's vir fluoorbevattende komplekse was a.g.v. die sterk elektron-onttrekkende uitwerking van die pentafluoorfenielringe dramaties stadiger. Die tempo van [Rh(FcCOCHCOCF$_3$)(CO){PPh$_2$(C$_6$F$_5$)}] (k$_2$ = 0.0003 dm^3 mol^{-1} s^{-1}) was ongeveer 20x stadiger as die van [Rh(FcCOCHCOCF$_3$)(CO)(PPh$_3$)], terwyl [Rh(FcCOCHCOCF$_3$)(CO){PPh(C$_6$F$_5$)$_2$}] (k$_2$

= 0.000010 dm^3 mol^{-1} s^{-1}) ongeveer 600x stadiger was. Die kompleks [Rh(FcCOCHCOCF$_3$)(CO){P(C$_6$F$_5$)$_3$}] het geen oksidatiewe addisie ondergaan nie.

Asetielasetonatoligande wat in of die α- of die β-posisie gesubstitueer is met 'n tetrathiafulvaleen-groep, is met rodium(I)-siklooktadieen gekomplekseer om [Rh(cod)(β-diketoon)] te gee. Die substitusiereaksies van die β-diketonato-ligande met 1,10-fenantrolien is bestudeer met behulp van stopvloeitegnologie, a.g.v. die hoë reaksietempos (k$_2$ = 1 x 10^3 dm^3 mol^{-1} s^{-1}).

'n Volledige elektrochemiese studie is uitgevoer op alle gesintetiseerde verbindings in CH$_2$Cl$_2$ / 0.1 mol dm^{-3} [N^{n}Bu$_4$][B(C$_6$F$_5$)$_4$] as oplosmiddel en hulpelektroliet. Waar van toepassing, is spektro-elektrochemiese studies ook uitgevoer. Hierdie studie was ook die eerste wat in staat was om tegnieke daar te stel waarmee kinetika van stadige reaksies elektrochemies bestudeer kan word. Die reaksie wat gekies is om die tegniek te ontwikkel was die isomerisasie van enol- na keto-vorms van die β-diketoon RcCOCH$_2$COFc.

Sitotoksiese toetse is op alle nuwe verbindings uitgevoer. Daar is gevind dat die pentafluoorfenielring 'n kragtige antitumor-fragment is met beduidende sinergisme in [Rh(FcCOCHCOCF$_3$)(CO){P(C$_6$F$_5$)$_3$}]. Groepelektronegatiwiteite (χ$_R$) is die bepalende faktor vir die voorspelling van die sitotoksisiteit verbindinge. In die afwesigheid van sinergistiese effekte dui hoër groepelektronegatiwiteit op hoër sitotoksisiteit. Tatrathiafulvaleen-bevattende ligande het ook sitotoksiese aktiwiteit getoon, maar nie rodium(I)-komplekse daarvan nie.

I, Eleanor Fourie, declare that the thesis hereby submitted by me for the Philosophiae Doctor degree at the University of the Free State is my own independent work and has not previously been submitted by me at another university / faculty. I furthermore cede copyright of the thesis in favour of the University of the Free State.

Signed: Date:

_____   _____